Design Synthesis Exercise - Group 01 – January 2013

The sustainable future of general aviation

Final Report

Zero EZE

TU Delft Delft University of Technology

Challenge the future

Zero EZE

The sustainable future of general aviation

Design Synthesis Exercise

Final Report

Authors:

S.P.M. BRONE (4001419)
H.I. ÇELIK (1536486)
Y. HABIBZADEH MARZOUNI (4048644)
R. van HARTINGSVELDT (1229281)
B.S.J.W. van LIEROP (4016432)
S. POSTHUMA (4024621)
G. PRINS (4015339)
M.H.R. STUURMAN (1332627)
W.P.J. VREEBURG (1526901)
Y. WANG (4048733)

Tutor:

R.N.H.W. van GENT

Coaches:

M. KOTSONIS
S. SHROFF

January 28, 2013

Delft University of Technology

Abstract

The general aviation industry has suffered from a declining reputation in the last decades. If the industry wants to turn around this reputation and thrive again, a more sustainable approach to general aviation has to be developed. In this approach, low or even zero emission aircraft will be essential. One first step towards this new future, is to redesign Burt Rutan's Long EZ, using near future technology, as a modern, low nuisance, low emission aircraft. To do this a fuel cell based propulsive system is integrated in the design. Using state-of-the-art structures and aerodynamics, the structural weight and aerodynamic efficiency of the aircraft are optimized, accommodating for the extra weight of the propulsive system. If sustainably produced hydrogen is used as propellant, the total emissions of a general aviation flight can be reduced by almost 100% in comparison to fossil fuels. Apart from having a lower range, the Zero EZE is comparable in performance and costs with other general aviation aircraft. These results show that zero emission, fully sustainable general aviation is possible in the near future.

Acknowledgements

> "Appreciation is a wonderful thing. It makes what is excellent in others belong to us as well." - Voltaire

We would like to express our very great appreciation to Ir. Ronald van Gent for his patient guidance, enthusiasm and constructive suggestions. We would also like to thank Ir. Sonell Shroff for her guidance on behalf of the structures and mechanics departement and Dr. Ir. Marios Kotsonis for sharing his extensive knowledge in the field of aerodynamics. Furthermore we would like to thank Ir. T. Woudstra, Dr. P.V Aravind and Ir. A.B. Monteiro Fernandes for donating their valuable time to assist this group with the design of the PEM fuel cell.

Contents

Abstract **I**

Acknowledgements **II**

Executive Summary **1**

Introduction **3**

1 Market Analysis **4**
1.1 Use of GA as Personal Transportation Device 4
1.2 Market Prospects for GA Aircraft 8
1.3 Market Demand for Zero Emission Aircraft 9
1.4 Conclusions on Market Analysis 9

2 Propulsion **11**
2.1 Introduction 11
2.2 Power Sizing 11
2.3 Propeller and Shroud Design 14
2.4 Fuel Cell 20
2.5 Electric Motor 30
2.6 Conclusions 32
2.7 Sustainable Development Strategy 33

3 Layout **34**
3.1 Internal Components Arrangement 34
3.2 Landing Gear 36
3.3 System Interactions 40
3.4 Fuselage Pressurization 42

4 Aerodynamics **44**
4.1 Fuselage 44
4.2 Main Wing 48
4.3 Canard 56
4.4 Winglets 57
4.5 Total Aerodynamic Performance 60

5 Stability **63**
5.1 Definitions and Reference System 63
5.2 Static Longitudinal Stability 63
5.3 Static Lateral and Directional Stability 65
5.4 Dynamic Stability 66
5.5 Linear Simulation 68

6 Flight Controls **70**
6.1 Ailerons 70
6.2 Rudders 71
6.3 Elevators 72

6.4 Overview Control Characteristics . . . 72

7 Structures **73**
7.1 An Introduction to Composite Materials . . . 73
7.2 Material detail design . . . 74
7.3 Manufacturing method . . . 76
7.4 Discussion . . . 79
7.5 Analytical Analysis . . . 81
7.6 FEM analysis . . . 84

8 Performance **99**
8.1 Flight Envelope . . . 99
8.2 Payload vs. Range . . . 99
8.3 Performance and Feasibility Analysis . . . 100
8.4 Compliance Matrix . . . 102

9 Operations & Logistics **103**
9.1 Propulsion System . . . 103
9.2 Structures & Materials . . . 103
9.3 Operations & Logistics Diagram . . . 104

10 Cost and Resource Allocation **105**
10.1 Weight Breakdown . . . 105
10.2 Power Breakdown . . . 106
10.3 Cost Estimation . . . 107
10.4 Cost Breakdown . . . 109

11 Risk Management **110**
11.1 Risk Identification . . . 110
11.2 Conclusions . . . 113

12 Project Development **114**
12.1 Project Design & Development Logic . . . 115
12.2 Post-Project Gantt Chart . . . 115

13 Functional Mission Description **117**
13.1 Functional Flow Diagram . . . 117
13.2 Functional Breakdown Structure . . . 117

14 Sensitivity Analysis **118**

15 Conclusion **120**

Recommendations **121**

Bibliography **122**

A Appendix Cycle-Tempo **128**

B Appendix Airfoil Data **129**

C Appendix Reference System **130**

D Appendix Tornado Model Data **131**

E Appendix Material Properties **132**

F Appendix Functional Mission Description Figures **133**

List of Figures

1.1 The relation between the costs per hour of time savings and the flight distance . . . 7

2.1 Sound Level with respect to Amount of Blades . . . 15
2.2 Lift to Drag 3 bladed propeller . . . 16
2.3 Propeller and shroud layout . . . 17
2.4 SPL distribution Far Field . . . 19
2.5 Single fuel cell composition . . . 21
2.6 Stacking of multiple fuel cells . . . 22
2.7 Schematic view of the total system . . . 22
2.8 Detailed view of the stack cooling [31] . . . 25
2.9 Hydrogen Tank Configuration . . . 29
2.10 Reliability reciprocating engine system . . . 31
2.11 Reliability fuel cell system . . . 31

3.1 Dimensions Electric Motor [mm] . . . 35
3.2 Recommended Cockpit Dimensions Homebuilt Aircraft [in] . . . 35
3.3 Internal Arrangement . . . 36
3.4 Disposition Requirements . . . 37
3.5 Wheel Track . . . 38
3.6 Communication Flow Diagram of the Zero EZE . . . 41
3.7 Hardware Diagram Propulsion System . . . 41
3.8 Electrical Diagrams . . . 42

4.1 Fuselage Shape Concepts . . . 46
4.2 Pressure Distribution Concept 2 . . . 47
4.3 3D Fuselage Shape . . . 48
4.4 Lift coefficient versus angle of attack for five selected airfoils (Re = 5,000,000) . . . 49
4.5 Lift coefficient versus drag coefficient for five selected airfoils (Re = 5,000,000) . . . 49
4.6 Effects sweep on dutch roll stability and lift coefficient . . . 52
4.7 Relation between C_L/C_D and A . . . 52
4.8 Normalized load over span of main wing . . . 53
4.9 Relation between C_L/C_D and the incidence and twist angle . . . 53
4.10 Relation between location main wing and the static margin . . . 54
4.11 GU25-5(11)8 airfoil characteristics (Re = 3,000,000) . . . 57
4.12 Simulation of 25.4 cm blend radius (apollocanard.com, 2012) . . . 58
4.13 Lift coefficient versus drag coefficient for the two selected airfoils (Re = 5,000,000) . . . 59
4.14 Blended winglet design of the Zero EZE . . . 59
4.15 Lift and drag polars cruise conditions . . . 61

5.1 Definitions neutral point computation . . . 64
5.2 Rendering of Zero EZE Tornado model . . . 66
5.3 Response aperiodic roll in linear Matlab model . . . 68
5.4 Response phugoid in linear Matlab model . . . 69
5.5 Response short period in linear Matlab model . . . 69
5.6 Response dutch roll in linear Matlab model . . . 69
5.7 Response spiral motion in linear Matlab model . . . 69

6.1 Control derivatives plotted versus control surface spans . . . 71

7.1 Work flowdiagram structures Zero EZE . . . 73
7.2 Vacuum bagging . . . 77
7.3 Filament winding . . . 78
7.4 Filament winding on mold . . . 78
7.5 Labour hour divisions . . . 80
7.6 Global and local Coordinate . . . 82
7.7 Ply numbering system . . . 83
7.8 Fuselage loadcase . . . 84
7.9 Isogrid . . . 85
7.10 First element and model A in Patran . . . 85
7.11 Displacement (magnitude) in mm . . . 86
7.12 Skin force distribution in y-direction in N/mm . . . 87
7.13 Model B with fixed end and loads applied on the other end . . . 88
7.14 Displacement (magnitude) in mm . . . 88
7.15 Skin force distribution in y-direction in N/mm . . . 89
7.16 First element of Model C . . . 89
7.17 Model C with fixed end and loads applied on the other end . . . 90
7.18 Displacement (magnitude) in mm . . . 90
7.19 Skin force distribution in y-direction in N/mm . . . 91
7.20 Optimization of Model A to Model B to Model C . . . 92
7.21 Surfaces wing . . . 93
7.22 Model of the main wing . . . 94
7.23 Total displacement of the wing, true scale . . . 94
7.24 Shear force distribution and bending moment distribution in the main wing . . . 95
7.25 Equivalent cross section . . . 95
7.26 Eigenmode 1 . . . 97
7.27 Eigenmode 2 . . . 97
7.28 Eigenmode 3 . . . 97

8.1 Flight envelope of the Zero EZE . . . 99
8.2 Payload-range diagram of the Zero EZE . . . 100
8.3 Compliance Matrix of the Zero EZE . . . 102

9.1 Operations and Logistics Flow Diagram . . . 104

10.1 Zero EZE Weight Breakdown . . . 106
10.2 Zero EZE Power Breakdown . . . 106
10.3 Zero EZE Cost Components . . . 108
10.4 Cost Breakdown Structure of the Zero EZE . . . 109

11.1 Risk Map Zero EZE . . . 112

12.1 Project Gantt Chart . . . 114
12.3 Post DSE Gantt chart . . . 115
12.2 Project Design and Development logic of the Zero EZE . . . 116

14.1 Sensitivity Analysis . . . 118

C.1 Reference System Zero EZE . . . 130

D.1 Input data Tornado model . . . 131

E.1 Grid-, skin- and ply properties . . . 132

F.1 Functional Breakdown Structure . . . 133
F.2 Functional Flow Diagram . . . 134

List of Tables

1.1 Overview of the operating costs of the Zero EZE. . . . 6

2.1 Power estimation Zero EZE . . . 13
2.2 Shaft Power estimation Zero EZE . . . 14
2.3 First Results from JavaProp . . . 17
2.4 Noise characteristics - Diameter . . . 18
2.5 Noise characteristics - RPM . . . 18
2.6 Stator Angle of Attack . . . 19
2.7 Final Dimensions and Results Propeller . . . 20
2.8 Hydrogen Tank Options . . . 29

3.1 Landing Gear Dimensions . . . 39
3.2 Weight and arm of aircraft components . . . 40
3.3 Center of Gravity Range . . . 40

4.1 Fuselage Design Constraints . . . 44
4.2 Drag Calculation Fuselage Parameters Zero EZE . . . 45
4.3 Tornado Drag Coefficient Results . . . 47
4.4 NLF(1)-0115 airfoil characteristics . . . 49
4.5 Estimations on wing surface, wing loadings and design lift coefficient . . . 51
4.6 Skin roughness values . . . 55
4.7 Wing skin friction parameters and results . . . 56
4.8 Canard skin friction parameters and results . . . 57
4.9 Winglet skin friction parameters and results . . . 60
4.10 Overview significant lift characteristics for cruise conditions . . . 62
4.11 Overview drag coefficients cruise and landing configuration . . . 62

5.1 Overview results of longitudinal static stability . . . 65
5.2 Stability derivatives of Zero EZE . . . 67
5.3 Results symmetric eigenmotions . . . 67
5.4 Results asymmetric eigenmotions . . . 68

6.1 Maximum control surface deflections . . . 70
6.2 Characteristics of the ailerons, rudders and elevators . . . 72

7.1 Properties of commonly used core materials [99] . . . 75
7.2 Comparison of core material relative costs and their characteristics and benefits [99] . . . 75
7.3 Characteristics of Model A . . . 86
7.4 Results model A . . . 87
7.5 Characteristics of Model B . . . 88
7.6 Results model B . . . 89
7.7 Characteristics of Model C . . . 90
7.8 Results model C . . . 91
7.9 Comparison of Model A, B and C . . . 91
7.10 Parameters from which the gust load factor is calculated . . . 93
7.11 Ply orientation . . . 93
7.12 Moment of inertia of the facing and foam and the stiffness of the wing . . . 94

7.13 Equivalent stiffnesses 94
7.14 Shear force distribution and bending moment distribution in the various surfaces of the main wing 95
7.15 Compressive normal stress in the facing and shear stress in the foam 96
7.16 Table of eigenmodes 96

10.1 All parts and their weight 105
10.2 Component Prices 107
10.3 Total Zero EZE Cost 108

B.1 NASA/Langley NLF Airfoils data 129

Nomenclature

List of Abbreviations

AC	Aerodynamic Center
AC	Aerodynamic Center
AMPR	Aeronautical Manufacturers Planning Report
AOA	Angle Of Attack
APU	Auxiliary Power Unit
AR	Aspect Ratio
AT	Air Traffic
ATC	Air Traffic Control
BOP	Balance of Plant
CBS	Cost Breakdown Structure
CFD	Communication Flow Diagram
CFD	Computational Fluid Dynamics
CPH	Costs Per Hour
ECU	Electric Control Unit
EOM	Equations Of Motion
ETOW	Empty Take-Off Weight
FBS	Functional Breakdown Structure
FEM	Finite Element Method
FFD	Functional Flow Diagram
GA	General Aviation
GE	Ground Effects
GTOW	Gross Take-Off Weight
HLD	High Lift Devices
MLW	Maximum Landing Weight
MTBF	Mean Time Between Failures
MTOW	Maximum Take Off Weight
MZFW	Maximum Zero Fuel Weight
NLF	Natural Laminar Flow
PDU	Power Division Unit
RDTE	Research, Development, Test and Evaluation
SDS	Sustainable Development Strategy
TFC	Total Fixed Costs
TFT	Total flight Time
TVC	Total Variable Costs
VLM	Vortex Lattice Method
VLS	Vertical Launch System

List of Symbols

$(t/c)_{max}$	Maximum thickness to chord ratio [%]
α	Angle of attack [deg]
$\alpha_{L=0}$	Zero-lift angle of attack [deg]
β	Blade Angle, Propeller [deg]

β	Side slip angle [deg]
Δttt	difference in total travel time [hr]
δ_a	aileron deflection angle [deg]
δ_e	elevator deflection angle [deg]
δ_r	rudder deflection angle [deg]
$\frac{1}{2}\rho V^2$	dynamic pressure [Pa]
γ_{12}	Ply Local Shear Strain [-]
γ_{xyo}	Shear Mid Plane Strain in the xy-axis [-]
γ_{xy}	Direct Shear strain in the xy-axis [-]
κ_x	Curvature of Laminate in the x-axis [-]
κ_y	Curvature of Laminate in the y-axis [-]
κ_{xy}	Curvature of Laminate in the xy-axis [-]
λ	Eigenvalue [-]
λ_w	Taper ratio of the main wing [-]
ν_{12}	Major Poisson's Ratio [-]
ν_{21}	Minor Poisson's Ratio [-]
ρ	Density of air [kg/m^3]
ρ_0	Density of air at sea level [kg/m^3]
σ_1	Ply Local Fiber Stress [MPa]
σ_2	Ply Local Off-fiber Stress [MPa]
σ_x	Direct Stress in the x-axis [MPa]
σ_y	Direct Stress in the y-axis [MPa]
τ_{12}	Ply Local Shear Stress [MPa]
τ_{xy}	Shear Stress in the xy-axis [MPa]
ε_1	Ply Local Fiber Strain [-]
ε_2	Ply Local Off-fiber [-]
ε_x	Direct Strain in the x-axis [-]
ε_y	Direct Strain in the y-axis [-]
ε_{xo}	Direct Mid Plane Strain in the x-axis [-]
ε_{yo}	Direct Mid Plane Strain in the y-axis [-]
A	Active Area [m^2]
A	Aspect Ratio [-]
a	Speed of sound [m/s]
a_0	Speed of sound at sea level[m/s]
A_d	Current Density [A/m^2]
A_{ij}	Laminate Membrane stiffness [GPa]
AR_{eff}	Effecitve Aspect Ratio [-]
B_{ij}	Laminate Coupling stiffness [N]
C_f	Skin friction coefficient [-]
C_{D_i}	Induced drag coefficient [-]
C_{f_l}	Skin friction coefficient laminar flow conditions [-]
C_{f_t}	Skin friction coefficient turbulent flow conditions [-]
C_{L_w}	Lift coefficient main wing [-]
$C_{L_{MAXunflapped}}$	Maximum lift coefficient total wing without flaps [-]
$C_{L_{MAX}}$	Maximum lift coefficient [-]
$C_{l_{max}}$	Maximum lift coefficient for infinite wing [-]
$C_{L_{tot}}$	Lift coefficient of total aircraft (main wing and canard combined) [-]
CPH_{total}	Total costs per hour [€/hr]
$D_(ij)$	Laminate Coupling stiffness [N/m]
d_{car}	travel distance by car [km]
d_{flight}	travel distance by aircraft [km]
e	Oswald efficiency factor = 0.85 [-]
E_1	Longitudinal Young's Modulus [GPa]
E_2	Transverse Young's Modulus [GPa]
G_{12}	Ply Shear Modulus [GPa]

GE	Ground Effects [-]
I	Stack Current [A]
L	rolling moment [Nm]
L/D	Lift to drag ratio [-]
M	pitching moment [Nm]
M_{tip}	Tip Speed, Propeller [-]
N	yawing moment [Nm]
n	Number of cells in a stack [-]
N_x	Laminate in-plane force per unit width in the x-axis [N/m]
N_y	Laminate in-plane force per unit width in the y-axis [N/m]
N_{xy}	Laminate in-plane force per unit width in the xy-axis [N/m]
P	Period [s]
P	Stack Power [W]
p	roll rate [deg/s]
q	pitch rate [deg/s]
Q_{ij}	Reduced Stiffness [Gpa]
r	yaw rate [deg/s]
$S_{flapped}$	Surface reference area flaps [m^2]
S_{LO}	Take Off Distance, ground run [m]
S_{ref}	Surface reference area [m^2]
S_{wet_w}	Wetted surface area wing [m^2]
S_{wet}	Wetted surface area total aircraft [m^2]
S_w	Surface area main wing [m^2]
$T_{\frac{1}{2}}$	Time-to-half-amplitude [s]
t_{ascent}	flight time ascent [hr]
$t_{descend}$	flight time descend [hr]
t_{flight}	flight time [hr]
$t_{groundmaneuvring}$	time spent ground maneuvering [hr]
tft	Total flight time [hr]
ttt_{car}	total travel time using a car [hr]
ttt_{GA}	total travel time using a GA aircraft [hr]
V	Stack Voltage [V]
v	Cell Voltage [V]
$V/(nD)$	Advance Ratio, Propeller [deg]
V_{LO}	Take Off Speed [m/s]
w_i	weight particular component aircraft [kg]
x_i	distance to COG of particular component with respect to reference line [m]

Executive Summary

General aviation has the potential to grow significantly in the near future, provided that certain barriers are overcome. The negative image regarding sustainability and the high operating costs for this form of transportation are problems that need to be dealt with. Progress can be made by increasing the quality, decreasing the costs and providing a solution to the environmental issues currently associated with general aviation. This report elaborates the design of the Zero EZE, a sustainable aircraft with low operational costs, based on Burt Rutan's Long-EZ. This Design Synthesis Exercise started first off as a project to redesign the Long-EZ into a hybrid propelled aircraft. However this objective changed radically when it turned out that a fuel cell powered aircraft, with a zero emission advantage, was feasible. The Zero EZE was born, representing the sustainable future of general aviation!

Before initiating the general design of the Zero EZE, knowledge has to be gained considering the power needed to guarantee that this aircraft can meet the requirements. These power calculations depend on the weight, the efficiency, the lift and the drag produced by the entire system and are altered throughout the course of this project. The maximum power that has to be delivered by the power source is 110 kW. To translate this power into motion, a three-bladed propeller has been designed, optimized for the cruise conditions. By implementing a stator system and a shroud, the efficiency of the propeller system becomes 88,6 %. By reconfiguring the diameter and the RPM of the propeller, the near field noise has been optimized to a value of 117 dB. When the airplane reaches the cruise height of 3000 meter, the sound pressure level on the ground will be 61 dB, which is comparable to a normal conversation and within regulations.

The power will be provided by two hydrogen fuel cells, capable of delivering a net power output of 122.5 kW with an efficiency of 49%. By placing these fuel cells in a parallel configuration, both reliability and safety are assured. One fuel cell is capable of delivering enough power to continue the cruise and landing phase in case of an emergency. The hydrogen will be supplied by multiple tanks, pressurizing the fuel to 700 bar, with a combined storage space for 15 kg of hydrogen. The fuel cells are accompanied by an auxiliary power unit, which can deliver the required power for startup and peak powers for the brief moment the fuel cell needs to shift to a higher power output. The electrical power provided by the fuel cell is converted to usable mechanical energy through the use of an electrical motor. This motor has a high reliability and can cope with peak powers of 220 kW, with an efficiency of 95%. The total efficiency of the propulsion system becomes 39% and the total 'mean time before failure' becomes 48.200 hours.

After sizing the propulsive system, the fuselage is designed. A low drag body has been analytically optimized to minimize the drag. The main wing and canard are optimized to create a high lift versus drag ratio and are equipped with winglets to reduce the induced drag. The canard has been redefined, and control surfaces are designed to ensure stability. By creating a retractable landing gear, a favorable flow is ensured, resulting in low drag and low interference with the propeller. The total lift to drag ratio for this aircraft will be approximately 18, which is high compared to other general aviation aircraft.

For the fuselage, an Advanced Grid Stiffened Structure is used. This is an innovative structural layout which has many advantages, such as a high damage tolerance, high resistance to buckling and no corrosion. The production of the fuselage will be done by an automated filament winding. A sandwich structure is chosen for the wing; here a prepreg lay up method is used as manufacturing method. Both the grid and the skin of the fuselage and wing will be constructed out of carbon fiber reinforced polymer. To ensure the strength of the structure, a Finite-Element-Method-analysis is performed. From this the grid was optimized, with at the same time ensuring sufficient resistance to the maximum applied loads. For the

structures a weight of approximately 88.6 and 85 kg was found for the fuselage and wing, respectively.

For the performance analysis of this design, the maximum cruise speed and maximum speed are found to be 166 kts and 200 kts, respectively. The maximum range and rate of climb is found to be approximately 1300km and 4.5m/s. At maximum throttle and load, the take-off distance is defined to be 490m. The noise requirements are achieved, since at a distance of 3000m, 61 dB is produced. These values were found to be compliant to the initial requirements, with exception of a few which are explained by the drastically changed project goals.

For the Zero EZE a cost and resource allocation was made, this investigation was subdivided into four parts. First a detailed weight breakdown is made, here it is seen that the major weight contributors are the hydrogen tanks. Secondly a power breakdown was performed where the main parts are found to be the fuel cell, electrical motor and propeller. When designing the power system, the efficiency of these three elements are taken into account. The third and fourth part, present the cost estimation and breakdown. From this section a purchase price of €472,500 is found. The profit was assumed to be 10% of the total manufacturing cost, which is well in line with other manufacturers.

To perform the risk analysis of this project, a risk map is made. Each potential risk is given a grade regarding its probability and consequence. The most critical risks are found to be the cost of the system, the time to market, the legislation of the Zero EZE and the nuisance aspect. For these main risks, a mitigation plan is made. Considering the cost, a safety margin is taken into account. For the time to market no real guarantee can be provided, however the expectations towards a highly suitable fuel cell are very high. The legislation factor especially affects the cost of the project; this risk can only be reduced and not entirely mitigated. To decrease the noise, a SRP and shroud are implemented. If this latter risk is inevitable, the project will not fail. However the reputation of the product will become worse.

To perform the sensitivity analysis of this project a closer look was taken to the main system parameters which are found to be the weight, lift, drag, performance requirements and overall efficiency of the system. From this the relation between the main output is investigated. The conclusion was made that the design of the Zero EZE has great adaptability and flexibility. These two aspects, that are highly favorable to have, ensure sufficient resistance with respect to any changes in the main input of the design.

As in every innovative design, recommendations towards future research are also presented in this Final Report. The most important recommendations have their focus on the main parts of this report. For the aerodynamics this is found to have more elaborated Computational Fluid Dynamics analyses, together with wind tunnel tests to improve the accuracy of the results. For the propulsion part the recommendations were to optimize the main subcomponents, by improving their efficiency and integration in the total design. For the propeller the incoming flow and interference between the blades should be more thoroughly investigated. Considering the structural part, the main recommendations are towards a more extensive research for the used grids and integration of the subcomponents.

Introduction

Making a significant change in the world of general aviation. That is not just a dream, but something which can be accomplished with the innovative design of the Zero EZE. With sustainability and safety as our main focuses, this group is proud to present a GA aircraft with zero emissions. The initial assignment was to redesign the Burt Rutan Long EZ into a hybrid-propulsed aircraft. Soon it was found that there is no good reason to design a semi-electric aircraft if a fully electric aircraft is feasible by the year 2020. Fuel cells and the accompanying hydrogen tanks will see significant improvement in the coming years. Combining this propulsion system with innovative aerodynamic and structural redesigns a big step forward can be made in the general aviation world. With medium range business trips as main use for the Zero EZE, it is important to offer a fast and easy accessible way of transportation between major economic cities. The Zero EZE fulfils these requirements and gives GA a green reputation at the same time.

Based on the previous findings in the Baseline and Mid-Term report, the detailed design will be presented in this Final Report. The fuel cell system has been analyzed and further developed for implementation in the aircraft. This required a lot of work, but the desired result has been accomplished. For the aerodynamic design a significant drag reduction has been obtained by optimizing the fuselage, wings, winglets and shroud. Furthermore, lighter materials and a state-of-the-art structural design have provided a weight reduction for the aircraft structures. Since the Long EZ was a very innovative design by that time, all these accomplishments are not as obvious as they seem to be. This report offers all required information to further develop, produce and operate the Zero EZE in the coming years.

This report starts with Chapter 1, where a concise market analysis for the Zero EZE is given. In Chapter 2 the propulsion system of the aircraft is explained, including important subsystems like the fuel cell, electric motor and propeller. This is followed by the layout of the aircraft in Chapter 3 with the overall configuration and the placement of the subsystems. In this chapter also the sizing of the landing gear can be found. When the internal layout of the aircraft is known, the aerodynamics can be presented in Chapter 4. The fuselage, main wing, winglets and canard are optimized in this chapter to reduce drag and increase lift. When the aerodynamic design is finished the static and dynamics stability of the aircraft is determined in Chapter 5. Based on the stability characteristics of the aircraft, the eigenmotions can be simulated. Following the stability of the aircraft, the flight controls can be sized in Chapter 6. The stability and controllability of the aircraft have to be assured to guarantee the passenger a safe flight. After this the third major part in the design, the structural redesign, is presented in Chapter 7. An extensive FEM calculation is combined with analytical methods to achieve structural optimization. In Chapter 8 a performance analysis is made by collecting data from all the subsystems of the Zero EZE. With the technical analysis finished, some non-technical aspects of the design are addressed. For the operational phase of the Zero EZE the operations & logistics are organized in Chapter 9. This is followed by the cost and resource allocation in Chapter 10. When the estimated costs are exceeded an aircraft can not be produced, which makes this part essential. In Chapter 11 an update is given of the risk assessment for the Zero EZE design and production. After this the project development and functional mission description are shown in Chapters 12 and 13, respectively. To analyze the adaptability of the design to changes, a sensitivity analysis is performed in Chapter 14. Finally, the conclusions of the entire project are given in Chapter 15.

Chapter 1

Market Analysis

In this section the future market for the Zero EZE is analyzed. Before the actual design process starts, it is important to know whether it is interesting from a business perspective to invest in the project. A full scale market analysis is not within the scope of this report. In this report a general analysis is done on what performance is necessary to be able to compete with the available personal transportation options. The focus will be on short flights up to 1300 km or 700 nm.

In the analysis a comparison will be made to the use of a car as personal transportation device. This analysis can be subdivided into three components. Firstly, in Section 1.1, an assessment is made for the use of a GA aircraft for a single user. Especially, the effect on costs and environment will be considered. Then, in Section 1.2, the market for GA aircraft in the business related personal transportation sector is discussed. Conclusions from the European Personal Air Transportation Study (2008) are a leading source in this section. In Section 1.3, the attractiveness of using hybrid aircraft in this sector is discussed. Finally, in Section 1.4 an overview of the main conclusions of the market analysis is given.

Commercial Airliner An obvious alternative to the use of GA would be using a commercial airliner. Calculating the average total travel time of trips up to 1300 km using commercial airliners is quite difficult. To do this, the availability and flexibility of flight should be included, which comprises the average taxi time at major airports, average delay and average time loss due to unavoidable transfers. However, it is possible to make some general remarks.

Firstly, the commercial airliners only offer a limited number of flights, so it does not offer the flexibility a GA aircraft or car does. Even on the most frequent flight routes there are rarely more than 10 flights per day. Especially if multiple destinations have to be reached on a single day, it will be increasingly difficult to create an efficient schedule. Secondly, for short flights (up to 800 km) the travel time is not going to be much faster (if at all), due to the fewer available airports, higher taxi duration, delays and waiting lines for customs on large airports. Thirdly, the costs for commercial flights can be said to be comparable with the prices of transportation by car (or only slightly higher). This is for the distances considered, up to 1300 km.

1.1 Use of GA as Personal Transportation Device

In this section the effects of using a GA aircraft as a transportation device are discussed. This is done by comparing the performance of a GA aircraft to a car, paying special attention to the costs and emissions.

1.1.1 Door to Door Travel Time

A few remarks should be made, in order to get a sensible estimate on the travel time. First of all, the calculations are based on the use of small GA airports. The logistics of using large airports is much more complicated and will consume more time. Secondly train transportation will not be taken into account. This is mainly because the public transportation system has been around a while (including the modern fast train connections) and it has not proven itself as a realistic alternative for most personal transportation in the high end business sector.

GA The internet provides excellent overview of all available airports in the world. Research shows that most of the major cities in Europe and America, the two biggest markets for GA, have small GA airports within a 50 km range. [1] [2] [8] Since most companies will reside in major cities, this distance is used as the average travel distance from door to airport and from airport to door.
The total travel time (ttt) in hours can be found by using Equation 1.1.

$$ttt_{GA} = t_{flight} + 2 \cdot t_{door \rightarrow airport} \tag{1.1}$$

The flight time can be divided into several components; the ascent, the cruise, the descent and the ground maneuvering. The following values are assumed, based on an electrically powered vertical airspeed of 5 m/s and a cruising altitude of 4000 m:

- Ascent: 0.20 hours at 0.8 times cruise speed
- Descent: 0.15 hours at 0.8 times cruise speed
- Ground Maneuvering: total of 0.20 hours

The flight distance is indicated by d_{flight} in km and the cruising speed by V_{cr} in km/h. The flight time can now by calculated with Equation 1.2.

$$t_{flight} = t_{groundmaneuvering} + t_{ascent} + t_{descent} + \frac{d_{flight} - (t_{ascent} + t_{descent}) \cdot 0.8 \cdot V_{cr}}{V_{cr}} \tag{1.2}$$

Assuming an average speed of 60 km/h and a 50 km range, the travel time on the ground (door to airport and airport to door) is found to be one hour and 40 minutes.

Car The travel time by car can easily be calculated. Quick research on the web showed that for travel by car a inefficiency factor of 1.2 should be taken into account with regards to the travel distance. This is because on average the roads do not run straight from departure to finish. For long distances an average speed of 100 km/h is assumed. This is consistent with leading travel planner websites. The total travel time by car is shown in Equation 1.3.

$$ttt_{car} = \frac{d_{car}}{100} = \frac{d_{flight} \cdot 1.2}{100} \tag{1.3}$$

Also, the difference in total travel time can be calculated with Equation 1.4.

$$\Delta ttt = ttt_{car} - ttt_{GA} \tag{1.4}$$

For example, if an airspeed of 150 kts is assumed and an equal flight- and car distance of 1000 km, the following travel times can be calculated; $ttt_{GA} = 5.56$ hours, $ttt_{car} = 12$ hours and $\Delta ttt = 6.44$ hours.

1.1.2 Average Operating Costs

In this section the average operating costs of both the Zero EZE and a business lease car will be compared. First the total operating costs for both alternatives is calculated. Then the costs per hour of time savings are calculated.

Zero EZE It is difficult to get an accurate estimation on the operation costs of the Zero EZE. This is because several major systems are not yet available on the market. This means that assumptions have to be made for maintenance and replacement costs. These assumptions are based on the operating costs of a Diamond DA12 Twin Star, adjusted for the systems used in the Zero EZE. The purchase price is based on the cost estimation performed in Section 10.3.

The maintenance, inspection and insurance costs were assumed about 1.25-1.5 times higher than the Diamond, since the systems used are new in the market. The average time to replacement for both the electrical engine and the fuel cell was assumed to be similar to piston engines. The engineering costs were assumed to be also slightly higher due to the new technology.

In general the costs can be divided into fixed and variable costs. The variable costs are fixed per flight hour, while the fixed costs per flight hour will decrease when the total number of flight hours per year is increased. In Table 1.1 an overview is given of all the costs.

Table 1.1: Overview of the operating costs of the Zero EZE.

Fixed Costs per year	
Depreciation (5% of purchase price €476.000)	€23.625
Maintanance and Inspections	€15.000
Insurance	€20.000
Hangar and Tie	€2.500
Avionics system subscriptions and updates	€1.000
Total Fixed Costs (TFC)	**€62.125**
Variable Costs per hour	
Engineering costs (including overhaul engines and propeller)	€90
Hydrogen	€15
Total Variable Costs (TVC)	**€105**

The total costs per hour (CPH) of flight can now be calculated with Equation 1.5.

$$_{total} = (TVC + \frac{TFC}{tft}) \cdot ttt_{GA} \tag{1.5}$$

Here CPH_{total} is the total costs per hour flight, TVC the total variable costs, TFC the total fixed costs and tft the total number of flight hours per year.

Car The costs of using a car can easily be determined, using a simple, yet representable, example. As an alternative to the GA aircraft the lease of an Audi A6 is analyzed. It is convenient to express the total costs for using the car in €/ km.

The lease of an Audi A6 is approximately €800 per month [11]. The travelling distance is assumed to be approximately 35000 km [12]. According to Audi, the car should be able to perform 100 km on 7.3 liters of standard fuel. This means, the total costs per year will be €14199. This equals €0.41 / km.

However, the usage costs of the car are not the only costs involved when travelling large distances. It has been shown that on average people travel only 800 km per day and then spend 10 hours for a stop. Of these 10 hours, 8 hours is considered sleep, so the remaining 2 hours can be added to the travel time. The costs for an accommodation are estimated to be €150 on average for business people. All these estimations are based on research performed by Williams and Weiss in 2002 [13]. So for every 800 km of driving, an additional 2 hours are added to the travel time and €150 to the travel costs.

1.1.3 Cost Benefit Overview

To make an accurate assessment on using a GA aircraft as personal transportation, it is interesting to see what the additional costs are (in comparison with using a car) per hour of time savings. Using the calculated time savings and costs in the previous sections, Figure 1.1 can be obtained.

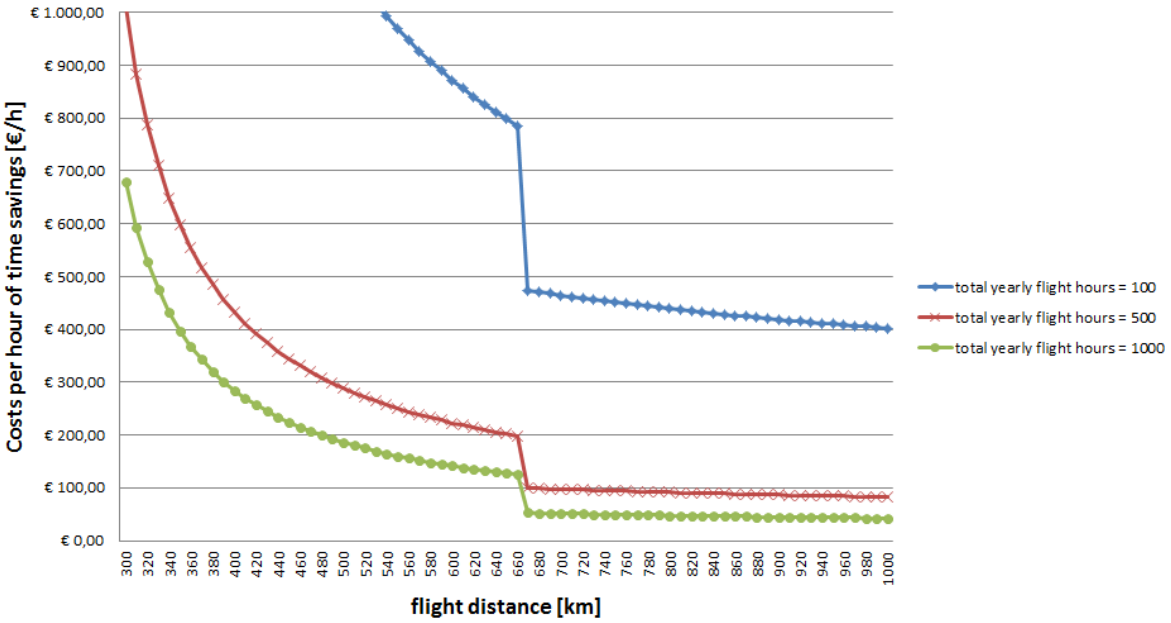

Figure 1.1: The relation between the costs per hour of time savings and the flight distance

When considering this Figure, some conclusions can be drawn. First of all, it shows that if the buyer is unable to use the aircraft a high number of hours per year, the costs can go up to the order of €1000 per hour time savings or higher. Since the projected range of the Zero EZE is approximately 750 km, it can be seen that to bring the costs per hour of time savings under €100, the aircraft has to fly at least 500 hours per year. If however, the buyer is able to efficiently put the aircraft to use and achieves 1000 flight hours per year or more, the costs can go down to €50 for flights of maximum range. Furthermore, the sudden drops in the graphs can be explained by the fact that when a stopover is made with a car, extra costs are made and extra time is spent, as explained earlier. This means that the costs difference per hour between a GA aircraft and a car suddenly drops overnight.

A factor that has not been taken into consideration when making the comparison is hiring a driver. It is quite common for business people to hire a driver for approximately €20/h, to give them the opportunity to work in the back of the car. In a plane this would of course be much harder. The effectiveness of the hours of work in the back of the car are difficult to quantify. However, it could in theory shift the costs per hour of time savings even higher up.

1.1.4 Emission Comparison

In this section a brief analysis will be made on the total emissions of the Zero EZE and a car. Other effects on the environment will be discussed in the next section on market prospects.

For a car, the estimation can be made quite simply. Like before, it is assumed the traveling distance by car is 1.2 times the traveling distance of the aircraft. It can be assumed that the total damaging emissions are 120 g/km, which is average for the Audi A6. For the Zero EZE the damaging emissions during the flight are zero. However, as will be discussed more elaborate in Chapter 2 the total emissions of the Zero EZE depend on the emissions during the production process of the hydrogen. These emissions can be brought down to almost zero too, if renewable energy sources are used in the process. This means that the total damaging emissions that can be saved by flying the Zero EZE over driving a car can be expressed by Equation 1.6

$$totalemissionssavings = 120g/km \cdot d_{flight} \cdot 1.2 \tag{1.6}$$

For a flight near the projected range of the Zero EZE (700 km), this leads to an emissions saving of 100.8kg per flight. This is the equivalent of three coniferous seedlings that grow for 10 years. Per year up to 40 tons could be saved (when operating 1000 flight hours), equivalent to the total emissions of two complete homes [14].

As already discussed previously in the baseline report, the emissions of a conventional GA aircraft is on average 1.5-2 times higher than the emissions of a car. This means that in comparison to other GA aircraft the Zero EZE can obtain even higher savings.

1.2 Market Prospects for GA Aircraft

In this section the potential for the GA aircraft market is discussed. As mentioned in all reports of EPATS and SATS, this is very difficult to predict, mainly due to the lack of solid data. However, both EPATS and SATS have made estimations in the past on how the market will develop. These reports will be assessed in this section. There are some difficulties in doing this. SATS has seriously dialled down its research after the terrorist attacks of 9/11 in 2001. Because of this, hardly any studies are available from 2001 on. This means that the reports that are available from SATS are mostly outdated.
EPATS has continued it's research after 9/11 and did some very elaborate studies in 2007-2008 on the GA market prospects. This study however, was just before the major economic crisis of 2008. Before 2008 the market growth was over 15%. [15] Because of that, it shows way too optimistic prospects. Still, some interesting remarks about the market can be made.

In this section firstly the general potential for the GA market will be discussed. Secondly the role for single engine propeller aircraft in this prospect. Lastly, the demand for a zero emission aircraft in the market is discussed.

EPATS EPATS is best described by their full name, European Personal Air Transportation System. It is a system which promotes a very abundant offer of personal aviation possibilities, from small piston engined aircraft to large private jet aircraft. Also, an elaborate network of small GA airports is incorporated to create a system that allows people to transfer fast from door to door, using personal air transport, with minimal costs. This system however, is not at all active yet. The capacity and diversity of the services available in the market is not nearly enough.

Europe vs. USA Because EPATS is focussing on Europe in her studies, it does not include the American market. The report concludes however, that the market prospects could be quite comparable, because the spread of the GA airports and the funds available are similar for the USA and Europe. In the USA there are over five times more GA aircraft available per capita than in Europe. EPATS concludes this is due to differences in regulations, administrative rules and the involvement of local governments in making it more attractive to use a GA aircraft for personal transport [2]. For the European market to be fully comparable to the USA market, a more cooperative attitude and flexibility of governments is necessary.

1.2.1 Potential for GA market

The conclusions of EPATS on the general market prospects must be interpreted in light of the large economic growth when the report was written. This means that the conclusions on the market growth and predictions on the number of required flights and aircraft cannot be considered accurate. Also, it is hard to scale these quantities to the current market.

However, there are some very interesting conclusions that still can be considered valuable.

- Even though the market is currently, in light of the economic crisis, not growing, it is sensible to believe that it will continue with growing when the economy will start to grow again. This is because flying a GA aircraft has become more and more attractive in the last decades, whereas the alternatives, such as transport by car or commercial airliners, have not seen the same progress. This is due to improvements in safety, efficiency, costs and flexibility.

- Transport by a GA aircraft is not quite as safe as commercial airliners, but still safer than transport by car. Especially if you take into account the fact that most accidents in GA occur with very old aircraft and it is likely in business transport relatively new models will be used [3].

- There is already an abundant offer of GA airports throughout Europe and the USA. Especially in Europe the number of itinerant operations is far below the capacity. These airports still have a lot of capacity to spare at the moment. [3]
- Even though the prospects in the EPATS report can be considered too optimistic, it does show that when the current GA fleet and services are expanded, the potential profits in time and money savings can certainly still improve.

1.2.2 The Role of Single Engine Propeller Aircraft in Personal Air Transport

Since the EPATS report focuses on personal air transport in general, a short analysis should be made on the role of single engine propeller aircraft in the prospects. A few conclusions can be summarized:

- Research shows that 74% of all business related trips are between 100-400 km. The car is the most dominant means of transport in this segment. Only for trips over 600 km air transport becomes dominant. [3]
- Single engine propeller aircraft are efficient for trips up to 600 km. For trips of over 600 km jet engined aircrafts are more efficient. Moreover, piston engined aircraft also produce less pollution in comparison to other GA aircraft on short flights [3].

This shows that single engine propeller aircraft are most efficient for short flights (under 600 km), but have strong competition from transport by car in the current market. As already previously concluded, this is mostly due to the high costs of using air transport for these short distances.

1.3 Market Demand for Zero Emission Aircraft

Even though the performance and costs of the Zero EZE are comparable to the current generation of GA aircraft, there are strong reasons to believe that the zero emission label of the Zero EZE increases the attractiveness of using the aircraft for personal transport.

First of all, by using zero emission aircraft like the Zero EZE, the general environmental footprint of GA can be reduced drastically. This is a focus of most (large) companies today and can thus make it more interesting.

Moreover, a major environmental problem and one of the reasons of the reticent attitude of the European market, is the opinion of society towards GA [4]. This can be improved if more zero emission or hybrid airplanes are used, which leads to lower nuisance in airport areas and a 'greener' label of the industry. To achieve this, noise reduction should also be a major focus. Already, modern planes show a reduction in noise, both the actual aircraft and the relative noise per passenger [4].

Lastly, as was discussed previously in the Mid Term Report, the total fuel costs of a fuel cell system would in the current market already be 12% less than a conventional kerosene propelled GA aircraft. Hydrogen is however expected to drop another 50% or more in price in the next decade, whereas fossil fuels are expected to increase in price. [5] [6] [7]

1.4 Conclusions on Market Analysis

When combining the analysis of the personal use of a GA aircraft for transportation and the general market analysis, several conclusions can be drawn.

- The GA market has the potential to grow in the future. Even though the economic crisis is making people and businesses reluctant to invest at the moment, still a lot of progress can be made in increasing quality and decreasing costs. Also, GA remains to be safer than transport by road.
- There is already a good infrastructure with a large amount of airports available in both the USA and Europe. Especially in Europe this system has not nearly reached its maximum capacity.
- Single engine propeller aircraft are of all GA aircraft most efficient for flights up to 600 km.

- The usage costs of small GA aircraft are quite high. For a GA aircraft to be financially interesting, the value of time savings is between €100 and €1000, depending on the hours of flight per year and the flight distance. Only if the aircraft is used more than 500 hours per year and the flight is 700km or over, the costs go below the €100.
- Zero emission aircraft can definitely make it more interesting for people or companies to invest in a GA aircraft. It can give a very green label to your person or company. This is in contrast with the current attitude towards GA.
- It is important that an effort is made to decrease the nuisance for society, to give the GA industry a better reputation. Noise reduction and less pollution are the most important factors to reach this goal.

Chapter 2

Propulsion

2.1 Introduction

In this chapter the detailed design of the propulsion system is elaborated. As determined in an earlier phase of this project, the required power is delivered by a SRP, fuel cells and a brushless DC electrical motor. Since the propulsion system is based on the required power during take-off, cruise and landing, the power budget has to be determined first. This can be found in Section 2.2. The propellers are sized using a program called JavaProp, which can be found in Section 2.3. A shroud is designed around the propellers to increase the performance, which is also part of Section 2.3. Section 2.4 gives the design of the fuel cell propulsion system and the storage of the hydrogen. The electrical motor selection is discussed in Section 2.5. This Section also elaborates the efficiency and the reliability of the entire propulsion system. Finally, the conclusions of all sections are summarized in Section 2.6.

2.2 Power Sizing

To size the fuel cell based propulsion system, the required power to perform the several manoeuvres has to be defined. This was done in an earlier phase of the project, however this is redone in a more detailed and accurate fashion. The previous estimation of 108.9 kW was based on conventional aerodynamic data available for general aviation and an estimation for the propeller efficiency of 84% [65].

Before initiating this section, different definitions of 'power' are explained. Three kinds are presented; the required power, the available power and the excess power. The power required, according to Ruijgrok [23], represents the power that is needed to perform the flight at a specific flight velocity. The excess and available power are defined in following sections, the relation between these terms is described in Equation 2.1. In this section it is seen that the aerodynamic properties of the airplane determine the estimations concerning the power output, the powerplant itself determines the available power.

$$P_{available} = P_{required} + P_{excess} \tag{2.1}$$

In this stage of the project the aerodynamic properties are specifically defined, this makes it possible to estimate the power requirements in a more detailed fashion. To determine the required thrust, the lift to drag ratio of the aircraft has to be known. To do so, first the lift coefficient at cruise speed is defined. This speed was depicted in the requirements to be 150 kts or approximately 280 km/hr. For this the basic lift equation is used, as can be seen in Equation 2.2. The assumption of steady symmetric flight was made, where the lift factor equals the weight factor.

$$C_L = \frac{W}{\frac{1}{2}\rho V^2 S} \tag{2.2}$$

For this equation, the weight was previously estimated to be 800 kilograms. This seems to be too optimistic and the value is changed to 1200 kg, since the concept of the aircraft and its propulsion system are also drastically altered. The surface of the wing is now fully defined as seen in Section 4.2, here a value of 14.67 m^2 is defined, for both the canard and the main wing.

Secondly, the aspect ratio is defined, this is again possible due to the fully known wing geometry.

$$AR = \frac{b^2}{S} \tag{2.3}$$

The following step is to calculate the drag coefficient. The zero lift drag-component consists of the drag component of the fuselage, the wing and the remaining parts; such as the propeller, shroud, landing gear, etc. The latter value is estimated to be 25 % of the total of the other two components. From this the total zero lift drag component has a value of approximately 0.013. Now the drag component is calculated by Equation 2.4.

$$C_D = C_{D,0} + \frac{C_L^2}{\pi e AR} \tag{2.4}$$

Here, 'e' represents the Oswald Efficiency Factor and is found to be 0.85. From these results the lift over drag coefficient is found, from which the required thrust factor is found, as shown in Equation 2.5 [24]. For the sake of clarity; this thrust is required to fly at the given velocity of 150 kts in level, unaccelerated flight.

$$T_{required} = \frac{W}{\frac{L}{D}} \tag{2.5}$$

Note that, for this aircraft, power estimations will be expressed in terms of shaft power. For this reason it is more convenient to examine the performance in terms of power required and power available.

From this the power can be found, using Equation 2.6.

$$P = T \cdot V \tag{2.6}$$

This power value is calculated according the cruise speed, obviously this can be calculated for every speed the aircraft will have to fly.

The required power is now defined. Only implementing this amount of power in the design is not sufficient. The maximum rate of climb is also depicted in the requirements of this project, being 500 fpm or 2.54 m/s. To be able to perform this maximum rate of climb, the difference between the power available and the power required should be large enough. This ensuring enough excess power and meaning that the excess power refers to the power that is required to climb. The relation between excess, available and required power was already given in Equation 2.1. To determine the needed excess power, Equation 2.7 can be used [23].

$$RC_{max} = \frac{P_{excess}}{W} \tag{2.7}$$

To obtain the power available, the required power, used for cruise speed has to be added to the excess power.

At this stage, the power required, excess power and power available are determined. The power required was found to be 50.6 kW, the excess power to be 29.9 kW and added together the power available had a value of 80.5 kW.

The meaning of this power available is that the aircraft will be able to perform maximum rate of climb, while still flying at cruise speed. However, until now all the calculations were performed without taking the efficiency losses of the propeller into account. To size the engine correctly, the propeller efficiencies have to be included. According to Ruijgrok [23], the available power is obtained by multiplying the brake power of the engine with the propulsive efficiency of the propeller, this can be seen in Equation 2.8

$$P_{br} = \frac{P_{available}}{\eta_{propeller}} \tag{2.8}$$

Here P_{br} represents the shaft power, which is the power the engine actually has to deliver and on which the aircraft is designed. To obtain the shaft power, the efficiency of the used propeller has to be known. This is found, by the use of the program JavaProp, to be 88.6 % during cruise or 69 % at take off and landing, as can be seen in Section 2.3. This due to the fact that the propeller was designed for cruise conditions. Since the power required is calculated in 'extreme' conditions, the efficiency can be taken as a constant, this because after a certain speed, the efficiency is seen as a constant value [23].

In Table 2.1 the required power, excess power, available power and shaft power are presented. For the shaft power the propeller efficiency is implemented as well as the efficiency of the electric motor, which is defined to be 95%. This table shows that to fly at a cruise speed of 150 kts, while climbing at 500 fpm, 96 kW is required, with all the efficiency losses included.

Table 2.1: Power estimation Zero EZE

Required Power	50 kW
Excess Power	30 kW
Available Power	81 kW
Shaft Power (SRP)	96 kW

These results have somewhat larger values than the currently available Long EZ, from the owner's manual [65], the available power is found to be 72 kW. This can be explained by the higher weight and improved aerodynamic properties.

2.2.1 Take-off Power Requirements

The power estimations are also performed for take-off conditions. This was necessary to estimate the power usage during a typical flight. The take-off requirement is based on the minimum available ground run, at maximum available power. The maximum available power the Zero EZE is able to deliver is approximately 110 kW. The following calculations are performed according to Anderson [24], to do so following assumptions are made.

- Constant Thrust
- Constant Weight
- Average value for the sum of the drag and resistance forces

The constant thrust is especially valid when considering a jet-powered aircraft, however for this approximation it will also suffice.

Considering the take-off another aspect is taken into account, this being the ground effect (GE). The induced drag, while flying close to the ground, is reduced by Equation 2.9.

$$C_{Di,takeoff} = GE \cdot C_{Di} \tag{2.9}$$

Here the ground effect is depicted by Equation 2.10, where 'h' is defined as the height of the wing above the ground. For the Zero EZE this distance has a value of 0.9 m.

$$GE = \frac{(\frac{16h}{b})^2}{1 + (\frac{16h}{b})^2} \tag{2.10}$$

Now the ground effect is defined, the following equation for the take-off speed is solved.

$$S_{LO} = \frac{V_{LO}^2 m}{2(T - (D + \mu_r(W - L))_{average})} \tag{2.11}$$

For this equation the take-off speed is defined as being 20% higher than the known stall speed. To define the average value of the sum of the drag and resistance forces, an average speed is defined with a value of 0.7 times the stall speed, as can be seen in Equation 2.12 and 2.13.

$$V_{LO} = 1.2 \cdot V_{stall} \tag{2.12}$$

$$V_{average} = 0.7 \cdot V_{stall} \tag{2.13}$$

The resistance coefficient is defined to be 0.02, considering a relatively smooth and paved surface. The lift and drag are calculated by their fundamental equations. Here the average speed is used, as previously mentioned and seen in Equations 2.14 and 2.15.

$$L = C_{L_{max}} \frac{1}{2} \rho V_{average}^2 S \tag{2.14}$$

$$D = (C_{D_0} + GE(\frac{C_L^2}{\pi e AR})) \frac{1}{2} \rho V_{average}^2 S \tag{2.15}$$

In case of maximum loading, the take off distance becomes 490 meters, while for light loading, e.g. no passenger and luggage, the take off distance becomes 445 meters. Note that the propeller efficiency changes to 0.69, this because the optimization was done for cruise speed and the efficiency is mostly dependend on the air speed. The minimum take off speed is 36 kts, as previously determined from the stall speed.

2.2.2 Landing Requirements

Considering the landing phase, a rough estimation to determine the required power is used. Here the speed, to calculate the lift at landing condition is defined by Equation 2.16.

$$V_{landing} = 1.2 \cdot V_{stall} \tag{2.16}$$

Also the propeller efficiency at sea level conditions and low speed flight is used. The power needed to obtain this speed at landing, with a propeller efficiency of 69 % is 33.4 kW. This is however merely an estimation and is used for completing the power used calculations in the flight envelope.

2.2.3 Conclusion

In table 2.2, the amount of power is seen that is needed for each stage of the flight. These values are the design requirements for the fuel cell. As already mentioned is the power required for cruise based on the cruise speed as well as the maximum climb rate whereas the take off sizing is based on the take off distance.

Table 2.2: Shaft Power estimation Zero EZE

Take-off	110 kW
Cruise	60.15 kW
Cruise with MROC	96 kW
Landing	33.41 kW

2.3 Propeller and Shroud Design

To size and develop the propeller of the Zero EZE, the software JavaProp is used, which is based on blade element theory. The different blades are divided into small sections, after which each section and blade is handled independently. For each segment, the chord and blade angle is defined together with the associated airfoil characteristics. This program is valuable to provide an estimation of the performance and initial sizing of the propeller.

However, some limitations have to be taken into account. Three dimensional effects are not included, this means that the interaction between the blades is not simulated. These interactions are however beyond the scope of this project. The sizing of the propeller is seen as a highly iterative process. The interaction with the shrouding will impose new constraints which will have to be taken into account.

2.3.1 Initial Sizing

A first step in the determination of the propeller setup is to obtain a set of main inputs, after which the performance is tested by JavaProp. This section describes the initial sizing of the propeller based on the different constraints. Throughout this section, a laminar incoming flow is assumed.

Diameter Calculation

To obtain the first results a diameter and corresponding RPM are determined. These numbers are, as already mentioned, merely a preliminairy estimation and will need to be optimized throughout the design process. By doing so an optimal result will follow. The general rule for sizing the diameter is "Concerning the diameter of the propeller; keep it as long a possible, as long as possible" [22]. This meaning that a larger diameter has a higher thrust outcome, due to the fact that it is able to 'handle' more air. This principle is explained by the definition of thrust. Thrust is given by time rate of change of momentum of the air that passes through the propeller [23]. Next to the performance, also the noise-factor is highly influenced by the diameter of the propeller. The larger the diameter, the lower the noise factor.

The tip speeds and physical constraints pose the limits concerning this parameter. First the physical constraint is taken into account, this being the ground clearance at take-off. For the Zero EZE, this is even more critical due to the used pusher configuration. Besides the ground clearance, the tip speed of the propeller blades are of extreme importance, this for both the efficiency as well as the noise production. The maximum tip speed is determined by the subsonic conditions of the tip of the blades. Once these conditions are reached, flow detachment will cause an incremental increase in noise as well as a decrease in performance. To perform the first output, this maximum tip speed with respect to the highest allowable noise production is taken into account. For general propeller configurations, a maximum allowable tip speed of 0.72 Mach is used.

According to Roskam [22], the following equation can be used to determine the maximum allowable diameter according to the engine speed. Most importantly is the tip speed, to assure low noise production and high efficiency, the tip speed should remain subsonic.

$$RPM = \sqrt{\frac{(a^2 \cdot (M_{tip}^2 - M^2))}{(D^2 \cdot pi^2)}} \cdot 60 \tag{2.17}$$

2.3.2 Implementation Of JavaProp

To perform a first calculation, by using Javaprop, the following inputs should be provided. Number of blades, RPM, the diameter of the propeller as well as the spinner, the velocity and the choice of airfoil with corresponding angle of attack. The number of blades has an influence on the sound generation of the propeller, this can be seen in Figure 2.1. The analysis shown in this figure is performed for static conditions, despite this it provides a clear view of the principle.

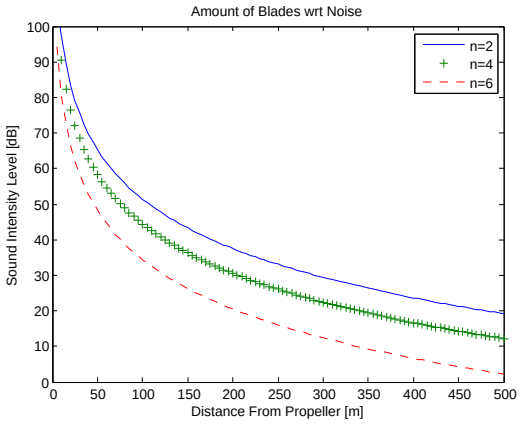

Figure 2.1: Sound Level with respect to Amount of Blades

For this case, it is determined to have a propeller with three blades. The most optimal amount of blades should be determined with respect to the mutual interference of the blades. This analysis would be well out of the scope of this DSE project and a program such as JavaProp, as already mentioned, is not able to cope with these kinds of effect. By using three blades, a sufficiently low interference and loading is ensured.

During a cruise a speed of 77 m/s is required. The spinner diameter was estimated to be 0.15 m, this value is chosen in comparison to the propeller of other similar aircraft. For the efficiencies at take off

and landing, a variable pitch system has been taken into account, due to time constraints however, this system has not been optimized for this report. To have the first results, an airfoil and angle of attack has to be chosen, this is explained in following subsection.

Airfoil Choice

In JavaProp, an airfoil is chosen. The program allows this choice for four segments of the blade. For each segment an optimal airfoil and corresponding angle of attack is determined. The most optimal choice for the angle of attack is seen as the value corresponding to the highest lift to drag ratio. In the general database of JavaProp, 10 standard airfoils are given. Taking the scope of this project into concern, no other types are investigated. The choice of the airfoils is done by the use of general observations. First, at the root more structural strength should be present, this to cope with the high applied momentum loads. A thicker airfoil is used, here the MH 112 16.2% airfoil is chosen, where the 16.2% indicates the thickness to chord ratio. For this airfoil, with regard to the highest lift to drag ratio, an angle of attack of 1.2 degrees is chosen. In Figure 2.2 a decrease in lift can be seen in the first part, this due to the lower performance characteristics of the airfoil at the root.
The highest lift force should occur at 3/4 of the chord, to ensure a high momentum. For this propeller, the second and third segment have the same airfoil and corresponding angle of attack. This being the MH116 9.8%. The thickness is lower and the performance higher. The most optimal lift to drag ratios are found at an angle of attack of 6.5 degrees. At the final section of the blade the same airfoil is chosen, however with a less optimal angle of attack to decrease the lift. This compensates for one of the limitations of the program. When high lift is produced at the end of the airfoil, vortices are generated due to the high pressure differences causing higher values for the induced drag component. For this reason the blade is designed to produce lower lift values at the end of the blade, which can be seen in Figure 2.2. With the airfoil and angle of attack known, the blade twist is calculated.

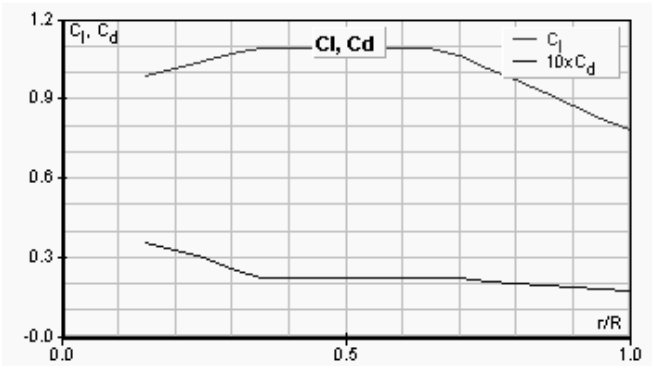

Figure 2.2: Lift to Drag 3 bladed propeller

First Results

At this stage, with the known parameters, results are generated by JavaProp. These are presented in Table 2.3. Here can be seen that the efficiency is calculated to be approximately 85%. It has to be mentioned, once again, that these results are a first approximation. Many assumptions are made throughout the process and the limitations of the program also causes some discrepancies. Despite this, the set of result can certainly be used, due to the fact that they are comparable to the propeller currently installed on the Long EZ. In the table it is seen that there is a low loading, which is especially favorable regarding the noise production. The advance ratio of the propeller is seen as quite high, indicating a good ratio between the distance the propeller moves forward and the diameter of the propeller itself. The values in this table are used as a benchmark to be able to compare the upcoming iterations with respect to the initial propeller.

Table 2.3: First Results from JavaProp

Parameter	Result	Parameter	Result
V/(nD)	1.283	β @ 75 %	37.1
η	84.90 %	loading	low
Power	58.3 kW	Pitch H	2.14m

2.3.3 Shrouding

The main purpose of the shroud, for this project, is to minimize the noise production. Besides this advantage, a shroud also ensures a more optimal air flow through the propeller, resulting in an increase of efficiency and thrust.

The increase in thrust can be explained by basic Bernoulli and mass conservation principles, given by Equation **??** and **??** respectively. However, as already stated, the noise criteria is decisive for this project. The principles of thrust increase will only be included for comprehensive reasons. To be able to use Bernoulli, the propeller is represented as an angular disk. The shrouding can be seen as a duct. For the scope of this project, it is important to remember that the shroud acts like an airfoil, thereby accelerating the flow. An accelerated airflow in front of the propeller is beneficial for the thrust generation. To use the Bernoulli and mass conservation principles, the propeller is seen as a simple disk area. Here the flow will increase, resulting in an increase in thrust.

Next to the increase in efficiency, another advantage of the shroud is the safety. Due to the pusher configuration of this airplane, there is a possibility that the propeller hits the ground during steep take-offs and landings. Without the protection of a shroud, the propeller will be ruined and the airplane will not be able to continue flying. With a shroud included, the propeller will not be able to hit the ground. A design constraint will be to make the shroud stiff enough so it will not deform when it comes into contact with an object. This results in a protective shell for the propeller.
The shrouding will be incorporated in the JavaProp program. Large limitations are coupled to this approach. Taking a closer look at the thrust distribution along the propeller blade, it is seen that this distribution drops to zero at the tips. A shroud is able to suppress these losses. This meaning that the additional thrust, caused by affecting the flow through the propeller, is not included in the program. Also the interaction between the propeller and shroud is neglected. These are all large approximations, however the basic theory is given in previous sections and including these factors is beyond the scope of this DSE-project. The efficiency of the propeller with shroud results in a value of 88.6%, an increase of almost 4%. The propeller, together with the shrouding is visualized in Figure 2.3.

Figure 2.3: Propeller and shroud layout

2.3.4 Noise calculations

With the initial sizing of the propeller and the basic thrust equations used in previous chapters, the returned values from JavaProp can be used to calculate the noise generated by the propeller blades. The major restriction is that the acoustics within the shroud will not be considered, due to its complexity. A recommendation for following projects would be to investigate this phenomenon. According to [21], the

noise prediction can be performed for the near field and the far field of a propeller, which is done in the following sections.

Near field Noise

The near field refers to the area outside the propeller disk, with a maximum range of the diameter of the propeller outside the disk. The near field noise depends on the tip speed, RPM, diameter and power of the propeller, as can be seen in Equation 2.18. It also depends on the distance to the center of the propeller disk, which is chosen to be 1 meter. This near field noise calculation only applies to the region outside the propeller cylinder and is not valid directly in front or behind the propeller. The standard propeller described above will serve as a reference, as can be seen in Table 2.4. For the optimization of the propeller the atmospheric units at 3 km above sea level are used to simulate cruise conditions.

$$SPL = 20 \cdot logW - 40 \cdot logD - (33.4 - 24.4 \cdot M_t) \cdot log\frac{z}{D} + 36.6 \cdot M_t + 75.8 + 20 \cdot log\frac{3}{m} - 10 \cdot log\frac{F + 460}{528} \quad (2.18)$$

Table 2.4: Noise characteristics - Diameter

RPM	**Diameter [m]**	**Efficiency [%]**	**Shroud**	**Power [kW]**	**SPL [dB]**
3800	1.2	86.2	NO	61.8	122.3
3800	1.2	88.8	YES	60.0	122.3
3800	1.1	87.7	YES	60.8	121.1
3800	1.0	86.2	YES	61.8	119.8

As can be seen in the table, the efficiency increases tremendously when a shroud is implemented. This means that the power the fuel cell system should deliver is lower when a shroud is included. The required power accounts for the efficiency of the propeller and the efficiency of the electrical motor, which is set to be 95%. This indicates that the depicted power represents the amount the fuel cell itself has to deliver. The calculated SPL, indicating the Sound Pressure Level is calculated without the acoustic damping effects of the shrouding. Calculating the sound propagation inside the shroud and the effects of this on the total SPL is beyond the scope of this report and is advised to be considered in a latter stage. By decreasing the diameter, the SPL is lowered, but so is the efficiency. At this instance, a diameter of 1.2 meter is chosen.

With the chosen diameter, the RPM of the engine can be considered. As can be seen in Table 2.5, lowering the RPM can lead to a decrease in near field SPL. Optimally, the RPM will be lowered in such a manner, that the propeller produces the lowest noise possible. Due to power restrictions however, a minimal RPM has to be taken into account. The fuel cells are dimensioned on delivering 110 kW at maximum power, indicating that 3000 RPM will be the best option for this 1.2 diameter propeller. This will lead to a SPL of 117.1 measured 1 meter from from the tip of the propeller, which can be compared to being present at a loud rock concert. The accompanied tip speed M_t will be Mach 0.62, which is well below the Mach 0.72 threshold. The optimization of the propeller with respect to the near field leads to a decrease of 5.2 dB.

Table 2.5: Noise characteristics - RPM

RPM	**Diameter [m]**	**Efficiency [%]**	**Shroud**	**Power [kW]**	**SPL [dB]**
3800	1.2	88.8	YES	60.0	122.3
3000	1.2	88.6	YES	60.2	117.1
2500	1.2	88.0	YES	60.6	113.9

Far field Noise

The far field noise indicates the range from more than one-propeller-diameter-distance from the propeller tip to kilometers away from the airplane. For this project, these calculations can be seen in Equation 2.19.

$$SPL_{avg} = PWL - 10 \cdot log(4 \cdot \pi \cdot r^2) + 10 \cdot log\left(\frac{\rho \cdot a}{\rho_0 \cdot a_0}\right) \tag{2.19}$$

Here the PWL indicates the overall power level of the propeller noise [21], which is found from experimental results. For a three blades propeller the PWL has a value of 143, depending on the total power delivered, the corrected rotational tip speed, the overall acoustic power level and the number of blades. The average sound pressure level can be found in Figure 2.4. As can be seen, the SPL ranges from 95 dB at 100 meters to 61 dB at 3000 meters distance, which is sufficiently low to meet the requirement of 65 dB. This requirement is actually reached at a distance of 2000 m cruise.

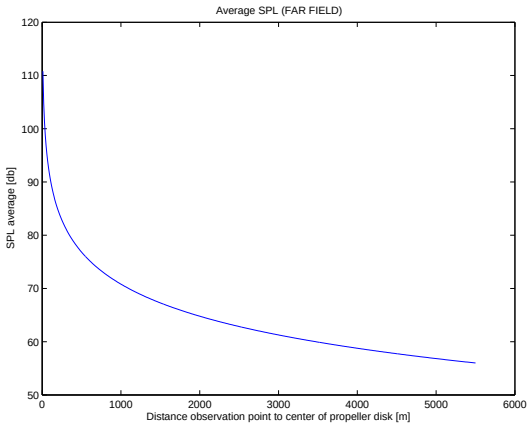

Figure 2.4: SPL distribution Far Field

2.3.5 Stator system

To even further increase the efficiency of the propeller system, a stator is implemented. A stator is, as the name depicts, a static propeller which uses the outflow of the main propeller as inflow. The flow behind the main propeller has a rotational property and when this hits the stator, the stator functions as a propeller which creates forward thrust. Due to the inevitable losses from the first propeller, this thrust factor is obviously much smaller. Despite this, it is still beneficial and preferable compared to an arbitrarily chosen shrouding support. To have this stator system optimized, it is important to know the optimal angle with which the flow hits the stator. Here a rather large assumption is made. For the scope of this project this angle is seen as the angle between the rotational and forward velocity of the main propeller. This angle is calculated at four points on the blade and is used as the input for the angle of attack, considering the stator as can be seen in Table 2.6. For the airfoil; a simple and symmetrical profile was chosen. In this case being a NACA0012. The amount of blades is not further investigated, to do this an intensive analysis of the flow interaction between the blades should be made. For this project the number of blades is chosen to be 3, the same amount the propeller has.

Table 2.6: Stator Angle of Attack

$\frac{R}{r}$	0	0.25	0.5	0.75	1
α	58.5	58.5	39.2	28.6	22.8

2.3.6 Materials, costs and weights

The used material for the propeller, stator and shroud is carbon fiber, this due to its ability to cope with the loads projected on the propeller blades and its relatively low weight and manufacturing costs. The total weight of the propeller is 10 kg, while the shroud weighs roughly 40 kg, calculated with the aid of Catia, these values are quite accurate. The costs for a 3 bladed carbon fiber propeller is approximately €2,000 [33], including labor costs, this will become approximately €2,500. The raw material costs for carbon fiber are €39 per kg, indicating that the shroud will cost approximately €975, including 50 hours for labour, assuming €50 per hour the costs for the shroud will become approximately €4,000.

2.3.7 Conclusions and Recommendations

In this section the propeller parameters are defined, this has proven itself as being an iterative process. The diameter is set to 1.2 m. The corresponding engine speed is defined in a such a way that a sufficient low tip speed is assured, this is needed to assure the noise criteria. For the general configuration, a number of three blades is chosen, this to ensure low interference between the blades. From this moment on everything was checked and optimized by using the program of JavaProp, here the airfoil could be chosen out of a given set of standard and commonly used airfoils. This selection was done for four segments, the corresponding angle of attack is determined with respect to the highest allowable lift to drag ratio. At the root and tip other airfoils were chose to cope with structural strength and induced drag, respectively.

For enhancing the efficiency and noise criteria of the propeller, a shroud is implemented. This is again done with the use of JavaProp. Noise calculations were performed, this for near and far distance. The results are in a reasonable range and differ from 117 dB, measured at a distance of 1 m from the propeller, to 61 dB, measured at 3000 m from the propeller. This was seen within the limits of the given requirements.

As the last feature, a stator system was implemented. This to have another efficiency increase by recovering the swirl losses from the main propeller. This stator has been kept simple, and should be optimized in a subsequent project.

The most important design aspects of the propeller and shroud are summarized in Table 2.7. This propeller has been designed within the time limits given to this project group, further optimization needs to be done however. In the recommendations chapter, several suggestions are given to further elaborate the propeller, shroud and stator system.

Table 2.7: Final Dimensions and Results Propeller

RPM	**Diameter (m)**	η	**Power (kW)**	**V/(nD)**	**Loading**	**SPL (dB)**
3000	1.2	88.6 %	110	1.28	low	117

2.4 Fuel Cell

As mentioned in the Introduction of this chapter, the PEM fuel cell is chosen to be the major power source of the propulsion system. The fuel cell was compared to a hybrid propulsion system in an earlier phase of this project, with a reciprocating engine/battery combination as the power source. As a result of a trade-off, the fuel cell was chosen as the main power source. How a single fuel cell works will be explained the next section, followed by clarification of all subparts that are needed in order to have a good working fuel cell. Further, the calculations of the fuel cell stack and the results are given. Finally the safety and reliability of the system will be discussed.

2.4.1 Single Fuel Cell

Fuel cells offer clean and efficient power production and are still fully in development for both stationary and mobile applications. For mobile applications, the PEM fuel cells are preferred due to the low operating temperature and thus short start-up time. Figure 2.5 shows how a single PEM fuel cell works.
PEM fuel cells use hydrogen and oxygen to produce electric power, with water as the only emission. As can be seen in Figure 2.5, the hydrogen is supplied at the left side of the fuel cell and the oxygen at the right. In Section 2.4.8 it is explained that the hydrogen is stored at 700 bar in special tanks. The oxygen needed is subtracted from the ambient air, using a pump.

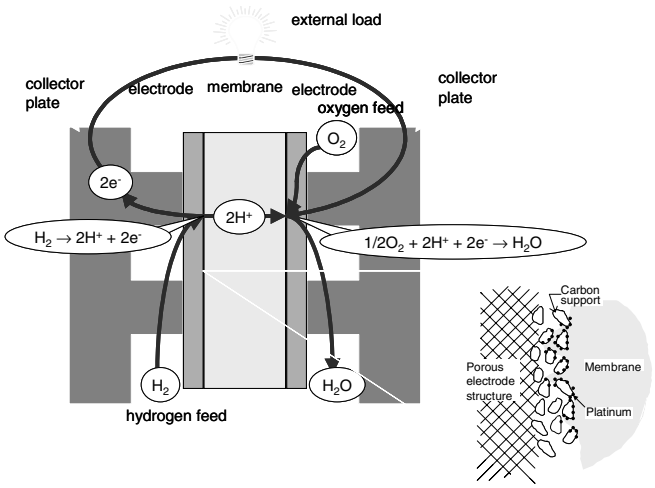

Figure 2.5: Single fuel cell composition

A PEM fuel cell consists of two electrodes with a special membrane in between. When hydrogen reaches the left electrode, the anode, a chemical reaction will occur. This reaction can be seen in Equation 2.20. The electrode, also called the catalyst layer, consists of carbon particles. The carbon particles are covered with small platinum alloys, to speed up the reaction. The membrane that is clamped between the anode and the cathode is impermeable to gases and only conducts protons. Thus the protons pass through the membrane to the cathode and the electrons use an external circuit to reach the cathode. The reaction that occurs at the cathode is shown in equation 2.21. Equation 2.22 shows the overall reaction. Attention should be paid, that only protons should pass through this membrane, since other particles can damage the membrane and influence the power output. [32]

$$H_2 \rightarrow 2H^+ + 2e^- \tag{2.20}$$

$$\frac{1}{2}O_2 + 2H^+ + 2e^- \rightarrow H_2O \tag{2.21}$$

$$H_2 + \frac{1}{2}O^2 \rightarrow 2H_2O \tag{2.22}$$

If the fuel cell would be under ideal conditions, it would produce 1.18 V and all the energy in the reactants would be converted to electricity [32]. However, in practice the voltage is lower and besides electricity, there is also some heat production. This heat has to be removed, in order to keep the fuel cell operational, which will be explained in a next section. Taking into account the heat losses, a single fuel cell can produce a maximum voltage of around 0.7 volts.

2.4.2 Fuel Cell Stack

To increase the power output of a fuel cell, multiple fuel cells have to be stacked together in series, as can be seen in Figure 2.6. The cells are separated by bipolar plates, which contain channels to supply the reactants and cooling water. In Section 2.4.4 the calculations for the power output are made. The maximum power required during a flight is calculated to be 110 kW in Section 2.2. Because of the degradation of fuel cells over their lifetime, they have to be designed for a higher power level, such that the desired power output can be delivered during the entire lifetime of the fuel cell. The total volume and weight of the stack is determined by using existing fuel cell systems, which is explained later in this section.

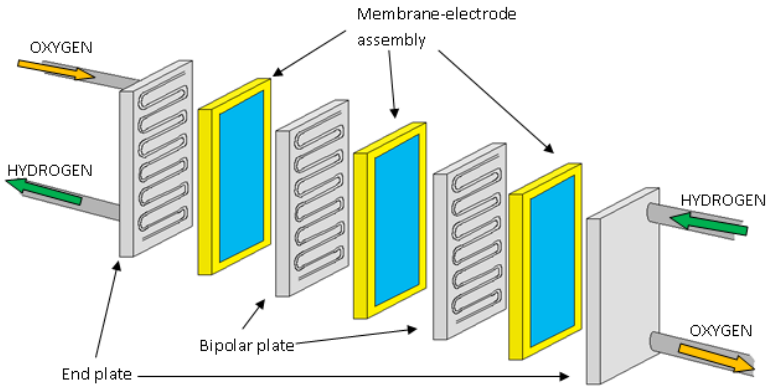

Figure 2.6: Stacking of multiple fuel cells

It is important that every cell is supplied with the same amount of reactants, such that every cell produces the same amount of power. If the reactant division is not done equally, certain cells will degrade faster than others, which affects the overall power output of the stack. Further, the amount of reactants that is provided to the cells should be divided equally over the cell, such that the whole membrane is used. To achieve this, bipolar plates are used to separate every cell and a gas diffusion layer is used to spread the reactants over the membrane. These bipolar plates provide hydrogen to the fuel cell at one side and provide air to the fuel cell at the other. Also the cooling water passes through the bipolar plates.

2.4.3 Balance Of Plant

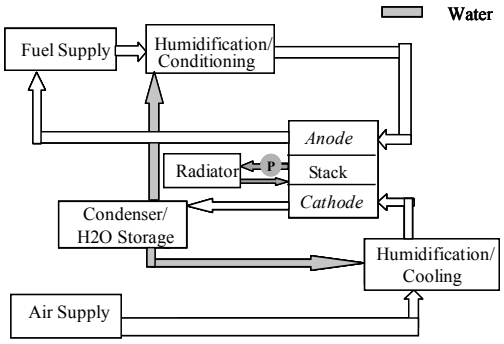

Figure 2.7: Schematic view of the total system

To propel an aircraft, only the fuel cell stack is not enough. The operating conditions of a fuel cell should be determined and controlled very carefully such that the efficiency and lifetime is increased. When this is not done properly, the fuel cells can be damaged or even fail. To keep these conditions in a certain range, a BOP (Balance Of Plant) is needed. The BOP contains every subsystem in a fuel cell propulsion system, except for the fuel cell stack. A schematic view of the fuel cell stack and the BOP is given in Figure 2.7. The BOP can be divided into several subsystems, which will be discussed in the remainder of this subsection [32]:

- Air Management
- Hydrogen Management
- Water Management
- Thermal Management
- Enclosure
- APU

- Electrical Subsystems
- ECU

Air Management

Air management can be described as the system that regulates the air supply that is needed for the fuel cell to produce the required power. The components that are needed to maintain a continuous air supply are explained below.

- Air Regulator
  For the fuel cell to work, ambient air is needed. To have enough air to react with the hydrogen, an air pump is used to control the amount of air that enters the fuel cell.
- Air Filter
  Ambient air can have harmful contaminants, such as dust. These contaminants can decrease the efficiency of the fuel cell or even cause failure. An air filter is used to clean the incoming air.
- Compressor
  The ambient air at cruise height has a lower pressure than the operating pressure required by the fuel cell. If the pressure difference between the fuel cell and the air is too high, this can damage the membrane. The air filter causes a pressure drop as well, so the air should be compressed to the operating pressure of the fuel cell. This is done using a compressor, which increases the pressure and the temperature of the flow.
- Humidifier
  The temperature and the humidity of the incoming air are not in the right condition. A humidifier is used, by spraying hot water, to correct the temperature and humidity of the air. this will be checked by temperature and humidity sensors.
- Moisture Separator
  After reaction of the oxygen in the air with the hydrogen, water is produced. The remaining elements in the air after the reaction, like nitrogen and carbon dioxide, are leaving the fuel cell mixed with the produced water. After separation of the water from these gases using a moisture separator, the gases are expelled into the environment and the water is used again, which can be seen in Appendix A.

Hydrogen Management

The hydrogen management is the system that regulates the hydrogen supply to the cells. The hydrogen is stored in the fuel tanks at very high pressure. The main task of the hydrogen management within the BOP is to decrease this pressure to the operating pressure. As mentioned before, the same amount of hydrogen should be supplied to all cells.

- Storage
  The hydrogen needed for the chemical reactions is stored in three high-pressure tanks. Specifications of these tanks can be found in Section 2.4.8.
- Pressure regulators/Valves
  The pressure in the tanks is 700 bars. The operating pressure of a PEM fuel cell is around 1.5 bar, which means that the hydrogen pressure has to be decreased drastically such that it can flow easily into the fuel cell without damaging the membrane. The pressure regulators are incorporated in the fuel tanks.
- Humidifier
  The hydrogen should be at the correct temperature and humidity before entering the anode, which is again checked by humidity and temperature sensors. The humidifier adds the needed humidity and heat to the hydrogen.

- Fuel exhaust
  The fuel cell is assumed to be able to perform in a very efficient way if the operating conditions are good. The percentage of hydrogen that reacts is assumed to be around 98%. This means that only 2% of the hydrogen leaves the anode without being used. The hydrogen that leaves the anode without reacting can be circulated back to the anode inlet, but such a system introduces much more weight and complexity. Therefore it is assumed that this small amount of fuel is released to the ambient.

Water Management

Water is needed in a fuel cell system to humidify the reactants before entering the fuel cell and to cool down the fuel cell. Two different loops are used, such that for the cooling flow, coolant can be used in stead of water.

- Water reservoirs
  Both reactants have to be humidified in such a way that both sides of the fuel cell and the membrane have the right humidity. In other cases the fuel cell operates poorly or can even fail. To provide both reactants of the right amount of water, there are sensors that measure the temperature and humidity. A water reservoir is present, in case the water level is too low in the loop. The temperature of the water in the reservoir can be regulated electrically such that it can be kept constant during flight. Another advantage is that if the water in the reservoir is frozen, this problem can be solved by heating up the reservoir.

- Water Pumps
  There are pumps needed in order to move the right amount of water to the right place in the system. There is one water pump present in the cooling loop and one in the main loop. Both pumps work individually and are connected to the ECU, that converts the power settings to the right pump settings.

- Heaters
  The water is heated to the right temperature such that the reactants are humidified correctly. The heaters are in connection with the sensors.

- Bipolar Plates
  The bipolar plates are designed such that the reactants flow vertically. This means that there is no extra pump needed to drain the water that is produced, because too much water in the membrane will decrease the performance of the fuel cell (flooding). If the reactants flow vertically, gravity can be used to drain the water.

Thermal Management

As explained earlier, the fuel cell is cooled using a coolant that continuously flows through the fuel cell. The temperature of the coolant that passes through the fuel cell has increased due to heat absorption and is cooled afterwards using a radiator. In Figure 2.8 it can be seen that the reactants flow vertically and the coolant passes these reactants horizontally. For the main loop, the temperature of the water to humidify the reactants has to be regulated such that the inlet temperature to the fuel cell is around the operating temperature of the fuel cell.

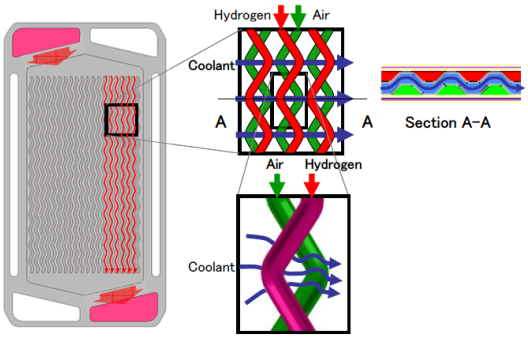

Figure 2.8: Detailed view of the stack cooling [31]

Enclosure

The fuel cell stack and BOP parts have to be held in a fixed orientation and position. This can be done by using a frame where everything is fixed and protected. The enclosure should also protect the system against vibrations and shocks. Further, the enclosure has to be pressurized such that the fuel cell is not affected by the ambient conditions at higher altitudes. Finally, the enclosure should protect the users of the airplane against the fuel cell, since this can be at a high voltage. There should be hatches for maintenance and safety issues. In case of a leakage, the hydrogen needs to be able to escape to the environment. When the leaked hydrogen is not ventilated, the risk of an explosion exists. Hydrogen leakage is discussed in more detail in Section 2.4.8

APU

The Auxiliary Power Unit has several functions. To start-up the fuel cell, electricity is needed which can be provided by an external source, such as the airport. When the airplane is not near an airport or when the airport has no electricity available, the APU, which is a battery, can deliver the needed start-up electricity. This is done by providing power to the BOP components, such that the fuel cell stacks start generating electric power. It takes around 30 seconds to start-up the fuel cell and another 30 seconds to provide full power [35]. Further, the APU can assist the fuel cell to deliver the peak power, since it takes some time for the fuel cell to shift from the nominal power to the peak power.
When a fast take-off is needed, the battery can assist the fuel cell to provide the required power for take-off. The battery can be recharged during cruise, when the fuel cell operates with a constant power output. When using the fuel cell at a lower power output during cruise, the efficiency will increase.
The Lithium-ion battery is still fully in development, so the probability that the capacity of these batteries will increase is quite large. The battery pack should be designed to be modular, such that it can be replaced when the battery suffers a too high capacity loss or when better batteries are available.
The next generation Lithium-ion battery is chosen, since batteries are analyzed for the mid-term report and this type came out best after a trade-off.

Electrical Subsystems

The voltage output of the stack is not a constant value, but shows small deviations. In order to have the desired voltage output the fuel cell stack voltage can be converted to the desired voltage using a DC-DC converter. This DC-DC converter is combined with a power distributor, that distributes the power to different subsystems. This is explained in more detail in Section 3.3.
When the stack voltage is lower than the desired voltage, this can be raised using a step-up or a boost converter. When the stack voltage is higher, a step-down converter can be used. Both of these devices can convert the voltage only one way, up or down. This means that the stack voltage should always be either higher or lower than the desired voltage output, such that one of the converters is needed instead of both.
When multiple stacks are used in parallel, two converters are needed. In case one of the stacks produces less power than desired or stops working, the converter can detect which one of the stacks has problems. This stack can than be shut off by the user, such that it cannot damage the other stack and fuel is not

wasted.
The electricity generated should off course provide power to the engine. But to keep the fuel cell operational, some subsystems need to be fed with power. This power is provided by the fuel cell output power, so it can be seen as a loss. These losses are called parasitic losses, which have to be taken into account when designing the fuel cell.

ECU

The Electrical Control Unit is the connection of the throttle settings with the fuel cell settings. To produce more thrust, the hydrogen and air supplies should increase. With these changes, the complete BOP settings have to be adjusted, since everything in the fuel cell is changing. The ECU control and regulates all the pressures, temperatures and mass flows in the propulsion system.

2.4.4 Calculations

Fuel Cell Stack and BOP

Before the fuel cell specifications can be determined it is important to determine the design power. The design power is the power that the fuel cell can deliver at the beginning of the lifetime. This power output will decrease over the lifetime, thus should be chosen such that at the end of the lifetime it is equal to the power needed. This degradation is assumed to be 10% of the total power output. Further, the power consumption of the BOP components have to be known.
The required power for the electric motor is calculated in Chapter 2.2 to be 110 kW. After taking the degradation factor into account, the design power will be 121 kW, but the BOP power consumption is not included yet. To determine the BOP power consumption for a net power output of 121 kW, the thermodynamic modelling software Cycle-Tempo is used. It is found that a total power of 140 kW is needed, such that the net power output is 122.5 kW and the BOP power consumption is 17.5 kW. The power that is left, is used for flight instruments and lights.The Cyclo-Tempo results are given later in this section.
The fuel cell stack characteristics can now be calculated using equations 2.23 to 2.25. There are a lot of combinations possible to design a stack with a power output of 140 kW if there were no constraints, so some limitations have to be set. The first constraint is that there have to be two fuel cell stacks connected in parallel, such that the aircraft can still land safely if one of the stacks fails. The second limitation is the available space for two stacks. From Section 4.1 the available area for both stacks is equal to 60 cm $\times$ 60 cm. This area is divided into two parts, one for the fuel cell stacks and one for the BOP, each having 1800 cm^2 available. Thus each stack has an active area of 900 cm^2. The current density for a maximum voltage of 0.7 volts is 0.6 A/m^2 [30]. For a power output of 70 kW and an active area of 900 m^2, the number of cells needed can be calculated to be 192 fuel cells per stack.

$$P = V \times I \tag{2.23}$$

$$V = v \times n \tag{2.24}$$

$$I = A_d \times A \tag{2.25}$$

Size and Weight Fuel Cell Stacks

With the calculated fuel cell specifications, the weight and volume of the system can be determined. The volume of one stack can be determined with a volume output density of 1.8 kW/L [34]. The active area is already known thus only the depth has to be calculated. For a power output of 70 kW and an active area of 900 cm^2, the depth of the stack is calculated to be 43 cm. The total volume of both stacks then is 78 L.
The weight of the stack is determined by using a weight output density of 1.5 kW/kg [34]. This gives a weight of 45 kg for one stack and a total weight of 90 kg for both stacks, including the BOP components. The weight and the size of the APU is not included and have to be determined separately.

APU

The APU can be used for start-up or to assist when peak powers are needed. To start-up the system, it can be assumed that the power needed is equal to 17.5 kW, which is the power needed for the BOP. The difference between the cruise power and the peak power is given to be 35 kW in Section 2.2. Thus the battery should be sized for the higher power requirement of 35 kW. Taking into account the degradation of the battery (10%), a safety factor (10%) and the battery discharge efficiency that was obtained from the mid-term report (98%), the battery is designed to have a power output of 43 kW.
It is mentioned before that the start-up time is 60 seconds and the time to deliver full power is 60 seconds. Thus the maximum time that the battery will be active is 60 seconds. Assuming a period of four minutes as the operating time, this corresponds to an energy of 1.33 kWh [36] [35].

Size and Weight APU

The weight of the APU will be 4 kg, if the energy density of Lithium-ion is assumed to be 0.35 kWh/kg. The volume to weight ratio is assumed to be 2.5, thus the volume of the battery pack will be 10 L. The values for the energy density and volume to weight ratio are obtained from the mid-term report.

2.4.5 Cost

The cost determination is vital since the aircraft has been assigned a limited budget and should be comparable in price to similar aircraft. The price per kg in 2005 was determined to 1200 $/kg [26] [27]. These costs are given for a production of around 500,000 fuel cells per year. Currently this is not realistic, but it is reasonable to assume this holds true for 2020. Based on these documents, the cost of the total fuel cell system is estimated to be 200 $/kg. Because these are only predictions, a safety factor of 50% is taken into account. The estimated cost then will be 300$/kg. This is equal to 250€/kg. When multiplying this value with the total power of 140 kW, the total fuel cell system will cost €31,500. The cost of the hydrogen and hydrogen storage is not included.
The cost per kg for the Lithium-ion battery is assumed to be 190 €/kWh in 2020 [28]. The total cost then will be €250 for a battery with an energy of 1.33 kWh.

2.4.6 Results

The final design will consist of two PEM fuel cell stacks, both made of 192 cells each. Each stack can deliver a power of 70 kW, which corresponds to a total power output of 140 kW. From Cycle-Tempo it is obtained that the BOP consumes 17.5 kW at full power, with a fuel cell efficiency of 49 %. The net maximum power output will thus be 122.5 kW. The total weight of the system is estimated to be 90 kg and both stacks and the BOP components will be placed in a box with a volume of 144 L.
The two stacks are connected in parallel, to increase the reliability of the system. The BOP power consumption for one fuel cell, with a power output of 70 kW, is obtained from Cycle-Tempo to be 13 kW. When one of the fuel cell stacks fails, there is thus a net power output available of 57 kW. This power output is enough to perform a safe landing, according to Section 2.2. Also the battery can assist the fuel cell in emergency cases.
The battery pack is investigated and explained in more detail in the midterm report. The lifetime was given to be between 400 and 1200 recharge cycles. This should be kept in mind when using the aircraft and the battery pack should be replaced by a new one when the capacity is under the desired level. The performance of the Lithium-ion batteries are expected to increase a lot in the near future, so the batteries can be lighter in time.
The results that are obtained from Cycle-Tempo can be found in Appendix A. The schematic drawing of the fuel cell system and the table with results are given and explained.

2.4.7 Reliability

The reliability of a system is dependent on the reliability of all subparts. For the PEM fuel cell, the major failure modes are caused by failure of the membrane, the catalyst or the bipolar plates [25]. These will be discussed in the following part of this section.

- Membrane
  The most commonly used membrane for PEM fuel cells is Nafion. Performance degradation or even failure of this membrane can be caused by several reasons. If the membrane is not assembled properly, cracks and holes can be caused. When the temperature or pressure in the fuel cell is not in the operating range, this can affect the performance of the membrane. Further, the air should be filtered such that dirt can not enter the membrane. The major issue with membranes is the humidity of the membrane. It can not be too dry and not too wet. That is one of the reason that the reactants flow vertically and the reactants are humidified before entering the fuel cell.

- Catalyst
  The platinum parts in the catalyst can dissolve from the carbon material. This can occur when the operating conditions of the fuel cell are not in the safe region. That is why the humidity, temperature and pressure are checked by sensors. When this is not done properly, the platinum parts can dissolve and they can enter the membrane. This will decrease the conductivity of the membrane drastically. Also the number of platinum parts in the catalyst will decrease, so the reaction time will increase, which will decrease the power output of the fuel cell.

- Bipolar Plates
  Bipolar plates are the thin plates that separates the fuel cells. Failure of these parts can be caused by vibrations and shocks, so the enclosure should be very well designed such that the whole stack is shock resistant. When a bipolar plate does not function properly, the membrane can be damaged.

It can be concluded that the BOP should be designed and maintained carefully. Basically all failure modes are caused by improper design of the BOP parts or a pressure, temperature or humidity that is out of range. Maintenance of the controlling equipment is very important, but when this is done correctly and frequently, the fuel cell can be considered as a reliable system. Other causes of failure can be shocks and vibrations: the alignment and position of components can change and be damaged. For the fuel cell itself, it can be considered a reliable system. By using two parallel stacks and an APU, the aircraft is able to continue the flight when one of the fuel cells fails.

2.4.8 Hydrogen Storage

One of the most significant contributors to the weight of the aircraft is the hydrogen storage tank. Also the volume of such a storage tank is large compared to other aircraft components. Since storage space is limited and the tank weight is critical for the Zero EZE design, it is vital that the storage tanks are carefully selected. Next to the storage technique and system properties of the hydrogen tanks, this section will also assess its safety.

Storage Technique

As been determined in the mid-term report, the hydrogen will be stored in gaseous form at 700 bar pressure to reduce volume. According to [38], there are four different types of gaseous hydrogen storage tanks:

- Type I: All metal cylinder
- Type II: Load-bearing metal liner hoop wrapped with resin-impregnated continuous filament
- Type III: Non-load-bearing metal liner axial and hoop wrapped with resin-impregnated continuous filament
- Type IV: Non-load-bearing non-metal liner axial and hoop wrapped with resin-impregnated continuous filament

Due to the use of carbon-fibre and polymers Type IV tanks are lighter than the Type I, II and III tanks, making them more suitable for aviation applications. Therefore also the Zero EZE will make use of these tanks. A list of state-of-the-art available Type IV hydrogen tanks is provided in Table 2.8 [37].

Table 2.8: Hydrogen Tank Options

#	Volume [L]	Pressure [bar]	H2 [kg]	Diameter [mm]	Length [mm]	Weight [kg]
1	51	700	2.0	400	743	43.0
2	55	700	2.2	366	960	40.0
3	93	700	3.7	557	711	62.5
4	108	700	4.3	307	2231	66.2
5	129	700	5.1	394	1640	92.0

Based on the hydrogen requirement of 13.5 kg determined in the midterm report, it is necessary to use multiple tanks. Due to the limited fuselage diameter and length, the volume required by the tanks should be as low as possible, while still achieving the fuel requirement. This can be achieved by placing two number 5 tanks next to each other, with a number 3 tank positioned on top. The storage tanks then comprise 13.9 kg of usable hydrogen, which is in line with the requirement. The empty weight of the combined tanks adds up to 246.5 kg.

The manufacturing cost of these tanks are assumed to be in the range of €4000 to €4500 per tank for small quantities, reducing with approximately 50% when larger production volumes are acquired [37]. However, for this project a purchase price of €4500 per tank is assumed, leading to a total storage system cost of €13.500.

To accommodate the fuel tanks, a minimum fuselage diameter of 1.20 m is required over a length of 1.64 m, as can be seen in Figure 2.9. This diameter also comprises the rack the storage tanks are placed in. For aerodynamic optimization it would be beneficial to position the tanks in the center of the fuselage. In this way the fuselage diameter can be reduced immediately after the fuel tanks in order to increase aerodynamic performance. However, it is also important to take in mind that at one point in the Zero EZE lifecycle the storage tanks have to be replaced. Therefore they should be easily accessible. The exact tank position within the fuselage will be determined in Section 3.1.

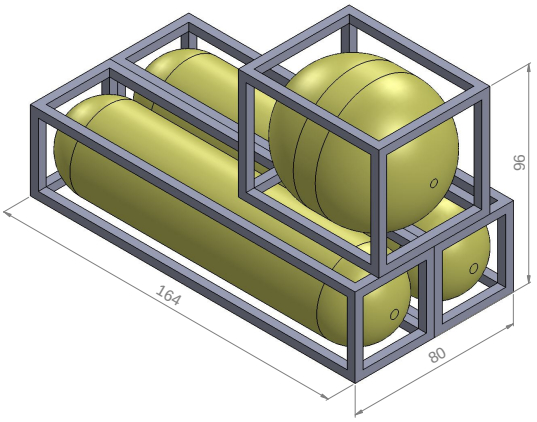

Figure 2.9: Hydrogen Tank Configuration

What is also important for this system is the refuelling. In order to be able to fill all the tanks, three filler caps should be made in the fuselage (one for each tank). In this way the tank system is less vulnerable to pipe leakage. The hydrogen tanks are provided with in-tank regulators, so only a connection between the three tanks and the fuel cell is needed [39]. To fuel the hydrogen tanks, a specialized fuelling system should be present at airports. The tanks should ideally be filled at -40 °C (Type A dispenser), but can also be filled at -20 °C (Type B dispenser) with a penalty of longer refuelling times [40] [42]. The type A dispenser is able to refuel a single tank within 4 minutes, which means that a total refuelling time of approximately 12 minutes can be achieved [40] [41]. This is perfectly acceptable for the Zero EZE.

Safety

Just like is the case with other fuels, the usage of hydrogen is accompanied by certain risks. Therefore it is important that the hydrogen system is designed in such a way that it can be safely operated in the Zero EZE.

The first problem that arises is leakage. The fuel cell system is exposed to the environment for quite a while, which may cause damage to the system components. When the piping system is exposed long enough, the possibility that hydrogen leaks out increases. To prevent this from happening, the piping system should be properly designed. For the Zero EZE the choice is made to separate the tanks in order to create a simple and safe refuelling system. The other piping system connects the tanks to a fuel management system, which in turn provides the fuel cells with hydrogen. The last part will be the most vulnerable to leakages and should therefore be properly sized.

In the event of leakage, each tank can be closed off individually by the regulators installed to prevent more hydrogen from escaping. To determine which part of the system should be shut down, leak detectors are placed throughout the fuel cell system area. However, some hydrogen has already been escaped before the tanks close off. When the concentration of hydrogen in the air reaches a value between 4% and 75%, the mixture becomes flammable [43]. Compared to kerosene with a flammability range of 0.7% to 5% [44], larger concentrations of hydrogen are needed before the mixture gets flammable, but it is flammable over a wider range. Therefore a ventilation system is needed that prevents such concentrations from occurring. Since hydrogen is lighter than air, the best solution would be to have this ventilation system in the top part of the fuselage. Finally the fuelling system should be provided with a purge valve system, which is able to dispose the entire hydrogen supply in a matter of seconds.

The fuel tanks themselves should be designed in such a way that they can withstand all possible impacts in a safe and secure way, such that in the event of a crash the tanks will not explode. Therefore drop tests are performed which simulate a severe accident such as a plane crash. A safety factor of at least 2.25 should be applied to the tank design to prevent rupture [46]. The tank used in the Zero EZE design is tested at a safety factor of 2.35 [39]. Flame resistance is also important such that in the event of a fire the pilot has time to safely escape from the aircraft [45].

2.5 Electric Motor

In contrast to a reciprocating engine, a fuel cell has a DC electrical output and needs an extra step to convert the energy to rotational motion. This can be performed by an electrical motor. The most important aspect when choosing or designing an electrical motor is the fact that it should suit the needs of the system. Every power conversion decreases the efficiency of the total system and therefore should be as efficient as possible. The reliability of the total system should also be taken into account as it determines whether redundancy is required for different subparts to increase the overall safety. This chapter discusses the implementation of the electrical motor and the efficiency and reliability of the total propulsion system. For the design of the electrical motor, it is of importance to take a look at the power sizing, earlier this report. The electrical motor should be able to handle a peak power of 120 kW and a 90 kW output at cruise speed, incorporating safety margins. During the mid-term of this project, it has been decided to implement the brushless DC electrical engine, due to its higher reliability than other motor options and its capability to cope with high RPM.
The electrical motor should be able to cope with the desired RPM and power output from the fuel cell. The biggest design constraint is the weight penalty. Since already a lot of research has been performed on this respective field, it would be beyond the scope of this report to design an electrical motor which is lighter than one made by experts. Therefore an existing one has been chosen. According to UQM [17] [19], the PowerPhase 220 is an electrical engine that is able to cope with a continuous power of 120 kW and peak powers of 220 kW. The maximum speed is 6000 RPM and the efficiency is 95 %. The motor has a power density of 2.7 kW/kg and the weight is 45 kg. This suits the needs for the fuel cell system and will be the best option to implement currently. This motor is available for €22.500.

2.5.1 Reliability

Calculating the reliability of the electrical motor on its own would not return very realistic values, and can not be compared to already existing reciprocating engines for example. This due to the fact that the electrical engine is part of a system which has its own combined reliability, consisting of the fuel cells, the propeller, the cooling and heating system and the electrical engine. To grade the reliability of the fuel cell configuration, first the reliability of a piston engine outlay has to be considered.

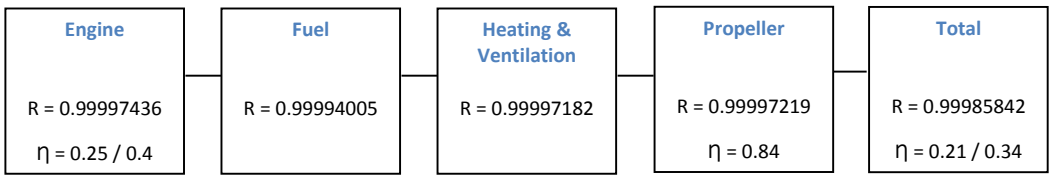

Figure 2.10: Reliability reciprocating engine system

In figure 2.10 it can be seen that the reciprocating system contains a piston engine, a fuel system, a cooling and heating system and a propeller. The combined reliability R of this system is 0.99985842, according to the Weibull definition for reliability. While the efficiency η will be between 21 and 34 %, depending on the efficiency of the piston engine [16]. This reliability can be rewritten into the MTBF according to the following formula.

$$Reliability = e^{-\frac{t}{MTBF}} \tag{2.26}$$

This leads to a MTBF of 42.250 hours for the reciprocating engine. Here, the engine contains only the components that are strictly part of the aircraft engine block, plus the exhaust system and crankshaft [16]. This MTBF should not be confused with the lifetime of the product or system. If for example 500.000 engines are considered over a year and 600 of them will fail during this year, the failure rate would become 0.12 percent. The MTBF is the inverse of this failure rate and would become 830 years in this case. This will not indicate that an individual engine will last this long, but for the entire batch, in this high reliability portion of its lifespan, it holds true that in a typical year, one only needs to replace 600 of these engines. The MTBF is merely a benchmark for marketing assets and allows engineers to improve weak spots during the design process.

The fuel cell configuration should be able to perform its required functions under the stated conditions for a specific period of time. The reliability of this configuration indicates the likelihood that the system will succeed within the identified mission time, with no failures. Figure 2.11 gives the overview of the reliabilities of the different components.

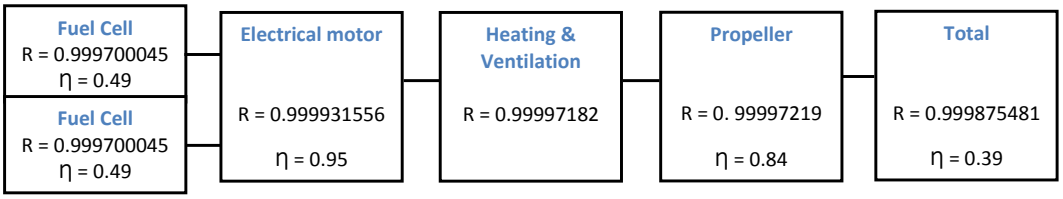

Figure 2.11: Reliability fuel cell system

The reliability of a single fuel cell is 0.999700045, considering a MTBF of 20.000 hours, while the typical MTBF for PEM fuel cells are between 20.000 and 40.000 hours. This is the major bottleneck of the design. By placing them parallel to each other, the reliability becomes $1-(1-0.999700045)^2 = 0.99999991$. The reliability of the electrical engine is based on a MTBF of 10 years [17]. The total MTBF for the fuel cell system becomes 48.200 hours, which is slightly better than the reliability of the reciprocating engine layout. For a single fuel cell, the MTBF would become 24.400 hours, which would be significantly lower than the MTBF of a comparable piston engine layout.

2.5.2 Conclusion

The efficiency of the fuel cell and electrical motor configuration is between 15 and 86 % higher than the efficiency of the reciprocating system, depending mostly on the piston engine. The reliability of the fuel cell system is mostly dependent on the reliability of the fuel cell itself. The heating and ventilation values are kept similar to the piston layout. By placing the fuel cells in a parallel configuration, the MTBF of this system becomes 48.200 hours, which is slightly better than the MTBF of a comparable reciprocating configuration.

The chosen electrical motor has a specific power of 2.7 kW/kg and is currently available on the market [17]. However Siemens is working on an electrical configuration with a specific power of 6.4 kW/kg [18]. This will lower the weight of the electrical motor by a substantial amount, which would be recommended to investigate in a latter stage.

2.6 Conclusions

In this chapter all subparts of the propulsion system have been determined and designed in detail. It was already decided earlier in this project that the propulsion system consists of a fuel cell. The fuel cell generates the required electricity to feed a brushless DC electric motor, which drives the SRP. The conclusions for the final propulsion system are given below.

In Section 2.2 the required power for the take-off, cruise and landing phase is determined. These powers are calculated to be 110 kW , 60 kW and 33 kW, respectively. The power sizing is done based on the aerodynamic properties and the weight of the aircraft.

The propeller selection and the shroud design have been based on the required power during cruise, this can be found in Section 2.3. Three propeller blades are chosen in order to ensure low interference levels between them. The propeller is designed by determining the airfoil shape and corresponding angle of attack of four segments of the blades, with respect to the highest allowable lift over drag. A shroud is implemented to increase the efficiency and hereby decreasing the produced noise. The resultant noise production ranges from 110 dB, measured at 100 meters distance, and 62.5 dB at 2,500 meters, which is reasonable.

The design of the fuel cell system can be seen in Section 2.4. For the fuel cell the maximum required power is used to design the fuel cell system. To increase the reliability of the system, two fuel cell stacks are connected in parallel, such that there is a redundancy in the propulsion system. When these stacks both are designed for a power output of 70 kW each, the net power output will be 122.5 kW. The power loss of 17.5 kW is consumed by the BOP components, to keep the fuel cell operating in a proper way and in the right conditions. When one of the fuel cell stacks fails, the other is able to provide a net power output of 57 kW, where 13 kW is provided to the BOP components. This means that the aircraft is able to perform a safe landing, even when half the power source fails. An APU is also present to assist the fuel cells when needed, able to provide a maximum power output of 40 kW. The total weight, size and cost of the total fuel cell system is calculated to be 90 kg, 144 L and €31,500 respectively. These values for the battery are: 4 kg, 10 L and €250. Compared to a reciprocating engine, the costs are slightly higher, which is acceptable because of the complexity of the fuel cell system.

For the hydrogen storage there were several possibilities to choose from. In Section 2.4 it is explained why it is decided that the hydrogen is stored at a pressure of 700 bar in composite tanks. Based on the power profile and the fuel cell efficiency, the amount of hydrogen required is determined to be 13.9 kg. To fit this amount of hydrogen in the fuselage, three tanks are used which have a combined total weight of 246.5 kg. The total costs of these tanks are determined to be €13.500.

In Section 2.5 the electrical motor selection can be seen. Since a lot of research has been done for the electrical motor, it would be out of the scope of this report to design a new one. Therefore an already existing motor is chosen. The electrical motor is selected based on the power requirements of the propellers. The PowerPhase 220 is chosen to be the electrical motor. It can handle peak powers of 220 kW and is

able to cope with a continuous power of 120 kW, with a maximum speed of 6000 RPM.

2.7 Sustainable Development Strategy

Although performance is important for the Zero EZE, sustainability is just as important in the design. This section will explain the sustainable development strategy with respect to the propulsion system. Each component will be discussed separately.

2.7.1 Propeller and Shroud

The propellers are optimized such that the efficiency is higher than for conventional propellers. Due to the high propulsive efficiency of the SRP, less fuel is needed to produce the same amount of thrust. The addition of a stator behind the propeller also increases the propulsive efficiency. Another aspect of the sustainable strategy for the propellers is the noise production. By including a shroud around the propellers, the noise level will be decreased. The acoustics within the shroud have not been calculated in this report, therefore it is recommended that this will be done in subsequent researches. By implementing the shroud a better airflow can be achieved at the propeller after which its efficiency increases. Due to this efficiency increase, the RPM can be lowered resulting in a near field noise reduction of around 6 dB.

2.7.2 Fuel Cell

The fuel cell consists of non-toxic materials and can therefore be safely discarded at the end of its lifetime. However, the PEM fuel cell makes use of a platinum catalyst, which is a scarce material. Therefore effort should be put in platinum recovery out of the fuel cell so that it can be reused. Otherwise the possibility exists that there is not enough platinum available for mass production of the PEM fuel cell.
One of the major advantages of using a fuel cell system is the high sustainability of such a system. By using hydrogen as fuel, the only exhaust produced is water. Some NOX will be present in the water, but this was already in the air and thus can not be seen as pollution. The major contributor to environmental pollution will be in the production of hydrogen. To produce hydrogen, electricity is needed that is still being generated in conventional power plants. This means that the hydrogen used will be as sustainable as the power plant that generates the electricity. Thus when using environmentally friendly methods such as solar power or wind energy, the hydrogen can be considered sustainable. These methods are already used and will only improve in the near future.

2.7.3 Electric Motor

The brushless DC motor can be considered very sustainable. The motor operates emission free and produces virtually no noise. The efficiency and lifetime of the motor can be considered high and due to the low amount of moving parts, wear can almost be considered negligible. The electrical engine is made out of metal parts, which are easily recyclable at the EOL.

Chapter 3

Layout

With the propulsion system defined, it can be concluded that there is a lot of space needed in the fuselage to incorporate it. Therefore it is important to make an internal layout of the fuselage, to see if this is possible. When the components are positioned, the center of gravity can be determined which is needed for stability calculations. Also the interaction between all the systems of the Zero EZE need to be analyzed to get an overview of all the hardware that has to be implemented in the design. This is done by making several diagrams that clarify the system interactions and ground communication. These diagrams are a communication flow diagram, a data handling diagram and an electrical block diagram.

This chapter begins with the determination of an arrangement of the internal components in Section 3.1. In this section the center of gravity is also calculated. The sizing and positioning of the landing gear is done in Section 3.2. After this the system interactions are elaborated on in Section 3.3.

3.1 Internal Components Arrangement

In the detailed design phase volumetric and shape parameters for all the subsystems of the aircraft are determined. With this information an internal layout for the Zero EZE can be decided on. Also the weights of all the internal components is gathered in order to compute the center of gravity of the aircraft, needed for calculations further on in the report. In Subsection 3.1.1 a list is provided of all the components which have to be fitted inside the fuselage. Subsection 3.1.2 discusses all these components in more detail and the volumetric and dimensional parameters are determined. Finally, the components are arranged into the fuselage in a logical fashion and visualized in 3D in Subsection 3.1.3.

3.1.1 Internal Components

For a first inventory of the components which have to be fitted inside the fuselage, a list is generated of the general layout components. The biggest deviations from the Long EZ internal layout is the integration of a fuel cell system. Another very important factor in the internal configuration is the sizing of the cockpit. The sizes of all the fuel cell system components and the cockpit are specified in Subsection 3.1.2. The first inventory list of internal components is shown below:

- fuel cell system
- cockpit
- luggage
- ballistic parachute
- landing gear

3.1.2 Volumetric Analysis of Components

Fuel Cell System One of the biggest challenges in fitting all the components into the fuselage is the incorporation of the fuel cell system, since this system takes up most of the space inside the aircraft. Of all

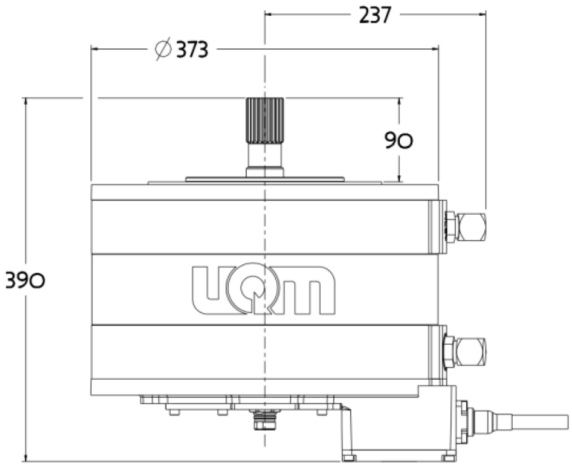

Figure 3.1: Dimensions Electric Motor [mm]

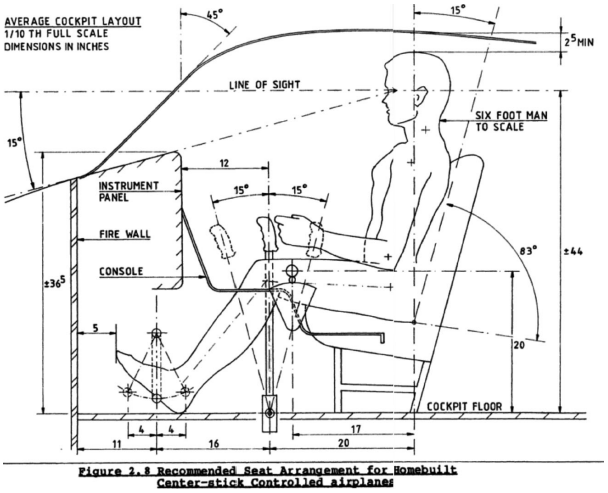

Figure 3.2: Recommended Cockpit Dimensions Homebuilt Aircraft [in]

the fuel cell system components, the fuel tanks take up the most space. In Section 2.4.8 it is determined that three fuel tanks are needed. The size of two of these cylindrical tanks are 394mm in diameter and 1640mm in length. The third fuel tank has a 557mm diameter and is 711mm in length. The fuel cell required to meet the performance requirements is sized to be 60mm × 60mm × 40mm. Considering the large empty weight of these fuel tanks, the tanks should be placed as close to the center of gravity of the aircraft to ensure proper controllability. The size of the electric motor which drives the propeller is determined in Section 2.5. The dimensions of the chosen electric motor are shown in Figure 3.1.The electric motor should be placed close to the propeller in order to prevent the added weight of transferring the rotary power to the propellers if they are positioned far apart.

Cockpit Another important aspect in the internal design is fitting the pilot and passenger into the aircraft while providing sufficient room for a comfortable flight. This is particularly important considering the Zero EZE is designed as a business commuter aircraft. Figure 3.2 gives a recommendation of the dimensions required for a pilot of a general aviation aircraft. From this picture it is found that a recommended fuselage height for fitting a pilot is approximately 1.30 m, a length of 1.42 m and a downwards visibility angle of 15 deg. Also the dashboard has approximated dimensions of 35 cm by 43 cm and an added weight of 36 kg [58].

Luggage As mentioned before the Zero EZE is designed for short-range business trips, which means that the luggage compartment does not need room for big suitcases. The space available for luggage is therefore assumed to be equal to the dimensions of standard aviation cabin baggage, which is 55cm × 40cm × 20cm. This is a luggage size per passenger, so the luggage compartment of the Zero EZE should have sufficient room for two of these.

Ballistic Parachute In the event of complete loss of flight controls during flight, it is of grave importance to ensure that the pilot and passenger can still perform a non-lethal landing. This is why a ballistic parachute is incorporated into the internal layout of the aircraft. The ballistic parachute consists of a fiberglass box called a VLS containing the parachute and a rocket motor. An activation cable runs from the rocket motor to the cockpit [82]. For the Zero EZE the chute needs to be positioned at the top of the fuselage and not too far to the back. Also a vertical take-off of the rocket is required, hence the choice of a VLS parachute. This is necessary since the Zero EZE is a pusher aircraft and it has to be ensured that the chute will deploy over the shroud in order to not be caught in the propeller. Based on information provided by BRS Aerospace, the Zero EZE can use a ballistic parachute with a size of 91.4cm × 45.7cm × 27.9cm [81] and a weight of 36 kg. The ballistic parachute should have multiple attachments to the fuselage in order for the plane to have a horizontal orientation during a descent using the parachute [83]. The specifics of the locations and amount of attachments should be determined in consultation with the company providing the ballistic parachute [84].

Landing Gear Considering the determination of the size and position of the landing gear requires extensive calculations, this is performed in a separate section, which is Section 3.2. With this data a 3D model of the landing gear is made. In Subsection 3.1.3 it is concluded if the landing gear can be fitted into the fuselage, opening up the option of making the landing gear retractable.

3.1.3 Final Internal Arrangement

Finally all the components are fitted into the fuselage to determine whether enough room is available. This assembly of all the components inside the fuselage is shown in Figure 3.3

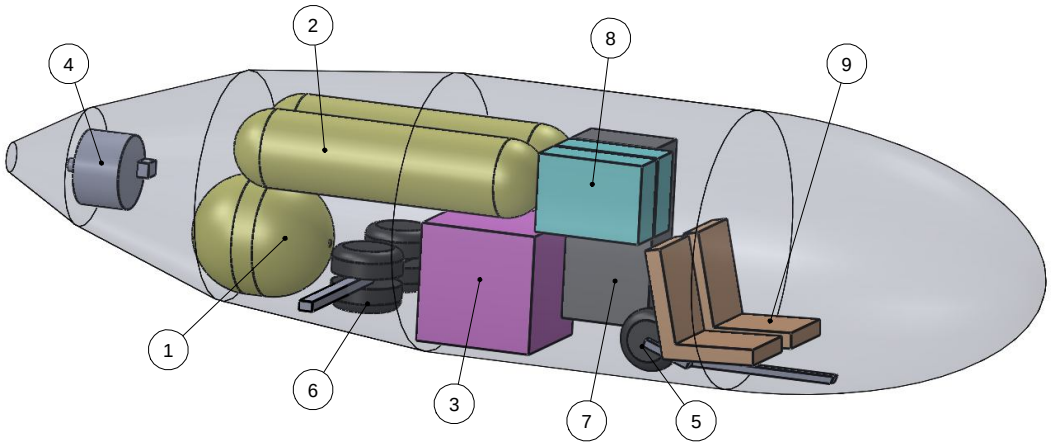

Item no	Description
1	Fuel Tank (3.7 kg H2)
2	2X Fuel Tank (5.1 kg H2)
3	Fuel Cell
4	Electric Motor
5	Nose Wheel
6	Main Landing Gear
7	Ballistic Parachute
8	2X Luggage
9	2X Seat

Figure 3.3: Internal Arrangement

From this figure it can be concluded that there is enough room to fit in all the components, even the landing gear. Therefore, the Zero EZE will incorporate a retractable landing gear, improving its aerodynamic performance and therefore its range. The design of the retractable system itself is out of the scope of this project. The luggage compartment is put right behind the seats, making it easily accessible from the cockpit. Next to the luggage is the ballistic parachute, orientated upwards and not too close to the propeller. The nose wheel can be fitted right behind the seats when it is retracted and the main landing gear between the fuel cell and a fuel tank. As can be seen from the figure, there is still some unoccupied space in the aft of the fuselage, opening up the possibility for aerodynamic improvement of the fuselage, which is performed in Section 4.1.

3.2 Landing Gear

For the Zero EZE, the position of the landing gear or undercarriage is completely redetermined due to the drastic changes in geometry and other properties with respect to the Long EZ. For the design of this undercarriage, the following plan of approach is used. The methods used are seen as preliminary sizing tools, which are sufficient considering the scope and duration of this project.

1. Define general configuration
2. Define position and wheel track of main and nose gear
3. Define loads on nose and main studs
4. Size the required tires, ensure the capability to cope with the static loads

5. Decide whether the undercarriage will be retractable or not

3.2.1 General Configuration

For the general configuration of the undercarriage, a tricycle gear is chosen. The most important advantages in this configuration, according to Reference [69], are as follows:

- Stable groundloop behavior
- Easy steering after touch down and during taxi-procedure.
- Good take-off rotation and easy take-off procedure

It is seen that the configuration is extra advantageous considering the take-off procedure. Since the Zero EZE is using a pusher configuration, this is highly preferable.

3.2.2 Strut Disposition and Wheel Track

After deciding the lay out of the undercarriage to be a tricycle one, the position of the landing gear is determined. This is done by keeping two geometric criteria in mind; the ground clearance and the so-called tip-over criteria. From this the minimum X-coordinate and height of the main gear, both with respect to the center of gravity, are determined.

Firstly, the ground clearance prevents the tail, or in this case the shroud, to hit the ground while performing the take-off or landing. The ground clearance is directly related to a maximum angle of rotation, which in this case is set to 15 degrees. This angle, depicting the ground clearance, needs to have a larger value compared to the take-off angle.

Secondly, the tip-over requirement prevents the aircraft, as the name depicts, from tipping back on its tail. To accomplish this the main gear has to be positioned after the maximum aft CG location, within a certain angle. Both of the requirements are visualized in Figure 3.4 [49].

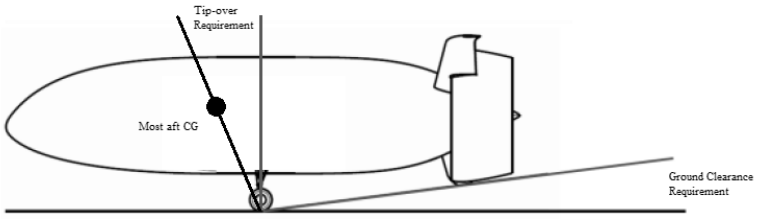

Figure 3.4: Disposition Requirements

The angles of the ground clearance and tip-over requirement, according to Raymer [72] are defined as follows: "The angle between the vertical line originating from the main wheel position to the center of gravity should be greater (or equal) than the tip back angle or 15 degrees, whichever is larger". For the case of the Zero EZE, the ground clearance angle is defined to be 15 degrees, as well as the angle between the vertical line from the wheel position and the line connecting the main gear with the center of gravity. With this information the coordinates of the main gear are defined. The minimum distance with respect to the center of gravity is 0.30m, whereas the minimum height has a value of 1.14m.

Secondly the wheel track is defined, which is the distance between the most left and most right gears [70]. This is visualized in Figure 3.5 [70], showing the front view of the undercarriage.

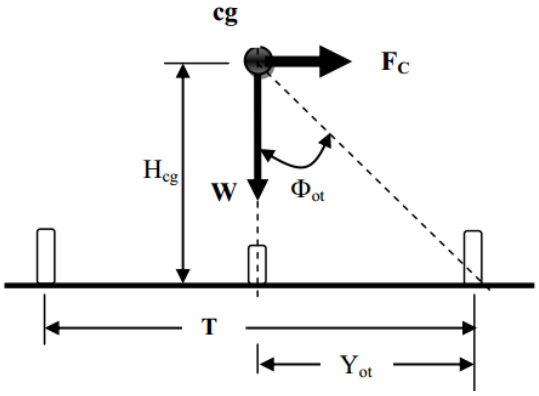

Figure 3.5: Wheel Track

This distance is defined by the ground lateral control, the ground lateral stability and the structural integrity. For this project, the focus will be on the ground lateral stability, which prevents the aircraft from rolling over during a ground turn or due to heavy cross winds.

The definition of the overturn angle is visualized by Figure 3.5. Two moments act on the aircraft while performing a turn, these being the centrifugal moment and the restoring moment of the aircraft's weight [70], which is a function of the wheel track. The two forces causing these moments are also shown in the figure. The resulting equation for the total moment, taken about the outer main gear, is shown in Equation 3.1.

$$\sum M_0 = W \cdot Y_{ot} + F_C \cdot H_{cg} \tag{3.1}$$

Where Y_{ot} and H_{cg} are also defined in Figure 3.5, F_C represents the centrifugal force and is defined by Equation 3.2.

$$F_C = m \cdot \frac{V^2}{R} \tag{3.2}$$

Where V and R are defined as the ground speed while turning and the turn radius of the aircraft, respectively. In our case these variables were defined to be 10m/s and 30m. From this the wheel track is defined, as well as the overturn angle. The wheel track, in the case of the Zero EZE, is seen to be a marginal value. This extremely low value is explained by the low speeds at which the aircraft turns.

As already mentioned, cross winds have an influence on this overturn angle [70]. The force generated by a cross wind is in fact a drag force, as shown in Equation 3.3.

$$F_W = \frac{1}{2} \cdot \rho \cdot V_W^2 \cdot A_S \cdot C_{D_S} \tag{3.3}$$

The drag coefficient C_{D_S} is called the aircraft side drag and A_S is defined as the affected area. To prevent the aircraft from being overturned by a cross wind, the moment of the aircraft weight has to be greater than the moment of the wind force [70], as seen in Equation 3.3. However, for the scope of this project and considering the large estimations that should be made, the cross wind component will not be included.

Besides these two requirement, the value could also be determined by a common rule of thumb. This basic design rule is used for the minimal disposition of the landing gear of this project. The rule of thumb [70] states that the overturn angle should have a value larger than 25 degrees. Here a safety factor of 20 % will be used, this stating a to be used overturn angle of at least 30 degrees. From this a corresponding wheel track of at least 1.32 m is found. Considering the large estimations before, and the fact that this value also satisfies the other two requirement, this wheel track is used as minimum value.

The last step is to define the distance from the nose gear to the center of gravity. This is doneby considering the minimum allowable nose loading to obtain sufficient steering power. Here the method of minimum loading is chosen. This is explained in the upcoming section.

3.2.3 Load Calculation

After defining the positions, the loads are calculated. The static loads on the main and nose gear are defined as follows.

$$P_n = \frac{W_{TO} \cdot l_m}{(l_m \cdot l_n)} \tag{3.4}$$

$$P_m = \frac{W_{TO} \cdot l_n}{n_s \cdot (l_m \cdot l_n)} \tag{3.5}$$

Where l_m and l_n define the distance of the main and nose gear to the center of gravity, respectively. The value of l_m was determined in the previous section. The value of l_n is obtained by the use of Equation 3.4. According to Raymer [72], the optimum range of weight acting on the nose gear is about 8% to 15% of the total weight, with respect to the most aft and most forward cg. From this minimum or optimal amount, the distance between the nose wheel and center of gravity is calculated. A nose load of 15% of the take-off weight is assumed, from this the l_n value is defined to be 1.72m. A total load of approximately 5000N is found on each stud of the main gear. Note that considering the nose gear an extra dynamic load, coming from the braking forces, is present. However for this first sizing, this is not necessary to include, according to [69].

3.2.4 Amount of Wheels and Tire Sizing

To choose the number of wheels, following criteria are normally considered; the load per tire, the associated bearing strength, the consequences of a tire blow out and the cost. The more wheels used, the smaller the diameters can be made. In this design the amount of wheels will be designed with respect to the possibility of having a retractable gear.

The size of the to be used tires depend on three different criteria; being the W_{TO}, the P_n/W_{TO} and the $P_m/(n_s\ W_{TO})$. The actual size is determined by using statistical values, given by Raymer [72]. For the diameter of the tire Equation 3.6 is used.

$$D = A \cdot W^B \tag{3.6}$$

Here W is the weight on each wheel. A and B are fixed coefficient found by statistics; for general aviation these are found to be 5.1 and 0.349, respectively [72]. The width of the tire is sized in the same manner, however with other coefficients. Here A and B are defined as 2.3 and 0.312, respectively. From this the diameter and width are found to be 0.35m and 0.13m.

The diameter and width of the nose wheel are calculated in the same way as the main gear. This results in a diameter of 0.31m and a width of 0.12m. According to Raymer [72], this nose gear should have a value in the range of 60% to 100% of the main gear, this can also be seen in these results. In these calculations it was chosen to have a single nose wheel and a double main wheel, this for retractability reasons.

3.2.5 Retractable Gear Feasibility

Now the preliminary dimensions of the undercarriage are known, Table 3.1 summarizes all previously calculated dimensions and locations.

Table 3.1: Landing Gear Dimensions

l_m	0.30 m
l_n	1.72m
H_{CG}	1.14 m
P_m	5003 N
P_n	1766 N
D_{main}	0.35 m
D_{nose}	0.31 m
T	1.32 m

3.2.6 Center of Gravity

The center of gravity is calculated by taking the weight of all components and their distance to the COG reference line. Inserting the Zero EZE data into Equation 3.7 gives a value for the COG. The obtained values can be found in Table 3.3. An overview of the weight and arm of the components is given in Table 3.2. The COG is calculated for both a fully loaded and a lightly loaded case to determine the range.

Since several components are not fully designed at this stage in the design process, the COG calculations can not be considered exact. The weight of comonents could still change. Also, some components, such as the internal structure are not incorporated yet into the calculations. However, since approximately 90% of the weight of the aircraft is probably accounted for, a margin of ± 10cm is used for the position of the COG.

$$COG = \frac{\sum_{i=1}^{i=n} w_i \cdot x_i}{\sum_{i=1}^{i=n} w_i} \tag{3.7}$$

Table 3.2: Weight and arm of aircraft components

Component	**Weight (heavy) [kg]**	**Weight (light) [kg]**	x_{tip}**[m]**
Pilot	80	80	1.7
Passenger	80	0	1.7
Fuel Tank (sphere)+ Fuel	66.2	62.5	4.5
Fuel Tank (Cilinders) + Fuel	194.2	184	3.4
Fuel Cell	90	90	2.9
Electrical Motor	40.8	40.8	5.0
Chute	38	38	2.3
Chiars	50	50	1.7
Dashboard/Controls	80	80	1.0
Luggage	27	0	2.3
Fuselage	100	100	2.25
Wings	95	95	3.6
Canard	10	10	0.5
L/G (front)	15.4	15.4	2.0
L/G (back)	61.6	61.6	3.5
Internal Structure	40	40	3.25
Propeller and Shroud	60	60	5.5
TOTAL	**1128.2**	**1007.3**	

Table 3.3: Center of Gravity Range

Configuration	x_{tip} **[m]**
Heavy	2.91
Light	3.01
Total range	2.91-3.01 ± 0.10

3.3 System Interactions

Next to the position of each system in the fuselage, it is also important to determine the interactions between them. In order to visualize these, several diagrams have been made. Subsection 3.3.1 describes the communication system between the Zero EZE and ground control, as well as the instruments necessary for communication. Although communication is not a main focus of this project, it remains important for the aircraft design and is therefore included in these system descriptions. Subsection 3.3.2 visualizes the systems needed for propulsion and provides them with a short description. Subsection 3.3.3 describes the electric flows through the system for both the start-up phase and the cruise.

3.3.1 Communication Flow Diagram

A Communication Flow Diagram is provided to present the flow of data through the system and to and from the external environment. Although the Zero EZE is a small aircraft and only carries two people, communication between the aircraft and air traffic control is needed. Therefore at least a couple of communication systems are needed. Two main ways of communicating are present, as well as one extra that can be used in emergency situations. This is visualized in Figure 3.6.

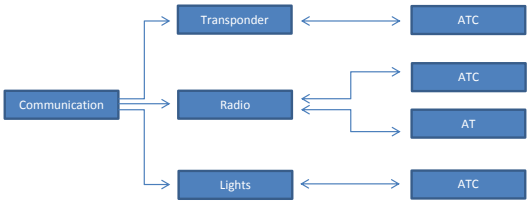

Figure 3.6: Communication Flow Diagram of the Zero EZE

The first manner represents the continuous communication of the ATC to the transponder located in the aircraft. This is done using a ground based radar. The ground station transmits, via the radar, an interrogation to the transponder of the aircraft. This is called the uplink. The reply of the transponder, the downlink, depends on the type of interrogation [86]. This downlink could be an identification code (mode A) or an altitude code (mode C), providing constant information of the identification, altitude, speed, etc. of the aircraft. The second main manner of communication is the communication through radio. This between the ATC as well as other air traffic in general. The remaining manner is only used in emergency cases. When the radio does not function, emergency signals can be given from and to the aircraft. The diagram did not need an update in the final stage of the project and is therefore similar to the CFD presented in the midterm report.

3.3.2 Hardware Block Diagram

For the Zero EZE one hardware diagram has been made, which describes the propulsion system. This is the most important part of the aircraft and is already discussed in Section 2.4. Figure 3.7 shows all the hardware components needed for the system.

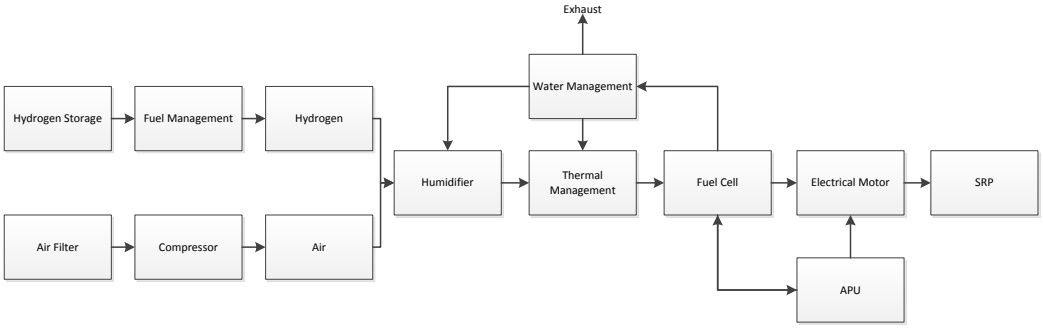

Figure 3.7: Hardware Diagram Propulsion System

As can be seen, the fuel management system will provide hydrogen from the storage tank to the humidifier in order to moisturize the hydrogen. A similar process applies to the air supplied to the fuel cell: first of all it is filtered to remove any particles that might damage the fuel cell, then it is compressed in order to optimize the airflow. Also the air runs through a humidifier. When both the hydrogen and air are heated to the proper inlet temperature, they enter the fuel cell where they are converted into electricity. The exhaust water generated is reused for humidification and temperature control within the system. The electricity generated by the fuel cell provides power to the electric motor and is used to recharge the APU. The electric motor delivers the energy to the propeller in order to create thrust. A more extensive flow diagram of the propulsion system can be found in Appendix A

3.3.3 Electrical Block Diagram

The electrical system of the Zero EZE has two different layouts; one for start-up and one for the cruise phase. They are described in Figure 3.8a and Figure 3.8b respectively.

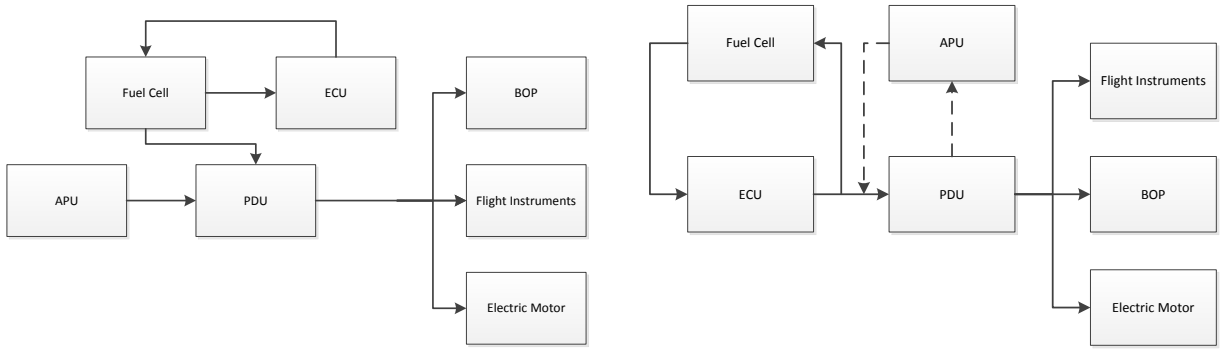

(a) Electrical Diagram for Start-up

(b) Electrical Diagram for Cruise

Figure 3.8: Electrical Diagrams

In order to start up the fuel cell system, reactants should be supplied to the fuel cell. As can be seen in Figure 3.8a, the APU provides power to the PDU, which in turn provides power to the BOP and flight instruments. The BOP initiates the inflow of hydrogen and air to the fuel cell, such that electricity is produced. The ECU controls the fuel cell system variables, like inlet temperature and mass flow. Once the fuel cell starts to generate power, the APU is no longer needed and the system will run completely on the fuel cell. The new electrical system layout can be seen in Figure 3.8b.

Now that the fuel cell generates electricity, the APU can be recharged by the PDU. The PDU provides the power to the flight instruments, BOP and electric motor in the same way as during start-up. The electricity needed by the PDU is mostly delivered by the fuel cell, but some exceptions exist. When the power output needs to increase, the fuel cell needs a while before the new power output is reached. This implies that the fuel cell is not capable of dealing with sudden changes in power output. In order to cope with these situations, extra power is provided by the APU during that period.

3.4 Fuselage Pressurization

When the Zero EZE is flown at a higher flight levels, the fuel consumption will be less than it will be at a lower altitude, as discussed in more detail in Section 2.2. Further, turbulence and bad weather conditions can be avoided by flying in the relative smooth air at high altitudes. Also to avoid mountain tops, it is convenient to be already at a high cruising altitude instead of flying around them. Because of these advantages of flying at high altitudes, more and more GA aircraft are being designed to operate in these conditions [85].

With these advantages taken in mind, the cruise altitude for the Zero EZE is assumed to be 10,000 feet, based on reference aircraft like the Panthera Hybrid and Volta Volare. This is also the altitude for which the propulsion system is optimized. However, for this cruise altitude a pressurization system is needed due to FAR regulations [87]. Concerning the passenger comfort, the conditions inside the airplane can than be improved.

A pressurization system generally maintains the cabin pressure at 8,000 feet or below, keeping pilots and passengers safe from altitude illness and other discomforts [88]. The desired cabin pressure is chosen to be such that safe and comfortable conditions inside the cabin are maintained. When choosing this cabin pressure at the maximum allowed pressure altitude of 8,000 feet, the pressure that needs to be added by the pressurization system will be minimal, thus the extra power required to compress and regulate the airflow will be minimal as well.

The minimum cabin pressure allowed by FAR regulations is equal to 0.74 atm, corresponding to the altitude of 8,000 feet [87]. Since the ambient pressure at cruise height equals 0.69 atm, a pressure difference of 0.05 should be overcome. However, as discussed in Section 7.6.1, a 0.6 atm pressure difference can be

achieved for the Zero EZE fuselage. As a result the fuselage is designed to be able to fly at a maximum of 25,000 feet without extra certification needs.

Chapter 4

Aerodynamics

Aerodynamic optimization is essential to design an innovative aircraft. The two main forces in aerodynamics, lift and drag, have a large influence on the structures and propulsion and will therefore be optimized in this chapter. In the case of this project where the Long EZ aircraft had to be redesigned to a fully electric Zero EZE aircraft, a significant drag reduction needs to be accomplished. If this is reduced the structures can be lighter and less power is needed.

In Section 4.1 the fuselage will be designed first. By designing a low-drag body a first step is taken and will be followed by designing the main wing in Section 4.2. In this section the low-drag airfoil is one of the steps to obtain drag reduction. The aerodynamic analysis and improvement of the canard and winglets are performed in Section 4.3 and Section 4.4 respectively. Finally, in Section 4.5 an overview of the Aerodynamic performance is provided.

4.1 Fuselage

For the detailed design phase, the fuselage aerodynamic design is further developed into a low drag shape, where all the components can be fitted into. This is accomplished by first looking at the updated design constraints for the fuselage. Where especially new parameters for the fuel cell system are of grave importance. This analysis is done in Section 3.1 and further developed for the fuselage in Subsection 4.1.1. Next an update of the analytical drag calculation is done in Subsection 4.1.2. Then several concepts are developed which are in conformity with the design constraints. These concepts are elaborated in Subsection 4.1.3. These concepts are then implemented in Tornado and the results are visualized in Subsection 4.1.4. Finally conclusions are drawn from the output of Tornado, a 3D fuselage model is made and recommendations for further development are elaborated in Subsection 4.1.5.

4.1.1 Design constraints

In the detailed design phase a lot of interaction is required between the design of different components in order to get a final result which is conform with all the design constraints. Therefore the first step in the redesign of the fuselage is to gather all these constraints. The constraints related to the fuselage redesign are shown in Table 4.1.

Table 4.1: Fuselage Design Constraints

Constraint	**Source**
fuselage width $\geq 1.4m$	Section 3.1
fuselage height $\geq 1.3m$	Mid-Term Report, Fuselage Design
trailing edge base diameter $= 0.15m$	Section 2.3
pilot visibility angle from horizontal downwards $= 15°$	Section 3.1

4.1.2 Analytical drag calculation Zero EZE

Now that the constraints for the fuselage are determined, an update of the analytical drag calculation done in the mid-term report for the Long EZ fuselage can be given. The new parameters of the Zero EZE

required for input in the equations are given in Table 4.2. The wetted fuselage area is estimated in the same fashion as in the mid-term report for the Long EZ.

Table 4.2: Drag Calculation Fuselage Parameters Zero EZE

Total Length	**Maximum Diameter**	**Wetted Surface Area**	**Wing Area**
$5.5m$	$1.4m$	$12m^2$	$13.2m^2$

Even though the presence of a base diameter is a constraint for the Zero EZE fuselage, the base drag is neglected, as with the previous Long EZ drag calculation. This is because the propellers attached at the trailing edge will distort the flow and therefore a base drag calculation is not applicable. When the same atmospheric conditions are used and fully turbulent flow is assumed because the point of flow seperation is unknown, the zero-lift drag coefficient for the Zero EZE fuselage becomes:

$$C_{D_0} = 0.0052 \tag{4.1}$$

This is a significant improvement on the Long EZ drag coefficient of 0.0066 as calculated using the same method in the mid-term report. This is mainly due to the increased wing area, which is a parameter in the analytical drag calculation method, and a slightly improved slenderness ratio of the fuselage. It is also noted that the drag coefficient is higher than the axisymmetric fuselage shape chosen in the mid-term report which was based on literature. This will be addressed in Subsection 4.1.3.

4.1.3 Concept description

With the design constraints defined, a shape for the fuselage can be developed. This is done by defining several fuselage shapes in accordance with these constraints, compute and compare their drag characteristics and finally choose the shape which produces the least drag. The program that is used to calculate the drag characteristics is Tornado, which uses a vortex lattice method. Since Tornado is designed for calculating wing characteristics, the required input for a certain shape are airfoil cross-sections and their relative positions to each other, defined by parameters such as a taper ratio and sweep angle. Therefore longitudinal sections of a fuselage shape have to be made for the implementation in Tornado. These longitudinal sections are generated using the method described by Parsons [47] [48]. For simplicity and consistency, the same longitudinal sections are used in each concept. Also, every cross-section is implemented in the same fashion regarding sweep and taper ratio parameters, hence for this concept description only longitudinal sections are shown.

In the midterm report an axisymmetric fuselage shape was chosen. In Section 3.1 all the internal components are fitted into this type of shape. With the maximum height and width defined by the cockpit requirements, the length is the next parameter to be determined. For the determination of the length, the slenderness ratio is the most important parameter to keep in mind for aerodynamic performance. The length is chosen to be 5.5m, which gives the Zero EZE a slightly higher, hence aerodynamically better, slenderness ratio. This makes the fuselage thicker and shorter, compared to similar aircraft. This is done for the following reasons. The main reason is that the propulsive efficiency of the propellers goes up, which means the range of the Zero EZE is increased. This is due to the fact that fuselage boundary layer air ingested by the propellers has lower momentum. Also the space inside the fuselage can incorporate a retractable landing gear and the considerably large fuel cell system, the fuel tanks in particular. Finally, a shorter fuselage decreases the distance between the main gear and the shroud, facilitating the aircraft with a higher take-off rotation [49]. With the height and the length defined, longitudinal sections can be modelled. The concepts generated with Matlab which are implemented in Tornado are shown in Figure 4.1. For all the concepts the bottom part is the same shape, which is made with the calculation method described by Parsons, and then mirrored about the x-axis. This is done because from the internal layout it can be concluded that there is no room for improvement of the shape at the bottom, hence the same, proper bottom shape is maintained for all the concepts.

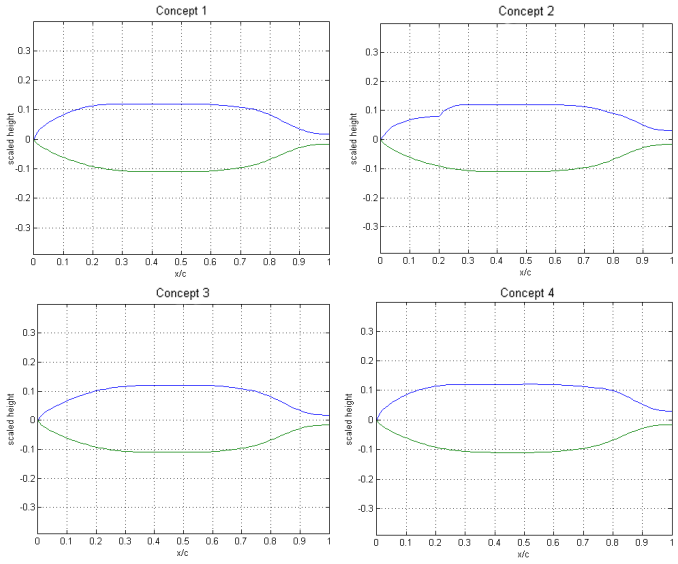

Figure 4.1: Fuselage Shape Concepts

As can be seen from Figure 4.1, there is limited space available for variations in the concepts. This is due to the dimensional constraints to keep the shape in accordance with the internal layout. There exist some possible critical points regarding the available space in the fuselage which are located at the x-values of 0.3 and 0.8. At $x = 0.3$ the head of the pilot and passenger is positioned and therefore requires ample height. At $x = 0.8$ the back part of the two long fuel tanks are positioned and the luggage compartment on top of these tanks as seen in Figure 3.3. If the top curve of the fuselage longitudinal section is too low, these components will not fit. As can be seen in Figure 4.1, concept 2 has a canopy shape at the front, which is shaped manually. This is necessary to fulfil the constraint of the pilot visibility. In the other three concepts, this constraint is not fulfilled by a certain fuselage shape, but can be solved by using cameras on the outside of the aircraft [50]. Since the aircraft nose in these concepts has a significantly larger volume than the concept with the canopy shape, there is ample room to fit these cameras and the corresponding displays [50]. Concept 1, 3 and 4 are generated using different parameters, but maintaining the proper height at the critical locations described earlier. The main difference between them is the sharpness of the nose section. Concept 3 has the sharpest nose, while concepts 1 and 4 have the bluntest nose. Concept 4 also has a higher curve at the back part of the fuselage to accompany more internal storage space.

4.1.4 Tornado implementation and results

As mentioned earlier Tornado requires longitudinal sections and several parameters regarding their scale and position relative to each other. Since the longitudinal section of a fuselage shape at the edge is only a dot or a line, the outer longitudinal section in the Tornado model is chosen slightly more to the center. In order to get a good approximation of the shape, three longitudinal sections are implemented in Tornado, which meshes the surfaces between these sections. For the top view shape of the fuselage, a wide parabolic shape is taken, where the taper ratio and the sweep angle for each section is estimated. A wide parabolic shape is chosen in order to ensure the maximum width is higher than the maximum height, as defined by the constraints. All the parameters which are implemented in Tornado can be found in Figure D.1 in Appendix D , where the sweep is in radians and the half-span is in meters. After the implementation of the shapes in Tornado, results have to generated and analyzed. The main focus in the aerodynamic improvement of the fuselage is the minimization of the drag coefficient. Therefore the drag coefficients calculated by Tornado using cruise conditions are shown in Table 4.3

Table 4.3: Tornado Drag Coefficient Results

Concept nr.	**1**	**2**	**3**	**4**
$\mathbf{C_D}$ $(\times 10^{-3})$ $[-]$	0.72997	1.7587	0.70168	1.3857

In order to get an indication of the shape that is generated with Tornado, an example plot of the pressure distribution of concept 2 is shown in Figure 4.2, which shows this shape. It can be seen that at the side edges a straight line is modelled instead of a curve, which is due to the method of implementation of Tornado.

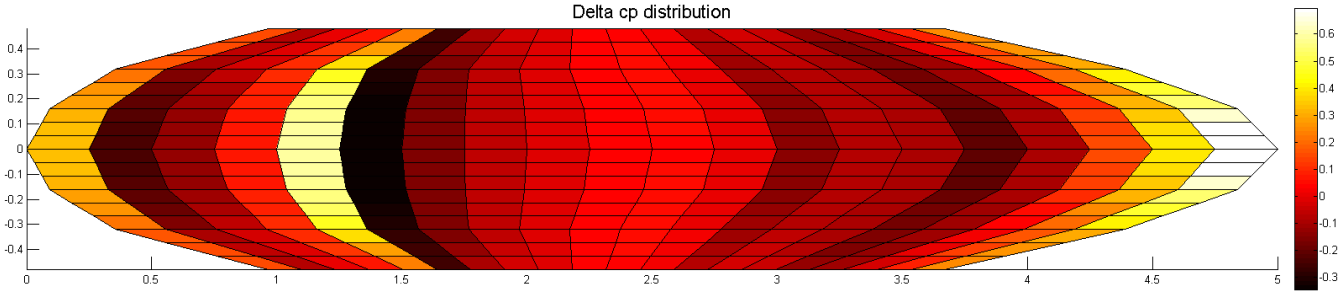

Figure 4.2: Pressure Distribution Concept 2

4.1.5 Conclusions and recommendations

From the mid-term report and the analytical drag calculations, the fuselage is designed to have a drag coefficient of around 0.004. As can be seen from the results of Tornado, the drag coefficients are significantly lower than that. This can be attributed to several factors. The first and foremost reason for this anomaly is that Tornado is a program designed for wing analysis and therefore is focused on generating lift characteristics as opposed to drag characteristics. Some experimentations with Tornado has led to the conclusion that the drag coefficient is calculated based on the lift coefficient. This was found by implementing a wing with symmetric airfoils without an angle of attack. This condition does not generate, but it should produce drag. Since in Tornado also the drag coefficient equalled zero, this conclusion is drawn. A fuselage generates very little to no lift whatsoever, resulting in a calculated drag coefficient which is far too low. Another reason for the low drag values is that Tornado uses a vortex lattice method and therefore does not take viscous drag into account, which also entails a significant part of the total drag of a body moving through the air. Finally the accuracy of Tornado also decreases due to the approximation of the shape that has to be made. A shape that is rounded of neatly at the front edges is difficult to model within a program which requires longitudinal sections to simulate a shape.

Even though the results generated by Tornado cannot be compared to analytical or experimental results, they can still be compared to each other to find the best of the several concepts. Since installing cameras is the solution to eliminate the canopy shape and when extra luggage storage is decided to be of less significance than the performance gain for the Zero EZE, concept 3 is chosen as the final shape for the fuselage. As for the drag coefficient, the result calculated with the analytical method is taken as the final answer to be used in further calculations in the report. This drag coefficient is:

$$C_{D_0} = 0.0052 \tag{4.2}$$

Finally, a 3D model is created based on the longitudinal section of concept 3. This model is shown in Figure 4.3. The model has a slightly oval shaped cross-section with the dimensions defined in Table 4.1. The main consideration regarding the aerodynamic improvement of the fuselage shape is the employment of a smooth surface, which contributes largely to the overall quality of the flow around the shape [51].

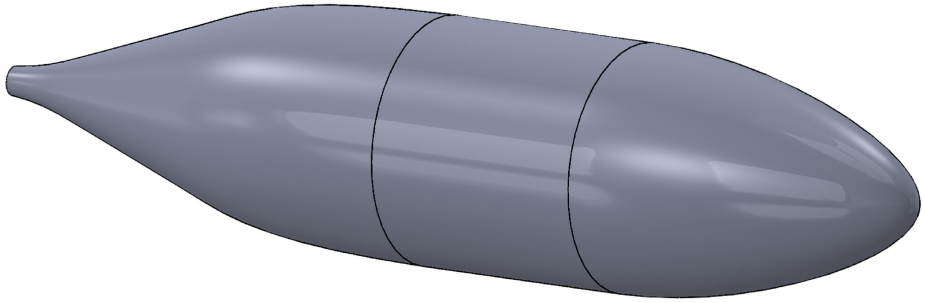

Figure 4.3: 3D Fuselage Shape

The feasibility of this design is very high due to the fact that it meets all the requirements set for the dimensions of the fuselage. As for recommendations for further detailed design, it is recommended to implement this 3D model into a far more advanced 3D CFD program like OpenFoam or CATIA Fluent in order to compute the drag characteristics more accurately. In these programs a fuselage model is far more accurately modelled than Tornado can achieve. The usage of these types of programs however proved too time-consuming and complex for the scope of this design exercise. Another recommendation regarding aerodynamic analysis of the fuselage shape is performing wind tunnel tests. Since with CFD it is relatively easy to analyze alternative models, this can already be used as soon as a basic geometry is available. Whereas wind tunnel testing is better suited in a later design stage where the initial concepts are reduced to a most promising design. It is highly recommended to use both tools of aerodynamic analysis, since both methods each have their inherent strengths and weaknesses and can therefore be used for their mutual benefit. Finally, the pilot visibility requires more investigation to ensure a safe visibility range. The size of the window has yet to be designed and from that the amount and the placement of cameras can be determined.

4.2 Main Wing

In this section the design process of the main wing will be discussed. The main wing is by far the largest contributor to the total lift and drag of the Zero EZE. It is therefor the main focus to optimize the lift over drag ratio.

First, in Section 4.2.1 the airfoil selection will be discussed. Next, all the wing dimensional parameters, such as the surface area, taper ratio, incidence angle, dihedral and wing placing, will be discussed in Sections 4.2.2 till 4.2.8. Finally, in Section 4.2.10, an estimate will be given on the drag produced by the main wing.

4.2.1 Airfoil Selection

As discussed in the conceptual design the Eppler 1230 airfoil of the Long EZ will be changed to an airfoil with a Natural Laminar Flow airfoil. This is done to obtain drag reduction and remain (or increase) the lift generation. Important parameters are the minimum drag coefficient, maximum lift coefficient and the stall angle.

An airfoil family designed to maximize laminar flow and widely used in GA is the NACA 6-series airfoil family [52]. The NACA 7-series is also designed to maximize laminar flow but reduces the maximum lift coefficient [53] which is not desired. However it was also shown during research that these airfoils have a reduced maximum lift coefficient for a rough leading edge surfaces. This roughness might appear due to contaminations. For safety reasons this is a disadvantage. [54] The newest airfoils designed by NASA, which are optimized for laminar flow and low drag, are the NASA/Langley NLF airfoils, like the NLF(1)-0215F and NLF(1)-0416 airfoils. This family of airfoils is used by GA aircraft like the Neico Lancair, Mooney 301 and Cirrus VK-30 [55]. Therefore one of the airfoils from this family will be chosen as the airfoil for the Zero EZE.

Four suitable airfoils with good characteristics are the NLF(1)-0215F, NLF(1)-0416, NLF(1)-0115 and NLF(1)-1015. It has to be noted that it is important to have a high stall angle for the main wing in order to let the canard stall before the main wing. To make a trade-off all airfoils are put in DesignFoil

to provide Cl-Cd and Cl-alpha diagrams. These diagrams can be seen in Figure 4.4 and 4.5. Furthermore the Eppler 1230 airfoil is added as a comparison with the Long EZ. In Table B.1 in Appendix B the characteristics of the four airfoils can be found. Only the information which is necessary for the airfoil trade-off is taken into account.

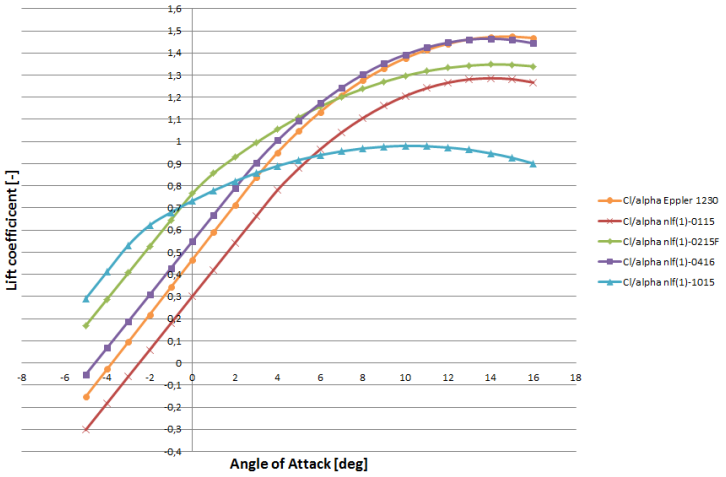

Figure 4.4: Lift coefficient versus angle of attack for five selected airfoils (Re = 5,000,000)

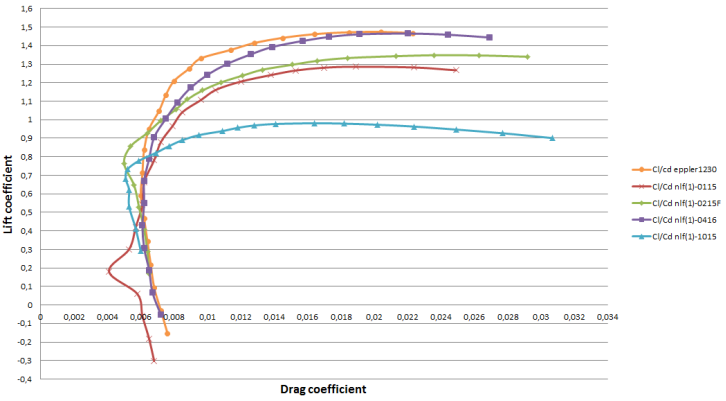

Figure 4.5: Lift coefficient versus drag coefficient for five selected airfoils (Re = 5,000,000)

From these figures it can be seen that the airfoil NLF(1)-1015 can be excluded based on the low maximum lift coefficient and $\alpha_{L=0}$. Also the airfoil NLF(1)-0416 is excluded because it shows no drag reductions in Figure 4.5. The third airfoil which can be discarded from this trade-off is the NLF(1)-0215F airfoil since it has a drag bucket at too high lift coefficients. Also the maximum lift coefficient is lower for this airfoil compared to the Eppler 1230 airfoil.

The best airfoil for the main wing of the Zero EZE therefore becomes the NLF(1)-0115 because it has a drag bucket at a lift coefficient of approximately 0.2. This is highly desired since it is the design lift coefficient of this aircraft. The maximum lift coefficient is lower than for the Eppler 1230 airfoil but this will be solved by the implementation of HLD. From references it has also become clear that this airfoil is highly suitable for GA applications and avoids the disadvantages of laminar flow loss due to leading edge contaminations and high aft loading [56]. The characteristics of the NLF(1)-0115 airfoil can be found in Table 4.4.

Table 4.4: NLF(1)-0115 airfoil characteristics

Airfoil code	NLF(1)-0115	Cruise L/D	44.0
$(t/c)_{max}$	15%	Maximum L/D	122.5
$C_{l_{max}}$	1.286	$\alpha_{(L/D)_{max}}$	7.0
Stall angle	14.0	$\alpha_{L=0}$	-2.5

It has to be noted that the $C_{l_{max}}$ in Table 4.4 is taken from the measurements in DesignFoil. From reference data however it is known that the NLF(1)-0115 airfoil can achieve a $C_{l_{max}}$ of 1.5 [56]. To avoid overestimation of the airfoil performance only the measurement data will be taken into account for further calculations.

4.2.2 Surface Area

To determine the surface area of the wing (S_w), the minimum wing loading should be determined. This loading occurs at maximum lift coefficient, when flying at stall speed. In the EASA CS23 regulations, it is determined a GA aircraft can not stall at speeds higher than 61 kts at MTOW. [57] From these values, the total wing loading at stall speed can be determined using equation 4.3. In this equation the air density at standard sea level conditions is used. It could be that the air density at some airports, on higher grounds and on a hot day, is lower. However, the maximum approach speed is considerably higher than the stall speed. So even if the stall speed increases slightly due to special location or weather conditions, landing at a safe speed is still possible.

$$\frac{W}{S} = \frac{1}{2} \cdot \rho \cdot V_{stall}^2 \cdot C_{L_{MAX}} \tag{4.3}$$

In the Baseline Report a weight of 800 kg was estimated for the Hybrid EZE. This weight estimation was very preliminary and now turns out to be slightly low. For the estimation of the wing area a weight of 1200 kg is assumed. Now, the total wing surface area (wing and canard combined) can be determined. In this calculation a safety factor is incorporated to ensure the required performance, even if the efficiency of the wing goes down (e.g. due to contaminations on the wing surface). This factor is assumed to be 1.1. From this surface area, the design lift coefficent can be determined using Equation 4.4. In this equation an assumption is made on the fraction of the total lift delivered by the main wing. It is assumed this is 90%, which means 10% will be delivered by the canard. Since all other wing characteristics are not yet fully determined, an important assumption is made. This assumption is that the airfoil lift coefficient C_l equals the wing lift coefficient C_L, corrected for the sweep angle, for cruise. However, since the maximum lift coefficient of the airfoil was estimated quite conservatively in the previous section, and the AR of the aircraft will be high, the net effect of this assumption is limited. This relation can be seen in equation 4.5

$$C_{l_{DES}} = \left(\frac{C_{L_w}}{C_{L_{tot}}}\right) \cdot \frac{1}{\frac{1}{2} \cdot \rho_{cruise} \cdot V^2} \cdot \frac{1}{2} \cdot \left\{ \left(\frac{W}{S}\right)_{cruise\_start} + \left(\frac{W}{S}\right)_{cruise\_end} \right\} \tag{4.4}$$

$$C_{l_{DES}} \cong \frac{C_{L_{DES}}}{cos^2\Delta} \tag{4.5}$$

Two configurations are considered, one with a HLD, and one without. For a HLD a plain flap is used, due to the complexity of other systems and the limited space in the wings to implement the systems. The lift coefficient of the flapped configuration can be estimated with Equation 4.6, provided by Raymer. [60]

$$C_{L_{MAX}} = C_{L_{MAX unflapped}} + 0.9 \cdot \Delta C_{l_{MAX}} \cdot \left(\frac{S_{flapped}}{S_{ref}}\right) \cdot cos(\Delta_{H.L.}) \tag{4.6}$$

In this equation the ratio between the flapped area and the reference area is assumed to be 0.5 and the sweep angle of the HLD hinge line ($\Delta_{H.L.}$) is calculated as a function of the LE sweep angle and the taper ratio. $\Delta C_{l_{MAX}}$ in this equation is the lift increment caused by plain flaps on an infinite wing. Based on references, this is assumed to be 0.9. [58] [59] An overview of the results of these calculations can be seen in Table 4.5. It shows that if no flaps are used in the wing design, the surface area of the wing will considerably increase.

Based on this design lift coefficient, an airfoil will be selected later. This process can be slightly iterative, so the wing surface can be adjusted after an airfoil is chosen and the exact performance can be estimated.

Table 4.5: Estimations on wing surface, wing loadings and design lift coefficient

Minimum landing speed	70 kts
Stall speed	58.3 kts
Safety factor surface area	1.1
$C_{L_w}/C_{L_{tot}}$	0.9
Sweep angle	9 deg
Unflapped	
$C_{L_{MAX}}$	1.28
$(W/S)_{cruise\_begin}$	633.9 N/m^2
$(W/S)_{cruise\_end}$	607.6 N/m^2
S_{tot}	18.6 m^2
$C_{l_{DESwing}}$	0.20
Flapped	
$C_{L_{MAX}}$	1.85
$(W/S)_{cruise\_begin}$	918.2 N/m^2
$(W/S)_{cruise\_end}$	879.9 N/m^2
S_{tot}	12.8 m^2
$C_{l_{DESwing}}$	0.29

From the total surface area, a wing planform area and wing reference area can be derived. Since the wing accounts for 90% of the surface area, the wing area becomes 11.5 m^2. Since the reference area of the wing surface propagates through the fuselage, an additional 1.7m^2 is added to the area. This number is based on the fuselage dimensions and the predicted root chord length. The total reference area for the wing (S_{ref}) now becomes 13.2m^2.

4.2.3 Sweep Angle

There are three reasons why a sweep angle could be necessary on the Zero EZE; to decrease the effective Mach number on the airfoil, to increase the longitudinal stability, to increase the directional stability (because of the winglets that act as vertical tailplanes). As can be seen in Equation 4.5, the sweep angle does effect the lift effectiveness of the wing in a negative way. So unless one of these reasons demands a sweep angle, the preferred quarterchord sweep angle is 0deg.

Since the Zero EZ will not operate at Mach numbers over 0.25, this does not concern the aircraft. The effective airspeed over the airfoil will not reach M$_{cr}$.

Another reason to use a sweep angle is to bring the AC further aft. In Section 5.2, it is explained that to ensure safe longitudinal stability of the aircraft, the AC should be at 10% of the MAC aft of the COG. To ensure this no sweep angle is necessary, because this can be achieved by placing the wing correctly.

The last reason to introduce a sweep angle is to bring the vertical winglets further aft to ensure directional stability. In Section 5.4 it is explained that the directional stability influences the dutch roll greatly. Using Tornado, a relation between the dutch roll stability and the sweep angle was calculated. In Figure 4.6b this relation can be seen. In Figure 4.6a it can be seen that the lift coefficient decrement increases when the sweep angle increases.

Based on these figures, it can be seen a compromise has to be made between controllability and efficiency of the aircraft. It is decided to implement a 9 deg sweep angle on the Zero EZE, which results in an 1 % loss in lift efficiency and a 43 % increase in dutch roll stability.

4.2.4 Aspect Ratio

The Aspect Ratio (AR) of the aircraft is an important characteristic that influences the induced drag of the aircraft. The relation between the AR and the induced drag can be seen in Equation 4.7

$$C_{D_i} = \frac{C_L^2}{\pi \cdot A \cdot e} \tag{4.7}$$

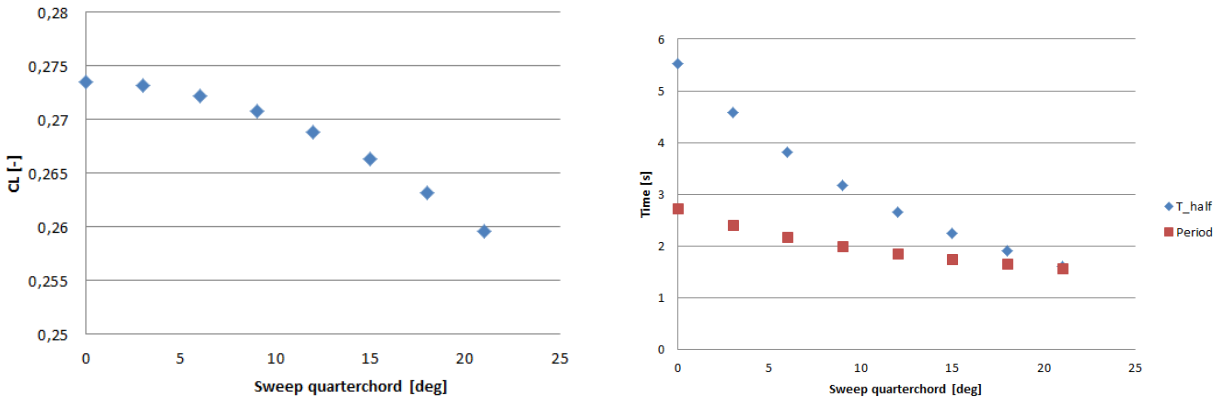

(a) Lift coefficient versus sweep

(b) Dutch roll versus sweep

Figure 4.6: Effects sweep on dutch roll stability and lift coefficient

To determine the best AR, for single engined aircraft, a compromise has to be made between reducing the induced drag by increasing the AR, and increasing the maneuverability by reducing the AR. In this section the AR will be optimized for minimal induced drag. There are limitations on the AR however. First, a sufficient maneuverability of the aircraft must be assured. Also, an increase in the AR leads to an increase in structural weight due to the increasing internal moments. Quick research on reference aircraft show that AR's average between 7-9, but AR's up to 11 are very possible. [58]

From equation 4.7 it can clearly be seen that the induced drag decreases proportional to the AR. This also shows (Figure 4.7) when an analysis is performed on a preliminary Zero EZE model in Tornado. Even though the lift over drag values are not representative for the Zero EZE, the linear relation is clear.

Based on this, the maximum aspect ratio for general aviation aircraft as determined by reference aircraft is chosen; A=11.

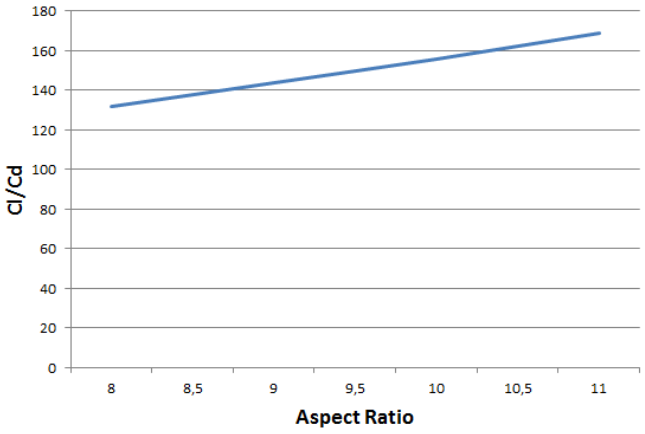

Figure 4.7: Relation between C_L/C_D and A

4.2.5 Taper Ratio

The taper ratio (λ_w) is used to approach an elliptically shaped load distribution of the wing loading, resulting in the lowest induced drag. Using a λ of 0.45 will approach the elliptical efficiency within a 1% efficiency loss. [58] This will be the taper ratio used on the Zero EZE. Since a tapered trapezoidal wing is considerably less complex to manufacture, this configuration is preferred over a fully elliptical wing.

4.2.6 Incidence Angle and Twist

In Figure 4.8a the distribution of the normalized C_l is shown of the wing without an incidence or twist angle. It can clearly be seen that the distribution is not elliptical, which is preferred for drag minimization. To counter this, an incidence and twist angle is introduced to the design. In order to prevent complete

stall of the wing, a negative twist angle (washout) is implemented. Numerical analyses can be performed to accurately calculate the local twist angle. However, the programs available to the project group are not sufficient to do this. Therefor, the Tornado model of the Zero EZE is used to determine the effect of implementing an incidence and twist angle.

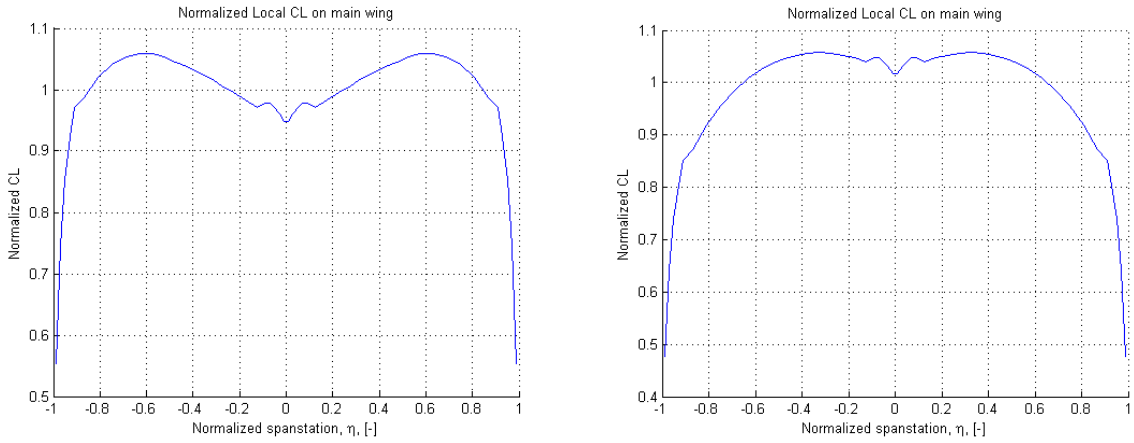

(a) Incidence = 0deg, washout = 0deg

(b) Incidence = 0.7deg, washout = 1deg

Figure 4.8: Normalized load over span of main wing

The CL/CD is calculated for a discrete number of incidence angles and twist angles. Interpolating this data, a graph can be made, showing the relation. In Figure 4.9 this relation can be seen. Again it should be noted that the actual values of the CL/CD are not representative, due to the flawed drag calculating functionalities of Tornado. It shows that the efficiency of the wing clearly goes down for higher incidence angles, regardless of the twist angle.

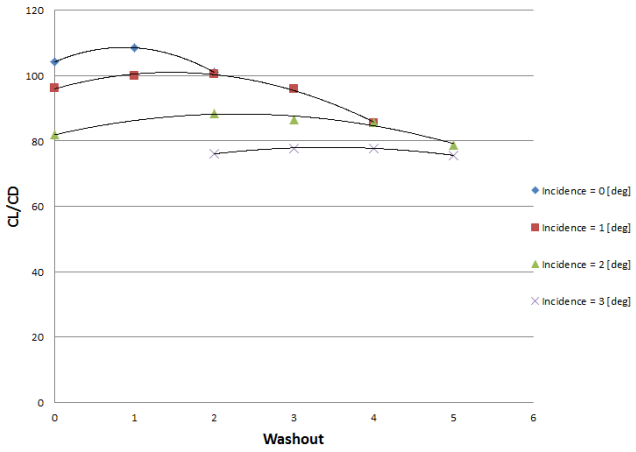

Figure 4.9: Relation between C_L/C_D and the incidence and twist angle

Based on this figure it is opted to have a washout of 1 deg. Because the total lift coefficient at zero angle of attack goes down, the incidence angle is adjusted to ensure enough lift at cruise speed to fly at zero angle of attack. This incidence angle is determined to be 0.7 deg. For the new configuration, the normalized C_l distribution over the wing span is shown in Figure 4.8b. It can clearly be seen that the shape is much closer to the ideal elliptical loading.

4.2.7 Dihedral Angle

Since the aircraft has a low to mid wing configuration, dihedral can be used to increase the lateral stability. In Section 5.3 it shows that the lateral stability is acceptable and no dihedral has to be introduced for stability reasons. Dihedral (or anhedral) decreases the efficiency of the wing, so in order to optimize for minimal drag, no dihedral is introduced in the design.

4.2.8 Wing Placing

In this section the placing of the main wing will be discussed. The placing is mostly driven by stability performance. The calculation and explanation on these stability factors is discussed in Chapter 5.

Longitudinal placing

The longitudinal placing of the wings is mainly driven by the longitudinal stability of the aircraft. In Section 5.2 it will be discussed that the longitudinal position of the AC has to be 10% MAC aft of the COG. The position of the AC is dependent mostly on the dimensions and position of the main wing. The method to calculate the position exactly will also be discussed in Section 5.2.

To determine the right location of the main wing, the relation of the location of main wing and the static margin has to be found. This was done by calculating the static margin for several positions of the main wing. The results can be seen in Figure 4.10. It clearly shows that the relation is linear. From this figure it was determined to locate the main wing at 2.6m measured from the tip of the aircraft to the main wing LE. This results in a static margin of 7% MAC.

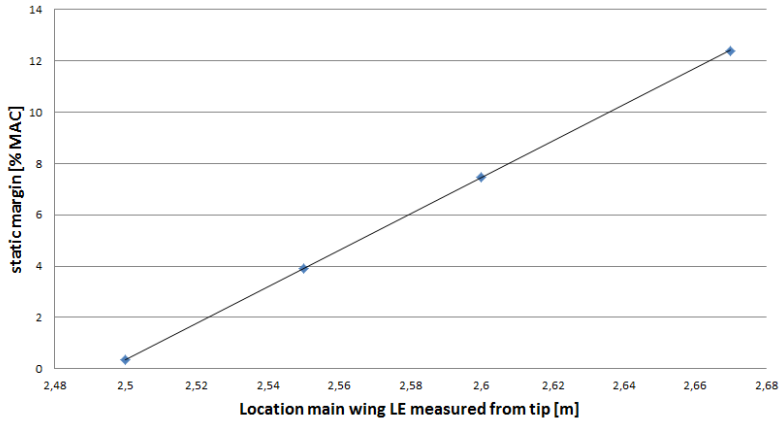

Figure 4.10: Relation between location main wing and the static margin

Vertical placing

The vertical location of the wing influences the lateral stability of the aircraft. The higher the wings, the higher the lateral stability. [58] This in turn will result in a decrease in dutch roll stability. To create a balance between the stabilities the wings were placed near the middle. Because of the interaction with the canard (which has to be placed above the main wing as discussed in Section 4.3, the wings were placed 10cm below the centerline of the fuselage.

4.2.9 High Lift Devices

In Section 4.2.2 it was already stated that plain flaps will be chosen as the type of HLD. This choice is based on the following reasons:

- Complexity of other HLD systems
- Limited amount of space in the wings available
- Plain flaps can achieve the necessary lift increment

For the dimensions of the HLD certain values have been assumed based on typical reference values [58]. For the chord length 25% of the total chord length is taken and 50% of the wing span is covered by HLD. These dimensions provided the required lift increase in Tornado.

4.2.10 Wing drag

The drag of the main wing consists of two components, parasitic drag and induced drag. Calculating the induced drag can easily be done using Equation 4.7. The parasitic drag is less straight forward to calculate. It is very difficult to exactly calculate the parasitic drag. There is no exact analytical method available to do this. As mentioned before, also the numerical model in Tornado is unable to calculate parasitic drag. However, there are methods available to make accurate approximations. To calculate the parasitic drag of the lifting surfaces of the Zero EZE (i.e. the main wing, the canard and the winglets) a methodology from Raymer will be used. [60] In this section the methodology will be shown.

To calculate the parasitic drag the drag can be divided into several components. First the flat plate skin friction component C_f; second the Form Factor FF; third the Interference factor Q and last the wetted area S_wet. These components are combined in Equation 4.8. In the equation subscript 'c' means that the coefficient is specific for each area.

$$(C_{D_0})_c = \frac{C_{f_c} \cdot FF_c \cdot Q_c \cdot S_{wet_c}}{S_{ref}} \tag{4.8}$$

To calculate C_{f_c} Equation 4.9 is used. In this equation the coefficient for the skin friction drag in laminar conditions and turbulent conditions are combined, weighted by the part of the chord the flow condition is present. For the wing NLF airfoil, this is 50% laminar and 50% turbulent. The laminar and turbulent coefficients can be calculated using Equations 4.10 and 4.11 respectively.

$$C_{f_c} = \left(\frac{c_l}{MAC}\right) \cdot C_{f_l} + \left(\frac{c_t}{MAC}\right) \cdot C_{f_t} \tag{4.9}$$

$$C_{f_l} = \frac{1.328}{\sqrt{Re}} \tag{4.10}$$

$$C_{f_t} = \frac{0.455}{(log_{10}Re_{cut-off})^{2.58} + (1 + 0.144 \cdot M^2)^{0.65}} \tag{4.11}$$

For the laminar friction drag coefficient, the normal Reynolds number (Re) can be used (Equation 4.12). For the turbulent conditions, the friction drag strongly depends on the roughness of the surface. Therefore, a so called 'cut-off' Reynolds number ($Re_{cut-off}$) is used (Equation 4.13). This 'cut-off' Reynolds number depends on skin roughness values (k) that depend on the surface and can be found in Table 4.6. These values were taken from reference [60]. It can be seen that the roughness of a smooth paint job is considerably higher than a smooth molded composite. The Zero EZE uses a composite material for the wing skin, but since no decision has been made on the finishing of the wing, the smooth paint job factor is assumed for the drag calculations.

$$Re = \frac{\rho \cdot V \cdot l}{\mu} \tag{4.12}$$

$$Re_{cutoff} = 38.21 \cdot (l/k)^{1.053} \tag{4.13}$$

Table 4.6: Skin roughness values

Surface	k [m]
Smooth paint	$0.634 \cdot 10^{-5}$
Smooth molded composite	$0.052 \cdot 10^{-5}$

For the FF Equation 4.14 is used in the case of wing or tail surfaces. In this equation $(x/c)_m$ is the location of the maximum thickness of the wing and (t/c) is the maximum thickness. Δ_m is the sweep angle for the maximum thickness location.

$$FF = \left[1 + \frac{0.6}{(x/c)_m} \cdot \left(\frac{t}{c}\right) + 100\left(\frac{t}{c}\right)^4\right] \cdot \left[1.34 \cdot M^{0.18} \cdot (cos\Delta_m)^{0.28}\right] \tag{4.14}$$

Finally, the interference factor Q has to be determined. For filleted high wings, the interference can be neglected. For low unfilleted wings, Q can take values from 1.1 till 1.4. Since our wings are placed near

the middle and the wings can be manufactured filleted, the interference factor for the wing is assumed to be 1.1.

Now the total skin friction drag of the wings can be calculated. An overview of the parameters used and the results obtained is shown in Table 4.7.

Table 4.7: Wing skin friction parameters and results

Wing Parameters		**Parasitic drag results**	
Part laminar flow	50 %	Re	$4.71 \cdot 10^6$
Part turbulent flow	50 %	$Re_{cut-off}$	$1.31 \cdot 10^7$
Air speed	77m/s	C_{f_l}	0.00061
Mach	0.24	C_{f_t}	0.00286
λ (air)	$1.512 \cdot 10^{-6}$	C_f	0.00174
ρ (3000m)	0.91 kg/m^2	FF	1.292
MAC	1.145 m	$(C_{D_0})_{wing}$	**0.00425**
k	$0.634 \cdot 10^{-5}$	$(C_{D_i})_{wing}$	**0.00267**
S_{ref}	13.2 m^2	$(C_D)_{wing}$	**0.00692**
S_{wet}	25.0 m^2		
Q	1.1		

4.3 Canard

Burt Rutan is well-known for his unusual-looking and innovative aircraft designs. The designs he produced in the 70's and 80's with the canard configuration are a perfect example of this. In the innovative design of the Zero EZE the canards will remain, and optimized for the aerodynamic design. In this section the positioning of the canard will be determined first, followed by the sizing and airfoil choice.

4.3.1 Positioning

The positioning of the canard has a significant influence on the main wing performance. The downwash of the canard varies across the span of the canard and actually creates an upwash on the main wing outboard of the canard [58]. (For stability reasons the canard has a longitudinal location of 0.40 meters from the front of the aircraft. This is based on the Long EZ dimensions and put slightly more to the front.)

Considering the vertical position of the canard the influence is harder to predict. Low-canard, mid-canard and high-canard positions will be compared. For the mid-canard (or coplanar) position the canard is approximately on the same vertical position as the main wing, which is the case for the Long EZ [65]. Experimental research [61] shows that a low-canard position has a significant loss of lift when the AOA increases. A high-canard wing position gives a slight increase in lift at an AOA higher than 4 degrees and better drag characteristics. Also wind-tunnel tests by NASA have shown that a low-canard position provides no advantages [62]. The differences when compared to a mid-canard configuration are determined relatively and not large. But since a high-canard position is still beneficial it is chosen. The structures of the aircraft can however limit the vertical position of the Zero EZE. To avoid the latter, a restriction for the vertical position of 0.20 meters above the main wing is chosen.

4.3.2 Sizing

For the sizing of the canard a division of the lift distribution has to be chosen between the canard and main wing. From Raymer [58] a typical division for the lifting surface of 1:9 to 2.5:7.5 was found. In order to shift the AC as much backwards as possible the smallest lifting surface for the canard is chosen as 10% of the total lifting surface. Since the main wing has a surface area of approximately 13.2 m^2, the canard will have a surface area of 1.41 m^2. To increase the AR, and reduce the induced drag, the span of the canard will be increased. If a chord length of 0.33 meters is maintained from the Long EZ, the span of the canard will become approximately 5.67 m. The latter includes the fuselage width of 1.4 meters.

Other characteristics of the canard which are assumed to remain equal are the sweep angle and taper ratio. As for the main wing a swept canard would increase the drag. Furthermore, a sweep angle would generate more lift only above 16 degrees AOA and if it is placed above the wing chord line [63].

4.3.3 Airfoil Canard

For the airfoil choice of the canard the most important parameter is the stall angle. If the main wing would stall before the canard the aircraft would become uncontrollable. First the airfoil of the Long EZ is considered to check whether it satisfies the needs. The lift and drag characteristics of the GU25-5(11)8 airfoil are shown in Figures 4.11a and 4.11b.

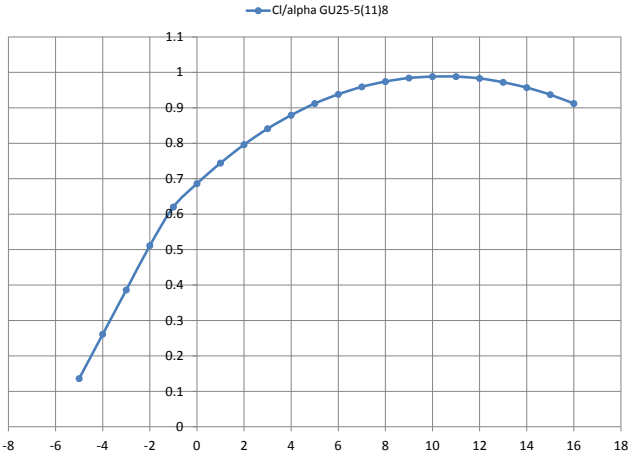

(a) Lift coefficient vs. AOA

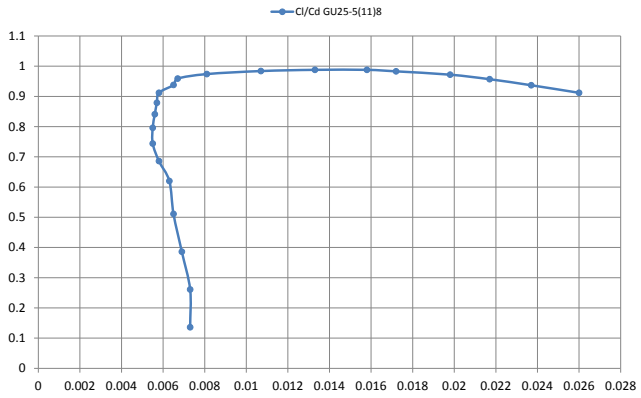

(b) Lift coefficient vs. Drag coefficient

Figure 4.11: GU25-5(11)8 airfoil characteristics (Re = 3,000,000)

From Figure 4.11 the conclusion can be drawn that the GU25-5(11)8 is also a suitable airfoil for the canard of the Zero EZE. The main criterion of a lower stall angle than the main wing (which is approximately 14 degrees) is met. Besides that a low drag coefficient of approximately 0.0055 can be obtained. As can be seen the minimum drag coefficient is obtained at a relatively high lift coefficient of 0.75. But since this is also the lift coefficient at an AOA of 0 degrees this does not cause any problems.

4.3.4 Canard Drag

The drag of the canard, similar to the wing, consists of two components. First the induced drag component, which will be calculated using Equation 4.7. The parasitic drag is calculated using the method explained in Section 4.2. An overview of all the relevant parameters can be found in Table 4.8.

Table 4.8: Canard skin friction parameters and results

Canard Parameters		**Parasitic drag results**	
Part laminar flow	20%	Re	$1.36 \cdot 10^6$
Part turbulent flow	80%	$Re_{cut-off}$	$3.54 \cdot 10^6$
Air speed	77m/s	C_{f_l}	0.00114
Mach	0.24	C_{f_t}	0.00355
λ (air)	$1.512 \cdot 10^{-6}$	C_f	0.00306
ρ (3000m)	0.91 kg/m^2	FF	1.508
MAC	0.33 m	$(C_{D_0})_{canard}$	**0.00104**
k	$0.634 \cdot 10^{-5}$	$(C_{D_i})_{canard}$	**0.00092**
S_{ref}	13.2 m^2	$(C_D)_{canard}$	**0.00196**
S_{wet}	2.82 m^2		
Q	1.05		

4.4 Winglets

In the aerodynamic design of the Zero EZE winglets are included to reduce the induced drag at the wing tip. Winglets produce a forward thrust inside the circulation field of the vortices [66]. They reduce the

fuel consumption and extend the range. Since the rudders of this design will be implemented in the winglets a significant winglet size is present. Furthermore a blended winglet design is chosen to create a more optimum loading and better vorticity distribution at the intersection with the wing [64]. This will be combined with an elliptical shape of the leading edge at the tip of the wing.

For the Long EZ the airfoil of the winglet is not known. Therefore a new airfoil will be chosen further on in this section. First the radius of curvature of the blend will be determined. The main parameters of the winglet (e.g. height, taper ratio, etc.) will remain equal because the design has proven itself and it provides sufficient space for the rudders. Gain is obtained from the new blended winglet design which also implies that the lower part of the winglet will be removed.

4.4.1 Blended Winglet Radius

For a blended winglet radius it is important to calculate the radius of curvature. In reference [67] it was shown that a blended winglet reduces the drag coefficient but that the results from different radii did not differ significantly. The main difference was the quality of the streamlines at 90 mph (78.2 kts). A radius of curvature of 25.4 cm gave the best results concerning the streamline quality. Therefore this is chosen as the radius for the winglet. A safe estimation of the drag reduction at 78.2 kts was 7%. At 190 mph (165 kts) the drag reduction is estimated at 3%. This data is obtained from XFLR5 software and applied on the Long EZ and can be seen in Figure 4.12.

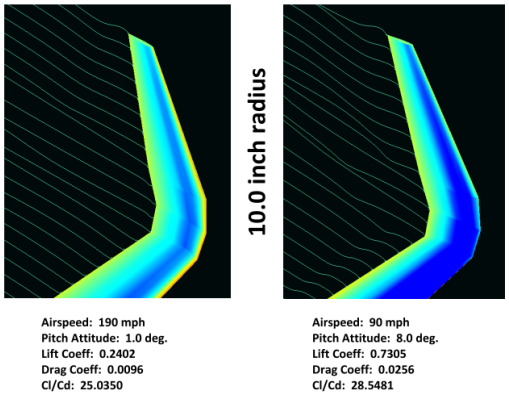

Figure 4.12: Simulation of 25.4 cm blend radius (apollocanard.com, 2012)

4.4.2 Airfoil Winglet

Since no airfoil is known yet for the current design, research has been done on finding airfoils optimized for winglets. The same trade-off is performed as for the main wing. This means that a suitable airfoil family is chosen and multiple airfoils are compared to choose the best one.

A family of airfoils optimized for winglets at low-speed aircraft with maximizing lift-to-drag ratios is the PSU airfoil family [68]. These airfoils are mainly designed for sailplanes but the low-drag design of the Zero EZE shows similarities with this type of aircraft. Therefore this airfoil family can be used. The two airfoils of which this family consists are the PSU-90-125WL and PSU-94-097. From DesignFoil the lift coefficient can be compared to the drag coefficient. Results can be seen in Figure 4.13.

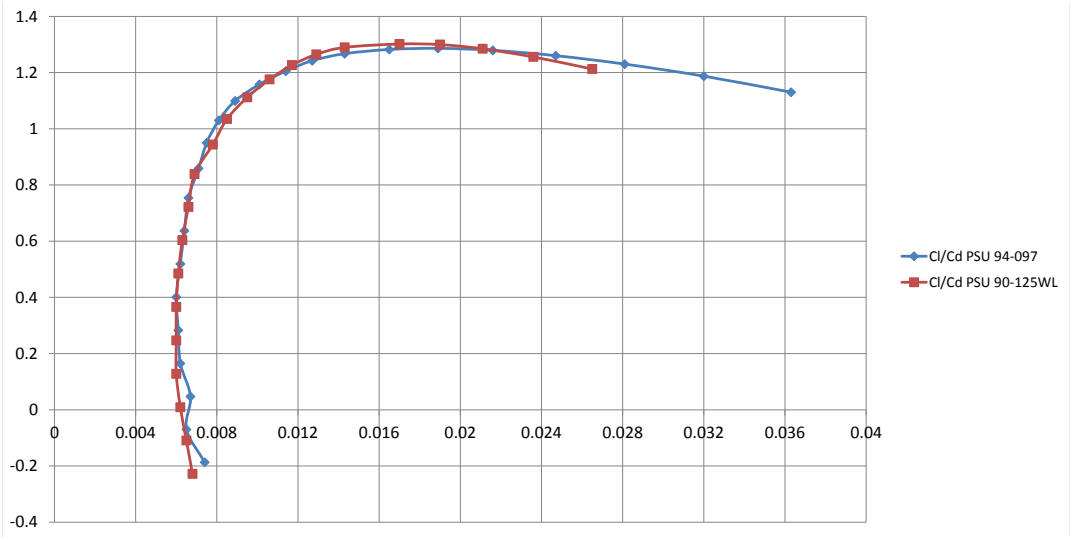

Figure 4.13: Lift coefficient versus drag coefficient for the two selected airfoils (Re = 5,000,000)

As can be seen in Figure 4.13 the two selected airfoils show almost no difference. Both reach a significantly lower drag coefficient than if the airfoil of the main wing (i.e. Eppler 1230) would be used as the airfoil for the winglet. Since the PSU 94-097 airfoil has a more slender and thinner profile with a slightly higher L/D-ratio than the PSU 90-125WL airfoil it is chosen as the airfoil for the winglet of the Zero EZE.

At last it has to be noted that it might seem strange that a winglet generates lift. However this lift can be slightly adjusted such that a forward vector is present and 'thrust' is created. This only has significant effects at high speeds. The main reason to use winglets is to create a thinner and longer wing which reduces the trailing edge vortex.

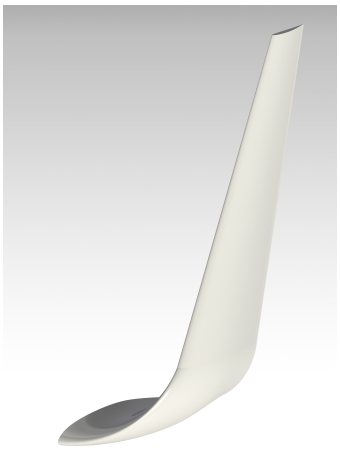

Figure 4.14: Blended winglet design of the Zero EZE

4.4.3 Size

In the Long EZ the tip of the winglet is located approximately 125 cm above the chord line of the main wing [65]. The lower part of the winglet will be removed due to the new blended winglet design. The height of the winglet will remain equal to avoid influencing the AR_{eff}. As stated before the taper ratio of about 0.4 will not change in the Zero EZE design. The root chord of the winglet is equal to the tip chord of the main wing (i.e. 67.95 cm) minus the 25 cm of the blend. This gives a root chord of 42.95 cm and a tip chord of approximately 17.18 cm.

Now all parameters of the winglets where gain could be obtained have been changed. Especially the conversion to a blended winglet type will give a drag reduction by the winglets. In Figure 4.14 a visualization of the winglet is provided.

4.4.4 Winglet Drag

The winglets contribute to the total drag in two ways. First, there is a drag reduction on the induced drag. Second, there is the parasitic drag of the winglets. In Raymer [58] Equation 4.15 was stated to calculate the effective AR of a wing with winglets.

$$AR_{eff} = 1.2 \cdot AR \tag{4.15}$$

With an AR of 11 for the main wing the AR_{eff} becomes 13.2. Since it is known that the AR is inversely proportional to the induced drag coefficient, an induced drag reduction of 16.7% is obtained. The calculation of the exact induced drag reduction is given in Equation 4.16. In Equation 4.16 the design lift coefficient of 0.28 is used and the e is assumed to be 0.85.

$$\Delta C_{D_i} = \frac{C_L^2}{\pi \cdot AR_{eff} \cdot e} - \frac{C_L^2}{\pi \cdot AR \cdot e} = 0.00222 - 0.00267 = -0.00045 \tag{4.16}$$

The parasitic drag was calculated using the method explained in Subsection 4.2.10. An overview of the parameters used for the calculations and the results of the drag can be seen in Table 4.9.

Table 4.9: Winglet skin friction parameters and results

Winglet Parameters		**Parasitic drag results**	
Part laminar flow	20 %	Re	$1.96 \cdot 10^6$
Part turbulent flow	80 %	$Re_{cut-off}$	$5.20 \cdot 10^6$
Air speed	77m/s	C_{f_l}	0.00058
Mach	0.24	C_{f_t}	0.00333
λ (air)	$1.512 \cdot 10^{-6}$	C_f	0.00174
ρ (3000m)	0.91 kg/m^2	FF	1.227
MAC	0.476 m	$(C_{D_0})_{winglets}$	**0.00062**
k	$0.634 \cdot 10^{-5}$	ΔC_{D_i}	**-0.00045**
S_{ref}	13.2 m^2	$(C_D)_{winglets}$	**0.00017**
S_{wet}	2.38 m^2		
Q	1		

4.5 Total Aerodynamic Performance

In this section an overview is given of the aerodynamic performance.

4.5.1 Lift and drag polars

To create the lift and drag polars the Tornado model is used. As previously mentioned, Tornado is unable to calculate parasitic drag. Because of this, the drag in the polars is the induced drag. Since the shape of the drag polar is only dependent on the induced drag, the results can still be considered accurate. The actual values of the drag however, must be incremented by the zero lift drag coefficients that can be found in the next section. Also, Tornado is unable to calculate the stall angles accurately. The stall angles of the canard airfoil is approximately 8deg and of the main wing airfoil about 12deg. The polar is therefore plotted till 12deg. More research is necessary, including wind tunnel tests, to determine the actual stall angles.

In Figure 4.15c, 4.15a and 4.15b, the lift, lift-drag and moment polars of the cruise conditions can be seen. In Table 4.10 significant values of these figures can be found.

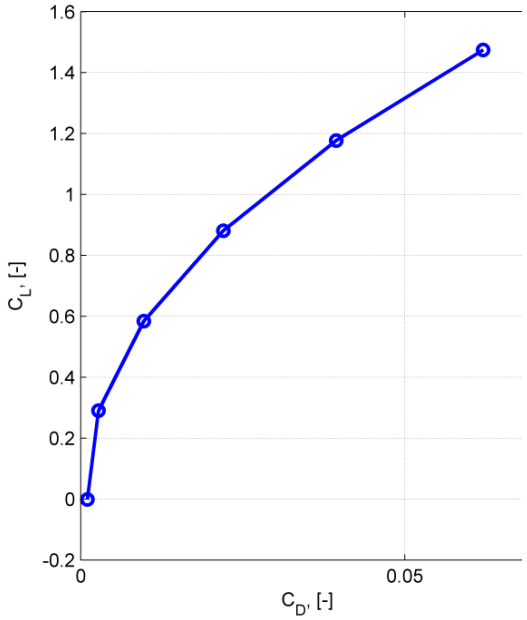

(a) Lift-drag polar cruise conditions

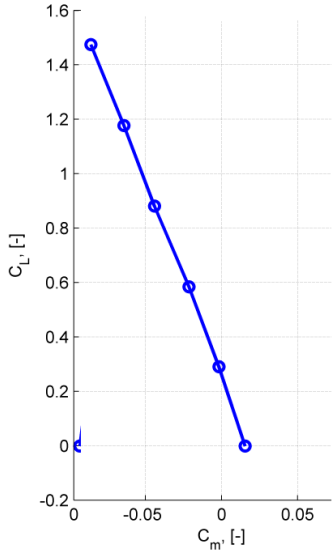

(b) Moment polar cruise conditions

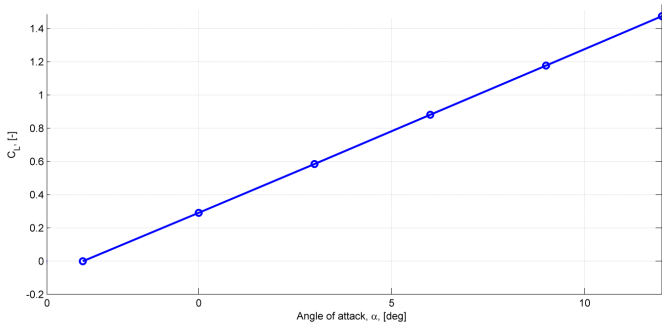

(c) Lift polar cruise conditions

Figure 4.15: Lift and drag polars cruise conditions

4.5.2 Drag coefficients

An overview is given of all drag coefficients and an estimation on the total drag in both cruise and landing configuration. The results for both configurations can be found in Table 4.11. The zero lift drag coefficient

Table 4.10: Overview significant lift characteristics for cruise conditions

C_{L_α}	5.61/rad
$C_{L_{\alpha=0}}$	0.290
α_0	-2.96deg
$\alpha_{L=1200kg}$	0.28deg

for the shroud was calculated using the same method that was used for wings, canard and winglets. The zero lift drag coefficient of the landing gear was based on reference data of landing gear components [60]. The induced drag was calculated for the wing and canard combined as a function of the total lift coefficient.

Table 4.11: Overview drag coefficients cruise and landing configuration

Zero lift drag		
Coefficient	**cruise**	**landing**
$(C_{D_0})_{fuselage}$	0.00520	0.00520
$(C_{D_0})_{wing}$	0.00425	0.00425
$(C_{D_0})_{canard}$	0.00104	0.00104
$(C_{D_0})_{winglets}$	0.00062	0.00062
$(C_{D_0})_{L/G}$	0	0.00435
$(C_{D_0})_{shroud}$	0.00076	0.00076
$(C_{D_0})_{interference}$	0.00119	0.00119
Induced drag		
Coefficient	**cruise**	**landing**
$(C_{D_i})_{wing}+(C_{D_i})_{canard}$	0.00327	0.11652
$(\Delta C_{D_i})_{winglets}$	-0.00045	-0.00045
Total drag		
Coefficient	**cruise**	**landing**
C_{D_0}	0.01304	0.01784
C_{D_i}	0.00282	0.11607
C_D	0.01587	0.13390
Lift over Drag Ratio		
$(C_L/C_D)_{\alpha=0}$	18.3	

Chapter 5

Stability

In this chapter the stability characteristics of the Zero EZE will be discussed. For an aircraft to be safe and easy to fly, good stability performance is essential. The stability analysis is an iterative process together with the aerodynamic design. The results of previous iterations were incorporated in the aerodynamic design. In this chapter the performance of the final design is shown.

First, in Section 5.1 the stability definitions and reference system are provided. In Section 5.2 the longitudinal static stability is discussed. In Section 5.3 the lateral and directional static stability are briefly discussed. Finally, in Section 5.4 the dynamic stability is discussed and the linear simulations of the eigenmotions are shown.

5.1 Definitions and Reference System

In this section the framework, in which the stability analysis is performed, will be provided. First, in Section 5.1.1 the definitions of the aircraft stability are shown. Second, in Section 5.1.2 the reference system which is used for the analysis is provided.

5.1.1 Definitions

There are three basic stability configurations possible for an aircraft. First, an aircraft can be statically unstable, meaning that once the aircraft moves away from the equilibrium position, the aircraft does not have the tendency to return to the equilibrium position. Second, an aicraft can be statically stable, but dynamically unstable. This means that when outside the equilibrium position, the aircraft has the tendency to return to the equilibrium, but overshoots the equilibrium and will start deviating from the equilibrium further over time. Finally, an aircraft can be both statically and dynamically stable, meaning that an aircraft outside the equilibrium position will eventually return to the equilibrium state.

For an GA business type aircraft, such as the Zero EZE, it is essential to be statically stable around all axes. For the dynamic stability it is also highly desirable for the aircraft to be stable. Light instability is possible, as long as the deviation does not occur too fast, so that the pilot can correct the motion and prevent potentially dangerous situations.

5.1.2 Reference System

In order to correctly interpretate all the forces and moments that act on the Zero EZE and incorporate numerical program outputs, the reference system must be defined clearly. The reference system can be seen in Figure C.1 in Appendix C.

5.2 Static Longitudinal Stability

To calculate the longitudinal stability the main wing and canard are considered since these are the two main contributors to the lift. In general it can be said that an aircraft has longitudinal static stability if the moment around the aerodynamic center, created by the increase of the angle of attack, tends to pitch down the aircraft [58]. This means that if Equation 5.1 is true, the aircraft is longitudinally statically stable.

$$dC_m/d\alpha < 0 \tag{5.1}$$

Since the total lift force increases when the angle of attack increases, the Aerodynamic Center (AC) must lay aft of the COG for the aircraft to meet this condition. The distance between the AC and the COG is called the static margin. The static margin is defined positive if the AC is aft of the COG. For GA aircraft, the static margin should be between 5% and 10% of the MAC to ensure a good longitudinal stability [75].

In Section 5.2.1 the analytical method to calculate the stability is explained. In Section 5.2.2 the numerical method is briefly discussed and in Section 5.2.3 the results of both methods are presented and discussed.

5.2.1 Analytical method

To analytically calculate the static longitudinal stability, the following methodology is used. First, the position of the AC is calculated. Second, the aerodynamic center is adjusted for thrust effects. Last, combining the positions of the AC and the COG the static margin is calculated. As mentioned before, this value must be between 5% and 10% of the MAC.

Aerodynamic Center

For the analytical computation a methodology developed by NASA for low Mach number canard configured aircraft will be used [73] [74]. For this method it is assumed that the tangential components are relatively small and can be neglected. This makes the neutral point equal to the aerodynamic center of the aircraft. The details of this method were already discussed elaborately in the Mid-Term Report. In Figure 5.1 the configuration used to calculate the aerodynamic center is shown.

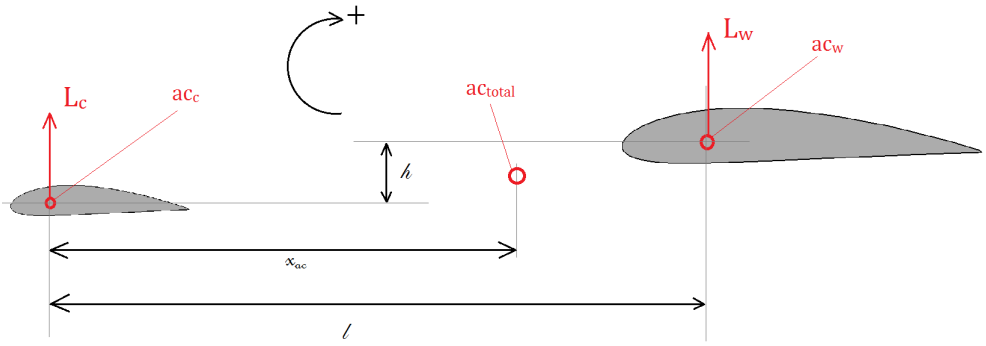

Figure 5.1: Definitions neutral point computation

The aerodynamic center location (measured from the tip of the Zero EZE) following from this method is 3.07m.

Thrust Effects

In Raymer it was stated that the thrust has three major effects on the longitudinal stability. [58] Firstly the direct moment of the thrust, secondly the propeller normal force due to turning air and the influence of the propwash upon the tail. They will be briefly discussed in that order.

The direct moment of the thrust is largely dependent on the moment-arm of the thrust force and the COG. A rough approximation can be made that the static margin positively increases by 0.25% of the MAC for 1% of the MAC that the thrust axis is above the COG [58]. In case the axis lies below the COG it decreases at the same rate. In Chapter 2 it was mentioned that the thrust axis has zero pitch. The vertical location of the COG cannot be calculated accurately at this point. However, since the heaviest components are quite evenly distributed throughout the fuselage and the wings are placed near the thrust axis line, it is assumed the arm between the thrust axis and the COG is 10cm or smaller. This leads to a static margin increase of 0-2.3cm.

The other two effects are assumed to be negligible. According to Raymer, since the airflow is not completely lined up with the propeller, the influence of the propeller normal force is very small. [58] The effect of the propwash is not relevant for a pusher configuration, since the vertical tail plane (winglets) is not affected by the propwash.

Static Margin

The static margin is the distance between the neutral point and the COG. Since the COG covers a small range, depending on the loading of the aircraft, the static margin is also expressed as a range. The static margin increase due to thrust effects are placed between brackets, because this addition is uncertain. The analytically calculated static margin for the aircraft now becomes 6.2-16.2cm (+2.3cm).

5.2.2 Numerical Method

For the numerical method, a Matlab model in Tornado is used. This model is discussed in detail in Section 5.4. The program has a functionality that directly calculates the static margin. As for the analytical solution, the static margin covers a range. Also, the thrust effects are incorporated. The numerically calculated static margin is 7.5-18.0cm (+2.3cm).

5.2.3 Overview Results

In Table 5.1 the results of both the analytical and numerical method are shown. It can be seen that the difference between the two methods is only 1.4% of the MAC. This means that the Tornado model is quite accurate for calculating the longitudinal stability. Also, it can be concluded that the Zero EZE is quite stable, scoring a little over the average 5-10% MAC static margin for GA aircraft. This is a necesary compromise to ensure dynamical stability (especially the dutch roll), as will be discussed in Section 5.4, and to optimize the wing sweep angle for low drag, as previously discussed in Section 4.2.

Table 5.1: Overview results of longitudinal static stability

	static margin (+thrust corr.) [cm]	**% of MAC (+thrust corr.)**
Analytical Method	6.2 - 16.2 (+2.3)	5.4 - 14.1 (+2.0)
Numerical Method	7.5 - 18.0 (+ 2.3)	6.6 - 15.7 (+2.0)
Average Difference	1.6	1.4

5.3 Static Lateral and Directional Stability

In this section the directional and lateral stability will be discussed. Since the analytical calculations of these stabilities are complex and depend on assumptions, it was decided not to use an analytical method and depend on the same numerical Matlab model in Tornado that was used for the longitudinal stability.

First the lateral stability of the aircraft is considered. This stability is not as important as the longitudinal and directional stability. In general an aircraft is laterally stable if the sideslip motion results in a counteracting moment around the X-axis. To ensure static directional stability, Equation 5.2 has to be true. [80]

$$C_{l_\beta} < 0 \tag{5.2}$$

For the directional stability the stability derivative C_{n_β} is important. In general an aircraft is directionally stable if the sideslip motion results in a counteracting moment around the Z-axis. When Equation 5.3 is true, the directional, or weathercock, stability is assured.

$$C_{n_\beta} > 0 \tag{5.3}$$

Results

In Table 5.2 the values obtained by Tornado can be seen. It shows that $C_{l_\beta} = -0.062$ and $C_{n_\beta} = 0.077$ and thus that the Zero EZE is both laterally and directionally stable.

5.4 Dynamic Stability

In the previous sections it has been shown the Zero EZE is statically stable, but it is important to also provide dynamic stability. The motions of the aircraft after a disturbance can be determined by the equations of motion of the aircraft. For these EOM the control and stability derivatives of the Zero EZE aircraft are needed. To obtain these derivatives, a Matlab based Tornado model is used.

In this section, first the Tornado model will be discussed. Then the control and stability derivatives are given. From these derivatives, the eigenvalues for both the symmetric and the assymetric motions are calculated. Finally, the results of a linear simulation of these eigenmotions are presented.

Tornado Model

For the stability analysis of the Zero EZE, a Matlab based program Tornado is used. Tornado is a Vortex Lattice Method (VLM) that models all lifting surfaces as thin plates. Figure 5.2 shows a rendering of the Zero EZE model used for all analyses. The colors indicate the pressure distribution over the surfaces. Tornado is accurate in calculating the lift and induced drag properties of surfaces. Since friction drag is not taken into account, the zero lift drag estimations cannot be considered accurate. [76] The Zero EZE model in Tornado contains all surfaces that behave like lifting surfaces. Therefore the landing gear was not included in the model. In Figure D.1 in Appendix D the values used to construct the Tornado model can be found.

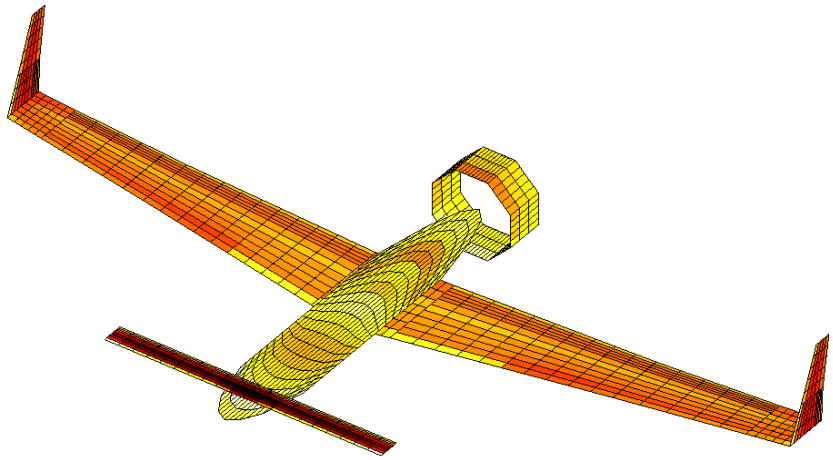

Figure 5.2: Rendering of Zero EZE Tornado model

In Table 5.2, all derivatives Tornado calculated using the Zero EZE model, can be found. Certain stability derivatives are not directly obtained from Tornado and require some extra explanation. First of all the derivatives C_{X_u}, C_{Z_u} and C_{m_u} are used when propulsion is neglected and can be calculated as $C_{X_u} = -2 \cdot C_D$, $C_{Z_u} = -2 \cdot C_L$ and $C_{m_u} = 0$. Furthermore, since no vertical tail is present the derivatives $C_{X_{\dot{\alpha}}}$, $C_{Z_{\dot{\alpha}}}$, $C_{m_{\dot{\alpha}}}$ are assumed zero. These derivatives describe the influence of the wing downwash on the tailplane. $C_{Y_{\dot{\beta}}}$ and $C_{n_{\dot{\beta}}}$ are assumed to be zero, because the AR of the Zero EZE is higher than 5. All these assumptions are based on [80].

5.4.1 Symmetric eigenmotions

Now that the stability derivatives are known the dynamic stability can be calculated. This will be performed for the symmetric case (i.e. longitudinal eigenmotions) and the asymmetric case (i.e. lateral

Table 5.2: Stability derivatives of Zero EZE

C_{X_0}	0	C_{Y_β}	-0.600
C_{X_u}	-0.021	$C_{Y_{\dot{\beta}}}$	0
C_{X_α}	-0.081	C_{Y_p}	-0.132
$C_{X_{\dot{\alpha}}}$	0	C_{Y_r}	0.193
C_{X_q}	-0.077	$C_{Y_{\delta_a}}$	0.043
$C_{X_{\delta_e}}$	-0.006	$C_{Y_{\delta_r}}$	0.097
C_{Z_0}	-0.331	C_{n_β}	0.077
C_{Z_u}	-0.662	$C_{n_{\dot{\beta}}}$	0
C_{Z_α}	-5.608	C_{n_p}	0.014
$C_{Z_{\dot{\alpha}}}$	0	C_{n_r}	-0.027
C_{Z_q}	-9.282	$C_{n_{\delta_a}}$	0.005
$C_{Z_{\delta_e}}$	-0.178	$C_{n_{\delta_r}}$	-0.010
C_{m_u}	0	C_{l_β}	-0.062
C_{m_α}	-0.481	C_{l_p}	0.407
$C_{m_{\dot{\alpha}}}$	0	C_{l_r}	0.034
C_{m_q}	-13.166	$C_{l_{\delta_a}}$	0.207
$C_{m_{\delta_e}}$	0.725	$C_{l_{\delta_r}}$	0.034

eigenmotions). When the symmetric EOM is solved with the obtained stability derivatives the following eigenvalues were determined:

$$\lambda_{1,2} = -6.8214 \pm 2.7998i$$
$$\lambda_{3,4} = -0.0061 \pm 0.1420i$$

There are two type of eigenvalues, namely real values and complex conjugates. The eigenvalues with only a real part correspond to non-periodic eigenmotions. The complex conjugates correspond to a periodic eigenmotion. Both symmetric eigenvalues are given according to the equation $\lambda = \xi \pm \eta i$ and are thus periodic motions. From all eigenvalues it can be seen whether the symmetric eigenmotions are stable or not. The motion is dynamically stable if the real part of the eigenvalue is negative [80].

For the Zero EZE, both symmetric eigenmotions are stable. The eigenvalues correspond to different motions. $\lambda_{1,2}$ corresponds to the short period and $\lambda_{3,4}$ corresponds to the phugoid.

The next step is to compute the time-to-half-amplitude and period of the eigenmotions. For the symmetric case these eigenmotions are the short period and phugoid. Using Equations 5.4 and 5.5 they are obtained. In Table 5.3 the results can be found.

$$T_{\frac{1}{2}} = -\frac{0.693}{\xi} \tag{5.4}$$

$$P = \frac{2\pi}{\eta} \tag{5.5}$$

Table 5.3: Results symmetric eigenmotions

	Time-to-half-amplitude [s]	**Period** [s]
Short period	0.102	2.24
Phugoid	112.8	44.3

5.4.2 Asymmetric Eigenmotions

Now the same process will be repeated for the asymmetric eigenmotions. The asymmetric eigenmotions which will be computed are the aperiodic roll, dutch roll and spiral motion. For this case the eigenvalues are:

$$\lambda_1 = -10.314$$
$$\lambda_{2,3} = -0.3596 \pm 3.9562i$$
$$\lambda_4 = 0.0125$$

The first eigenvalue corresponds to the aperiodic roll and is stable because of the negative real part. The second and third eigenvalue are for the dutch roll, which is a damped motion where the aircraft sideslips, yaws and rolls [80]. This eigenmotion is stable since the real part is negative. At last, the spiral motion is the third asymmetric eigenmotion and corresponds to eigenvalue 4. This eigenmotion is slightly unstable.

The time-to-half-amplitude and period of these eigenmotions are calculated again using Equations 5.4 and 5.5. The results can be found in Table 5.4. Note that for the spiral motion a negative time to half amplitude is obtained. This means that the motion is divergent and has a time to double amplitude of 55.48s. Most aircraft are unstable for the spiral motion and since the time to double amplitude is high, the pilot has enough time to correct the motion.

Table 5.4: Results asymmetric eigenmotions

	Time-to-half-amplitude [s]	**Period** [s]
Aperiodic roll	0.067	-
Dutch roll	1.927	1.588
Spiral motion	-55.48	-

It can be concluded that the Zero EZE has a good dynamic stability. The only unstable motion is the spiral motion, but this can easily be corrected by the pilot and will therefore not lead to uncontrollability or potentially dangerous situations.

5.5 Linear Simulation

In this section plots of the significant responses for all eigenmotions are provided. A linear simulation model in Matlab was used to generate the plots. The model shows the responses of the Zero EZE at cruise. Using the symmetric and asymmetric models previously derived for calculating the eigenvalues and modeled control inputs, the following results were obtained. In Figure 5.4 the phugoid is shown; in Figure 5.5 the short period; in Figure 5.6 the dutch roll; in Figure 5.3 the aperiodic roll and in Figure 5.7 the spiral motion.

The plots are coherent with the calculated time-to-half-amplitude and period values in the previous section. It clearly shows that all motions are statically stable. Also, it can be seen that only the spiral motion is dynamically unstable. This shows in the roll angle plot because it is diverging and in the roll rate and yaw rate plot because they don't converge to zero.

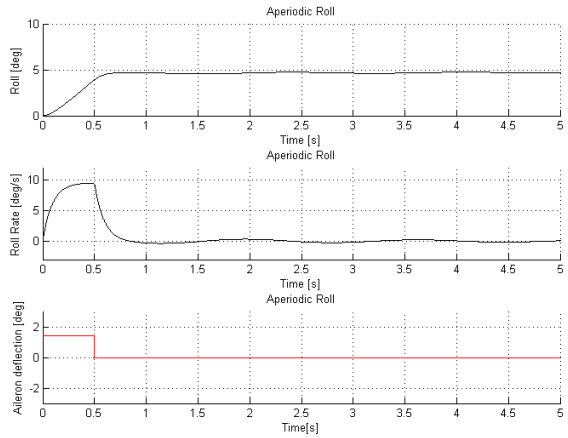

Figure 5.3: Response aperiodic roll in linear Matlab model

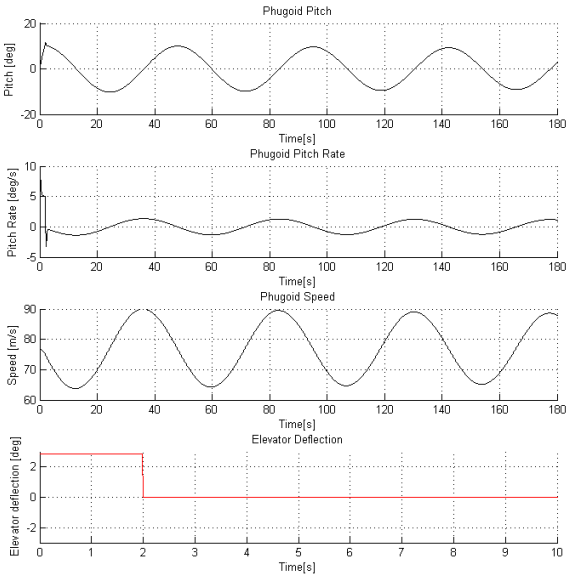

Figure 5.4: Response phugoid in linear Matlab model

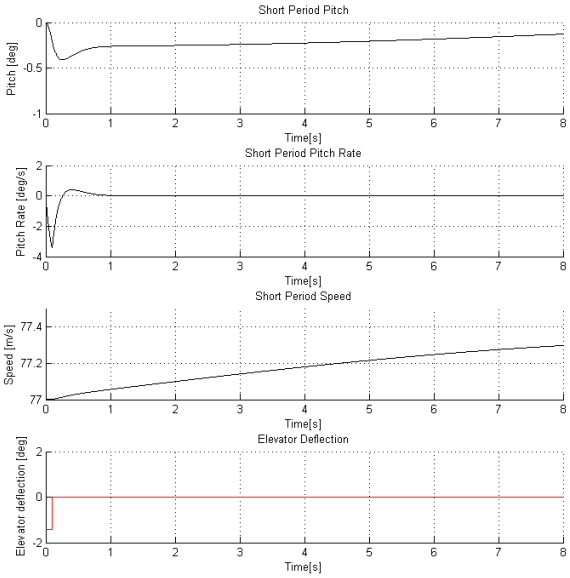

Figure 5.5: Response short period in linear Matlab model

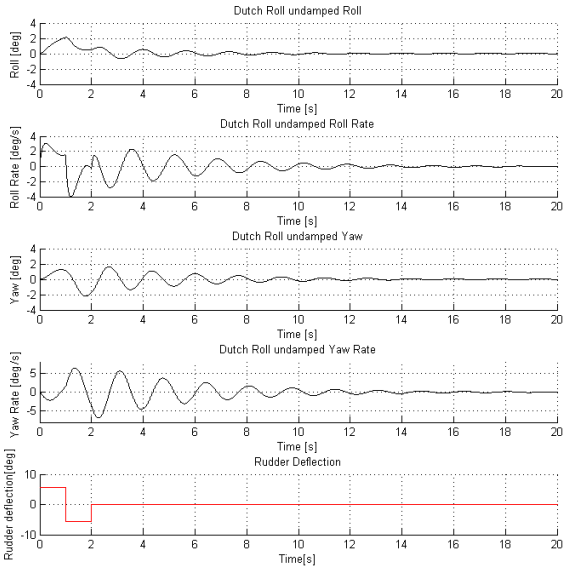

Figure 5.6: Response dutch roll in linear Matlab model

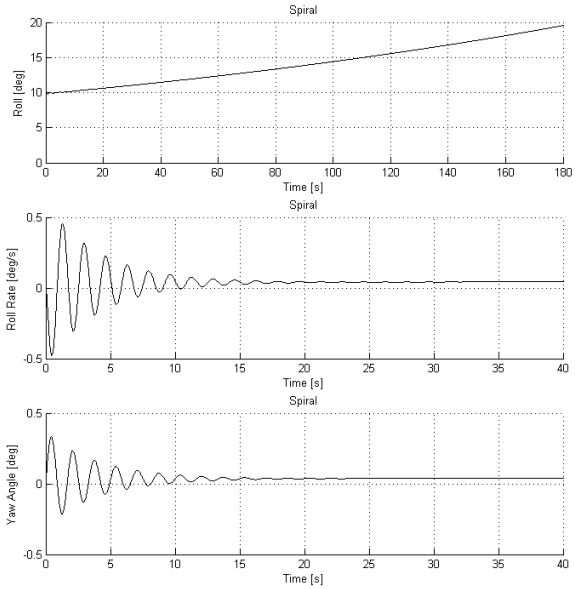

Figure 5.7: Response spiral motion in linear Matlab model

Chapter 6

Flight Controls

In this chapter the size and position of the flight controls of the Zero EZE will be determined. Flight controls are required on every aircraft to provide roll, yaw and pitch control. The three flight controls present on the Zero EZE are as follows:

- Ailerons
- Rudders
- Elevators

Certain data is required to determine the flight control sizing. The control surface deflections are obtained from reference data and provided in Table 6.1 [77]. In the aileron, elevator and rudder sizing sections the roll, pitch and yaw rate respectively will be determined. In these sections an initial estimation is made first based on literature. If the outcome is feasible the control surface deflections are kept. The size and positions can be found in Sections 6.1 to 6.3.

Table 6.1: Maximum control surface deflections

	Maximum deflection $[deg]$
Roll	± 20
Yaw	± 30
Pitch	± 20

6.1 Ailerons

In order to have the an optimum roll controllability the ailerons should be positioned as close to the tip as possible to provide a large arm. They typically cover between 50% and 90% of the wing span [79]. In chord-wise direction ailerons occupy typically between 15% and 25% of the chord length at the trailing edge of the wing. Since HLD will also be present at the aircraft, the span-wise length of the ailerons is minimized to 30%. Also the high span/AR of the wing justifies this choice, because it provides a long arm. From historical guidelines, based on [58], the initial chord length was determined to be 26%. Winglets will also be present on the Zero EZE and therefore a distance of 10% of the wing span is reserved between the aileron and the wing tip.

After an initial estimation has been performed for the ailerons, it has to be verified whether the ailerons are large enough. This will be done by using the control derivatives obtained from Tornado. A certain roll rate will follow from this calculation. When this gives a feasible outcome the ailerons are sized correctly.

First the rolling moment around the longitudinal axis created by the ailerons is calculated, using Equation 6.1 [80]. This moment will be calculated at low speeds because then a smaller moment is created. The stall speed is 30 m/s, which was calculated in Chapter 4.

$$L = C_{l_{\delta_a}} \cdot \delta_a \cdot \frac{1}{2}\rho V^2 \cdot S \cdot b \tag{6.1}$$

The dynamic pressure, wing surface and wing span are obtained from Section 4.2. The aileron deflection is obtained from Table 6.1 and the control derivative $C_{l_{\delta_a}}$ has a value of -0.207. Now the rolling

moment due to aerodynamic damping is considered, using Equation 6.2. Combining this with Equation 6.1 the roll rate can be calculated. This is shown by Equation 6.3.

$$L = C_{l_p} \cdot \frac{pb}{2V} \cdot \frac{1}{2}\rho V^2 \cdot S \cdot b \tag{6.2}$$

$$p = \frac{C_{l_{\delta_a}} \cdot 2V \cdot \delta_a}{C_{l_p} b} \tag{6.3}$$

The stability derivative C_{l_p} is taken from Section 5.4 and equals -0.407. From that a roll rate of 50.4 deg/s at low speed is achieved. This roll rate is considered too high when compared to other aircraft [78]. A roll rate of 35 deg/s is estimated to be a correct value. When inserting this into Equation 6.3 it follows that a $C_{l_{\delta_a}}$ of -0.143 is required. In Figure 6.1a this control derivative is plotted versus the aileron span. It has to be noted that the values for $C_{l_{\delta_a}}$ in this figure are not corrected for the right reference system.

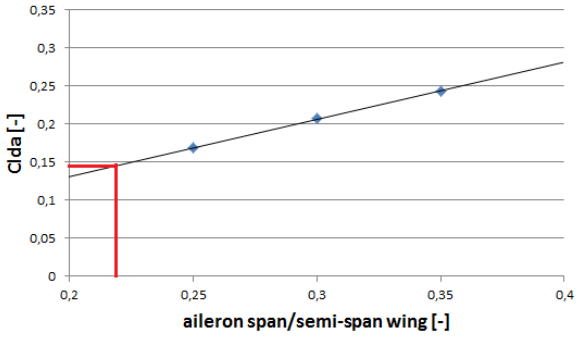

(a) Control derivative $C_{l_{\delta_a}}$ plotted versus aileron span

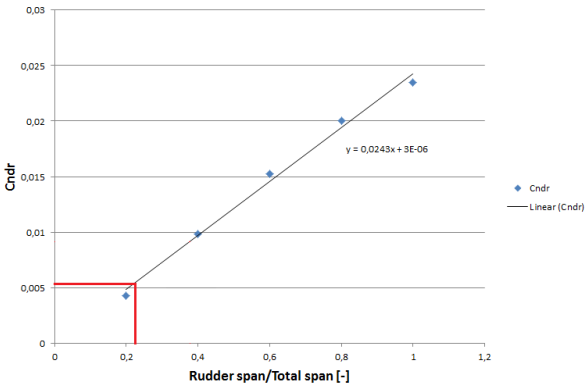

(b) Control derivative $C_{n_{\delta_r}}$ plotted versus aileron span

Figure 6.1: Control derivatives plotted versus control surface spans

From the relation between the aileron span and the control derivative $C_{l_{\delta_a}}$ it follows that an aileron span of 22% is required to achieve the desired roll rate.

6.2 Rudders

From reference [58] it is known that rudders typically have a span of approximately 90% of the tail span. Taking into account the large arm and placement on the winglets this will be reduced to 40% for the Zero EZE. In the original Long EZ design the rudder only covers about 25% of the winglet span but in many modified versions this was increased to 90% [65]. The chord length of the rudder usually lies between 25 and 50%. As an initial value the rudder chord is taken as 25% of the winglet chord since it has a high span.

The initial estimation now has to be checked on feasibility. This is done according to the yaw characteristics. The yawing moment due to rudder deflection is given in Equation 6.4 [80].

$$N = C_{n_{\delta_r}} \cdot \delta_r \cdot \frac{1}{2}\rho V^2 \cdot S \cdot b \tag{6.4}$$

Here the control derivative $C_{n_{\delta_r}}$ is provided by Tornado calculations. This gives a value of -0.0095. In order to find the desired yaw rate the yawing moment due to aerodynamic damping is required. This can be calculated using Equation 6.5. Tornado calculations provide a C_{n_r} value of -0.0265.

$$N = C_{n_r} \cdot \frac{rb}{2V} \cdot \frac{1}{2}\rho V^2 \cdot S \cdot b \tag{6.5}$$

When the latter is combined with Equation 6.4 the yaw rate can be determined, using Equation 6.6.

$$r = \frac{C_{n_{\delta_r}} \delta_r 2V}{C_{n_r} b} \tag{6.6}$$

From Equation 6.6 a yaw rate of 53.3 deg/s is found. This is not considered controllable when compared to reference aircraft [78]. A yaw rate of 30 deg/s is desired and the rudder span has to be decreased to achieve this. When the desired yaw rate is inserted in Equation 6.6, the control derivative $C_{n_{\delta_r}}$ is estimated to be -0.00534. When this control derivative is plotted versus the rudder span, as can be seen in Figure 6.1b, the correct rudder span can be calculated.

The rudder span following from Figure 6.1b is 22% of the semi-span. This is considered to be low but this is compensated by the large span of the aircraft which provides a long arm for the yawing moment.

6.3 Elevators

For the Zero EZE the elevators will be located on the canard. This is necessary to create sufficient arm length in longitudinal direction. Elevators are designed to control the pitching of the aircraft. On a conventional aircraft the elevators cover about 90% of the tail span and 25% to 50% of the tail chord length [58]. Since the elevators of the Long EZ also have a span of about 90% this is maintained for the Zero EZE. For the chord length of the elevators a value of 25% assumed.

Again a first estimation has been performed for a control surface. The pitching moment around the lateral axis created by the elevators will be calculated first, using Equation 6.7 [80].

$$M = C_{m_{\delta_e}} \cdot \delta_e \cdot \frac{1}{2}\rho V^2 \cdot S \cdot c \tag{6.7}$$

The elevator deflection is obtained from Table 6.1 and the control derivative $C_{m_{\delta_e}}$ follows from Tornado with a value of 0.725. The pitching moment due to aerodynamic damping will be calculated accordingly by using Equation 6.8. Combining the latter with Equation 6.7, the pitch rate q of the Zero EZE can be calculated. For this the MAC is used as the value for c and the stability derivative C_{m_q} follows from Tornado with a value of -13.17.

$$M = C_{m_q} \cdot \frac{qc}{V} \cdot \frac{1}{2}\rho V^2 \cdot S \cdot c \tag{6.8}$$

$$q = \frac{C_{m_{\delta_e}} \delta_e V}{C_{m_q} c} \tag{6.9}$$

From Equation 6.9 a pitch rate of -30.5 deg/s follows for low speed conditions. The pitch rate is negative because it is a canard configuration and the value is feasible [78].

6.4 Overview Control Characteristics

In Table 6.2 an overview is provided of all the important characteristics of the three flight controls.

Table 6.2: Characteristics of the ailerons, rudders and elevators

Parameter	Value
Aileron span	22%
Aileron chord	26%
Roll rate	35 deg/s
Rudder span	22%
Rudder chord	25%
Yaw rate	30 deg/s
Elevator span	90%
Elevator chord	25%
Pitch rate	-30.5 deg/s

Chapter 7

Structures

In the conceptual design phase, the materials and structures for the Zero EZ have been determined. In this chapter the detailed configuration of the Zero EZE will be shown. A work flowdiagram is presented in Figure 7.1.

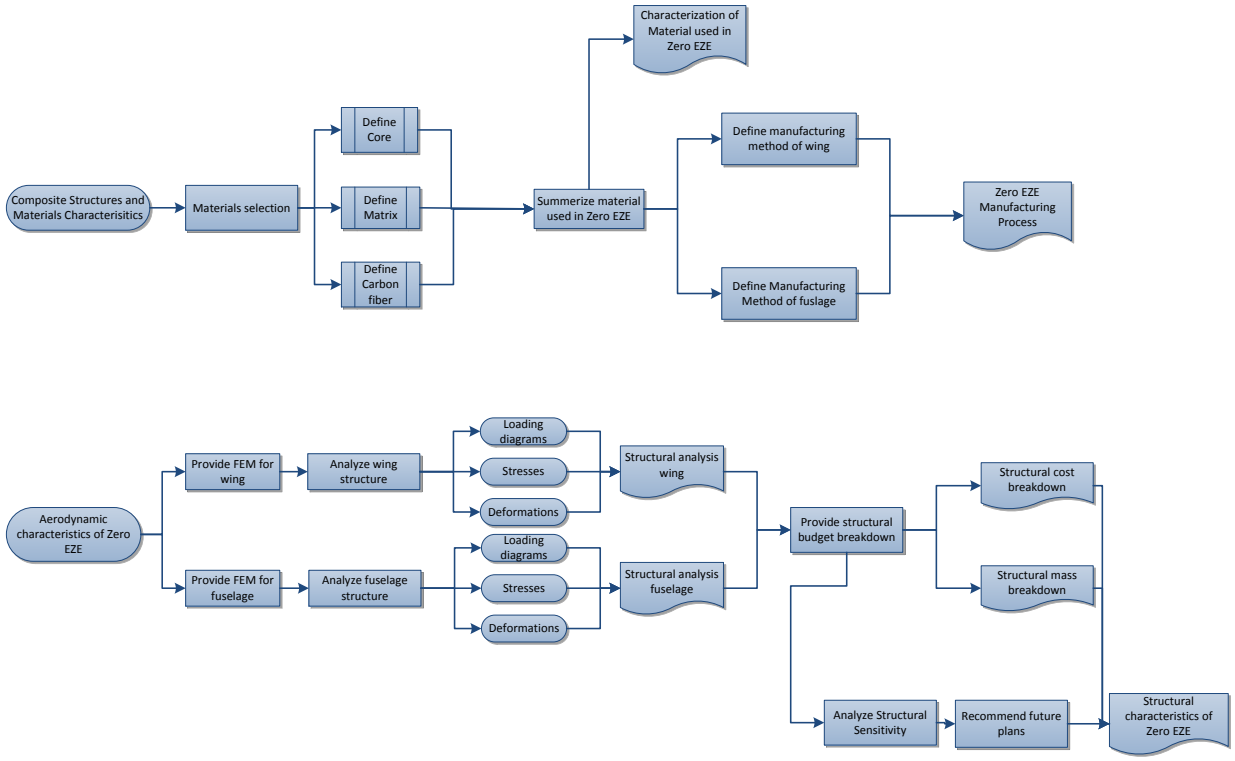

Figure 7.1: Work flowdiagram structures Zero EZE

The two main parts in this chapter will be manufacturing and structural analysis. First the manufacturing methods will be thoroughly examined. Thereafter analysis will determine the exact layout of the Zero EZE.

7.1 An Introduction to Composite Materials

By definition, composites are materials which consist of two or more materials that produce better properties combined than any of them can provide separately. The most commonly used composite material is

fiber-reinforced composite material. This type of composite consists of matrix material and reinforcement fiber. Fibers are carrying the load exerted on the composite structure, while providing stiffness, strength and thermal stability. The main functions of the matrix material are binding the fibers together and transferring the loads between fibers. It also protects fibers against chemical attacks or environmental effects like moisture, humidity, etc. [89]
The main advantages of composite materials are their high strength, stiffness and low density compared to bulk materials. These advantages translate to great weight reductions and result in improved performance. Another important advantage that should be mentioned is that assembly costs can be reduced, due to fewer detailed parts and fasteners [90].
Conclusively, the four important requirements in aerospace applications, which are light weight, high specific strength, high specific stiffness and great fatigue resistance can be met efficiently with the use of composite materials. As mentioned before, composites can provide a higher strength-to-weight ratio than metals, which results in lower consumption and emissions [92]. If all the metal in aircraft is replaced with lightweight composite materials, the fuel consumption could be reduced by 25% [91]. The major drawback of composites is their high cost.

7.2 Material detail design

AS it has been mentioned before, the CFRP is used to construct the composite material. Therefore, the matrix and fiber of CFRP will be determined, in order to obtain the property of the composite. Then the core material that is needed to build the sandwich structure is also going to be defined in this section.

7.2.1 Matrix types for CFRP

Nowadays, there are three different types of carbon fiber reinforced matrices that are used in the aviation industry, which are epoxy, bismaleimide and polyimide. When a different matrix mixes with carbon fiber, the mechanical features of the composite material will be different.
The most recent example is the T800 carbon fiber with epoxy and bismaleimide. They have been applied to several sections on the Boeing 787 based on their different stiffness properties. Therefore, all three matrices are used in order to come up with the suitable carbon fiber reinforced polymer.
In the following section the properties of three matrices are briefly analyzed in order to select the proper matrix for carbon fiber.

EP(epoxy)

Epoxy is a commonly used polymer for carbon fiber; the high bonding capacity makes it easy to fuse with fibers and reduces the possibility of delamination at the same time. Also compared with bismaleimide, it has a higher strength which can be used to produce strong elements. However, epoxy is a brittle material which needs extra processing to increase the stiffness. Further, it has a very low compressive strength, which means that the ability to resist compressive forces is low. This is a critical drawback for composite materials. In the application for the Boeing 787, particulate interlayer toughening technology has been performed to increase the compressive strength after impact. As a result a new epoxy 3900-2 is found and combined with carbon T800H as the material on the fuselage.

BMI(bismaleimide)

Bismaleimide is not as popular as epoxy for aircraft applications. It has a low stiffness and needs a lot of improvements and reconstructions before it can be applied to aircraft. But it has high adaptability to different environment such as high temperature and moisture.

PI (polyimide)

Polyimide has the highest temperature resistance compared with the other two, namely can be operated in both high and low temperature environments. Also it has good mechanical properties and isolation. After

analyzing all three matrices, it can be concluded that epoxy is the most suitable polymer for composite material. Because it can be not only manufactured easily but also provide high strength and strong bonding capacity. In addition, the material properties of CFRP at low temperatures is very stable. For instance, a hydrogen tank for the fuel cell can also be made by CFRP.

7.2.2 Carbon fiber

Carbon fiber normally carries the tensile and compression stresses in composite material. The fiber which current technology could produce has a tensile strength around 5 GPa and T800h is the most advanced fiber which has been used on the Boeing 787 fuselage. When mixing it with the polymer, for instance the epoxy, the tensile strength can reach 2650Mpa. [96] This is currently the best carbon fiber which is largely produced on the market. Therefore in this design carbon fiber is chosen to be T800h.

7.2.3 Core Material Selection

In the sandwich structure of the wing, the core does not carry any loads. Therefore it should be as light as possible, but still have enough strength and stiffness in order to not collapse under pressure during cure and transfer loads between facings [97]. In the Long EZ wing design, styrofoam is used as the core material, which is a type of polysterene foam. Foams with similar strength and stiffness will be considered as foam material; cost and density will determine whether another foam will be used.

In Table 7.1 the properties of different cores are shown. In table 7.2 the relative costs and characteristics of these cores are presented.

Table 7.1: Properties of commonly used core materials [99]

Core Material Family	*Typical Density Range, kg/m^3 (lb/ft^3)*	*Shear Strength, MPa (psi)*	*Shear Modulus, MPa (ksi)*	*Compression Strength, MPa (psi)*	*Maximum Service Temperature, °C (°F)*
Balsa Wood (closed end grain)	96-250 (6-16)	1.85-4.94 (270-720)	108-312 (15.7-45.3)	6.5-26.6 (945-3860)	165 (325)
Polyurethane Foam (PUR)	21-400 (1.5-25)	0.15-3.1 (20-450)	1.55-104 (0.23-15.0)	0.2-0.35 (29-50)	135 (275)
Polystyrene Foam (PS)	30-60 (2-4)	0.25-0.60 (36-90)	4.5-20 (0.65-2.9)	0.3-0.9 (44-130)	100 (212)
Polyvinylchloride Foam (PVC)	30-400 (2-25)	0.35-4.5 (50-655)	8.3-108 (1.2-15.7)	0.3-5.8 (44-840)	55-120 (130-250)
Polymethacrylimide Foam (PMI)	30-300 (2-20)	0.8-7.5 (115-1090)	19-290 (2.8-42.1)	0.8-16 (116-2325)	140 (285)
Polyetherimide Foam (PEI)	60-110 (4-7)	0.8-1.4 (120-200)	18-30 (2.6-4.4)	0.7-1.4 (100-200)	180-190 (355-375)
Styrene-acrylonitrile Copolymer Foam (SAN)	48-160 (3-10)	1.3-3.5 (180-510)	13.8-41.4 (2.0-6.0)	0.35-10.3 (50-1500)	135 (275)
Epoxy Foam	80-320 (5-20)	0.45-5.2 (65-755)		0.62-7.4 (90-1075)	177 (350)
Phenolic Foam	5-160 (0.5-10)	0.01-1.45 (1.4-210)		0.014-2.07 (2.0-300)	145-200 (300-390)
Carbon/Graphite Foams	30-560 (2-35)	0.05-3.9 (7.3-566)		0.2-60 (29-8700)	~2500 (~4530)

Note: The various properties noted above are heavily dependent upon the foam density with an increase being proportional to degree of compaction, cell density, and use temperature

Table 7.2: Comparison of core material relative costs and their characteristics and benefits [99]

Core Material Family	*Relative Core Material Cost*	*Characteristics and Benefits*
Balsa Wood (closed end grain)	Low	Good shear strength, high fatigue endurance, easily bonded, easily finished, good temperature range, but absorbs moisture, potential for fungus
Polyurethane Foam (PUR)	Low	Good solvent resistance, good temperature capability, moderately fire resistant, wide density range of products
Polystyrene Foam (PS)	Low	Lowest temperature capability, lowest cost material, moderate mechanical properties, fairly fragile material
Polyvinylchloride Foam (PVC)	Low	High strength, high stiffness, easily bonded , good impact resistance, only moderate temperature capability
Polymethacrylimide Foam (PMI)	High	High dimensional stability at temperature, excellent mechanical properties, solvent resistance, low thermal conductivity, high strength and stiffness
Polyetherimide Foam (PEI)	High	Low moisture absorption, high thermal stability, high strength, good fire resistance, good dielectric properties
Styrene-acrylonitrile Copolymer Foam (SAN)	Moderate	No outgassing, high stiffness, high impact and fatigue strength, no environmental problems with resin or recycling
Epoxy Foam	Moderate	High strength and stiffness, compatible with numerous laminate systems, excellent high temperature properties, moderate fire resistance
Phenolic Foam	Moderate	Excellent fires/smoke/toxicity properties, somewhat brittle, good high temperature properties, very good insulator
Carbon/Graphite Foams	High	Excellent high temperature properties (best), high stiffness mechanical properties, high cost main deterrent, used as tooling materials as well as structures

It can be concluded from these tables that the cost and density of polysterene are relatively low, while its strength and stiffness has proven itself to be sufficient. Therefore this material will be used as core material in the wings of the Zero EZE

7.3 Manufacturing method

One of the most important steps in the application of composite material is choosing a fabrication process. Selecting a well-defined, reliable manufacturing method can have a large influence on the final mechanical properties of the composite structure and can also reduce the production cost.
Selecting the right manufacturing technique for the production of a part is essential, since it has an significant impact on the final material properties and overall production costs. The main criteria that should be considered to select the right process method in different applications are production rate, cost, strength, size and shape.

7.3.1 Manufacturing Process of Wing

The manufacturing process of the wing can be split into three different steps. The first step is performing a prepreg lay-up. It can be used to produce complex shapes with good quality. Also the fiber resin ratio after vacuum bagging is superior to other methods which will improve the composite material properties [108].
The second step is the pre-curing process, for which vacuum bagging is chosen. This method has relatively low production cost. In addition, higher strengths can be achieved by minimizing the voids caused by trapped air within the laminate. Another advantage of vacuum bagging is in the simplicity and variety of the molds used. One of the drawbacks of this technique is low production rate. However, in the aerospace market production requirements are usually in the range of 10 to 1000 products per year. Therefore vacuum bagging can be used in this low-volume production environment.
The final step in the manufacturing process is solidification. For this step, autoclave can be used. This process provides high temperature and pressure to improve resin curing.

Prepreg Lay-up

In the pregreg lay-up, composite laminates are formed by placing perpergs at desired angles and at places where they are needed. It is an open molding process with low volume capability. The performance of composite structures is highly dependent on their fiber orientation and lay-up order. It should be mentioned that one of the main challenges during the hand lay-up process is maintaining accurate fiber orientation. Automated tape placement equipment can be used for exact fiber orientation control.

Vacuum Bagging

Vacuum bagging is a clamping method applied after laying-up the prepregs over the mold surface. A pressure difference is used to hold the adhesive or resin-coated components of the lamination in place until the adhesive cures. The pressure differential between the inside and outside of the envelope determines the amount of clamping force on the laminate.
There are several items used in the vacuum bagging process. Typical components of a vacuum bagging system are shown in Figure 7.2 [109].

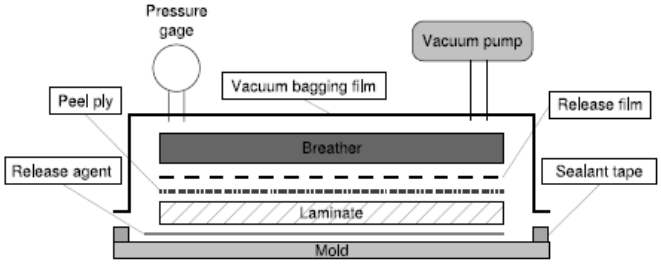

Figure 7.2: Vacuum bagging

As mentioned before, one of the important components that are required during vacuum bagging process is a mold. Molds come in a wide variety of shapes, sizes and method of construction. They are designed to hold the wet-out laminate in a specific shape until the resin has cured. So the mold structure should be rigid enough to support the mold surface in its correct shape during the laminating process. A closed object, such as a wing, requires at least two molds. The part can then be laminated in two halves and bonded together. These molds are often built in two stages. Firstly, a plug is built to the exact dimensions of the wing. After that a mold is cast from that plug. [109]

Manufacturing Procedure

The manufacturing process of the wing can be divided into several steps. In this section the basic steps of the manufacturing process are listed, including a brief description.

- The materials preparation: Prepreg and core material should be cut to the required shape and placed in a convenient area for placement in the mold.
- The surface preparation: The mold surface needs to be cleaned to ensure a smooth surface. After that, release agent can be applied.
- Layer placement: The layers of carbon fiber prepreg should be placed in the mold in the sequence mentioned in the manufacturing chart.
- Core material placement: At this point each piece of core should be placed in position in the mold.
- Filling gaps between core: Thickened epoxy should be applied to fill gaps and to fillet the edges of cores.
- Breather material placement: Perforated film and breather fabrics should be placed over the release fabric in this stage.
- Vacuum bag envelope preparation: The mold and lay-up should be placed inside a vacuum bag envelope.
- Pre-curing process: Vacuum pump is used to remove the air from the bag and allow the epoxy to cure.
- Curing process: The entire assembly is placed into the autoclave

After the laminate has cured, the finished lower half of the wing can be removed from the mold. Then the upper half can be laminated in the same way. Finally the upper and lower halves can be bonded together. [109]

7.3.2 Manufacturing Process of Fuselage

In the conceptual design, a grid stiffened structure has been chosen. The manufacturing process of the fuselage can be split into two different steps. The first one is filament winding. Filament winding is an automated method for creating composite structures by winding filaments under tension over a rotating

mandrel. Filament winding has several advantages. Firstly, the automated processes will not only reduce the labor costs, it will also cause less imperfections in the assembly, due to standardization of products. Secondly, filament winding uses a continuous fiber which leads to very good material strength and stiffness [108]. Finally, this method is capable of winding all types of fiber in the optimized orientation.
Secondly for the curing process autoclave is chosen. After extensive winding, the resin needs to be cured in a short period of time, which is possible using this curing method.

Filament Winding

As indicated in Figure 7.3 the fiber is soaked in a resin bath before being wound by a machine with two or more axes of motion. Filament winding is suitable for manufacturing cylindrical structures such as the fuselage.

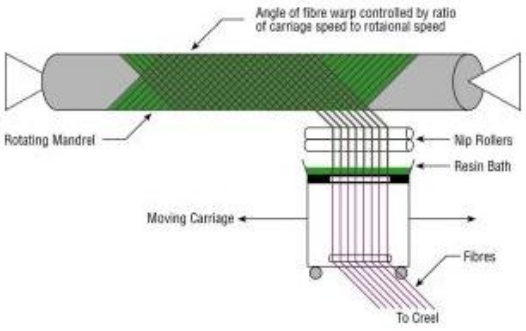

Figure 7.3: Filament winding

Basic winding machines have two axes of motion. However, for aerospace applications, more complex fiber orientations are required. Therefore a filament winding machine with six axes is used. This will increase the difficulty and cost of the manufacturing process. Even though the development and implementation of winding machines is complex, the benefits of automation still make filament winding the most suited manufacturing method.

Mold Construction

The grid stiffened structure of the fuselage consists of different combinations of carbon reinforced polymer ribs. Generally there are two different techniques to wind the fiber, free winding and groove winding. For aerospace applications, groove winding is preferred for which different tooling concepts and tooling materials can be employed. Therefore, in order to wind the ribs in the vested orientation, a special mold needs to be made. The materials used in making such a tool should be cheap and easy to manufacture. Also the material should maintain the shape in high temperature, so structure can be cured. In this case rigid polyurethane is preferred [110].
In Figure 7.4 it shows the fibers are accurately placed inside the groove on the foam. During this process it is important that the right resin velocity and fiber tension is maintained, in order to ensure a high quality, final product. Therefore a proper programming for the pay-out-roller is necessary to have a high quality grid stiffened structure.

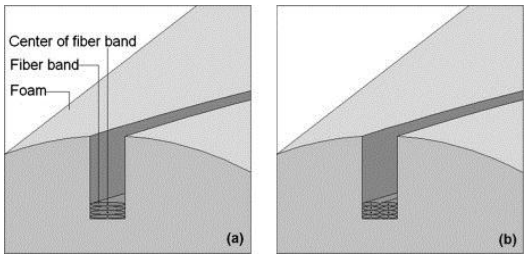

Figure 7.4: Filament winding on mold

Manufacturing Procedure

The major steps performed during the filament winding process and curing procedure are described here [108]:

- Spools of fiber yarns are placed in the creels.
- Several yarns of spool are taken and passed through guided pins to the payout eye.
- Hardener and resin systems are mixed in a container and then poured into the resin bath.
- The mode is placed between the head and tail stocks of the filament winding machine.
- Resin-impregnated fibers are pulled from the payout eye and then placed at the starting point of the groove. Fiber tension is created using a tensioning device.
- The computer system in the machine creates winding motions to guide the fiber into the groove.
- The mode is removed from the structure by the machine.
- Wind skin on the structure with a standard procedure.
- To obtain a smooth surface finish on the outer surface, a teflon-coated bleeder or shrink tape is rolled on top of the outer layer after winding is completed.
- For post-curing, the autoclave is used to improve the curing.

7.4 Discussion

In this final section, the cost of structure manufacturing will be introduced. Also the sustainable analysis will be discussed through operation and production aspects.

7.4.1 Manufacturing cost

The analysis of manufacturing cost of composites are normally emphasized on recurring cost and nonrecurring cost. The recurring cost is the cost that is incurred every time a part is fabricated. The nonrecurring cost is the cost that is incurred once during the fabrication run. However, nonrecurring cost are not easy to analyze in the development phases of the design. This also has less influence on production. Therefore nonrecurring costs are not going to be taken into account for the manufacturing cost of Zero EZE.
The recurring cost includes 4 different parts:

- Material cost
- Labor cost
- Equipment cost
- Support cost

As it has been defined in the manufacturing methods, hand lay-up and filament winding are applied to produce the wing and fuselage. Typical labour hours of hand lay-up and filament winding can be divided into parts and is shown the following pie charts in Figure 7.5a.

The chart on the right hand side shows the labour hours breakdown of hand lay-up, which mainly consists of pregreg and routing. On the other side is the chart of filament winding. Compared with the hand lay-up, the filament winding only needs half of the labour hours that hand lay-up needs.

The costs vary according to the nature of the part, the volume of parts made and the efficiencies of each manufacturers operation. Figure 7.5b shows the cost of the manufacturing processes for several composites while making the same part. As predicted, the more highly automated processes have the lowest overall costs. Also the principal raw materials which have been used in filament winding are low costs materials, tow and resin. However, the preprags which are used in the hand lay-up are expensive. Finally, based on the percentages indicated in the graph, the total cost can be derived from the partial cost.

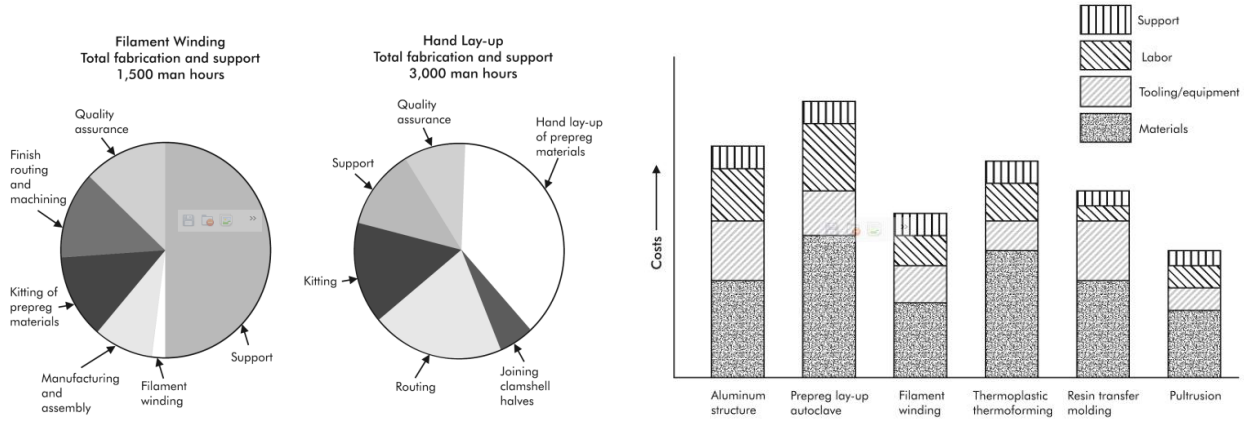

(a) Labor hours for filament winding

(b) Labor hours for different materials

Figure 7.5: Labour hour divisions

Material cost

The weights of wing and fuselage can be determined from the FEM as 85kg and 98kg respectively. Also the price of the fiber and resin is $ 51.7 per kg for the wing and $ 34.9 per kg for the fuselage. The mix ratio of carbon fiber is 60% in this case. From this the total material cost can be estimated to be approximately $ 8000.

7.4.2 Sustainable Strategy Structures

The environmental study of materials and structures is a complicated issue, but because sustainability is one of the most important design aspects of the Zero EZE, this should be analyzed in detail. When discussing the sustainability three major phases can be distinguished; the production, the utilization and the disposal phase. These phases are discussed in this section.

Production phase

The production phase can be split up into the wings and fuselage. During the construction of the wings hardly any energy will be used. Due to the complexity of the manufacturing process, the wing will be made mainly by hand, using hand lay-up and vacuum bagging, no complications with respect to sustainability will be suspected here. The production of the fuselage will be done automatically, using a process called filament winding. The main advantages are the lower labor costs and the accuracy of the product. However, by using machines, more energy will be used.

Utilization phase

The environmental impact of the product is not only determined by the materials selected, but also by the function of the product itself. While using CFRP, the structural weight of the Zero EZE will be low compared to conventional materials use. This will result in a lower energy consumption during the lifetime of the airplane.
When the structure gets damaged, it needs to be maintained. The structure used for the Zero EZ is a closed structure, indicating that difficulties will occur during the inspection phase. Different methods can be used to cope with this; Ultra-sonic inspection, Thermography and tap-testing are commonly used for the detection of flaws in composite structures. These methods are very accurate, but need the aid of complex measurement tools. When flaws are detected, they need to be repaired. The two basic types of composite repairs are bonded and bolted processes. With the bonding process, the composite component is formed into a desired shape using heat and pressure during the cure process. Since many of the composite parts have already been cured, bonded repair requires adhesive bonding on at least one of the repair surfaces. Autoclaves can be used for curing large epoxy prepreg laminate components. This method provides vacuum, heat and pressure to the bagged composite part. Due to this complex nature, repairing a large part of the aircraft is time and energy consuming. Bolting composite materials is similar

to bolted metal repairs, damaged sandwich panels typically require local core removal and a bonded repair to the face sheet. This again is a time and energy consuming method. It can be concluded that repairing CFRP is an energy and time consuming process, but due to high impact resistance and its low weight, less repairs are needed compared to metal aircraft.

Disposal phase

The current annual worldwide carbon fiber consumption is 30.000 tonnes, with the principal markets being aircraft, racing cars and sporting goods. At present, there is no way to recycle fiber materials. However, multiple research institutions are currently investigating re-usability of carbon fiber. Several methods have been researched for recovering CFRP. One is a fluidized bed technology where the fibers and resin are separated at high temperatures, energy is extracted from the polymer and the fibers are left in a clean condition, with slightly reduced properties. According to [103], recycled carbon fibers have been made into bulk and sheet moulding compounds forms and have been successfully moulded into laboratory-scale samples. Although the results are very promising, this method still needs to be developed for larger scales. Microwave pyrolysis is another form of CRFP recycling under development by companies and universities all over Europe and America. This method yields a rapid resin decomposition and recovery of fibers, which again has been tested successfully on small scale projects.
Aircraft manufacturing methods play a critical role in making CFRP recyclable. Boeing for example aims to boost the amount of recycled aircraft material from 70 % today to 90 % by 2016. The company began recycling CRFP from retired F-18A military planes in 2005, carried this through 777 composite components and even used 787 pre-production scrap from a fuselage test article to prototype a seat arm rest and composite lay-up tool. Airbus aims to enhance the eco-efficiency of new aircraft so that 90 % of components and materials could be recycled, reused or recovered. They are working on developing a pyrolysis-based recycling plant for the recovery of carbon fibers from both CFRP manufacturing scrap and decommissioned Airbus aircraft [102].

Conclusions

Currently CFRP is not the most sustainable way of producing airplanes, due to the difficulties in the cradle-to-cradle principle. However due to its low weight and high impact resistance, operational sustainability will be better compared to metal aircraft. Continuous research show promising results for the re-usability of carbon fiber based polymers. Based on pyrolysis recycling techniques, carbon fiber can be extracted from the resin and can be reused, however having a slightly lower strength. Due to these principles, it can be concluded that producing the wings and fuselage of the Zero EZE will have a low impact on the carbon footprint left by this airplane, assuming research will continue to develop in the near future. Only recyclability of the CFRP components of the Zero EZE remain an unresolved issue for this moment.

7.5 Analytical Analysis

By using the classical sandwich laminates theory, the stresses and moments on the face laminates can be analyzed. First an introduction to sandwich structures is given in Subsection 7.5.1. Then their failure criteria are examined in Subsection 7.5.2, also using the so-called Tsai-Wu failure criterion.

7.5.1 Sandwich Structures theoretical background

Composite materials are anisotropic by nature. This means that different directions should be considered for their strength and stiffness properties, as opposed to isentropic materials. In this section, by using classical laminate theory, it will be shown how orthotropic composite structural components can be analyzed.

Stiffness of Orthotropic Laminates

For unidirectional fiber reinforced lamina, there are two perpendicular planes of symmetry that define the principal axes of the material properties. These principal axes correspond to the direction of the fibers and a direction transverse to the fibers. This is shown in Figure 7.6.

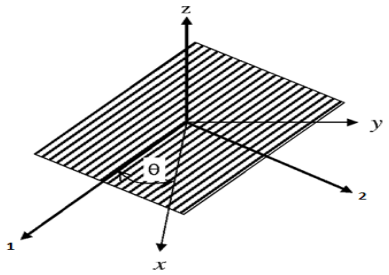

Figure 7.6: Global and local Coordinate

For thin composites, where the thickness of the laminate is much smaller than other dimensions, the stress-strain relationship in the local coordinate system can be defined as:

$$\begin{Bmatrix} \sigma_1 \\ \sigma_2 \\ \tau_{12} \end{Bmatrix} = \begin{Bmatrix} Q_{11} & Q_{12} & 0 \\ Q_{12} & Q_{22} & 0 \\ 0 & 0 & Q_{66} \end{Bmatrix} \begin{Bmatrix} \varepsilon_1 \\ \varepsilon_2 \\ \gamma_{12} \end{Bmatrix} \tag{7.1}$$

Where Q_{ij} represents the reduced stiffness in different directions.
By defining the major PoissonâĂŹs ratio ν_{12} as the slope of the transverse strain ε_y versus longitudinal strain ε_x and minor PoissonâĂŹs ratio as the inverse of the major PoissonâĂŹs ratio, different reduced stiffness can be rewritten as follows:

$$\begin{aligned} Q_{11} = \frac{E_1}{1-\nu_{12}\nu_{21}}, Q_{22} = \frac{E_2}{1-\nu_{12}\nu_{21}} \\ Q_{12} = \frac{\nu_{12}E_2}{1-\nu_{12}\nu_{21}} = \frac{\nu_{21}E_1}{1-\nu_{12}\nu_{21}}, Q_{66} = G_{12} \end{aligned} \tag{7.2}$$

By inserting equation (7.1) in equation (7.2) the final form of the stress-strain equations for orthotropic ply under plane stress can be obtained.

$$\begin{Bmatrix} \sigma_1 \\ \sigma_2 \\ \tau_{12} \end{Bmatrix} = \begin{Bmatrix} \frac{E_1}{1-\nu_{12}\nu_{21}} & \frac{\nu_{21}E_1}{1-\nu_{12}\nu_{21}} & 0 \\ \frac{\nu_{21}E_1}{1-\nu_{12}\nu_{21}} & \frac{E_2}{1-\nu_{12}\nu_{21}} & 0 \\ 0 & 0 & G_{12} \end{Bmatrix} \begin{Bmatrix} \varepsilon_1 \\ \varepsilon_2 \\ \gamma_{12} \end{Bmatrix} \tag{7.3}$$

Laminate properties calculation

At this point the stress-strain relations for any ply rotated by an angle θ should be obtained. The stresses and strains can be expressed in a global coordinate system as:

$$\begin{Bmatrix} \sigma_x \\ \sigma_y \\ \tau_{xy} \end{Bmatrix} = \begin{Bmatrix} Q_{11} & Q_{12} & Q_{16} \\ Q_{12} & Q_{22} & Q_{26} \\ Q_{16} & Q_{26} & Q_{66} \end{Bmatrix} \begin{Bmatrix} \varepsilon_x \\ \varepsilon_y \\ \gamma_{xy} \end{Bmatrix} \tag{7.4}$$

These quantities can be related to the corresponding ones for an orthotropic ply by transforming stresses, strains and stiffnesses by the angle θ. Then, for a laminate of thickness (h), the resultant force and moment can be defined as:

$$\begin{Bmatrix} N_x \\ N_y \\ N_{xy} \end{Bmatrix} = \int_{-h/2}^{h/2} \begin{Bmatrix} \sigma_x \\ \sigma_y \\ \tau_{xy} \end{Bmatrix} dz, \begin{Bmatrix} M_x \\ M_y \\ M_{xy} \end{Bmatrix} = \int_{-h/2}^{h/2} \begin{Bmatrix} \sigma_x \\ \sigma_y \\ \tau_{xy} \end{Bmatrix} z dz \tag{7.5}$$

Finally the general constitutive relation for any laminate can be defined by using equation (7.4) and (7.5).

$$\begin{Bmatrix} N_x \\ N_y \\ N_{xy} \\ M_x \\ M_y \\ M_{xy} \end{Bmatrix} = \left(\begin{pmatrix} A_{11} & A_{12} & A_{16} \\ A_{12} & A_{22} & A_{26} \\ A_{16} & A_{26} & A_{66} \end{pmatrix} \begin{pmatrix} B_{11} & B_{12} & B_{16} \\ B_{12} & B_{22} & B_{26} \\ B_{16} & B_{26} & B_{66} \end{pmatrix} \right) \left(\begin{pmatrix} B_{11} & B_{12} & B_{16} \\ B_{12} & B_{22} & B_{26} \\ B_{16} & B_{26} & B_{66} \end{pmatrix} \begin{pmatrix} D_{11} & D_{12} & D_{16} \\ D_{12} & D_{22} & D_{26} \\ D_{16} & D_{26} & D_{66} \end{pmatrix} \right) \begin{Bmatrix} \varepsilon_{xo} \\ \varepsilon_{yo} \\ \gamma_{xyo} \\ \kappa_x \\ \kappa_y \\ \kappa_{xy} \end{Bmatrix} \tag{7.6}$$

Where $\varepsilon_{xo}, \varepsilon_{yo}, \gamma_{xyo}$ represent the mid-plane strains and $\kappa_x, \kappa_y, \kappa_{xy}$ are the curvatures of the laminate. It should be noted that the matrices [A] and [D] represent the laminate membrane and bending stiffness respectively while the matrix [B] represents the coupling stiffness and are defined in terms of the ply stiffness as:

$$\begin{aligned} A_{ij} &= \sum_{k=1}^{n} Q_{ij}(Z_k - Z_{k-1}), \\ B_{ij} &= \frac{1}{2}\sum_{k=1}^{n} Q_{ij}(Z_k^2 - Z_{k-1}^2), \\ D_{ij} &= \frac{1}{3}\sum_{k=1}^{n} Q_{ij}(Z_k^3 - Z_{k-1}^3) \end{aligned} \tag{7.7}$$

Where $Z_k - Z_{k-1}$ are the upper and lower z coordinates of the kth ply as shown in Figure 7.7.

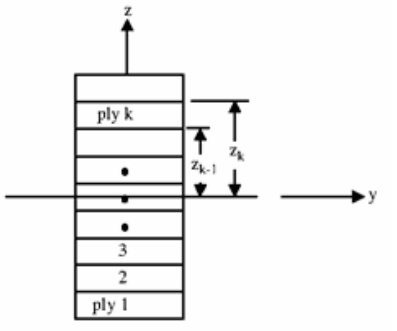

Figure 7.7: Ply numbering system

By using these three matrices the stiffness of a laminate in different directions can be determined and the response of a laminate to in-plane forces and moments can be described.

7.5.2 Failure criteria

Sandwich structures under bending and shear loads may fail in various ways including tension or compression failure of the facings, shear failure of the core, wrinkling failure of the compression facing, local indentation, debonding at the core-facing interface and global buckling. Each of these failure modes should be studied and analyzed separately.
Failure criteria for composite material are more complex than yield criteria for metals. One of the failure theory which is widely used for anisotropic composite materials is the Tsai-Wu failure criterion. In the following section the Tsai-Wu failure theory is explained briefly.

Tsai-Wu failure criterion

The laminate of sandwich structures is orthotropic material with three planes of symmetry oriented with the coordinate directions. From this the Tsai-Wu failure criterion can be derived:

$$F_{xx}\sigma_x^2 + 2F_{xy}2\sigma_x\sigma_y + F_{yy}\sigma_{yy}^2 + F_{ss}\tau_{xy}^2 + F_x\sigma_x + F_y\sigma_y = x \tag{7.8}$$

In this equation, F_{ij} represents the six different intensity parameters in a laminate. By introducing the strengths along lengthways and crosswise, X and Y, and shear strength in plane S, five parameters can be calculated in such a way:

$$\begin{aligned} F_x = \frac{1}{X_t} - \frac{1}{X_c}, F_{xx} = \frac{1}{X_t X_c} \\ F_y = \frac{1}{Y_t} - \frac{1}{Y_c}, F_{yy} = \frac{1}{Y_t Y_c}, F_{ss} = \frac{1}{S^2} \end{aligned} \tag{7.9}$$

The last parameter F_xy varies for different loading cases. For example when the ply is under the biaxial tensile force P, the mathematic expression is:

$$F_{xy} = \frac{1}{2P^2}[1 - P(\frac{1}{X_t} - \frac{1}{X_c} + \frac{1}{Y_t} - \frac{1}{Y_c}) - P^2(\frac{1}{X_t X_c} + \frac{1}{X_t X_c})] \tag{7.10}$$

In reality every material has limited strength. This leads to the stable condition of the structure:

$$F_{xx} F_{yy} - F_{xy}^2 > 0 \tag{7.11}$$

Substitute intensity parameters into the equations (7.11) and if the condition is not satisfied, then the structure will face the risk of failing.

7.6 FEM analysis

Patran is the pre/post-processing software used in this project for FEM analysis. By modeling and meshing in Patran numerical solutions are obtained to achieve structural optimization. In between this the analyses are executed by Nastran and send back to Patran.

This section starts by providing the FEM analyses for the fuselage after which the wing is analyzed.

7.6.1 Fuselage

Load Case Before a model of the fuselage can be made, the loading and constraints should be determined. In Figure 7.8a a side view of the fuselage is shown. The exact location and weight of each component is known and can be found in Section 3.1.

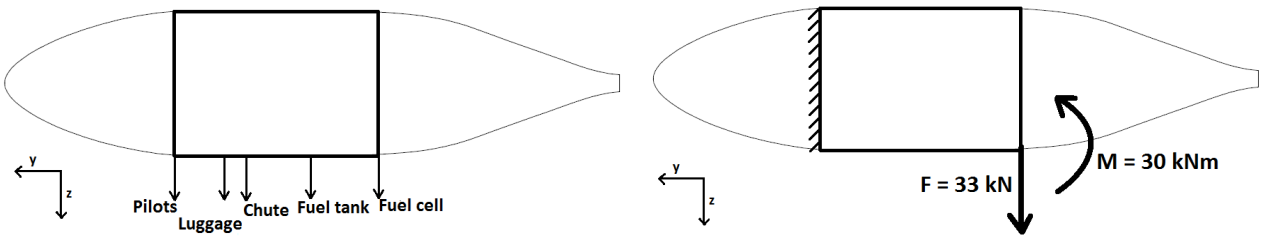

(a) Fuselage loads

(b) Fuselage equivalent loadcase

Figure 7.8: Fuselage loadcase

The part of the fuselage on which the highest loads act is shown. From this section a model is made. The diameter of the fuselage for this part is assumed to be constant; 1400mm. Its length is 1700 mm. The loads on this segment of the fuselage can be replaced by one force and one moment, which is shown in Figure 7.8b.

The force in z-direction is distributed over the entire circumference of the right part of the cylinder, as is the moment about the x-axis. The force and the moment have been multiplied by a critical load factor of 6 for maneuvering, which is stated in CS-23 [100]. The load factor is applicable to aerobatic aircraft, while the Zero EZE is a normal commuter aircraft. This higher load factor is taken into account as an extra safety measure. The circumference of the left part of the cylinder is fixed. In this way, the load case relates to the worst case scenario; 6g downwards. If the structure is proven to be strong enough under this loading, it will certainly be strong enough during flight. From regulations, the cabin does not necessarily

have to be pressurized. However, analysis will be performed with and without cabin pressurization, to check whether it is possible to pressurize the cabin in future design. The pressure difference is 0.06 MPa. A safety factor of 1.5 from regulations [100] is taken into account, so the pressure load acting on the inside of the skin will be 0.09 MPa.

Grid Type There are different types of grids.. The fuselage structure will consist of an isogrid, which can be seen in Figure 7.9. The grid angles are all defined to be 60 degrees. For the hoop rib spacing, helical rib spacing and grid cross section dimensions for the first model, reasonable values were chosen. These values can be adapted in a later stage of the design, in order to optimize the model.

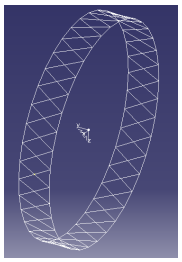

Figure 7.9: Isogrid

Model A First one element of the model is created in Patran. This element is shown in Figure 7.10a. All grid properties (1 dimensional) are applied to this element; the vertical curves and diagonal curves contain these properties. The material is assumed to be isotropic, while in reality this is not the case. This assumption is valid, since there will only be axial forces in the grid; in the direction of the fibers. The characteristics of the grid material are shown in Appendix E. The horizontal curves are placed in the element because of the skin; they do not contain grid properties (since there are no longitudinal ribs).

The surfaces between the 4 triangles resemble the skin. Shell element properties (2 dimensional) have been assigned to these surfaces. Some of these properties are shown in Appendix E. The strongest properties relate to the y-axis (11). The z-axis of the skin always points inwards (out of plane). Weaker properties relate to the axis perpendicular to the y-z plane; the local x-axis.

The aircraft industry uses an unwritten rule which says that the minimum skin thickness should be at least 1.625 mm, therefore 11 plies are used. The ply properties and orientation can be found in Appendix E. Nastran will use these values to calculate the Tsai-Wu failure index. After the material properties have been put into the initial part, the element can be rotated and translated to resemble a part of the fuselage. Hereafter one end can be fixed and on the other end the loads can be applied. This is shown in Figure 7.10b.

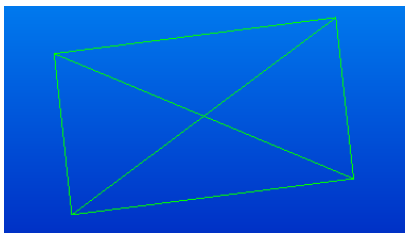

(a) First element of Model A

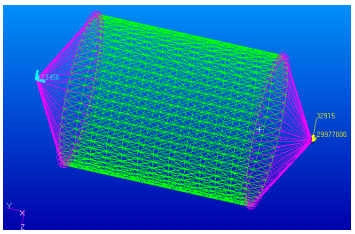

(b) Model A with fixed end and loads applied on the other end

Figure 7.10: First element and model A in Patran

All characteristics of this model are shown in Table 7.3.

Table 7.3: Characteristics of Model A

Grid cross section width	4 mm
Grid cross section height	12 mm
Hoop rib spacing	146.68 mm
Helical rib spacing	73.24 mm
Diamond skin elements	33.33 %
Triangular skin elements	66.67 %
Skin elements in one ring	208
Number of rings	12
Length fuselage	1760.14 mm
Diameter fuselage	1400 mm

Next a linear static analysis can be performed in Nastran.

Results Model A Firstly, the displacement is shown in Figure 7.11. The displacements are scaled by 10%, so they can be observed more easily. This means that the largest displacement in the mesh is scaled to be 10% of the maximum model size. In reality the maximum displacement for the non-pressurized and pressurized case is 0.6 mm and 1.09 mm, respectively. In Figure 7.11c the skin elements between the grid are pushed outside, this phenomenon is called pressure pillowing.

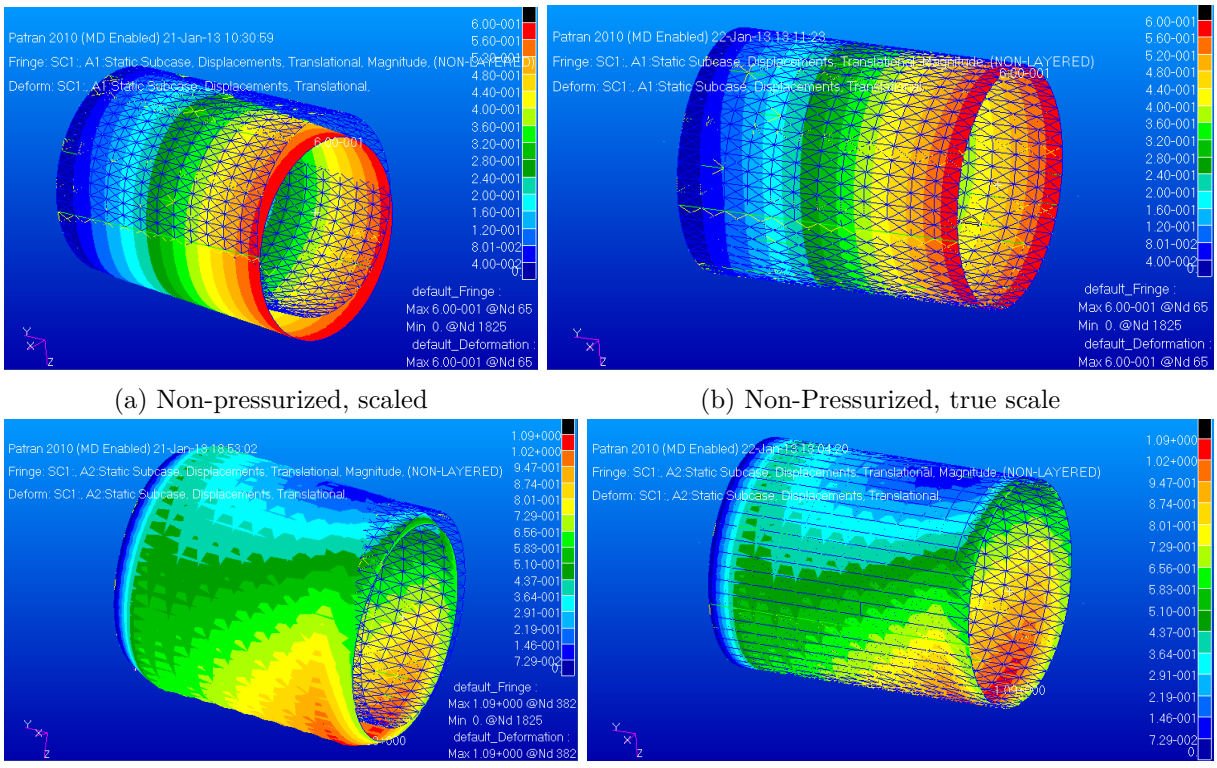

(a) Non-pressurized, scaled

(b) Non-Pressurized, true scale

(c) Pressurized, scaled

(d) Pressurized, true scale

Figure 7.11: Displacement (magnitude) in mm

Next the skin force distribution in y-direction is shown in Figure 7.12. Tension can be seen on the top and compression on the bottom of the model. The stress concentration stays within the triangular skin elements, therefore it can be assumed that global buckling will not occur. However, this can be verified later with different models.

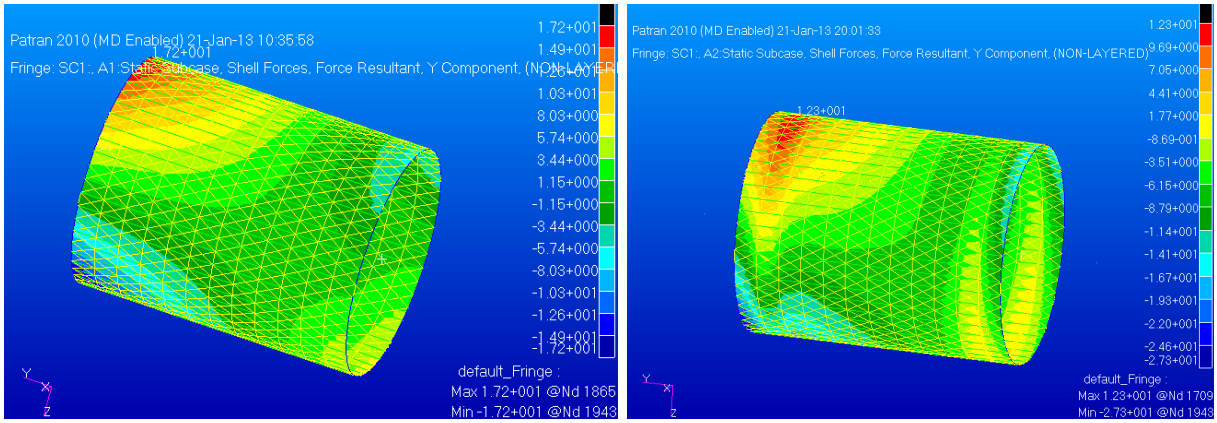

(a) Non-pressurized (b) Pressurized

Figure 7.12: Skin force distribution in y-direction in N/mm

In Table 7.4 all relevant results of model A are shown. When calculating the buckling bar force, hinged ends are assumed. Also the output file which Nastran creates shows whether the plies fail; a Tsai-Wu failure index larger than 1 means ply failure. The critical local skin buckling force is calculated using a method shown in reference [101].

Table 7.4: Results model A

	Non-pressurized	**Pressurized**
Buckling bar force (grid)	-10843 N	10843 N
Maximum axial bar compressive force	-438 N	-366 N
Margin of safety	23.76	28.63
Buckling of grid?	**No**	**No**
Triangular critical buckling force	240.88 N/mm	240.88 N/mm
Maximum skin buckling force	17.2 N/mm	27.4 N/mm
Margin of safety	13	7.79
Pocket buckling of triangular skin element?	**No**	**No**
Ply failure? (Tsai-Wu failure index > 1)	**No**	**No**
Weight of model	41.42 kg	41.42 kg
Weight of fuselage	**99.34 kg**	**99.34 kg**

It is interesting to see that for the pressurized cabin, the tension in the grid becomes higher, which relieves compression forces in the grid. Also the displacements change, due to the pressure load. Table 7.4 shows that fuselage A does not nearly fail. Local skin buckling, grid buckling or ply failure (Tsai-Wu) are often critical failure criteria. However, these failure modes are not reached. Therefore the grid spacing will be increased in Model B, which will decrease the weight of the fuselage.

Model B Again first one element of the model is created in Patran. This element is similar to the element in Figure 7.10a. The hoop- and helical spacing are increased to be 200.93 mm and 100.21 mm, respectively. The grid-, ply- and skin properties remain unchanged. The element is rotated and translated to resemble a part of the fuselage. This is shown in Figure 7.13. All characteristics of this model are shown in Table 7.5.

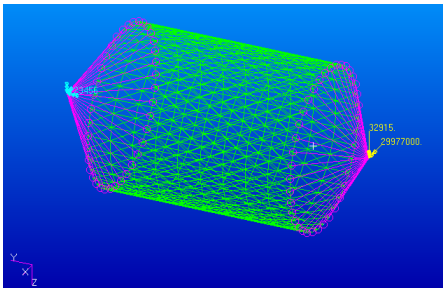

Figure 7.13: Model B with fixed end and loads applied on the other end

Table 7.5: Characteristics of Model B

Grid cross section width	4 mm
Grid cross section height	12 mm
Hoop rib spacing	200.93 mm
Helical rib spacing	100.21 mm
Diamond skin elements	33.33 %
Triangular skin elements	66.67 %
Skin elements in one ring	152
Number of rings	9
Length fuselage	1808 mm
Diameter fuselage	1400 mm

Now a linear static analysis will be performed in Nastran.

Results Model B First the displacement is shown in Figure 7.14. The maximum displacement for the non-pressurized and pressurized case is 0.72 mm and 1.48 mm, respectively.

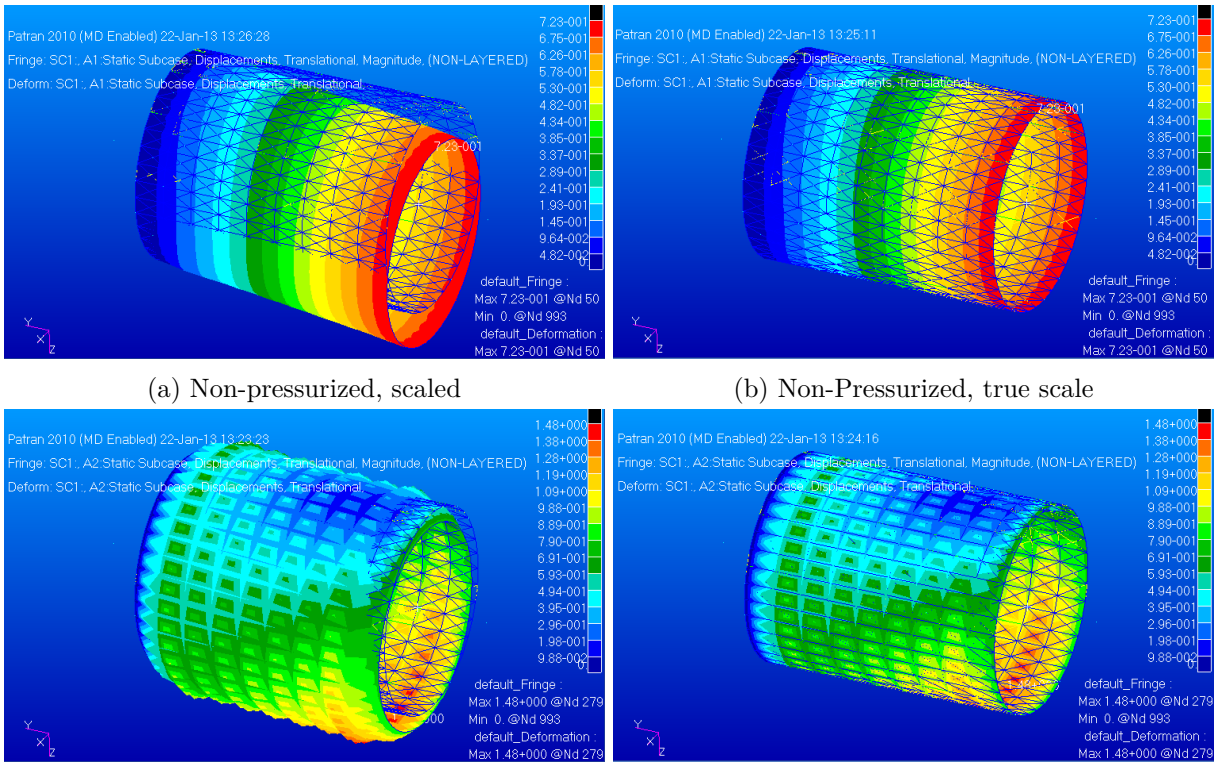

(a) Non-pressurized, scaled

(b) Non-Pressurized, true scale

(c) Pressurized, scaled

(d) Pressurized, true scale

Figure 7.14: Displacement (magnitude) in mm

Next the skin force distribution in y-direction is shown. Tension can be seen on the top and compression

on the bottom of the model. The stress concentration stays within the triangular skin elements, therefore it can be assumed that global buckling will not occur. The distribution changes gradually from one end to the other end. However, the dispersion is not totally continuous, which is shown by the rapid transition of one color to the other. Therefore the fineness of the mesh should be increased in the next model.

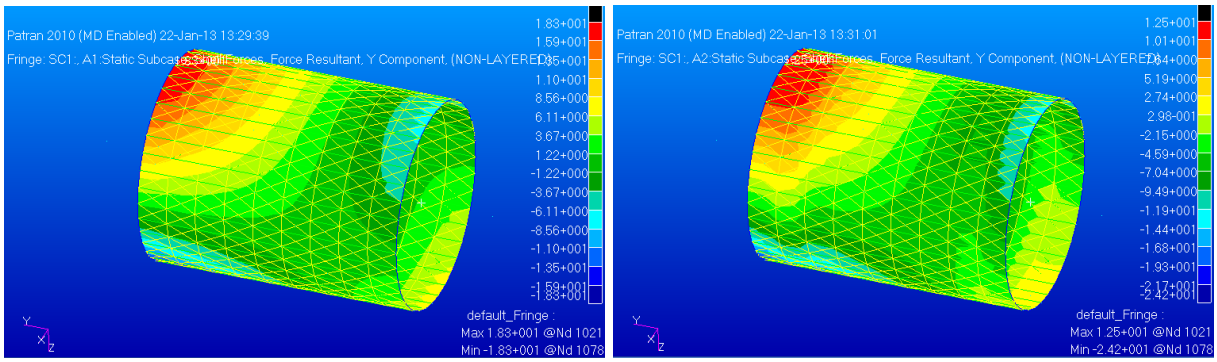

(a) Non-pressurized (b) Pressurized

Figure 7.15: Skin force distribution in y-direction in N/mm

In Table 7.6 all relevant results of model B are shown.

Table 7.6: Results model B

	Non-pressurized	**Pressurized**
Buckling bar force (grid)	-5778 N	-5778 N
Maximum axial bar compressive force	-495 N	-211 N
Margin of safety	10.67	26.38
Buckling of grid?	**No**	**No**
Triangular critical buckling force	129.5 N/mm	129.5 N/mm
Maximum skin buckling force	18.4	24.3
Margin of safety	6.04	4.33
Pocket buckling of triangular skin element?	**No**	**No**
Ply failure? (Tsai-Wu failure index > 1)	**No**	**No**
Weight of model	36.96 kg	36.96 kg
Weight of fuselage	**88.57 kg**	**88.57 kg**

Table 7.4 shows that fuselage A does not fail. However, the fineness of the mesh should be increased in the next model, in order to obtain more reliable results.

Model C One element of the model is created in Patran. This element is shown in 7.16.

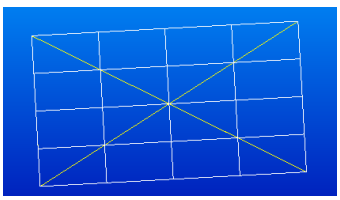

Figure 7.16: First element of Model C

The dimensions and material properties remain the same, compared to Model B. However, the mesh of the skin is finer and divided into quad elements instead of triangular elements. The element is rotated and translated to resemble a part of the fuselage. This is shown in Figure 7.17.

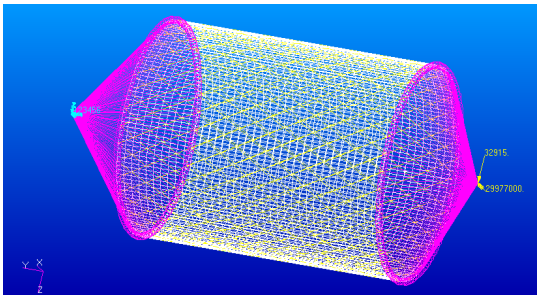

Figure 7.17: Model C with fixed end and loads applied on the other end

All characteristics of this model are shown in Table 7.7.

Table 7.7: Characteristics of Model C

Grid cross section width	4 mm
Grid cross section height	12 mm
Hoop rib spacing	200.93 mm
Helical rib spacing	100.21 mm
Skin elements in one ring	608
Number of rings	9
Length fuselage	1808 mm
Diameter fuselage	1400 mm

Results Model C The total displacement is shown in Figure 7.18. The maximum displacement for the non-pressurized and pressurized case is 0.72 mm and 1.42 mm, respectively.

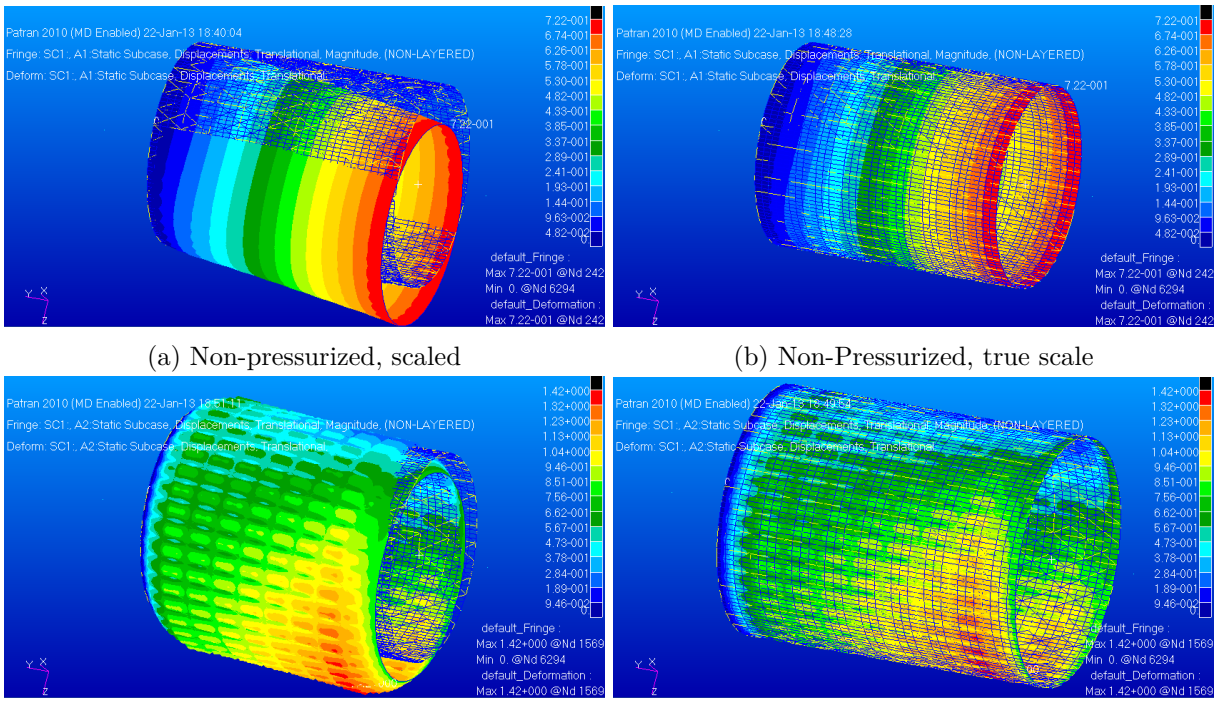

(a) Non-pressurized, scaled

(b) Non-Pressurized, true scale

(c) Pressurized, scaled

(d) Pressurized, true scale

Figure 7.18: Displacement (magnitude) in mm

Next the skin force distribution in y-direction is shown. Again tension can be seen on the top and compression on the bottom of the model. The stress concentration stays within the triangular skin elements, therefore it can be assumed that global buckling will not occur. Looking at the pressurized case, a difference can be seen compared to Model A and B. This is due to the fineness of the mesh. Where grid is present, the skin will be compressed more. Outside the grid, more tension can be seen.

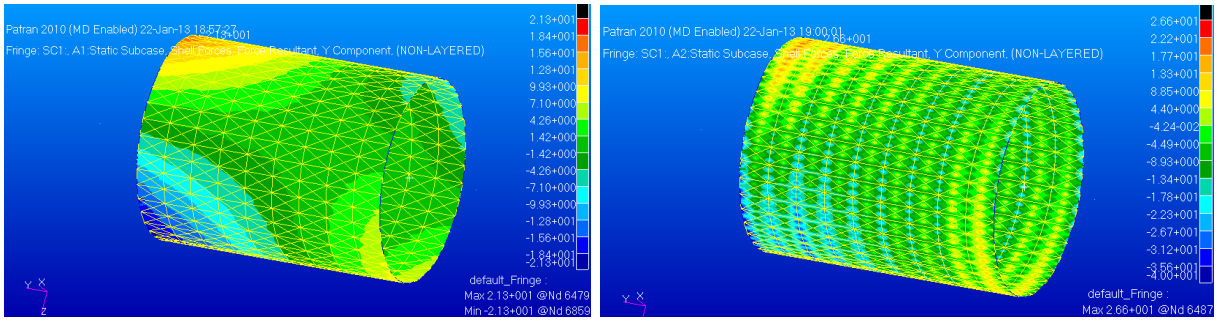

(a) Non-pressurized (b) Pressurized

Figure 7.19: Skin force distribution in y-direction in N/mm

In Table 7.8 all relevant results of model C are shown.

Table 7.8: Results model C

	Non-pressurized	**Pressurized**
Buckling bar force (grid)	-5778 N	-5778 N
Maximum axial bar compressive force	-495 N	-211 N
Margin of safety	10.67	26.38
Buckling of grid?	**No**	**No**
Triangular critical buckling force	129.5 N/mm	129.5 N/mm
Maximum skin buckling force	18.4	24.3
Margin of safety	6.04	4.33
Pocket buckling of triangular skin element?	**No**	**No**
Ply failure? (Tsai-Wu failure index > 1)	**No**	**No**
Weight of model	36.96 kg	36.96 kg
Weight of fuselage	**88.57 kg**	**88.57 kg**

Table 7.8 shows that fuselage C does not fail.

Table 7.9: Comparison of Model A, B and C

	Model A		**Model B**		**Model C**	
	Non-pressurized	**Pressurized**	**Non-pressurized**	**Pressurized**	**Non-pressurized**	**Pressurized**
Buckling bar force (grid)	-10843 N	10843 N	-5778 N	-5778 N	-5778 N	-5778 N
Maximum axial bar compressive force	-438 N	-366 N	-495 N	-211 N	-995 N	-822 N
Margin of safety	23.76	28.63	10.67	26.38	4.81	6.03
Buckling of grid?	**No**	**No**	**No**	**No**	**No**	**No**
Triangular critical buckling force	240.88 N/mm	240.88 N/mm	129.5 N/mm	129.5 N/mm	129.5 N/mm	129.5 N/mm
Maximum skin buckling force	17.2 N/mm	27.4 N/mm	18.4	24.3	21.3 N/mm	40.1 N/mm
Margin of safety	13	7.79	6.04	4.33	5.08	2.23
Pocket buckling of triangular skin element?	**No**	**No**	**No**	**No**	**No**	**No**
Ply failure? (Tsai-Wu failure index > 1)	**No**	**No**	**No**	**No**	**No**	**No**
Weight of model	41.42 kg	41.42 kg	36.96 kg	36.96 kg	36.96 kg	36.96 kg
Weight of fuselage	**99.34 kg**	**99.34 kg**	**88.57 kg**	**88.57 kg**	**88.57 kg**	**88.57 kg**

Comparison of Model A, B and C Table 7.9 shows that all models are strong enough. The third model is most reliable, since its skin mesh is finest. The margin of safety is defined as:

$$Margin\ of\ safety = \frac{allowable}{applied} - 1 \tag{7.12}$$

This value should be positive (or equal to zero), but as close to zero as possible. Since the margins of safety for Model C are still considerably large, there is room for optimization. If in future models the

margins of safety are close to zero, the model would be fully optimized, which means in this case the fuselage will be as light as possible. In Figure 7.20 the optimization of Model A to Model B to Model C is shown. The weight reduces (left vertical axis) while the margin of safety (right vertical axis) approaches zero.

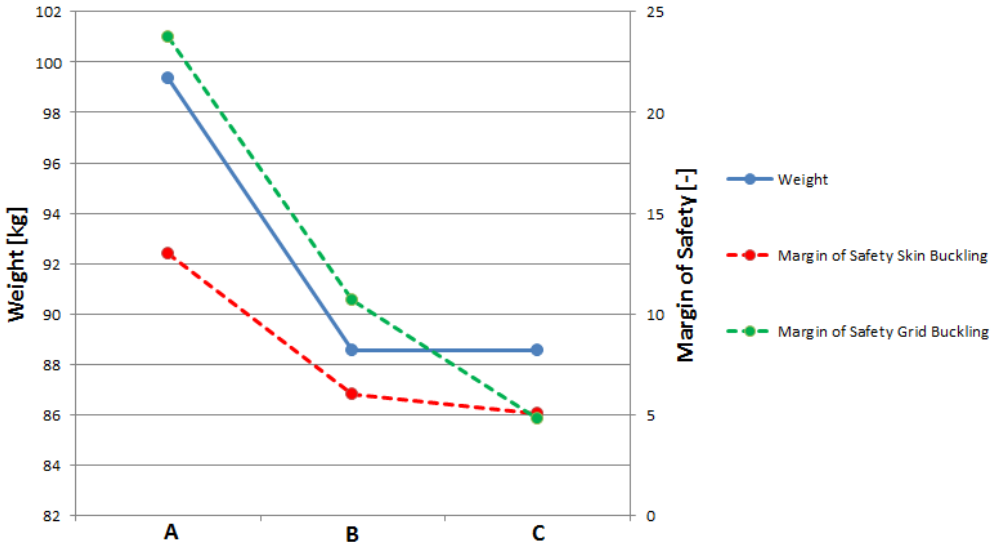

Figure 7.20: Optimization of Model A to Model B to Model C

7.6.2 Main Wing

Load Case Just as for the fuselage model, first the load case must be determined. The load factor for the wing is not equal to the load factor for the fuselage. CS-23 provides equations [100] to calculate the gust load factors for the wing.

$$N = 1 \pm \frac{k_g \rho_0 U_{de} V a}{2(W/S)} \tag{7.13}$$

$$K_g = \frac{0.88 \mu_g}{5.3 + \mu_g} \tag{7.14}$$

$$\mu_g = \frac{2(W/S)}{\rho \, MAC \, ag} \tag{7.15}$$

The maximum gust speed comes from regulations and is 15.24 m/s. All other values are known from Chapter 4. Table 7.10 shows these values and the gust load factor for cruise- and take-off conditions.

Table 7.10: Parameters from which the gust load factor is calculated

Gust speed	15.24 m/s
Density of air at sea-level	1.225 kg/m^3
Density of air at cruise	0.905 kg/m^3
Wing loading at cruise	891.82 N/m^2
Wing loading at take-off	1098.48 N/m^2
Mean aerodynamic chord	1.145 m
Gravitational acceleration	9.81 m/s^2
Equivalent airspeed at cruise	66.18 m/s
Equivalent airspeed at take-off	35 m/s
Lift slope curve	5.44 /rad
Gust allevation factor cruise	0.85
Gust alleviation factor take-off	0.85
Aercraft mass ratio cruise	175.46
Aircraft mass ratio take-off	159.67
Gust load factor cruise (max)	**4.22**
Gust load factor cruise (min)	-2.22
Gust load factor take-off (max)	2.38
Gust load factor take-off (min)	-0.38

The maximum gust load factor for cruise will be used (4.22), since this is the largest load factor. The resultant lift force during cruise on one wing is 5297.4 N. It acts on the wing, 3.02 m from the root. Taking the gust load factor into account, the force acting on the wing will be 22350 N. The force is assumed to act on 25 % of the chord.

Wing Model In order to create a model, the wing will be divided into 6 surfaces. These surfaces are shown in red in Figure 7.21. No material will be put into the area 0, because of the presence of the

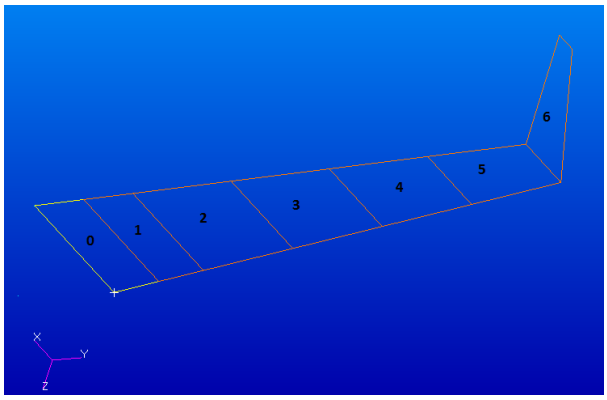

Figure 7.21: Surfaces wing

fuselage. All surfaces are of equal length, except for surface 1, which has half the length compared to the other surfaces. The surfaces contain homogeneous shell element properties, which have the same stiffnesses

Table 7.11: Ply orientation

Ply	Orientation
1	45°
2	-45°
3	0
4	-45°
5	45°

(EI) compared to the real wing stiffnesses at these locations. In order to calculate these stiffnesses, the

moment of inertia of the foam and facing, the Young's modulus of the foam and the Young's modulus of the facing in y-direction (strongest direction; 11) must be known. First the Young's modulus of the facing in y-direction is determined, using the following ply orientation. The ply thickness is 0.1524 mm. Therefore the thickness of the facing is 0.762 mm. The ply properties can be found in Appendix E. The Young's modulus (11) of the facing can calculated to be 38600 MPa. The Young's modulus of the foam is 25 MPa. The moment of inertia of the facing and foam of the different surfaces can be found using CATIA. The stiffness can be calculated using Equation 7.16.

$$EI_{total} = E_{facing} \cdot I_{facing} + E_{foam} \cdot I_{foam} \tag{7.16}$$

Using the Young's moduli stated above, the following equivalent stiffnesses can be found in Table 7.12. Using a constant thickness of 150 mm, an equivalent Young's modulus for the homogeneous shell can be

Table 7.12: Moment of inertia of the facing and foam and the stiffness of the wing

Surface	Moment of inertia facing [mm^4]	Moment of inertia foam [mm^4]	Stiffness real wing [Nmm^2]
1	1.12E+07	4.25E+08	4.41E+11
2	7.51E+06	2.50E+08	2.96E+11
3	4.75E+06	1.36E+08	1.87E+11
4	2.77E+06	6.64E+07	1.08E+11
5	1.43E+06	2.77E+07	5.59E+10
6	3.34E+04	3.50E+05	1.30E+09

found so that the stiffness of the shell equals the stiffness of the real wing. These Young's moduli are shown in Table 7.13.

Table 7.13: Equivalent stiffnesses

Surface	Equivalent Young's modulus [MPa]
1	1.17E+03
2	8.93E+02
3	6.56E+02
4	4.56E+02
5	2.92E+02
6	16.98

These shell properties (thickness, Young's modulus) are applied to the surfaces. A mesh is created on the wing. Also the wing is fixed at the root and the lift force is applied at its location. This is shown in Figure 7.22. Now a linear static analysis, as well as a normal mode analysis will be performed in Nastran.

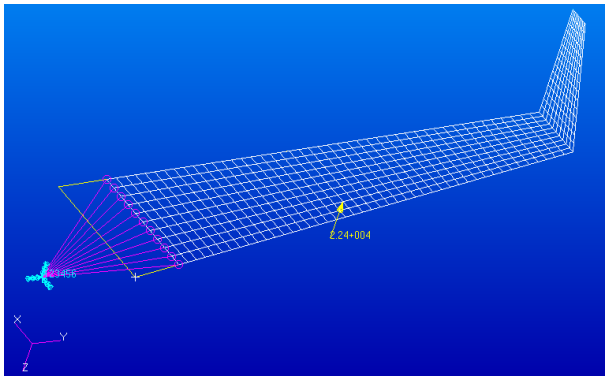

Figure 7.22: Model of the main wing

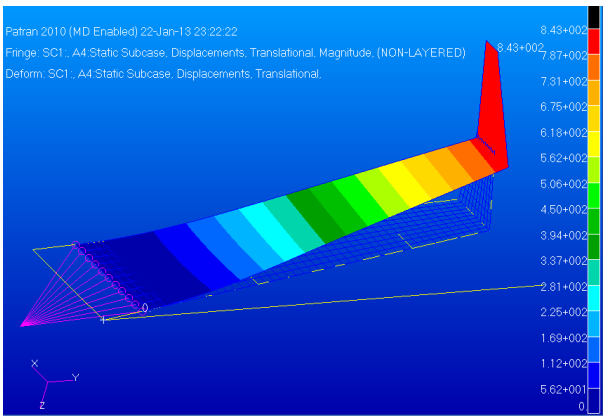

Figure 7.23: Total displacement of the wing, true scale

Results Wing Model First the total displacement is shown in Figure 7.23. A maximum displacement of 84.3 cm can be found on the top of the winglet. The maximum displacement in z-direction is 82 cm at the tip of the wing.

The moment- and shear force distribution of the model is inaccurate, therefore the beam theory will be used to calculate these distributions. These distributions are shown in Figure 7.24 and Table 7.14.

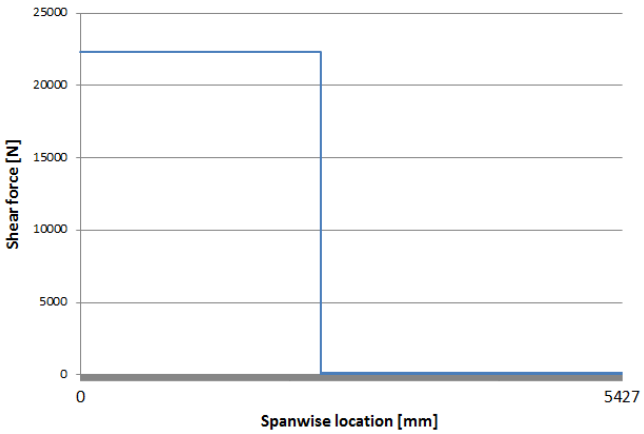

(a) Shear Force in N

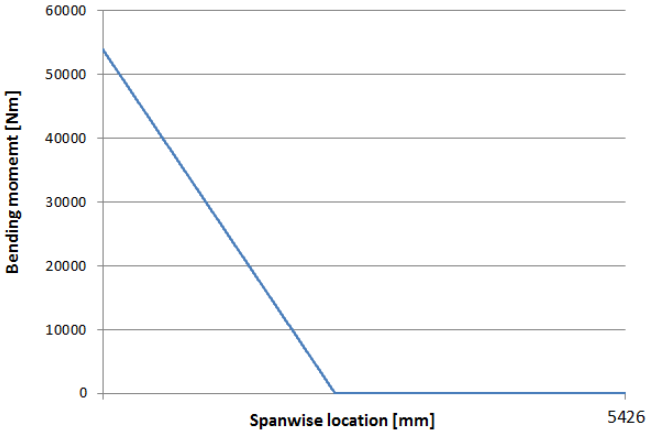

(b) Bending Moment in Nm

Figure 7.24: Shear force distribution and bending moment distribution in the main wing

Table 7.14: Shear force distribution and bending moment distribution in the various surfaces of the main wing

Surface	Bending moment [Nm]	Shear force [N]
1	53908	22350
2	40431	22350
3	13477	22350
4	0	0
5	0	0
6	0	0

It is known that in a sandwich structure the normal force is carried by faces and that the shear stress is mostly carried by core material. By using the superposition principle the problem can be divided into two different parts. First, the maximum normal stress on the face sheets is calculated. After that the average shear stress on the core can be obtained.

After some simplifications, the normal- and shear stresses can be calculated with Equation 7.17 and 7.18, respectively.

$$\sigma_y = \frac{M_x}{I_{xx}} z \tag{7.17}$$

$$\tau = \frac{V}{A} \tag{7.18}$$

The z-direction will be calculated using a simplified cross section, which is shown in Figure 7.25. The

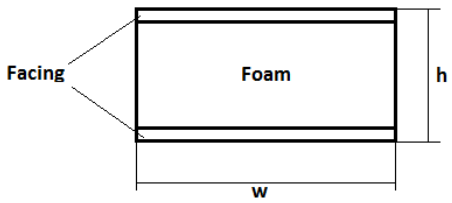

Figure 7.25: Equivalent cross section

width of this cross section is the width of the cross section of the real wing at a certain location. The height can be calculated, so that the stiffness of this equivalent cross section is equal to the stiffness of the real wing.

Now the normal stresses in the facing and shear stresses in the foam can be calculated. These values are shown in Table 7.15. As can be seen from Table 7.15 the maximum normal stress appears at the root

Table 7.15: Compressive normal stress in the facing and shear stress in the foam

Surface	Equivalent height [mm]	Equivalent moment of inertia of the facing mm^4	Compressive normal stress [MPa]	Shear stress [KPa]
1	147.9	1.12E+07	355.9	112.4
2	129.5	7.53E+06	347.8	146.5
3	111.1	4.76E+06	157.3	198.8
4	92.8	2.77E+06	0	0
5	74.4	1.43E+06	0	0
6	18.0	3.35E+04	0	0

as -355.9 MPa. Compared to an allowable compressive normal stress of -1000 MPa of one ply, this gives a margin of safety of **1.81**. The normal stress in the separate plies will not be much higher than -355.9 MPa, therefore the facing will not fail due to bending.

A maximum shear stress of 198.8 kPa occurs in section 3 of the wing. Compared to the shear strength of the core material, which is 500 kPa, it can be concluded that core material is capable of handling the in plane shear stress. The margin of safety is **1.52**.

Eigenmodes Main Wing The wing of Zero-EZE uses a high aspect ratio and lightweight material to achieve a large cruise range and a low drag coefficient. This usually leads to a series of aero-elastic problems which would add extra local stress and deformation to the structure. The most important and interesting one is the vibration of the wing. Through Nastran simulation, 10 different eigenmodes are analyzed in order to verify the structure of wing. For the future design, results of the eigenmodes can also be used to optimize the wing structure.

From Nastran, the 10 eigenmodes are determined: For general aviation aircraft, only the first three

Table 7.16: Table of eigenmodes

Mode	Eigenvalue	Frequency
1	3.43	0.29
2	34.80	0.94
3	78.52	1.41
4	101.38	1.60
5	293.10	2.72
6	564.47	3.78
7	981.63	4.99
8	990.64	5.01
9	1389.44	5.93
10	2264.26	7.57

eigenmodes from the Table 7.16 would appear during flight. These are shown in Figures 7.26 to 7.28. These figures are scaled, so the deformation shown is very exaggerated. The actual displacement is shown in the legenda in mm.

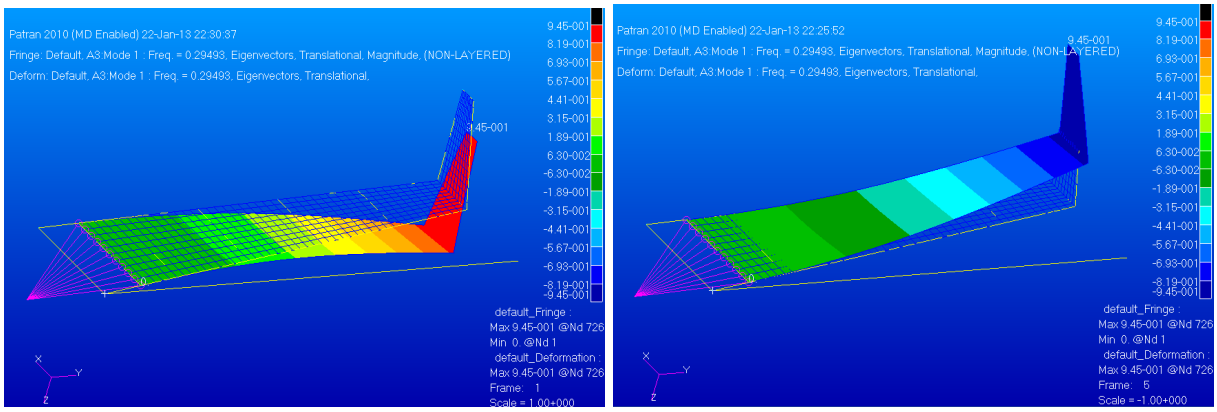

(a) Eigenmode 1a (b) Eigenmode 1b

Figure 7.26: Eigenmode 1

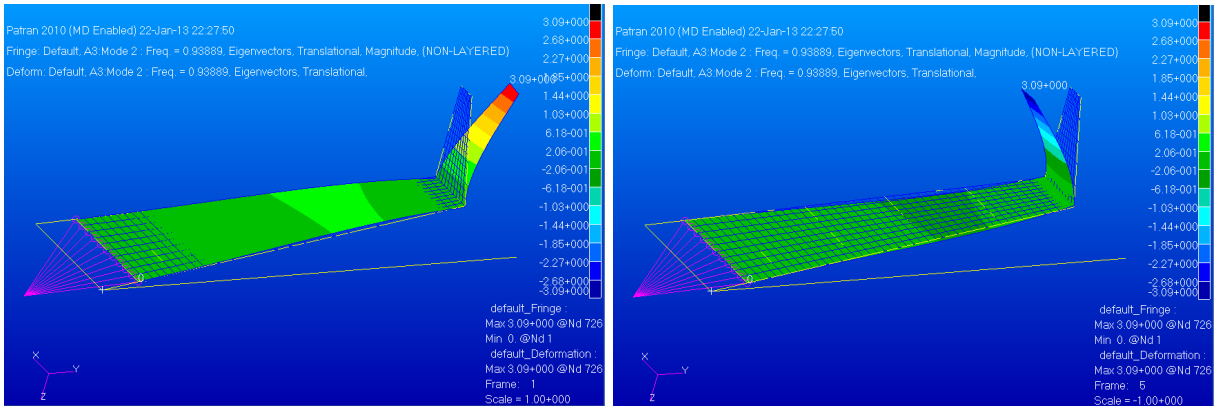

(a) Eigenmode 2a (b) Eigenmode 2b

Figure 7.27: Eigenmode 2

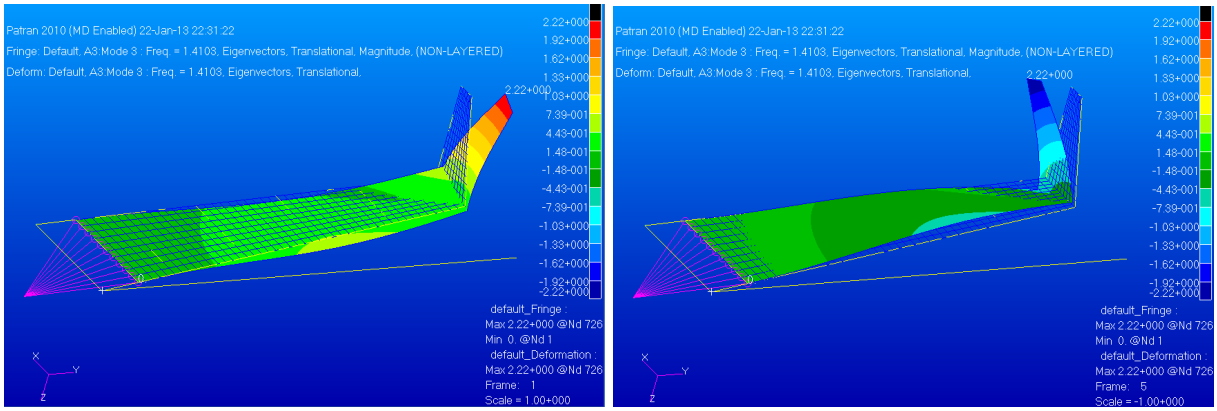

(a) Eigenmode 3a (b) Eigenmode 3b

Figure 7.28: Eigenmode 3

As Figure 7.26 shows, the first mode gives the simplest, one stage bending deformation. This is the most common vibration case of wings where the deformations are in a single direction. Figure 7.27 corresponds to eigenmode 2, in this case the wing has two stages of bending deformations. The difference with respect to case 1 is that the middle section of the wing is bended upwards and the tip is bended downwards. Therefore the local bending stresses will differ along the wing. Figure 7.28 is about case 3. As the figure indicates, the wing is twisted at the tip, and this will add extra torsion to the wing structure. The extra torsion is also critical for the wing structure design.

One thing that can be concluded from the FEM result is that different frequencies will lead to different wing deformations. Also the current wing structure is capable of handling the first three vibration cases.

Conclusion and Recommendations The current main wing will weigh approximately 85 kg. It will not fail under shear the shear force or bending moment, since the normal stress in the facing and shear stress in the foam do not approach the allowable stress. However, not all failure modes are examined, due to lack of time. In future designs different model should be created, which can examine different types of failure of the wing.

Chapter 8

Performance

8.1 Flight Envelope

In this section the flight envelope for the mission of the Zero EZE is presented. A diagram that shows the different stages during a typical flight of the aircraft and their duration is presented in Figure 8.1. The three most important stages are the cruise, climb and descent which have a duration of 150, 16 and 16 minutes, respectively. The cruise altitude is taken as 3048 meters (10,000 feet) but higher cruise altitude are possible, as discussed in Section 3.4.

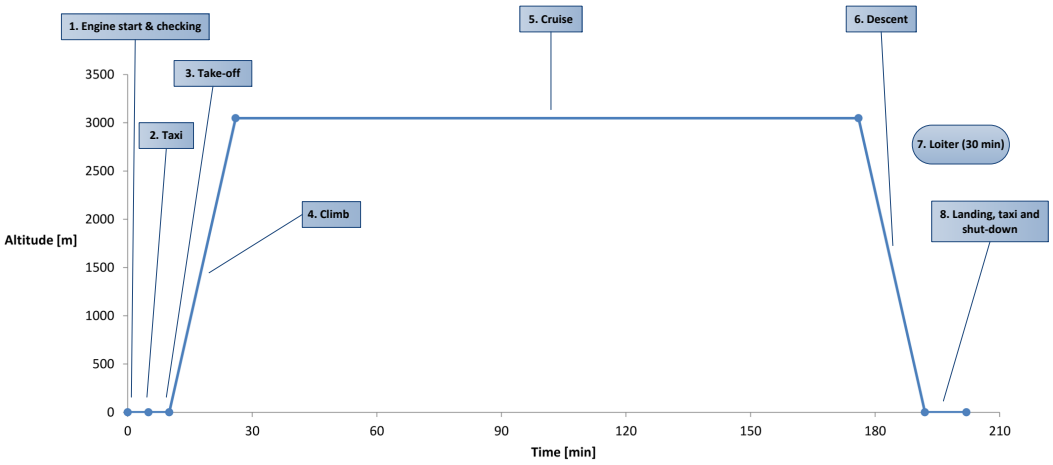

Figure 8.1: Flight envelope of the Zero EZE

8.2 Payload vs. Range

For the payload-range diagram of the Zero EZE, presented in Figure 8.2, a small difference over time can be noted. In comparison to a conventional kerosine-propulsed aircraft the fuel weight is much lower for a fuel cell system. Hydrogen has a low density and therefore gives only a small difference between MTOW and Maximum Zero Fuel Weight in the diagram.

However, by flying without a second person, luggage or with lower speeds, the range can be extended. This gives only an increment of about 9.8% but could be necessary to reach a certain destination. Furthermore a reserve fuel of 3 kg for the loiter is taken into account. Another aspect which can be noticed is that the MTOW is equal to the MLW for this aircraft.

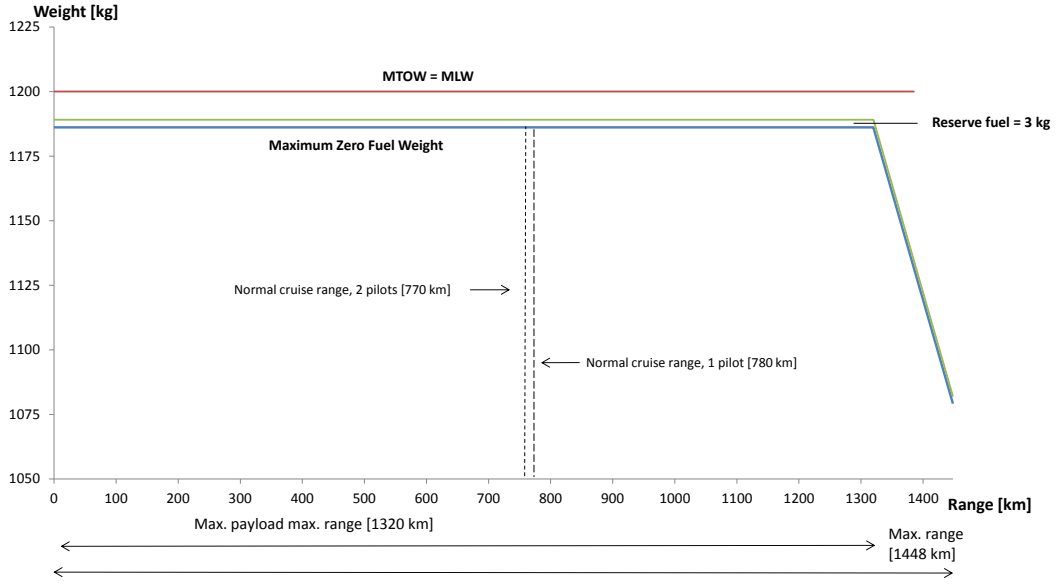

Figure 8.2: Payload-range diagram of the Zero EZE

8.3 Performance and Feasibility Analysis

At the beginning of this project, several design requirements were given concerning the performance of the Zero EZE. Now that all the design parameters have been established, the performance should be examined. This is done in the remainder of this section. In the calculations it is assumed that the aircraft is fully loaded, which means there are two persons within the aircraft, as well as the maximum amount of luggage. Since the formulas used in this section are similar to the ones used in Section 2.2, they are not repeated here.

8.3.1 Cruise Speed

One of the design requirements determined in the beginning of the DSE, is the ability to reach a cruise speed of at least 150 knots. This cruise speed should be maintained during the entire cruise, which consists of 2.5 hours of flight plus half an hour reserve. From Section 2.4 a fuel capacity of 13.9 kg of hydrogen was found. With an energy density of 142 MJ/kg, 1974 MJ of energy can be provided by the hydrogen.

During the 16-minute take-off and landing, the power required equals 109.8 kW and 33.4 kW for both phases respectively. Since the fuel cell has a net efficiency of 49 %, the electric motor an efficiency of 95 % and the propeller an efficiency of 89 %, the energy needed for these manoeuvres is equal to 281 MJ. This means that 1693 MJ is available for cruise. With a 180 minute cruise, 76.8 kW can be delivered by the fuel cell during this period, so that all the fuel is used.

In Section 2.2 the required power has been determined as a function of the cruise speed. When this process is reversed, the velocity can be found when the power required is known. With a required power of 76.8 kW, the maximum cruise speed is equal to 85.5 m/s (166 knots).

As can be seen, the achievable cruise speed is higher than the requirement of 150 knots the Zero EZE was designed on. This speed increase is possible due to the fact that the chosen fuel tanks provide a 0.2 kg higher fuel capacity then needed. Also the aircraft turned out to be slightly more efficient.

8.3.2 Maximum Speed

Next to the maximum cruise speed, the maximum speed of the Zero EZE can be determined. However, this speed cannot be reached during the entire cruise phase. As seen in Section 2.4, 122.5 kW of power is available from the fuel cell. With the aforementioned efficiencies for the propeller and the electric motor, the maximum power delivered to the propeller then equals 102.9 kW. In the same way as for the cruise

speed, the velocity can be determined via the power requirement. With a required power of 102.9 kW, the maximum achievable speed of the Zero EZE is found to be 102.6 m/s (200 kts).

8.3.3 Maximum Range

During the course of the DSE, the initial range requirement of 1000 km has been changed. Instead of a minimum distance, a maximum flight time of 2.5 hours has been set. With a limited amount of flight time, the maximum range is only dependent on cruise speed.

As been determined previously, the maximum cruise speed equals 85.5 m/s. With the maximum flight time of 2.5 hours, the achievable range is 770 km. This is less then the original requirement of 1000 km, but the new requirement of 2.5 hours is met. Also, as was concluded in the Market Analysis in Chapter 1, single engine propeller aircraft will be used mostly for flights up to 600 km. This is also consistent with the range of the Zero EZE.

However, when flying with a speed of 85.5 m/s, the aircraft is not flying at optimal conditions. Theoretically a longer range can be achieved when the speed setting is optimized. To achieve maximum range, lift over drag should be maximum. The lift coefficient can then be calculated as follows:

$$C_L = \sqrt{C_{D_0} \pi A e} \tag{8.1}$$

With the lift coefficient known, the desired flight speed follows from basic flight mechanics:

$$V = \sqrt{\frac{W}{S} \frac{2}{\rho} \frac{1}{C_L}} \tag{8.2}$$

Filling in the equations results in a desired flight speed of 54.7 m/s. Calculating the hydrogen flow required and converting to flight time, this speed can be maintained for 402 minutes. Multiplying the speed with flight time results in a maximum range of 1320 km. However, this range is not deemed realistic due to sanitary needs for the pilot.

8.3.4 Maximum Rate of Climb

To determine the maximum achievable rate of climb, it is assumed the aircraft flies at cruise altitude with a speed of 150 knots. To fly at this speed, the fuel cell should provide 60 kW to the electric motor. However, the fuel cell is sized to deliver a maximum power output of 122.5 kW. Therefore 62.4 kW is available for climbing. If the excess power of 62.4 kW is divided by the weight of the aircraft and multiplied with the efficiencies of the electric motor and propeller, the maximum rate of climb during cruise is found. This maximum rate of climb is equal to 4.5 m/s.

8.3.5 Take-off Distance

As calculated in Section 2.2, the ground run of the Zero EZE is equal to 490 m when maximum throttle is applied. The original Long EZ can take-off in 253 m [112], which is only half the distance the Zero EZE needs. Even though this is a big increase, it was inevitable due to the large increase in MTOW while the power output remained about the same. It would be possible to decrease the runway length by increasing the size of the fuel cell and electric motor, but this again would cause an increase in aircraft weight. Furthermore, all other performance requirements are met so this increase in runway length is acceptable. When further research is done on the Zero EZE, the disadvantages of an increase in performance might be investigated to see whether it is possible to reduce the runway length.

8.3.6 Landing Speed

Next to a take-off requirement, a maximum landing speed has been given. Section 2.2 states that the landing speed equals 1.2 times the stall speed, which is dependent on the aerodynamic design of the Zero EZE. With a stall speed of 30 m/s, the landing speed is estimated at 36 m/s. This is equal to 70 knots, which meets the requirement.

8.3.7 Noise Production

One of the important design constraints of this project was the noise production of the aircraft. In Section 2.3 a complete analysis has been made, which states 110 dB is produced at a distance of 100 m, reducing to approximately 61 dB at a distance of 3000 m. This means that for all areas outside an airport, the requirement is met.

8.3.8 Limit Loads

The original requirement for the limit loads was to achieve at least +6 / -4 G. However, these loads are based on acrobatic aircraft performance. For the Zero EZE it would suffice to reduce these limit loads, as discussed in Section 7.6.1. From Section 7.6.1 and 7.6.2, maximum loadings of +6 G and +4.2 G are found for the fuselage and wing respectively.

8.3.9 Zero EZE Cost

To determine the Zero EZE cost, the total purchase price has been divided into several components. The cost of every component has been determined, after which they have been added up to determine the Zero EZE cost. As it turns out, the Zero EZE can be purchased for a price of €472,500. The complete overview of the individual components can be found in Section 10.3.

8.4 Compliance Matrix

To determine whether or not the Zero EZE design meets the original requirements, a compliance matrix is made. In this compliance matrix, both the original requirements and the adapted ones are stated. The final column states whether the Zero EZE meets the requirement or not.

	Requirement	**Modified**	**Requirement fulfilled**
1	1000 km range	Instead of a minimum range, a maximum cruise time of 2.5 hours has been set.	Yes, the Zero EZE is able to fly 770 km in 2.5 hours.
2	150 kts cruise speed	-	Yes, the maximum achievable cruise speed equals 166 kts.
3	<70 kts landing speed	-	Yes, a landing speed of 70 kts is needed at maximum payload.
4	Take-off distance equivalent to Long EZ	-	No, with a take-off distance of 490 m the initial take-off distance is almost doubled.
5	2 person aircraft	-	Yes, the Zero EZE fits two persons side-by-side.
6	Limit loads more than +6 / -4 G	The original limit load applies to acrobatic aircraft.	Partly, fuselage has a limit load of +6 G, wings have a limit load of +4.2 G.
7	EASA CS-23 certifiable	-	Uncertain, due to the implementation of a fuel cell system certification becomes more difficult. Apart from the propulsive system the aircraft is certifiable.
8	Hybrid operation based preferably on two electrical engines and a CRP. Batteries used for take-off and landing. Biodiesel/jet fuel range extender recharges batteries and provides electrical power to engines.	The original battery-range extender system is replaced by a zero-emission fuel cell system.	Partly, due to the implementation of a fuel cell system the Zero EZE is more sustainable than required. However, instead of a CRP a SRP is implemented.
9	Climb rate of 500 fpm for at least 15 minutes on battery power only	The climb rate has not been changed, but the battery requirement has dropped.	Yes, a maximum rate of climb of 4.5 m/s (886 fpm) can be achieved at cruise altitude.
10	Noise cancelling or noise shielding if possible resulting in DNL of less than 65 dB for all areas outside an airport	-	Yes, 61 dB is produced at a distance of 3000 m. This is within the requirement.
11	Provision of ballistic recovery chute	-	Yes, a ballistic chute is present in the Zero EZE
12	Operable as a self-fly commuter type of aircraft for short range business trips	-	Yes
13	Aircraft cost aimed at less than 500K euro	-	With a purchase price of € 472,500, the requirement is met.

Figure 8.3: Compliance Matrix of the Zero EZE

Chapter 9

Operations & Logistics

In this chapter the operations and logistic concept description of the Zero EZE is provided. The operations and logistics overview will be given for the propulsion system and structures & materials of the aircraft. The operation of the aircraft includes multiple stages like pre-flight, flight, maintenance, etc.. In Sections 9.1 and 9.2 descriptions are given of the operations & logistics. In Section 9.3 a flow block diagram is presented to give an overview.

9.1 Propulsion System

The propulsion system of the Zero EZE consists of the PEM fuel cell, hydrogen tank, electric motor and SRP. Especially the hydrogen supply at airports is a critical factor, since its infrastructure has yet to be set up. However, it is already possible to have the hydrogen delivered at airports at reasonable costs [113]. This has to be arranged by the owners/users of the Zero EZE themselves. A proper infrastructure is required to accommodate this transport, but since the Zero EZE will mainly be used by business people to fly to big cities, no problems are expected here.

Further, there are no moving parts in fuel cells, which makes the fuel cell a very reliable system. By replacing the range extender with a fuel cell, there will be no emissions. Moreover the maintenance of fuel cells is low, which means saving time and reducing costs. A big advantage is that the fuel cells can be monitored remotely and any problems can be dealt with easily.

For the electric motors and SRP maintenance places have to be available. At every airport these places will be available as for the external knowledge needed for repairs.

9.2 Structures & Materials

The operations and logistic concept description for the materials and structures focuses on the prevention of possible damage to the aircraft.

9.2.1 Damage characterization

The Zero EZE uses a composite structure. Unlike metal structures, where fatigue crack initiations are the primary threat to the structural integrity, accidental damage is a critical threat for composite materials. In order to keep the aircraft operating safely it is very important to have expertise and maintenance places available at every airport. This will be available at all main airports. If necessary the infrastructure towards the airports allows it to bring in mechanics for repairs. The latter will only increase costs and is not preferred.

9.2.2 Damage Inspection

Maintenance is mainly done by the use of visual inspection methods, but there are techniques that can be applied for detecting the non visible damage:

- Tap Testing

- Ultrasonic Inspection
- X Ray
- Thermography

For each inspected damage a specific repair method can be applied. Every airport should facilitate the use of these techniques.

9.3 Operations & Logistics Diagram

In this last section the operations & logistics are given in the form of a flow block diagram. The information from the previous sections is included in this diagram. The diagram presented here can be found in Figure 9.1.

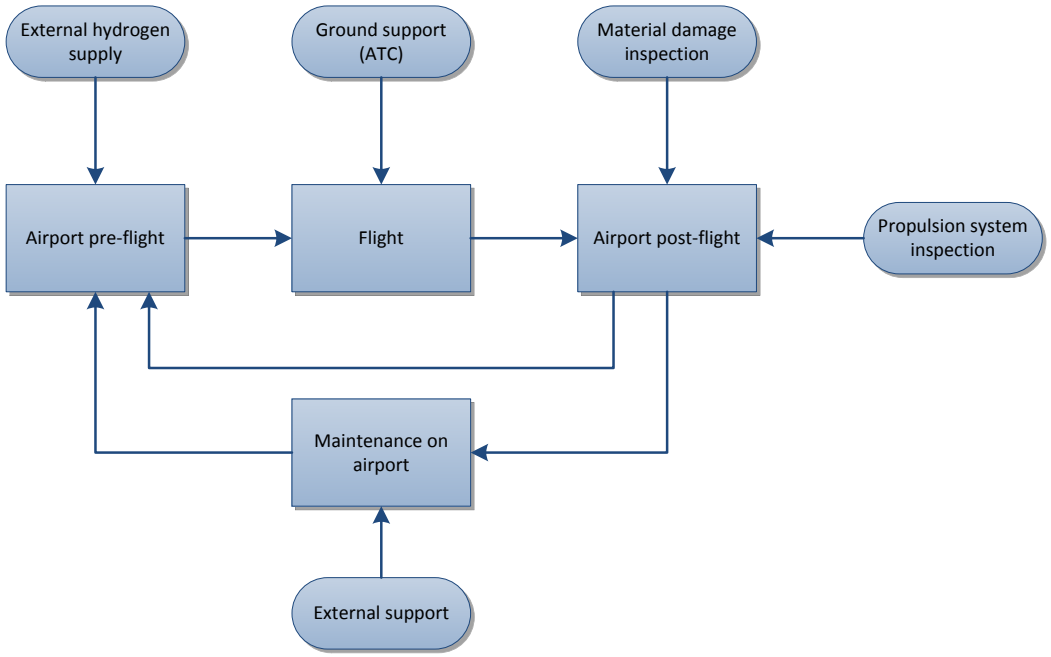

Figure 9.1: Operations and Logistics Flow Diagram

Chapter 10

Cost and Resource Allocation

In this chapter both the cost and technical resources of the Zero EZE are allocated. First the weight and power budgets of the aircraft are defined. These technical resources usually drive the cost of the product and have the tendency to grow during the development. The second step is then to create a cost estimation of the Zero EZE including all information from the weight and power estimation. At last the cost breakdown can be found in Section 10.4 and focuses on post-project activities.

10.1 Weight Breakdown

To come up with a detailed weight breakdown of a product, the weight of every subpart has to be determined. Some of these can be calculated and some of these have to be estimated. In Table 10.1 the weights of every subpart can be seen and if the weight is calculated or estimated.

Table 10.1: All parts and their weight

	Weight [kg]	**Calculated**	**Estimated**
Pilot	80		x
Passenger	80		x
Fuel Tank + Fuel	260.4	x	
Fuel Cell	90	x	
Electrical Motor	40.8	x	
Chute	38	x	
Chairs	50		x
Dashboard/Control	80		x
Luggage	27		x
Fuselage	100	x	
Wing	95	x	
Canard	10		x
Landing Gear	77		x
Internal Structure	40		x
Propeller/Shroud	60	x	

Since the weight of all the parts are know, they can be combined and a weight breakdown can be made. In Figure 10.1 the weight breakdown of the Zero EZE can be seen.

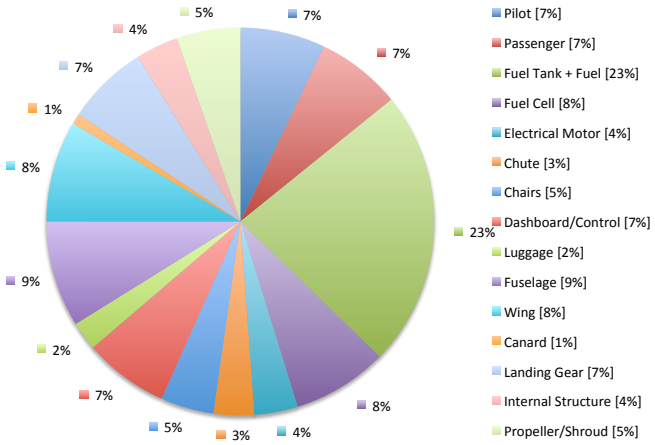

Figure 10.1: Zero EZE Weight Breakdown

It can be seen that the major weight contributor is the fuel tanks with the hydrogen. The hydrogen is stored at a pressure of 700 bars, which is the reason for the size and weight of the tanks. The MTOW of the aircraft can be calculated by adding up all these weights, which results in a MTOW of 1,128 kg. To calculate the ETOW, the weight of the passenger and the luggage should be excluded. This results in an ETOW of 1,021 kg.

10.2 Power Breakdown

The Zero EZE has two power sources, as explained in Section 2.4: the fuel cells and the APU. How these sources are used and how the power is distributed differs during the flight. During take-off, the required power is higher than for the cruise phase. Further, the APU is used to start-up and for quick peak power production. The APU is recharged during cruise.
In Section 3.3 it is explained that the power that is produced in the fuel cell is distributed to the electrical motor, the BOP and flight instruments. From Section 2.4, the power required for the electrical motor is determined to be 110 kW during take-off. The BOP and flight instruments require a power of 17.5 kW and 6 kW respectively. For the cruise phase, the power required by the motor is equal to 71 kW. For the BOP and the flight instruments it is assumed that the required power is equal to the power for take-off. Figure 10.2a and 10.2b show the power breakdown for the take-off and landing phase.

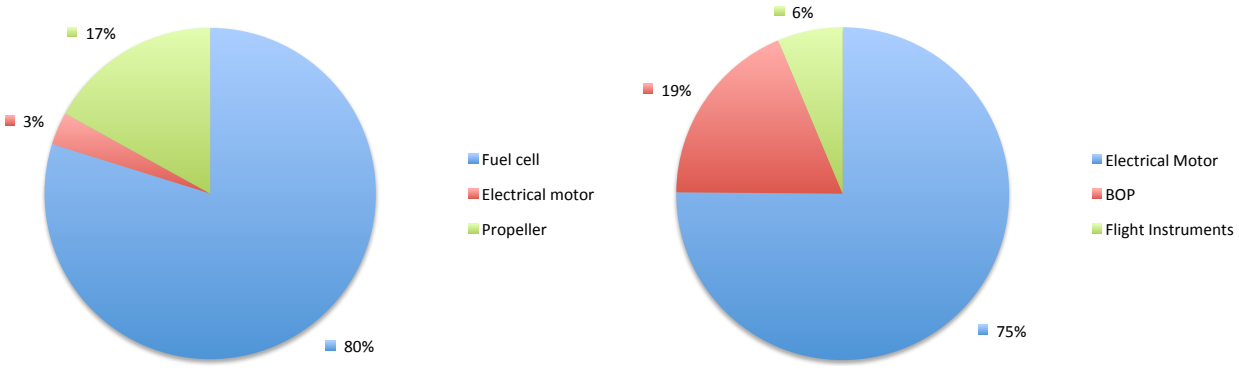

(a) Power Breakdown during take-off

(b) Power Breakdown during cruise

Figure 10.2: Zero EZE Power Breakdown

In ideal conditions, the chemical energy in the reactants would be equal to the power output. Unfortunately there are losses in every propulsion system and this should be taken into account when designing the propulsion system for a desired power output. To make a power breakdown, it should be carefully determined what the total power available is. For the Zero EZE this would be the chemical energy in the reactants that is available.

The reactants flow into the fuel cell, for which the net efficiency was given to be 49% in Section 2.4. The electrical power output of the fuel cell is converted to the electrical motor, which has an efficiency of 94 %. The propeller has an efficiency of 69% during take-off and 88.6% for the cruise phase.

10.3 Cost Estimation

With all the aircraft components determined, a new cost estimation can be made. This will be done based on a method presented by Roskam [114], which is used to determine the final purchase price. Since this method is extensive and involves a lot of calculations, only the results will be stated. For a complete overview of the method used, reference [114] should be consulted.

10.3.1 Cost Estimation Inputs

To properly execute the cost estimation, several aircraft properties have to be determined. Also some component prices should be established, which are presented in Table 10.2. All prices have already been determined in previous chapters, except for the avionics system. Roskam suggests to appoint 5 to 15 % of the budget to the avionics, where the highest border is maintained for the Zero EZE. Therefore approximately 15 % of the budget is reserved.

Component	**Price [€]**
Fuel Cell	31,500
Fuel Tanks	13,500
Electric Motor	22,500
Propeller	2,500
Shroud	4,000
Avionics	15,000

Table 10.2: Component Prices

Next to these cost components, the AMPR weight and maximum cruise speed are needed. The AMPR weight can be found when the empty weight is reduced by the weight of most of the internal components. Based on the weight breakdown in Section 10.1, the AMPR weight is determined to be 850 lbs. From Section 8.3, the maximum cruise speed is taken as 166 knots.

10.3.2 RDTE Cost

The first cost source considered is the research, development, test and evaluation cost. These are the costs for all activities involved with the project planning and conceptual design stage up to certification. The RDTE costs have been divided into seven cost components:

1. Airframe Engineering and Design Cost
2. Development Support and Testing Cost
3. Flight Test Airplanes Cost
4. Flight Test Operations Cost
5. Test and Simulation Facilities cost
6. RDTE Profit
7. Cost to finance the RDTE phases

From these components, it is assumed that no extra test and simulation facilities are needed, so this expenditure will be zero. Also the RDTE profit is assumed to be zero. With engineering cost assumed to be €50 per hour, the total RDTE cost are estimated at 20.5 million euros.

10.3.3 Manufacturing Cost

The major cost contributor to the purchase price is the manufacturing cost, which accounts for the entire production process of the Zero EZE. A distinction is made between engineering and design cost, program production cost, flight test operations cost and finance cost.

First of all, an estimation of the total production has to be made. The Zero EZE is assumed to be produced for 10 years, at a production volume of 100 aircraft per year. With the five test planes also taken into account, a total production volume of 1005 aircraft is reached. However, one should keep in mind that the test planes are not sold but only used for evaluation purposes. Therefore the manufacturing cost can be divided over 1000 aircraft.

Next to the production volume, assumptions have to be made for the interior cost. Normally interior costs of 500 dollars per passenger are reserved for general aviation aircraft, but since the target group of the Zero EZE is business related the interior should be slightly more luxurious. Therefore a budget of 1000 dollars per passenger is assumed.

The final assumption is made for the flight test operations cost. Due to the fact that these cost are almost negligible compared to the production cost, they are not taken into account for this cost estimation.

Just as for the RDTE cost, an hourly rate of €50 per hour is assumed for the manufacturing stage. Adding up all contributors and taking into account the assumptions made, a total manufacturing cost of 411 million euros has been found.

10.3.4 Profit

To determine the final purchase price, not only the expenses made should be considered, but the aircraft manufacturer also wants to make profit out of its product. Therefore a certain profit margin has to be added. For the Zero EZE, this margin has been assumed to consist of 10% of the manufacturing cost, which is well in line with other manufacturers [114].

10.3.5 Purchase Price

Now that all cost contributors have been calculated, the Zero EZE purchase price should be established. Table 10.3 provides an overview of the total costs for the Zero EZE:

RDTE Cost [mln €]	Manufacturing Cost [mln €]	Profit [mln €]	Total Cost [mln €]
20.5	411	41	472.5

Table 10.3: Total Zero EZE Cost

When dividing the total cost by the number of aircraft sold, which equals 1000 pieces, a unit price of €472,500 is found. The cost components of this unit price are visualized in Figure 10.3.

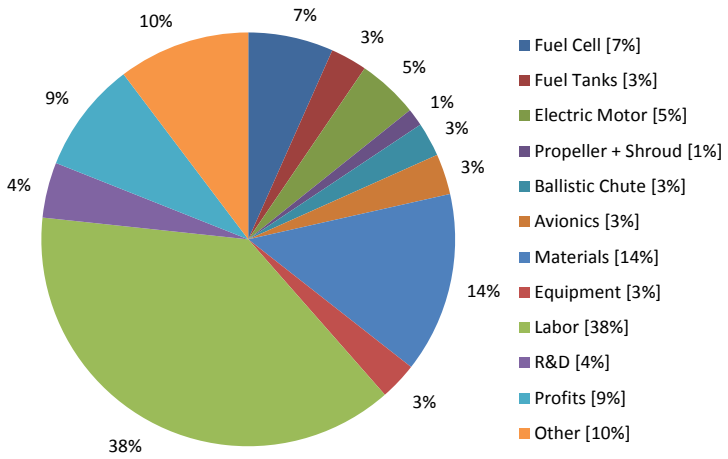

Figure 10.3: Zero EZE Cost Components

10.4 Cost Breakdown

An oftenly used tool to provide an overview of all the costs included is a Cost Breakdown Structure. The CBS divides the costs into different stages of the product development. In this case the post-project phase is taken into account after the preliminary design has been delivered. It is an AND tree and the detailed design, production, operation & maintenance and disposal phases are taken into account. The diagram can be found in Figure 10.4.

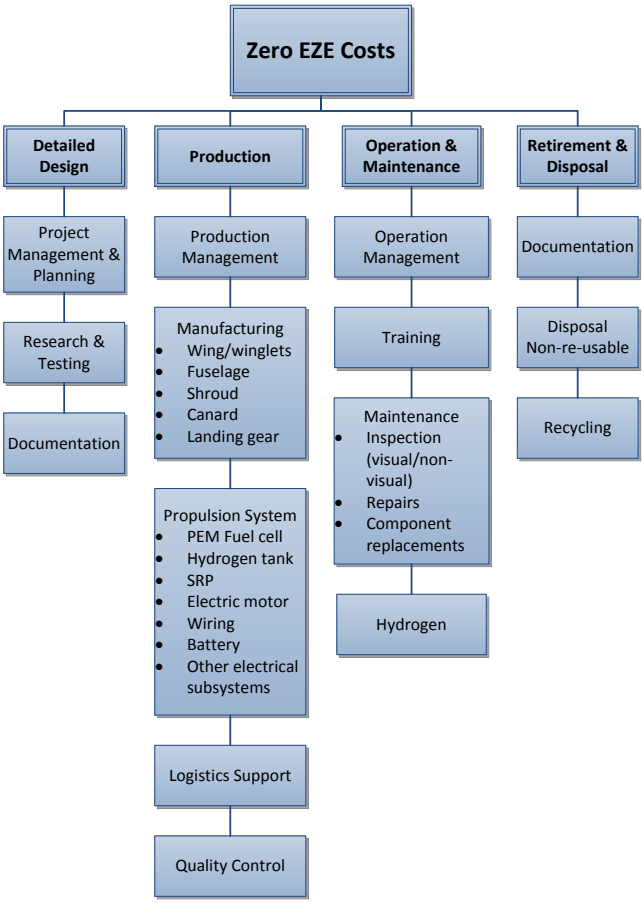

Figure 10.4: Cost Breakdown Structure of the Zero EZE

Chapter 11

Risk Management

A risk is an uncertain event or circumstance that can have an impact on the success of a project. Risk cannot be completely removed, but can be made negligible. Risk management is performed for the Zero EZE to identify, assess and control uncertainty and, as a result, improve the ability of the project to succeed. This chapter focuses on the risks initiated from the change in design compared to the current, zero-emission aircraft. According to the course of System Engineering [116], the risk management can be subdivided into risk identification, risk assessment, risk analysis and handling, which are described in the following sections. Here the risks of the all subsystems are assessed and updated from earlier analyses.

11.1 Risk Identification

During the risk identification phase, the potential adverse outcomes and associated root causes are recognized and prioritized. This section handles the final mission statement and requirements, the risk bearing ones are the fuel cell system, the propeller and the optimization of the structural and aerodynamic layout of the aircraft. The aim of this chapter is to see what risks can already be considered to be negligible, by means of looking at the probability and the influence of an event. These events are elaborated in this section and are divided into seven parts; the electrical motor, the fuel cell, the propeller, the structural and aerodynamically optimization, the material use and the battery, respectively.

The consequences of the risk can also be divided into four categories of severity; negligible, marginal influence, critical influence and bottleneck. Bottleneck means that if the risk is not handled correctly, the project will eventually fail entirely or the main design requirements will not be met. It is expected to have no bottlenecks with a 100% probability any more in this stage of the project. The level below a bottleneck is the large influence one. This states that the success and performance of the project and product will be questionable or will be reduced tremendously when no actions are taken. The consequences, divided into the marginal influence, will have a small reduction in technical performance and do not affect the main requirements. Negligible is the lowest level of severity, this is more an inconvenience than a real consequence and should have no major impact on the further development of the product.

1. **Fuel Cell**
   The chosen PEM fuel cell can be seen as a reliable power source, there are however still risks involved regarding cost ant time to market. Since fuel cells of this size are still under development and very expensive, the risk of having high cost and time to market is very high. Expectations are that the price will drop in the near future and availability will increase, but there is always uncertainty about this. One of the largest bottlenecks of this project is the legislation of the fuel cell. Since fuel cells are not yet used in aircraft, there is still a big uncertainty about whether the system is certifiable to EASA standards or not. When this cannot be done, the project is likely to fail. Weight, power delivery and efficiency have already been determined in large detail and will therefore not cause any major risks.

2. **Electrical motors**
   After finishing the final design, the brushless DC motor still proofs itself as being the best choice considering electrical motors. The probability of having any cost-related design risks, considering

brushless DC motors, can be seen as very low. These would also have marginal influence on the design process. The chance of exceeding the initial estimated price is low for this part. The same counts for the weight of this component. A too low efficiency would have large influence on the design. However, due to the high efficiency rates associated with electrical motors, the chance of this happening is very low.

3. **Propellers**
   The propeller part consist of the single-rotating configuration. Since SRP are considered as widely used it is easy to control the cost of this part. For the propeller, noise is a highly valued requirement. This is likely to exceed expectations and will have a large influence to the overall design. The risk of this happening has been handled sufficiently, not being eliminated but reduced to an acceptable level. To obtain the required performance the propellers propulsive efficiency should be sufficient. The probability of not reaching this required efficiency is rather low, though with consequences that have a high influence on the design.

4. **Structural and Aerodynamic Optimization**
   By optimizing the structure of the aircraft the weight has been lowered, which is done to have the ability of implementing the heavy hydrogen tanks. Critical consequences can follow due to the fact that performance requirements cannot be met. For the structure, manufacturability was taken into account. Suitable manufacturing methods have been chosen, which has lowered the probability that a structure cannot be manufactured. Moreover it would have marginal effects on the design. By optimizing aerodynamics; the airflow is altered resulting in lower noise production and better overall performance of the aircraft. Without this optimization the noise produced by the propellers will exceed allowable limits.

5. **Materials**
   Especially during designing an aircraft it is important to keep in mind that the weight of the total aircraft depends, for a large part, on the used materials. When using better materials the weight can be lowered, however the costs might rise. The probability of this exceeding the estimated budget was expected to be quite high, though the associated consequences are marginal. In the final phase of the project these costs however turned out to be lower than expected, which lowered the probability of exceeding. All chosen materials are well-known and the risk of falling behind schedule are almost eliminated.

6. **Battery**
   In the final design a battery is only used as a secondary source of electricity to power small subsystems in the aircraft. Therefore it will not be considered in the risk map. The probability of failure is reduced by the two ways of recharging the battery (i.e. on the ground and during flight by the fuel cell). Furthermore, the widely used Li-ion battery type is chosen. The fact that a next generation of this type of battery is used increases the risk slightly.

11.1.1 Risk Assessment

The most important project risks have now been identified and can be plotted into a risk map. During this process, the mentioned risks are given a probability value and a consequence value. When both these values are high, the risks involved are high. The risk map for the fuell cell system can be seen in Figure 11.1.

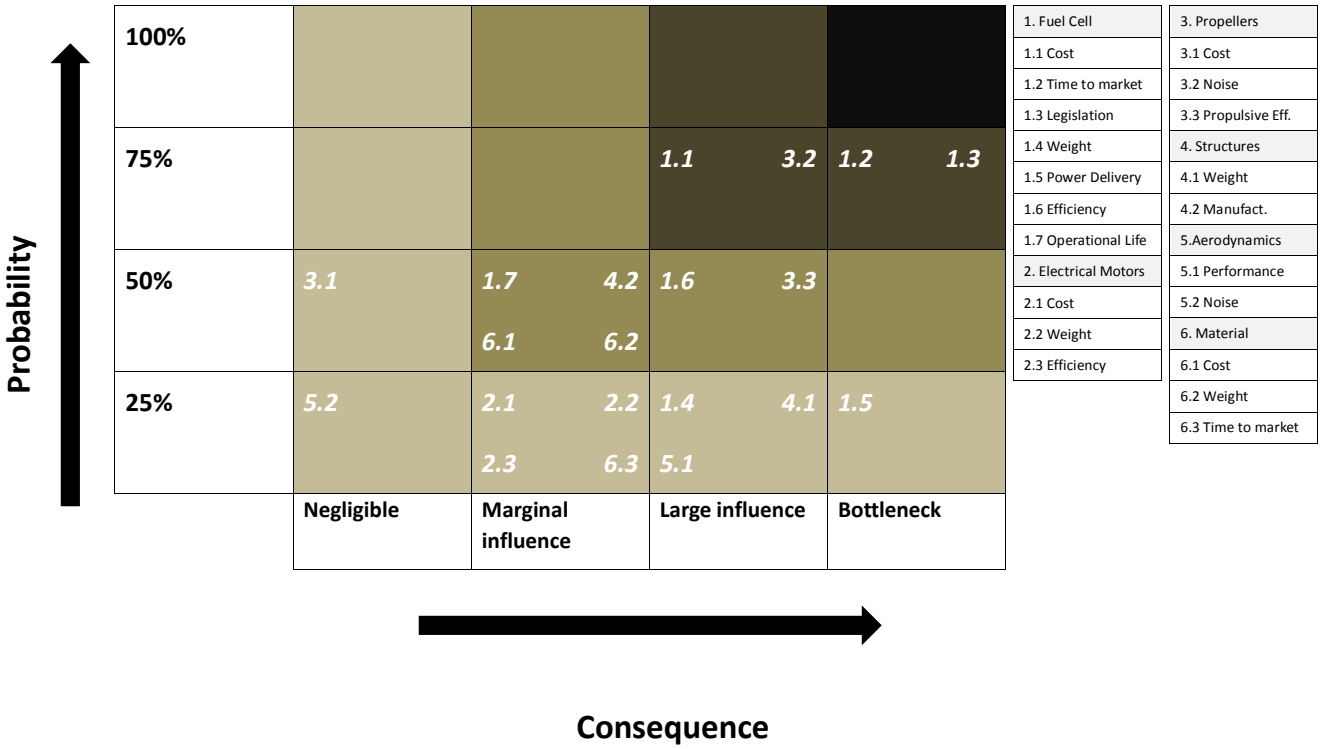

Figure 11.1: Risk Map Zero EZE

11.1.2 Risk Analysis and Handling

In the risk analysis phase, costs and benefits associated with available risk mitigation options are discussed in order to eliminate unacceptable risks. Only the major risks and their corresponding mitigation actions are stated, so that the most probable and severe risks will be coped with. In this way overview is obtained, as well as focus on the most essential risks of this project development. The area of these major risks, as mentioned before, is situated on the right top corner on the risk map. During the conceptual phase, changes have been made to the design as a whole. this has ensured that most risks have moved to the lower left hand corner of the risk map. In the following section, the specific mitigation actions are discussed.

- **Fuel Cell Costs (1.1)**
  The PEM fuel cell is still in development. To reduce the probability of exceeding the cost estimations a safety margin is taken into account in the cost budget. The modular structure of the fuel cell implies that it is suitable for mass production and the cost could be greatly reduced if mass production would be applied.

- **Fuel Cell Time to Market (1.2)**
  The time to market of fuel cells has a crucial role in the success of this project, since the fuel cell is currently in development. If the expected technology improvements can not be realized, fuel cells will fail to be a valid design option. However in the final phase of the project market research is performed to investigate the current stage of fuel cell development. Based on this research it is expected that the required fuel cell can be delivered, but no guarantee can be given.

- **Fuel Cell Legislation (1.3)**
  For the legislation of the fuel cell, the same risks apply as for the time to market aspect. The technology still has not been tested over a significant time span. But for legislation the risk focuses more on the costs. It is placed in the 'bottleneck' column since it can only be reduced and not mitigated.

- **Propeller Noise (3.2)**
  One of the major requirements for this project is to design a propulsion system that produces a DNL of less than 65 dB for all areas outside of an airport. By implementing SRP, the probability that the

aircraft will produce more noise than the 65 dB limit has been lowered already. Furthermore, the shroud and fuselage integration have been designed in a way to lower noise production. The noise production is expected to be within the limits set but in case of exceeding it will not fail the Zero EZE project. Costs will increase and the reputation will become worse. All effort should be put in to avoid these consequences.

11.2 Conclusions

Uncertainty is always present, risk management should therefore perform a major role in each project. It prevents heading a dead end and ensures a more efficient way of working. The consequence and probability can only be coped with or minimized if all risks are properly identified, assessed, analyzed and handled. This all should be seen as a continuous process and should be done over several phases of the project. For this report the management is performed based on the final design. The major risks can be found in the risk map and are summarized here, together with the risk handling.

- Fuel cell costs
  If the fuel cells appears to be more expensive than the determined budget, this is mitigated by a safety margin.

- Propeller noise
  Propeller noise is a critical factor for the design of this aircraft. To minimize the risk of exceeding the allowable requirements a SRP system is chosen. Also a shroud is implemented around the propeller, which reduces the noise even more.

- Structural weight
  The structural weight is of high importance for the design but its risk has been reduced significantly during the final design. A solution to this risk can be found in the use of different materials.

- Legislation
  Legislation can become a major drawback, every part has to be certified before it can be used in GA. Using new technologies might lead to legal problems, which can be catastrophic for the outcome of the project. Again using conventional aeronautical materials and technologies, the risk can be made negligible.

These are the major risks concerning the development of the Zero EZE. Other risks need to be considered, but these deserve the most attention, since they have the largest influence on the overall outcome of this project.

Chapter 12

Project Development

In this chapter two important tools for the further development of the project are presented. First of all the Gantt chart is given for the current project phase, which is an update of the Gantt charts provided in earlier phases of the project. After that the Project Design and Development Logic this describes how the development of the Zero EZE has to continue once the preliminary design is finished. A Gantt chart of the post-project phase is presented at last in this chapter. The post-project phase includes the detailed design, production, operations and disposal phase. Without an appropriate post-project planning the Zero EZE cannot be further developed so it should not be underestimated.

12.0.1 Gantt Chart

The Gantt Chart of Figure 12.1 provides an overview of all the tasks, including these features.In the left table each task is displayed together with the people assigned to that specific task, as well as an estimation of the amount of work needed to finish the task. A schematic display of this schedule can be seen at the right. In this way the tasks that can be executed parallel can be identified quickly, as well as the predecessors for upcoming tasks.

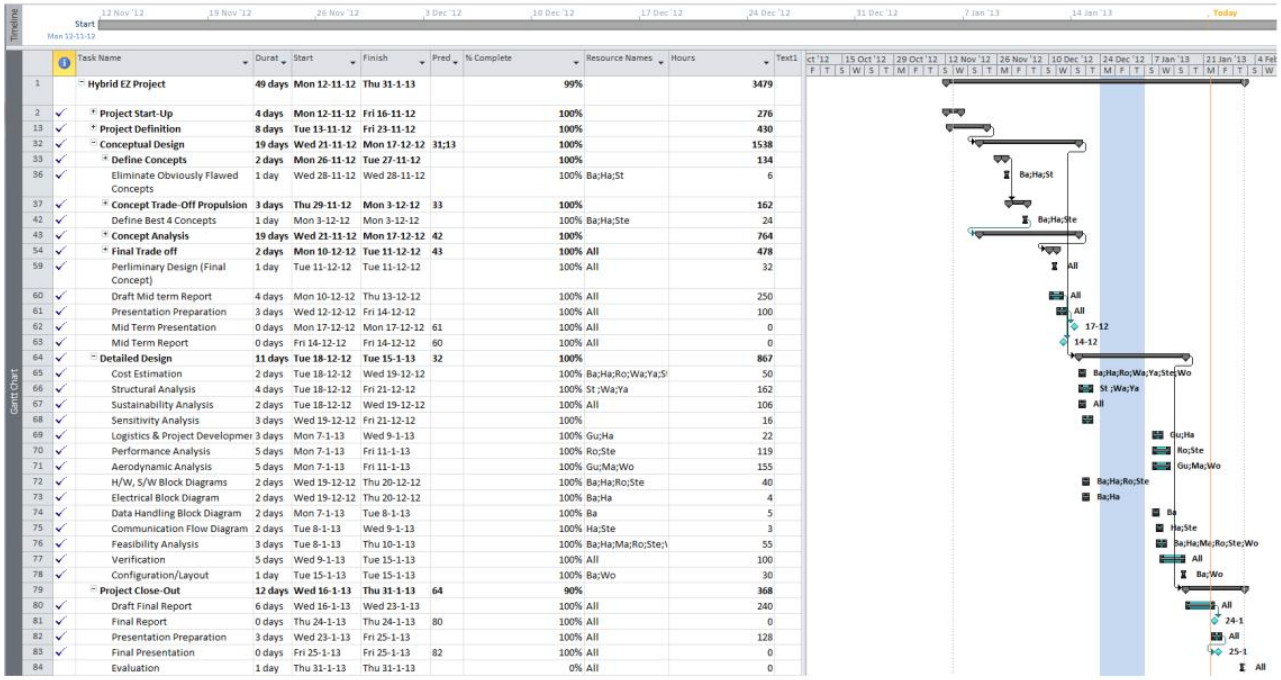

	Task Name	Durat	Start	Finish	Pred	% Complete	Resource Names	Hours
1	**Hybrid EZ Project**	**49 days**	**Mon 12-11-12**	**Thu 31-1-13**		**99%**		**3479**
2	**Project Start-Up**	**4 days**	**Mon 12-11-12**	**Fri 16-11-12**		**100%**		**276**
13	**Project Definition**	**8 days**	**Tue 13-11-12**	**Fri 23-11-12**		**100%**		**430**
32	**Conceptual Design**	**19 days**	**Wed 21-11-12**	**Mon 17-12-12**	**31;13**	**100%**		**1538**
33	**Define Concepts**	**2 days**	**Mon 26-11-12**	**Tue 27-11-12**		**100%**		**134**
36	Eliminate Obviously Flawed Concepts	1 day	Wed 28-11-12	Wed 28-11-12		100%	Ba;Ha;St	6
37	**Concept Trade-Off Propulsion**	**3 days**	**Thu 29-11-12**	**Mon 3-12-12**	**33**	**100%**		**162**
42	Define Best 4 Concepts	1 day	Mon 3-12-12	Mon 3-12-12		100%	Ba;Ha;Ste	24
43	**Concept Analysis**	**19 days**	**Wed 21-11-12**	**Mon 17-12-12**	**42**	**100%**		**764**
54	**Final Trade off**	**2 days**	**Mon 10-12-12**	**Tue 11-12-12**	**43**	**100%**	**All**	**478**
59	Perliminary Design (Final Concept)	1 day	Tue 11-12-12	Tue 11-12-12		100%	All	32
60	Draft Mid term Report	4 days	Mon 10-12-12	Thu 13-12-12		100%	All	250
61	Presentation Preparation	3 days	Wed 12-12-12	Fri 14-12-12		100%	All	100
62	Mid Term Presentation	0 days	Mon 17-12-12	Mon 17-12-12	61	100%	All	0
63	Mid Term Report	0 days	Fri 14-12-12	Fri 14-12-12	60	100%	All	0
64	**Detailed Design**	**11 days**	**Tue 18-12-12**	**Tue 15-1-13**	**32**	**100%**		**867**
65	Cost Estimation	2 days	Tue 18-12-12	Wed 19-12-12		100%	Ba;Ha;Ro;Wa;Ya;S	50
66	Structural Analysis	4 days	Tue 18-12-12	Fri 21-12-12		100%	St ;Wa;Ya	162
67	Sustainability Analysis	2 days	Tue 18-12-12	Wed 19-12-12		100%	All	106
68	Sensitivity Analysis	3 days	Wed 19-12-12	Fri 21-12-12		100%		16
69	Logistics & Project Developmer	3 days	Mon 7-1-13	Wed 9-1-13		100%	Gu;Ha	22
70	Performance Analysis	5 days	Mon 7-1-13	Fri 11-1-13		100%	Ro;Ste	119
71	Aerodynamic Analysis	5 days	Mon 7-1-13	Fri 11-1-13		100%	Gu;Ma;Wo	155
72	H/W, S/W Block Diagrams	2 days	Wed 19-12-12	Thu 20-12-12		100%	Ba;Ha;Ro;Ste	40
73	Electrical Block Diagram	2 days	Wed 19-12-12	Thu 20-12-12		100%	Ba;Ha	4
74	Data Handling Block Diagram	2 days	Mon 7-1-13	Tue 8-1-13		100%	Ba	5
75	Communication Flow Diagram	2 days	Tue 8-1-13	Wed 9-1-13		100%	Ha;Ste	3
76	Feasibility Analysis	3 days	Tue 8-1-13	Thu 10-1-13		100%	Ba;Ha;Ma;Ro;Ste;\	55
77	Verification	5 days	Wed 9-1-13	Tue 15-1-13		100%	All	100
78	Configuration/Layout	1 day	Tue 15-1-13	Tue 15-1-13		100%	Ba;Wo	30
79	**Project Close-Out**	**12 days**	**Wed 16-1-13**	**Thu 31-1-13**	**64**	**90%**		**368**
80	Draft Final Report	6 days	Wed 16-1-13	Wed 23-1-13		100%	All	240
81	Final Report	0 days	Thu 24-1-13	Thu 24-1-13	80	100%	All	0
82	Presentation Preparation	3 days	Wed 23-1-13	Fri 25-1-13		100%	All	128
83	Final Presentation	0 days	Fri 25-1-13	Fri 25-1-13	82	100%	All	0
84	Evaluation	1 day	Thu 31-1-13	Thu 31-1-13		0%	All	0

Figure 12.1: Project Gantt Chart

12.1 Project Design & Development Logic

In this section a logical order of activities is described which have to be executed in the post-project phase. To visualize this a Project Design & Development logic diagram is provided in Figure 12.2. The square blocks contain activities which have to be performed in between the four post-project phases. The latter is displayed in the hexagons and include the detailed design, production, operation & maintenance and disposal & retirement phases. Most operations are performed parallel. The diagram is in coherence with the CBS of Section 10.4.

12.2 Post-Project Gantt Chart

The currently designed Zero EZE has been optimized within the given timeframe for this DSE project. To continue designing the Zero EZE, more investigations and calculations need to be performed though. These post DSE topics are given in the following Gantt chart.

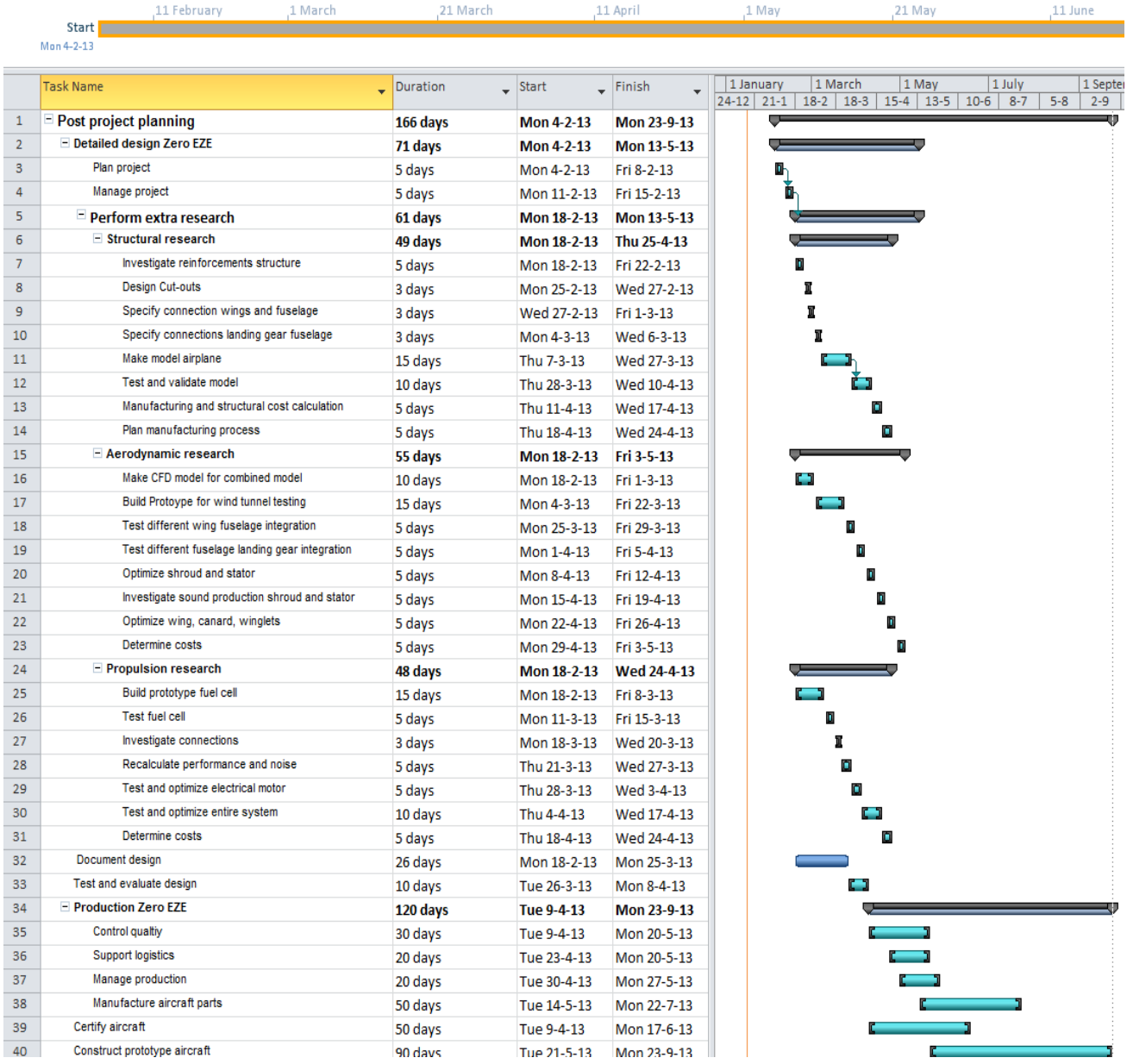

	Task Name	Duration	Start	Finish
1	**Post project planning**	**166 days**	**Mon 4-2-13**	**Mon 23-9-13**
2	**Detailed design Zero EZE**	**71 days**	**Mon 4-2-13**	**Mon 13-5-13**
3	Plan project	5 days	Mon 4-2-13	Fri 8-2-13
4	Manage project	5 days	Mon 11-2-13	Fri 15-2-13
5	**Perform extra research**	**61 days**	**Mon 18-2-13**	**Mon 13-5-13**
6	**Structural research**	**49 days**	**Mon 18-2-13**	**Thu 25-4-13**
7	Investigate reinforcements structure	5 days	Mon 18-2-13	Fri 22-2-13
8	Design Cut-outs	3 days	Mon 25-2-13	Wed 27-2-13
9	Specify connection wings and fuselage	3 days	Wed 27-2-13	Fri 1-3-13
10	Specify connections landing gear fuselage	3 days	Mon 4-3-13	Wed 6-3-13
11	Make model airplane	15 days	Thu 7-3-13	Wed 27-3-13
12	Test and validate model	10 days	Thu 28-3-13	Wed 10-4-13
13	Manufacturing and structural cost calculation	5 days	Thu 11-4-13	Wed 17-4-13
14	Plan manufacturing process	5 days	Thu 18-4-13	Wed 24-4-13
15	**Aerodynamic research**	**55 days**	**Mon 18-2-13**	**Fri 3-5-13**
16	Make CFD model for combined model	10 days	Mon 18-2-13	Fri 1-3-13
17	Build Protoype for wind tunnel testing	15 days	Mon 4-3-13	Fri 22-3-13
18	Test different wing fuselage integration	5 days	Mon 25-3-13	Fri 29-3-13
19	Test different fuselage landing gear integration	5 days	Mon 1-4-13	Fri 5-4-13
20	Optimize shroud and stator	5 days	Mon 8-4-13	Fri 12-4-13
21	Investigate sound production shroud and stator	5 days	Mon 15-4-13	Fri 19-4-13
22	Optimize wing, canard, winglets	5 days	Mon 22-4-13	Fri 26-4-13
23	Determine costs	5 days	Mon 29-4-13	Fri 3-5-13
24	**Propulsion research**	**48 days**	**Mon 18-2-13**	**Wed 24-4-13**
25	Build prototype fuel cell	15 days	Mon 18-2-13	Fri 8-3-13
26	Test fuel cell	5 days	Mon 11-3-13	Fri 15-3-13
27	Investigate connections	3 days	Mon 18-3-13	Wed 20-3-13
28	Recalculate performance and noise	5 days	Thu 21-3-13	Wed 27-3-13
29	Test and optimize electrical motor	5 days	Thu 28-3-13	Wed 3-4-13
30	Test and optimize entire system	10 days	Thu 4-4-13	Wed 17-4-13
31	Determine costs	5 days	Thu 18-4-13	Wed 24-4-13
32	Document design	26 days	Mon 18-2-13	Mon 25-3-13
33	Test and evaluate design	10 days	Tue 26-3-13	Mon 8-4-13
34	**Production Zero EZE**	**120 days**	**Tue 9-4-13**	**Mon 23-9-13**
35	Control qualtiy	30 days	Tue 9-4-13	Mon 20-5-13
36	Support logistics	20 days	Tue 23-4-13	Mon 20-5-13
37	Manage production	20 days	Tue 30-4-13	Mon 27-5-13
38	Manufacture aircraft parts	50 days	Tue 14-5-13	Mon 22-7-13
39	Certify aircraft	50 days	Tue 9-4-13	Mon 17-6-13
40	Construct prototype aircraft	90 days	Tue 21-5-13	Mon 23-9-13

Figure 12.3: Post DSE Gantt chart

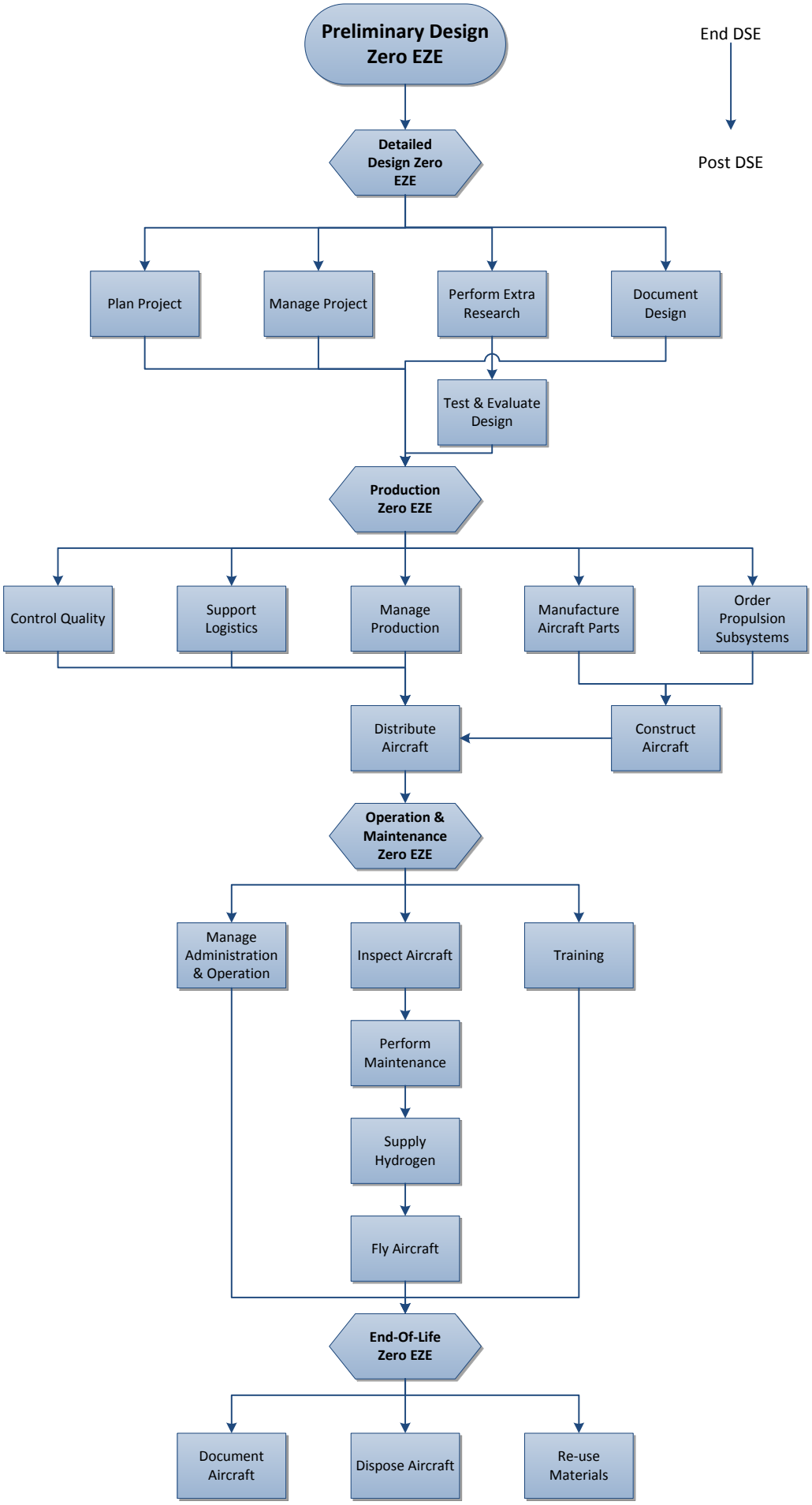

Figure 12.2: Project Design and Development logic of the Zero EZE

Chapter 13

Functional Mission Description

In this chapter a description is given of the different functions that the Zero EZE has to perform for the given mission. Some functions will be similar to most aircraft while other functions, as the fuel cell system, differ significantly. It is of grave importance to have a good overview of all the functions to guarantee that the aircraft satisfies all needs. Two different diagrams are presented in Sections 13.1 and 13.2 which are updated from an earlier stage of the project.

13.1 Functional Flow Diagram

In the Functional Flow Diagram all the functions that the entire system of the Zero EZE has to perform are logically ordered. The active functions are described in blocks, which are connected by arrows. The needs of the customer should be satisfied by the combination of these functions.

The structure of the FFD is hierarchical. This means that the diagram is divided into system functions, subsystem functions and so on. The FFD presented in Figure F.2 in Appendix F, is composed out of four levels. It is an update of the FFD provided in the baseline report of the project. The main aspect which is updated is generating power from the fuel cell instead of the range extender. The mission of the aircraft did not change, which implies that most functions remain equal.

13.2 Functional Breakdown Structure

The functions of the Zero EZE system can also be presented in a Functional Breakdown Structure. It is a structure which uses exclusively AND trees. Furthermore, subtasks can be added. The presentation of the FBS is on a high level and only functions of essential subtasks are included. The FBS can be found in Figure F.1 in Appendix F. The structure is first divided in the three main functions: provide power, perform flight and guidance & navigation. Only in the first main function of power provision the structure will be updated. This means that the electrical power is only provided by the fuel cell and a battery instead of the range extender and batteries.

Chapter 14

Sensitivity Analysis

The sensitivity analysis shows the impact of several changes on the current design. To perform an accurate analysis, first the main system parameters of the design have to be determined. Note that there are numerous parameters that have an influence on the design, here the most important ones are discussed. By changing these parameters, some subsystems and components of the Zero EZE will be influenced accordingly. The main parameters are as the Weight, the Lift, the Drag, the Performance requirements and the efficiency, η.

The impact of the potential changes, with respect to these main parameters, have to be monitored. This is required to discover the limits and boundaries of the current design. The analysis is performed for the main output; being the aerodynamic components, structural part, propulsion system, cost and sustainability of the system. The level of influence, for each output, can be seen in Figure 14.1. Here the part 'aerodynamic shape' includes the design of the main wing as well as the fuselage and canard.

	Aerodynamic Shape	Structures	Propulsion System	Cost	Sustainability
Weight	++	+/-	++	+/-	0
Lift	++	+/-	++	0	0
Drag	++	+	++	+/-	0
Performance	++	+	++	+/-	0
η	0	0	++	+	0

Figure 14.1: Sensitivity Analysis

With ++ indicating a high relation, + shows a normal relation, +/- indicates a small to negligible relation and 0 indicates zero relations between the paramaters. For each output component, a short explanation is presented.

- Weight

  Changing the weight would have a large impact on the design of the propulsion system. When the weight changes the needed power changes directly with it, this because the thrust and excess power alters directly with respect to the weight. The increase in power will require an improvement in the propulsion system, regarding take-off requirements. A higher outcome will be required, resulting in a higher fuel consumption and again an increase in weight.

  Due to the higher weight a higher lift output is required, this requires an increase in the size of the wings. These parameters are highly related.

  Higher structural stresses will be present, however these are seen as minimal and a structural redesign will only be necessary if the weight changes dramatically.

The cost and sustainability have no direct relation with a change in weight. Due to the change in needed power, more or less fuel is needed, this increases or reduces the operational cost and sustainability aspect. Taken into account that the Zero EZE only consumes hydrogen, also this aspect is seen as marginal. However a change in the required power, or a change in the power system can also indicate an increase or decrease in the purchase price of the electric motor and fuel cell. The attempt should be, as always, to keep the weight as low as possible. Increasing the weight is possible however highly unfavorable for the design.

- Lift

  Enhancing the lift characteristics of the aircraft has a beneficial relation with respect to the propulsion system. The required thrust is defined as the weight divided by the the lift to drag ratio. Improving the characteristics of the airfoil has also an impact on the size of the wing, this in direct relation. The increase in lift has a small influence on the structural part, in extreme cases reinforcements should be taken into acount. This parameter has no influence on the cost or sustainability aspect of the aircraft.

- Drag

  An increase in drag by changing the fuselage, wings or other components will require a higher thrust or power outcome. This results in a similar situation as the weight increase. More lift will have to be generated to compensate this loss. Due the higher power requirement, the purchase price of the fuel cell or electric motor can be higher. Operation costs are again seen as marginal considering the fact of the small amount of used hydrogen.

- Performance Requirements

  It can be seen as obvious that higher power requirements, such as a higher climb of rate, range or cruise speed will result in a required increase in the outcome of the propulsion system. This can also be compensated by an improved fuselage or wing geometry. The same is applicable for the cost requirements, this is only when the power system has to be scaled.

- η_{system}

  The efficiency of the system, meaning the efficiency of the propeller, electric motor and fuel cell have a direct relation to the propulsion system, this can be seen as obvious. A change in efficiency would result in changes of the propulsion system directly affecting the costs of it.

From Table 14.1 it is seen that the design is relatively dependent on the main system parameters, if this would change the design would have to be updated. In most cases however only one specific subsystem has to be resized; no real redesign has to be performed.

The Zero EZE is designed in such a way that a high level of adaptability is achieved. To realize this, two important aspects were taken into consideration, being scalability and flexibility. The scalability represents the capability of the design to scale up or down with respect to a change in the system parameters. The flexibility of the design indicates the ease of changing some parameters without having to perform a huge redesign or rescaling, this to have the ability to change one parameter instead of altering

For the propulsion system it means that the fuel cell and electric motor are linearly scalable to the demands of the buyer, this mainly with respect to the performance requirements. A change in amount of fuel should not cause real difficulties. In the case of the zero EZE, only the extra weight of the enlarged fuel tanks have to be taken into account if higher power requirements are set. Also, for cruise speed and rate of climb, a safety margin is included. This means that the current design should be able to reach higher output than the requirements depicted.

The scalability and flexibility is also found in the structural design. Here the choice was made to use a grid stiffened structure, ensuring scaling capability. The flexibility of the structures is analyzed by the limit loads given through regulations.

Also the aerodynamic shape can be scaled up or down, only the propeller system should be redesigned when the main system parameters are altered, which can be easily using currently available programs such as JavaProp.

Chapter 15

Conclusion

This project focuses on innovating general aviation by designing a small, two person airplane capable of travelling a maximum distance of 1300 km and reaching a maximum cruise velocity of 200 knots. Meanwhile no emissions are produced. This final report has dealt with the detailed design of the Zero EZE, an innovative airplane based on Burt Rutan's Long EZ, a commonly used means of transportation, considering GA.

Market analysis shows that a trend can be observed where GA suffers from a declining reputation and economic situation. The design of the Zero EZE can be seen as a contribution towards a sustainable future for general aviation. By configuring a hydrogen fuel cell system, accompanied by optimized fuel tanks, the foundation for the next step towards sustainable flight has been laid.

An electrical motor has been designed to convert the energy provided by this fuel cell system to mechanical motion needed to power the propeller. This propeller has been configured for having optimal efficiency at cruise conditions and has been situated inside a shroud, to increase its performance even further. The total efficiency for the system is 39%, which can be considered quite high compared to typical efficiencies ranging from 21 to 34% for piston engine configurations. Due to the parallel placement of two fuel cells, the reliability is slightly higher as well.

To implement the fuel cell system major adjustments to the fuselage have been made. Due to the size of the fuel tanks, the new length of the Zero EZE becomes 5.5 meters and by setting a new standard for pilot and passenger comfort, the maximum diameter has been changed to 1.4 meters. Increasing the fuselage obviously contributes to the drag and the performance. To cope with this hindrance, a low drag body has been designed, which is also able to store the retractable landing gear. The fuselage is designed according to advanced grid stiffened structure methods, is made from CFRP and can take loads up to 6 g.

By reconfiguring the wings and canard, additional lift is gained while drag is reduced and the necessary performance and weight criteria are met. Control surfaces are designed to ensure the stability of the airplane. The wings and canard are constructed using a lightweight sandwich structure, composed of CFRP and polystyrene. With this lay-out, the wings can take loads up to 4.2 g.

It is indeed possible to design a sustainable aircraft, capable of flying 1300 km and reaching a maximum cruise speed of 200 knots, producing zero emission and complying with safety standards. With current hydrogen prices, refilling the tanks will cost only €45, but since prices are dropping rapidly, it can be safely assumed that in 2020 this will cost approximately €11. If ten students can initiate such an innovative design within only ten weeks time, imagine the possibilities if time is on your side.

Recommendations

> ""Learning is a never-ending process. It has no boundaries. Follow your heart and pursue learning & updating on all that you are interested in." - CV Varghese (2008)

In the scope of a 10-weeks project there is never enough time to design every aspect to perfection. Before the production of the Zero EZE could start, the design requires more research and testing. Therefore the group has certain recommendations for further development of the Zero EZE project. These will be discussed in the following content, based on the different technical aspects.

Aerodynamics

The first part of the design which will be discussed is the aerodynamical design. For the entire design it is recommended to perform 3D CFD analyses and wind tunnel tests to get more accurate results. For the specific parts the following is recommended:

- Perform research on a 'propulsed fuselage' which gives a smoother integration between the fuselage and shroud
- Design a custom-made airfoil for the main wing which provides an increase in the generation of lift
- Perform wind tunnel tests on the lift and stall performance of the aircraft
- Investigate the flight control system (e.g. fly-by-wire) and the sizing of the trim tabs
- Perform extra research on canard airfoils such that a drag reduction is also obtained for this airfoil
- Vary the lifting surface ratio between the canard and main wing. Possible advantage could be a more aft placement of the main wing which would reduce the sweep angle
- Place the vertical tails with rudder on shroud. Possible advantage could be that the size of winglet will be reduced and be more efficient
- Find more information about the possibility to implement more complex HLD
- Change the winglets to a tilted winglet design. Not much research has been performed on this but it could make the winglet more efficient
- Research can be done on finding the optimal cruise altitude for the range of the aircraft, to increase the total efficiency of the flight

Propulsion

Secondly the propulsion part of the Zero EZE design will be discussed. The subsystems in this part have been analyzed thoroughly but improvements are still possible. The following recommendations are given:

- Investigate methods to use waste heat of the fuel cell (e.g. for cabin heating)
- Test if operating conditions (i.e. temperature, pressure, etc.) can be improved for the fuel cell
- Perform more research on the ideal combination of active area size and number of fuel cells

- Try to incorporate hydrogen tanks into the structure of the fuselage to reduce weight and combine functions
- Vary amount of blades and calculate the interference between blades. Thrust and noise benefits could be obtained
- Perform research on a variable pitch configuration of the propeller
- Due to time constraints the efficiency of entire propeller configuration with stator and shroud has been assumed. A more accurate calculation should be performed for further development
- Perform a more accurate noise analysis for far field conditions

It has to be noted that for all recommendations given here the group is not sure it will provide benefits but it is expected to improve the design.

Structures

The last main part of this project is the structural design of the Zero EZE. To perform a thorough structural analysis is a time-consuming job and therefore also recommendations for this part are given.

- The topology design of the fuselage structure can be designed more efficiently by reinforcing the bottom and make the top lighter
- Perform extra research on the wing-fuselage integration which could not be done due to time constraints
- Before production local reinforcements should be placed due to cut-outs
- When more time is available the FEM analyses can be performed with a finer mesh to obtain more accurate results
- For the fuselage structure other grid types can be analyzed to see if benefits can be obtained

These are all the recommendations to further develop the Zero EZE. It was a pleasure to start with this project but there is always room for improvement and we can only hope that our work will be continued.

Bibliography

[1] Anonymous, 2012. *Worldaerodata* [online] Available at: <http://worldaerodata.com/> [Accessed 16 November 2012]

[2] Baron A. et al., 2007. *EPATS Report on European Business & Personal Aviation Database and Findings* [pdf] Available at: <http://www.epats.eu/Publications/delivearbles.htm> [Accessed at 16 November 2012]

[3] Laplace A., Chertier C., Baron A., Maczka M., 2008. *EPATS Potential transfer of passenger demand to personal aviation by 2020.* [pdf] Available at: <http://www.epats.eu/Publications/delivearbles.htm> [Accessed at 16 November 2012]

[4] Schaik F.J. van, Hogenhuis R.H., Wever R., 2008. *EPATS Airports General Requirements including Safety and Environmental Issues.* [pdf] Available at: <http://www.epats.eu/Publications/delivearbles.htm> [Accessed at 16 November 2012]

[5] Busby R., 2005. *Hydrogen and Fuel Cells, a comprehensive guide* 1st ed. Pennwell, p. 99,216-217

[6] NYSERDA Energy Innovation Solutions *Average Kerosene Prices* Available at: <http://www.nyserda.ny.gov/en/Energy-Prices-Supplies-and-Weather-Data/Kerosene/Average-Kerosene-Prices.aspx> [Accessed at 12 December 2012]

[7] National Renewable Energy Laboratory *Hydrogen Refueling Infrastructure Cost Analysis* Available at: <http://www.hydrogen.energy.gov/pdfs/review12/an020_melaina_2012_o.pdf> [Accessed at 13 December 2012]

[8] NASA, 2011. *NASA satellite* [online] Available at: <http://www.nasa.gov/vision/earth/improvingflight/sats_2005_demo.html/> [Accessed at 16 November 2012]

[9] Diamond Aircraft Industries, 2012. *Diamond Aircraft Data* [online] Available at: <http://www.diamond-air.at/> [Accessed at 19 November 2012]

[10] Anonymous. *Airliners.net Aircraft Data* [online] Available at: <http://www.airliners.net/> [Accessed at 19 November 2012]

[11] Anonymous, 2012. *Directlease Car Data* [online] Available at: <http://www.directlease.nl/> [Accessed at 19 November 2012]

[12] Maarten Keswiel, 2011. *Leaseauto als grindtegel* [online] Available at: <http://www.nuzakelijk.nl/special-zakelijk-rijden/2436696/leaseauto-als-grindtegel.html/> [Accessed at 19 November 2012]

[13] Williams, A., Weiss, W., 2002. Demand for a Future Air Transportation System, CSSI, Inc., December 2002

[14] U.S. Environmental Protection Agency, http://www.epa.gov/cleanenergy/index.html. [Accessed at 21 January 2013]

[15] Barr Group Aerospace, 2012. *Barr Group Aerospace Data* [online] Available at: <http://www.bga-aeroweb.com/> [Accessed at 20 November 2012]

[16] Petit, D.,Turnbull, A 2001.*General Aviation Aircraft Reliability Study.*[pdf] Virginia: FDC,NYMA, Inc. Available through: NASA <http://archive.org/details/nasa_techdoc_20010027423>[Accessed 11 January 2013].

[17] Unknown. 2009.*PowerPhase 220.*[pdf] Longmont: UQM Technologies Inc. Available through <http://uqm.com/powerphase%20hd%20select%20200.html>[Accessed 14 January 2013].

[18] Electricity in the air *Electricity in the air* [online] Available at: <http://www.siemens.com/innovation/apps/pof_microsite/_pof-fall-2011/_html_en/aviation.html> [Accessed at 13 January 2013]

[19] A, Densu. 2010 .*DA-II Electric-Powered Sport Aircraft Utilizing Fuel Cell and Liquid Hydrogen Technologies "Master's Thesis"*[pdf]. University of Tennessee, Available at: <http://trace.tennessee.edu/cgi/viewcontent.cgi?article=1642&context=utk_gradthes>

[20] Abrego, A.I., Bulaga, R.W.2002.*Performance Study of a Ducted Fan System.*[pdf] San Francisco: American Helicopter Society International, Inc. Available through: NASA <http://rotorcraft.arc.nasa.gov/publications/files/abrego2_ahs02.pdf>[Accessed 30 December 2012].

[21] Franken, P.A., Kerwin, E.M.1958.*Methods of flight noise prediction.*[pdf] Ohio: Wright air development center air research and development command US air force Available through: <http://contrails.iit.edu/DigitalCollection/1958/WADCTR58-343.pdf> [Accessed 09 January 2013].

[22] Roskam, J., Lan, E. 1997. *Airplane Aerodynamics and Performance*. Kansas: DARcorporation.

[23] Ruijgrok, J.J., 2009. *Elements of airplane performance*. Faculty of Aerospace engineering: Delft University of Technology.

[24] Anderson, J.D., 2008. *Introduction to Flight*. Mc Graw Hill: New York.

[25] Jinfeng W. 2008. *A review of PEM fuel cell durability: Degradation mechanisms and mitigation strategies* [online] Available at: <http://xa.yimg.com/kq/groups/3004572/636040941/name/A%20review%20of%20PEM%20fuel%20cell%20durability.pdf> [Accessed at: 15 Januari 2013]

[26] Vargas J.V.C. 2005. *International Journal of Heat and Mass Transfer* [online] Available at: <http://www.sciencedirect.com/science/article/pii/S0017931005003558> [Accessed at: 15 Januari 2013]

[27] Tsuchiya H. 2002. *Fuel Cell Cost Study by Learning Curve* [online]. Available at: <http://webarchive.iiasa.ac.at/Research/ECS/IEW2002/docs/Paper_Tsuchiya.pdf>. [Accessed at: 15 Januari 2013]

[28] Eaves S. 2004. *A cost comparison of fuel-cell and battery electric vehicles* [online]. Available at: <http://www.sciencedirect.com/science/article/pii/S0378775303012175> [Accessed at: 15 Januari 2013]

[29] Larminie J. 2003. *Fuel Cell Systems Explained* [book]. Available at: <http://cs5450.userapi.com/u11728334/docs/765b149a3617/4857X_08.pdf> [Accessed at: 8 Januari 2013]

[30] Anonymous *Fuelcelletc.* [online]. Available at: <http://fuelcellsetc.com/>. [Accessed at: 8 Januari 2013]

[31] Zuhang G. 2012.*A critical review of cooling techniques in proton exchange membrane fuel cell stacks* [article]. Available at: <http://www.rit.edu/kgcoe/mechanical/taleme/Papers/Journal%20Papers/J104.pdf> [Accessed at: 8 Januari 2013]

[32] Ballard 2006. *Liquid-cooled PEM Fuel Cell Systems Design Guide*[pdf]. Available at: <www.ballard.com>. [Accessed at: 7 Januari 2013]

[33] Sensenich *3 Blade Rotax Ground adjustable propeller*. Available at: <http://www.sensenich.com/products/item/103>. [Accessed at: 16 Januari 2013]

[34] Matsunaga M. 2009. *Powertrain System of Honda FCX Clarity Fuel Cell Vehicle* [pdf] Available at: <www.honda.com>. [Accessed at: 7 Januari 2013]

[35] Greenhub. *00 5KW .5KW – 44 2KW HYDROGEN FUEL CELL .2KW HYDROGEN FUEL CELL POWER SUPPLY FOR UPS AND OFF-GRID USE* [online]. Available at: <http://www.horizonfuelcell.com/file/Greenhub_installations.pdf> [Accessed at: 9 Januari 2013]

[36] Bullis K. 2009. *Ultra-High-Power Lithium-Ion Batteries* [Article] Available at: <http://www.technologyreview.com/news/412494/ultra-high-power-lithium-ion-batteries/>. [Accessed at 28 Januari 2013]

[37] This information is company proprietary. Therefore this source will not be mentioned in the report.

[38] European Commission *Hydrogen Storage: State-of-the-art and Future Perspective* [pdf] Available at: <http://publications.jrc.ec.europa.eu/repository/bitstream/111111111/6013/1/EUR%2020995%20EN.pdf> [Accessed at 8 January 2013]

[39] Quantum Technologies *Hydrogen Composite Tank Project* [pdf] Available at: <http://www1.eere.energy.gov/hydrogenandfuelcells/pdfs/iiia1_sirosh.pdf> [Accessed at 18 December 2012]

[40] SAE International *Worldwide Hydrogen Fuelling Protocol* [pdf] Available at: <http://www.energy.ca.gov/contracts/notices/2012-07-10_workshop/presentations/SAE_Jesse_Schneider_Fueling_Protocol.pdf> [Accessed at 9 January 2013]

[41] Air Liquide *Hydrogen Refuelling Stations* [pdf] Available at: <http://www.airliquideadvancedtechnologies.com/file/otherelement/pj/fc/c1/e6/ee/al_plaquette_hydrogene_uk1910402522316753852.pdf> [Accessed at 9 January 2013]

[42] General Motors *Pressure Vessels for Hydrogen vehicles* [pdf] Available at: <http://www1.eere.energy.gov/hydrogenandfuelcells/pdfs/ihfpv_hansen.pdf> [Accessed at 9 January 2013]

[43] *Hydrogen Properties* [pdf] Available at: <http://www1.eere.energy.gov/hydrogenandfuelcells/tech_validation/pdfs/fcm01r0.pdf> [Accessed at 9 January 2013]

[44] The Engineering Toolbox *Flammability Concentration Limits* [online] Available at: <http://www.engineeringtoolbox.com/explosive-concentration-limits-d_423.html> [Accessed at 15 January 2013]

[45] International Conference of Hydrogen Safety *Fire safety of Hydrogen-Fueled Vehicles* [pdf] Available at: <http://www.mvfri.org/MVFRI_reports/ICHS%20Piza%20-%20Stephenson%20Sep%202005.pdf> [Accessed at 10 January 2013]

[46] Hydrogen 2000 *Hydrogen: the Matter of Safety* [pdf] Available at: <http://www.hydrogen2000.com/sfty_booklet.pdf> [Accessed at 10 January 2013]

[47] Parsons, J.S., Goodson, R.E. and Goldschmied, F.R., 1974. *Shaping of Axisymmetric Bodies for Minimum Drag in Incompressible Flow* [pdf] Available at: <http://www.cafefoundation.org/v2/pdf_tech/Drag.Reduction/5.AIAA-48131-445.pdf> [Accessed 4 December 2012].

[48] Dodbele, S.S., van Dam, C.P. and Vijgen, P.M.H.W., 1986. *Design of Fuselage Shapes for Natural Laminar Flow* [pdf] Available at: <http://ntrs.nasa.gov/archive/nasa/casi.ntrs.nasa.gov/19860014381_1986014381.pdf> [Accessed 3 December 2012].

[49] Stückl, S., van Toor, J. and Lobentanzer, H., 2012. *Voltair - The all electric propulsion concept platform - a vision for atmopheric friendly flight.*

[50] Lewison, G.L., 2002. *Aerial View Systems*[pdf] Available at: <http://www.aerialviewsystems.com/ArielView.pdf> [Accessed 2 January 2013].

[51] de Mattos, B.S., Papa, R. and de Castro Santos, L.C., 2004. *Considerations about Forward Fuselage Aerodynamic Design of a Transport Aircraft*[pdf] Available at: <http://www.aer.ita.br/~bmattos/download/fuselage_aiaa.pdf> [Accessed 28 December 2012].

[52] Peterman, B.E., 1987. *Laminar flow: The Cessna perspective.* [pdf] Available at: <http://ntrs.nasa.gov/archive/nasa/casi.ntrs.nasa.gov/19900003191_1990003191.pdf> [Accessed at 18 December 2012]

[53] Abbott, I.H., von Doenhoff, A.E., 1959. *Theory of Wing Sections.* Toronto: General Publishing Company, Ltd.

[54] Fujino, M., Yoshizaki, Y., Kawamura, Y., 2003. Natural-Laminar-Flow Airfoil Development for a Lightweight Business Jet, *Journal of Aircraft*, [online] Available at: <http://164.109.24.31/pdf/tech_papers/Journal_of_Aircraft_Vol40_No4_P609_P615_SHM_1_NLF.pdf> [Accessed at 18 December 2012]

[55] Lednicer, D. *The Incomplete Guide to Airfoil Usage* [online] Available at: <http://www.ae.illinois.edu/m-selig/ads/aircraft.html> [Accessed at 18 December 2012]

[56] Selig, M.S., Maughmer, M.D., Somers, D.M., 1995. Natural-Laminar-Flow Airfoil for General-Aviation Applications. *Journal of Aircraft*, 32(4).

[57] EASA, 2003. *Certification Specifications for Normal, Utility, Aerobatic and Commuter Category Aeroplanes CS-23*, pp. 2-FTG-2-10 [pdf], available at http://www.easa.europa.eu/agency-measures/docs/agency-decisions/2003/2003-014-RM/decision_ED_2003_14_RM.pdf [Accessed at 19 December 2012]

[58] Raymer D.P., 1999. *Aircraft Design: A Conceptual Approach.* 3rd ed. Reston: AIAA Inc.

[59] Abbott I.A., Von Doenhoff A.E., 1949. *Theory of Wing Sections*, Dover ed. General Publishing Company, Canada, Toronto.

[60] Raymer D.P., 1999. *Aircraft Design: A Conceptual Approach.* 3rd ed. Reston: AIAA Inc., pp. 340

[61] Tu, E.L., 1996. *Numerical Study of Steady and Unsteady Canard-Wing-Body Aerodynamics* [pdf] Available at: <http://www.engbrasil.eng.br/index_arquivos/art111.pdf> [Accessed at 27 December 2012]

[62] Yip., L.P., 1985. *Wind-Tunnel Investigation of a Full-Scale Canard-Configured General Aviation Airplane* [pdf] Available at: <http://purl.access.gpo.gov/GPO/LPS54941> [Accessed at 30 December 2012]

[63] Gloss, B.B., 1974. *The Effect of Canard Leading-Edge Sweep and Dihedral Angle on the Longitudinal and Lateral Aerodynamic Characteristics of a Close-Coupled Canard-Wing Configuration* [pdf] Available at: <http://ntrs.nasa.gov/archive/nasa/casi.ntrs.nasa.gov/19750004860_1975004860.pdf> [Accessed at 21 December 2012]

[64] Gratzer, L.B., 1994. *Blended Winglet.* U.S. Pat. 5,348,253.

[65] Rutan Aircraft Factory, Inc., 1980. *Long EZ Owner's manual, First edition.* [pdf]

[66] Brian Dunbar, 2008. *Dryden Flight Research Center, Fact Sheet Winglets.* [online] Available at: <http://www.nasa.gov/centers/dryden/about/Organizations/Technology/Facts/TF-2004-15-DFRC.html> [Accessed at 20 December 2012]

[67] Fox., M., 2012. *Optimizing Blended Winglet Radii on Homebuilt Canard Aircraft* [online] Available at: <http://www.apollocanard.com> [Accessed at 9 January 2013]

[68] Maughmer, M.D., Swan, T.S., Willits, S.M., 2004. *The Design and Testing of a Winglet Airfoil for Low-speed Aircraft* [pdf] [Accessed at 10 January 2013]

[69] La Rocca, G., 2009. Fuselage Systems and Landing Gear, *AE1201 Aerospace Design and Systems Engineering*. TU Delft, unpublished.

[70] Sadraey, M., *landing Gear Design*. [internet] Available at: <http://faculty.dwc.edu/sadraey/Chapter%209.%20Landing%20Gear%20Design.pdf> [Accessed 14 January 2013]

[71] Roskam, J., 2000. *Part4; Layout of Landing Gear and Systems*. 3rd ed. lawrence, Kansas: DAR Corporation.

[72] Raymer, D.P., 1999. *Aircraft Design: A Conceptual Approach*. 3rd ed. Ohio:AIAA.

[73] Philips J.D., 1985. *Approximate Neutral Point of a Subsonic Canard Aircraft*, [pdf], available at http://ntrs.nasa.gov/archive/nasa/casi.ntrs.nasa.gov/19850016894_1985016894.pdf, [11-1-2012]

[74] Philips J.D., 1985. *Downwash in the Plane of Symmetry of an Elliptically Loaded Wing*, [pdf], available at http://ntrs.nasa.gov/archive/nasa/casi.ntrs.nasa.gov/19850007384_1985007384.pdf, [11-1-2012]

[75] Raymer D.P., 1999. *Aircraft Design: A Conceptual Approach*, AIAA Educational Series, Reston, Virginia. pp.487

[76] Melin T., 2000. *A Vortex Lattice MATLAB Implementation for Linear Aerodynamic Wing Applications*. Royal Institute of Technology, Stockholm. Available at http://www.redhammer.se/tornado/thesis.pdf

[77] M., Sadraey, 2012. *Aircraft Design: A Systems Engineering Approach, Chapter 12* [pdf] Available at: <http://faculty.dwc.edu/sadraey/Aileron%20Design.pdf> [Accessed at 11-1-2013]

[78] Anonymous. *TL Sting-2000 Specifications* [online] Available at: <http://www.aopa.pt/files/NoticiasAopa/Noticias014.pdf> [Accessed at 14-1-2013]

[79] Gill, E. *Lecture slides AE2-101 Lecture 04* [ppt]

[80] Mulder J.A. et al., 2011. *Lecture Notes AE3302 Flight Dynamics*, Control and Simulation division, Delft University of Technology

[81] BRS Aviation, 2009. *Ballistic Parachute Weight* [pdf] Available at: <http://www.brsaerospace.com/cessna_182_faq.aspx/> [Accessed at 14 January 2013]

[82] BRS Aviation, 2009. *BRS Ballistic Parachutes* [pdf] Available at: <http://www.brsaerospace.com/files/brsparachutes/files/First%20Responders.pdf/> [Accessed at 14 January 2013]

[83] Cessna Aircraft Company, p96, 1979. *Cessna 182Q Dimensions* [online] Available at: <http://www.aboveallsba.com/Airplane%20data/POH/C182-POH.pdf/> [Accessed at 14 January 2013]

[84] BRS Aviation, 2009. *BRS Experimental Aircraft* [online] Available at: <http://www.brsaerospace.com/experimental_aircraft.aspx/> [Accessed at 14 January 2013]

[85] FAAtest *Pressurized Airplanes* Available at: <http://www.faatest.com/books/FLT/Chapter16/PressurizedAirplanes.htm> [Accessed at 18 January 2013]

[86] Rogers, T., 1998. *Transponder Basics* Available at: http://www.avweb.com/news/avionics/183231-1.html [Accessed 18 January 2013]

[87] Flightsim Aviation Zone *FAR Pressurized Cabins* Available at: <http://www.flightsimaviation.com/data/FARS/part_25-841.html> [Accessed at 18 January 2013]

[88] USAPHC *Altitude Effectson the Human Body* Available at: <http://phc.amedd.army.mil/topics/discond/ai/Pages/AltitudeEffects.aspx> [Accessed at 21 January 2013]

[89] Reddy, J. N.*Mechanics of Laminated Composite Plates*, CRC Press, 1997.[Accessed at 7 January 2013]

[90] Turgut.R *Manufacturing srtcutral analysis of a lightweight sanwich composite UAV wing.*Middle east technical university sept 2007.[Accessed at 7 January 2013]

[91] Sanderson.K. *Flights of green fancy.*[online] Available at: http://www.nature.com/news/2008/080514/full/453264a.html

[92] *MATERIALS REVOLUTIONISE AEROSPACE ENGINEERING.*[online] Available at: http://aero103.blogspot.nl/2011/03/composite-materials-revolutionise.html

[93] Shroff, S., 2012. *A review of grid stiffened structures in aerospace applications* [report] Renieri, G. D. Continuous filament advanced composite isogrid: a promising structural concept. *Fibrous Composites in Structural Design.* New York: Plenum Press, 1980.

[94] Meink, T. E., n.d. *Composite Grid vs. Composite Sandwich: A Comparison Based on Payload Shroud Requirements* [report] Available at: <http://ieeexplore.ieee.org/stamp/stamp.jsp?tp=&arnumber=686820> [accessed 29 November 2012].

[95] Huybrechts, Steven M., Hahn, Steven E. and Meink, Troy E.1999. *Grid Stiffened Structures: A survey of fabrication, analysis and design methods* [Paper] Available at: <http://www.iccm-central.org/Proceedings/ICCM12proceedings/site/papers/pap357.pdf>[accessed 29 November 2012].

[96] TORAYCA *Data sheet of T800* Available at: <http://www.google.com/url?sa=t&rct=j&q=carbon+fiber+T800h+compression+strength&source=web&cd=1&ved=0CDcQFjAA&url=http%3A%2F%2Fwww.toraycfa.com%2Fpdfs%2FT800HDataSheet.pdf&ei=zBvTUPeCParA0QXtl4GAAg&usg=AFQjCNEexMZn3kwsZVyj6BViNdpyGDqYjg&bvm=bv.1355534169,d.d2k&cad=rja>

[97] Kassapoglou, C., 2010. *Design and Analysis of Composite Structures* Chichester: John Wiley & Sons Ltd.

[98] Beckwith, S. 1998. *Sandwich Core Materials & Technologies - Part I.* [online] Available at: <http://www.sampe.org/news/TechTidbitJulyAugust08.pdf>. [Accessed at: 21 December 2012]

[99] Brent Strong, A. unknown. *Core Materials - Part I: The Meat Of The Sandwich* [online] Available at: <http://strong.groups.et.byu.net/pages/articles/articles/cores.pdf>. [Accessed at: 21 December 2012]

[100] N.a. 2012 *Certification Specifications for Normal, Utility, Aerobatic, and Commuter Category Aeroplanes* [pdf] Available at: <http://www.easa.europa.eu/agency-measures/docs/certification-specifications/CS-23/CS-23%20Amdt%203.pdf> [Accessed 18 January 2013]

[101] Pavlov, L., 2012. *Analysis, Optimum Design, Cost-eiňĂective Manufacturing and Testing of Advanced Composite Grid-StiiňĂened Structures for Aircraft Fuselage Applications* M. Sc. Delft University of Technology.

[102] Warrior, N., 2005 *Recycling carbon fiber* [online] Available at: <http://www.bis.gov.uk/files/file34992.pdf> [Accessed 21 January 2013]

[103] de Vegt, O.M., Haije, W.G., December 1997 *Comparative environmental life cycle assessment of composite materials* [online] Available at: <Comparativeenvironmentallifecycleassessmentofcompositematerials> [Accessed 21 January 2013]

[104] Black, S., 12 December 2011 *CompositesWorld carbon fiber conference features demand/supply update.* CompositesWorld [online] Available at: <http://webcache.googleusercontent.com/search?q=cache:18H0ia1dDOwJ:www.compositesworld.com/news/compositesworld-carbon-fiber-conference-features-demandsupply-update+&cd=2&hl=nl&ct=clnk&gl=nl> [Accessed 21 January 2013]

[105] Black, S., 12 December 2011 *Carbon fiber market: Gathering momentum.* CompositesWorld [online] Available at: <http://webcache.googleusercontent.com/search?q=cache:wGBT_BfmkoEJ:www.compositesworld.com/articles/carbon-fiber-market-gathering-momentum+&cd=1&hl=nl&ct=clnk&gl=nl> [Accessed 12 December 2012]

[106] Anonymous, 6 March 2012 *Carbon Fibre Industry Set For Strong Growth to 2020.* [online] Available at: <http://www.netcomposites.com/news/carbon-fibre-industry-set-for-strong-growth-to-2020/7300> [Accessed 13 December 2012]

[107] Warren, D., 2010. *Low Cost Carbon Fiber Overview.* Oak Ridge National Laboratory.

[108] Sanjay K. Mazumdar, 2002*Composites Manufacturing: Materials, Product, and Process Engineering.*(Second edition) CRC Press

[109] Unknown,2010 *Vacuum bagging techniques*,Seventh editionWEST SYSTEM,Published by Gougeon Brothers

[110] Unknown,*The filament winding process*,Cadfil Available at:<http://www.cadfil.com/filamentwindingprocess.html>[Accessed 6 January 2013]

[111] Burgohain, M. and Velmurugan, R. 2011,*Study of filament wound grid-stiffened composite cylindrical structures.* Composite Structures, pp. 1031-1038.

[112] Stargazer Online *Rutan Model 61 'Long-EZ'* [online] Available at: <http://stargazer2006.online.fr/aircraft/long-ez.htm> [Accessed at 18 January 2013]

[113] Cadwallader, L. C., Herring, J. S., 1999. *Safety Issues with Hydrogen as a Vehicle Fuel* [PDF] Available at: <http://inl.gov/hydrogenfuels/projects/docs/h2safetyreport.pdf> [Accessed 13 December 2012]

[114] Roskam J., 1990. *Airplane Design Part VIII: Airplane Cost Estimation: Design, Development, Manufacturing and Operating* Faculty of Aerospace Engineering, University of Kansas

[115] Piper Aircraft Corporation *General Avaiation* [ppt] Available at: <http://www.eas.ee/media/com_events/attachments/59/5.%20General%20Aviation%20Overview%202012%20-%20William%20Piper.pdf> [Accessed at 18 January 2013]

[116] Gill, E., 2012. Risk & Reliability. *AE3-201 Systems Engineering for Aerospace*, TU Delft

Appendix A

Appendix Cycle-Tempo

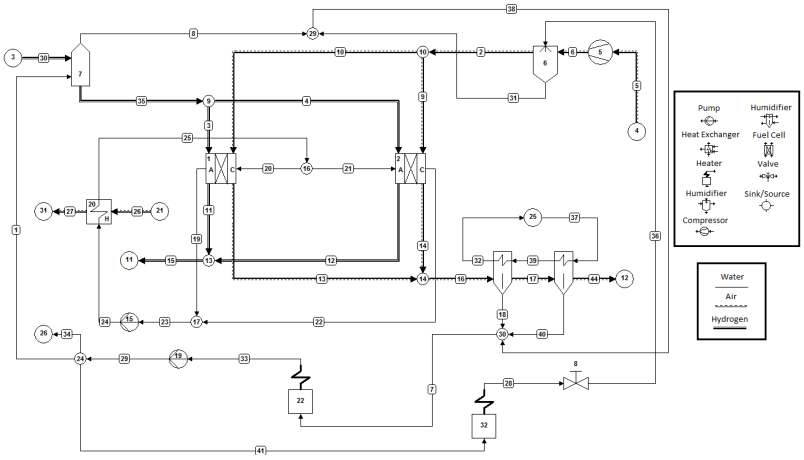

Appendix B

Appendix Airfoil Data

Table B.1: NASA/Langley NLF Airfoils data

Airfoil code	NLF(1)-0215F	NLF(1)-0416	NLF(1)-0115	NLF1015	Eppler 1230
$(t/c)_{max}$	15%	15.9%	15%	15%	17.4%
$C_{l_{max}}$	1.72	1.53	1.29	1.70	1.612
Stall angle	14.0	13.5	14.0	8.0	15.0
Maximum L/D	122.5	59.0	122.5	54.6	44.6
$\alpha_{L=0}$	-6.2	-4.2	-2.2	-7.4	-3.8

Appendix C

Appendix Reference System

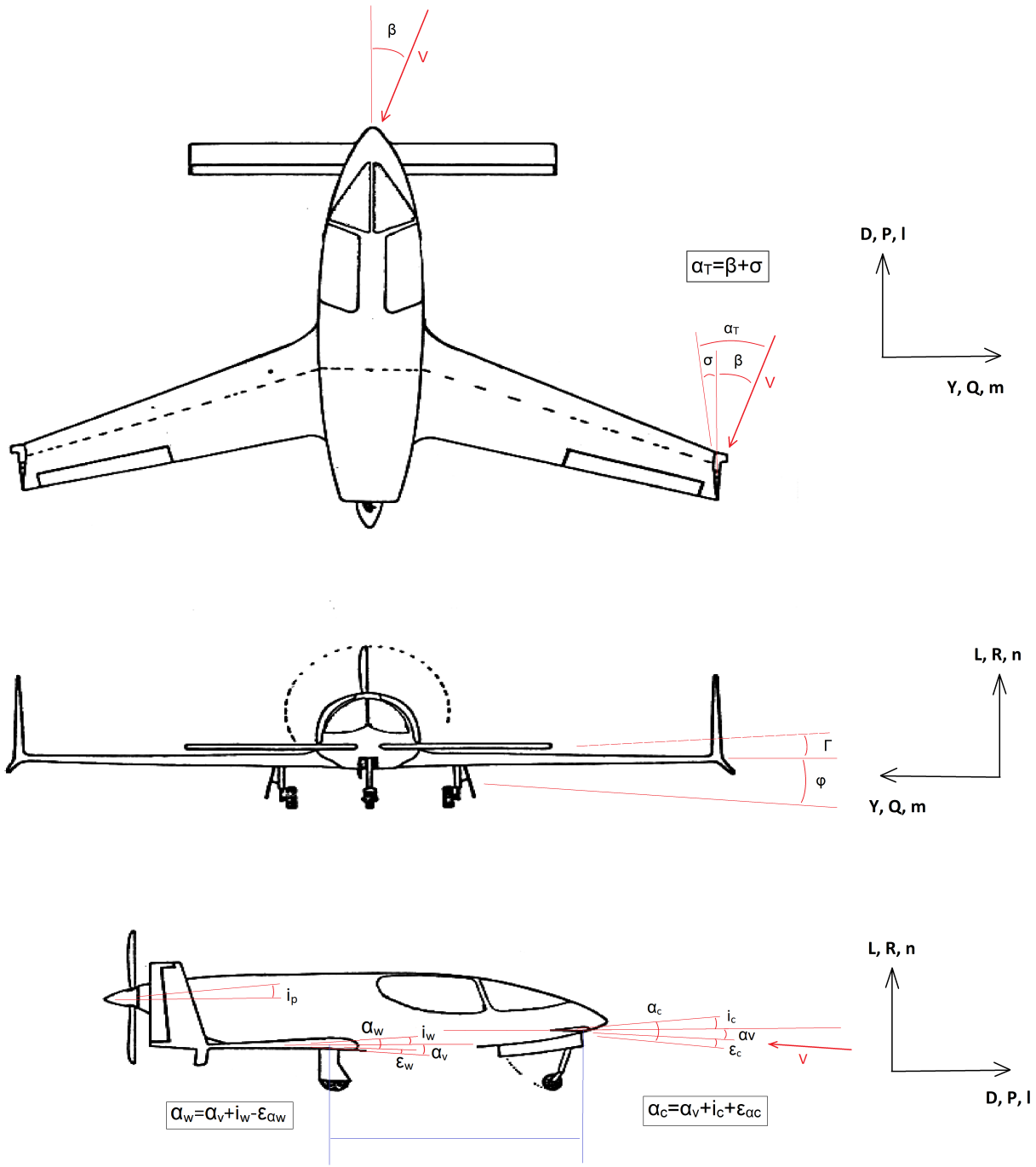

Figure C.1: Reference System Zero EZE

Appendix D

Appendix Tornado Model Data

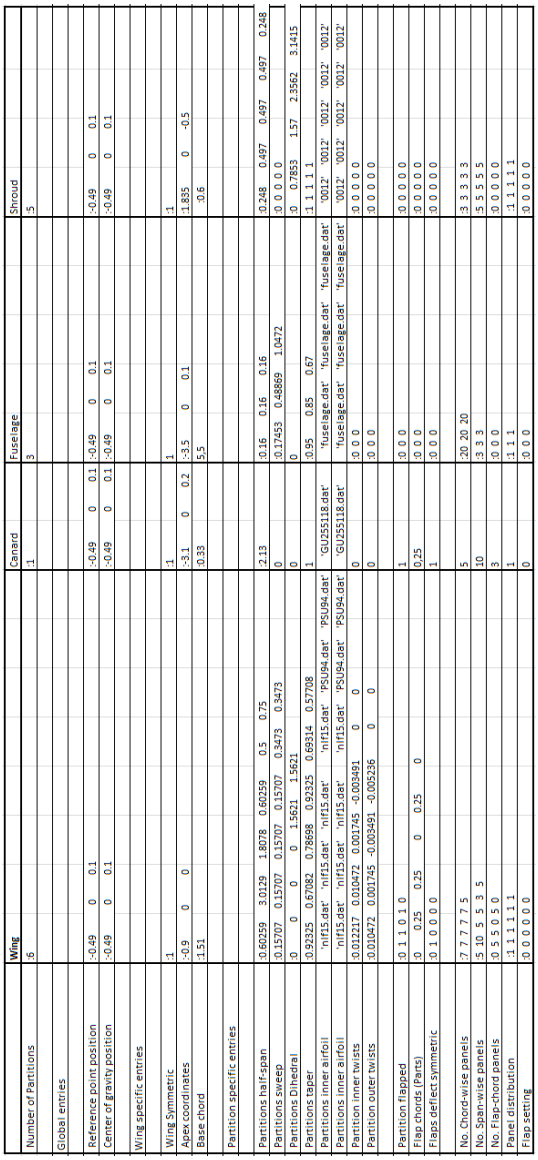

	Wing	Canard	Fuselage	Shroud
Number of Partitions	6	1	3	5
Global entries				
Reference point position	-0.49 0 0.1	-0.49 0 0.1	-0.49 0 0.1	-0.49 0 0.1
Center of gravity position	-0.49 0 0.1	-0.49 0 0.1	-0.49 0 0.1	-0.49 0 0.1
Wing specific entries				
Wing Symmetric	1	1	1	1
Apex coordinates	-0.9 0 0	-3.1 0 0.2	-3.5 0 0.1	-1.835 0 -0.5
Base chord	1.51	0.33	5.5	0.6
Partition specific entries				
Partitions half-span	0.60259 3.0129 1.8078 0.60259 0.5 0.75	2.13	0.16 0.16 0.16	0.248 0.497 0.497 0.497 0.497 0.248
Partitions sweep	0.15707 0.15707 0.15707 0.15707 0.3473 0.3473	0	0.17453 0.48869 1.0472	0 0 0 0 0
Partitions Dihedral	0 0 0 0 1.5621 1.5621	0	0	0 0.7853 1.57 2.3562 3.1415
Partitions taper	0.92325 0.67082 0.78698 0.92325 0.69314 0.57708	1	0.95 0.85 0.67	1 1 1 1 1
Partitions inner airfoil	'nlf15.dat' 'nlf15.dat' 'nlf15.dat' 'nlf15.dat' 'PSU94.dat' 'PSU94.dat'	'GU255118.dat'	'fuselage.dat' 'fuselage.dat' 'fuselage.dat'	'fuselage.dat' '0012' '0012' '0012' '0012'
Partitions inner airfoil	'nlf15.dat' 'nlf15.dat' 'nlf15.dat' 'nlf15.dat' 'PSU94.dat' 'PSU94.dat'	'GU255118.dat'	'fuselage.dat' 'fuselage.dat' 'fuselage.dat'	'0012' '0012' '0012' '0012' '0012'
Partition inner twists	0.012217 0.010472 0.001745 -0.003491 0 0	0	0 0 0	0 0 0 0 0
Partition outer twists	0.010472 0.001745 -0.003491 -0.005236 0 0	0	0 0 0	0 0 0 0 0
Partition flapped	0 1 1 0 1 0	1	0 0 0	0 0 0 0 0
Flap chords (Parts)	0 0.25 0.25 0 0.25 0	0.25	0 0 0	0 0 0 0 0
Flaps deflect symmetric	0 1 0 0 0 0	1	0 0 0	0 0 0 0 0
No. Chord-wise panels	7 7 7 7 7 5	5	20 20 20	3 3 3 3 3
No. Span-wise panels	5 10 5 5 3 5	10	3 3 3	5 5 5 5 5
No. Flap-chord panels	0 5 5 0 5 0	3	0 0 0	0 0 0 0 0
Panel distribution	1 1 1 1 1 1	1	1 1 1	1 1 1 1 1
Flap setting	0 0 0 0 0 0	0	0 0 0	0 0 0 0 0

Figure D.1: Input data Tornado model

Appendix E

Appendix Material Properties

Grid material properties

Young's Modulus [MPa]	Poisson Ration [-]	Density [kg/m^3]
135000	0.3	1600

Skin properties

Number of plies	11
Ply thickness	0.1524 mm
Skin thickness	1.6764 mm
Young's Modulus 11	84000 MPa
Young's Modulus 22	30800 MPa

Ply orientation

Ply	Orientation
1	45°
2	-45°
3	0°
4	0°
5	0°
6	90°
7	0°
8	0°
9	0°
10	-45°
11	45°

Ply properties

Young's modulus 11	135000 MPa
Young's modulus 22	10000 MPa
Poisson Ratio [-]	0.3
Shear Modulus 12	3800 MPa
Density	1600 kg/m^3
Tension Stress Limit 11	1500 MPa
Tension Stress Limit 22	50 MPa
Compression Stress Limit 11	1200 MPa
Compression Stress Limit 22	250 MPa
Shear Stress Limit	120 MPa
Bonding Shear Stress Limit	120 MPa

Figure E.1: Grid-, skin- and ply properties

Appendix F

Appendix Functional Mission Description Figures

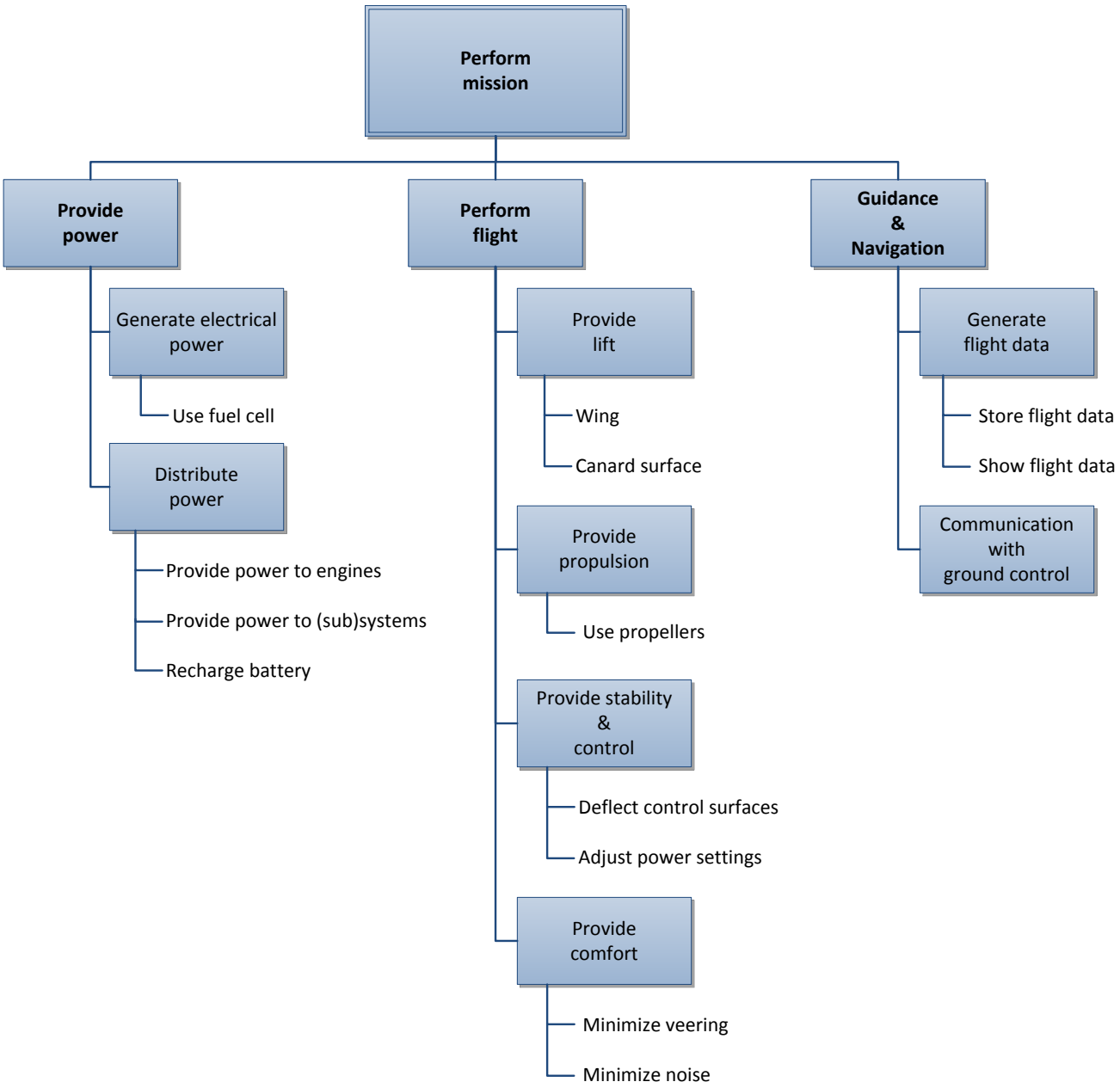

Figure F.1: Functional Breakdown Structure

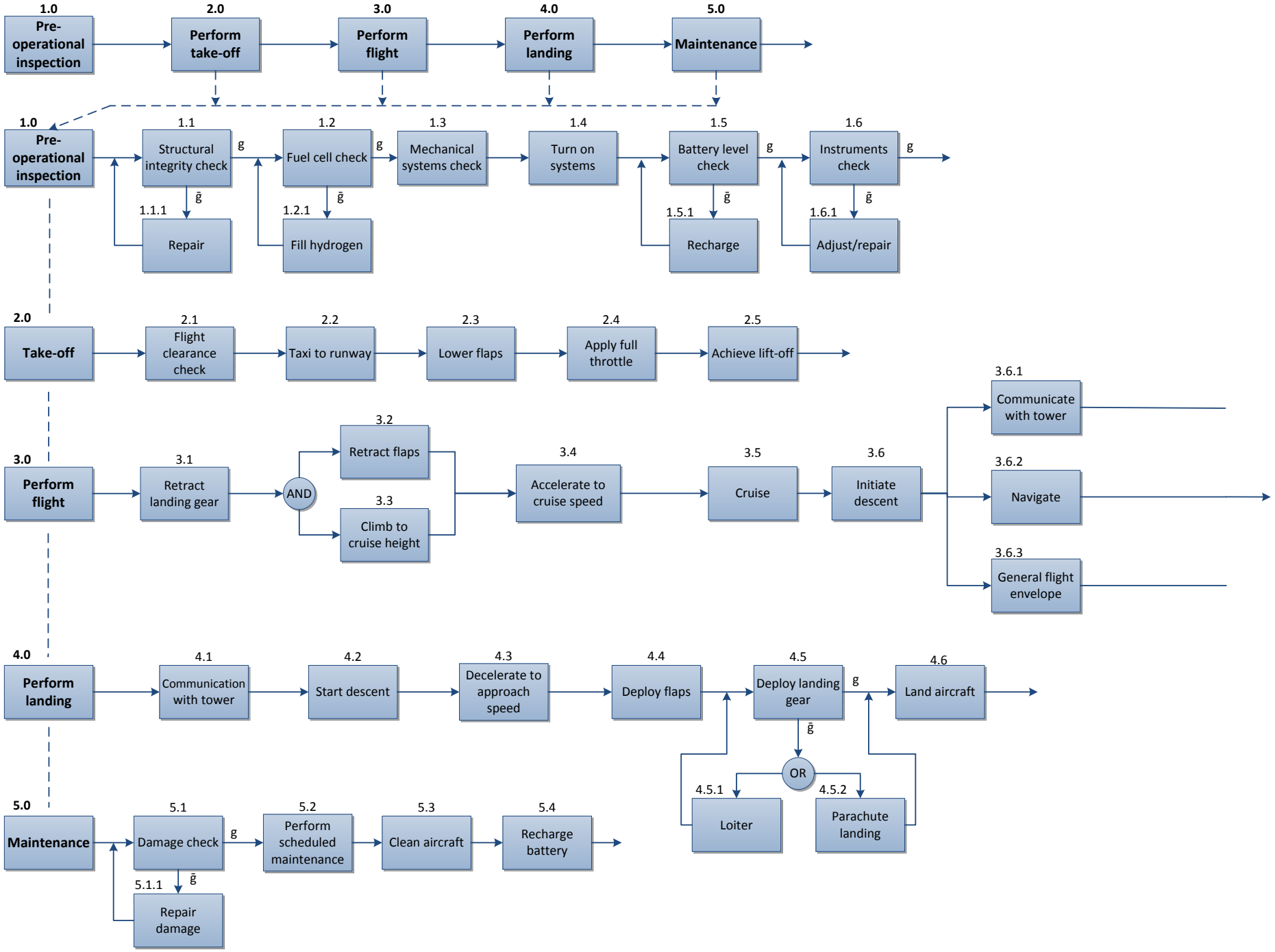

Figure F.2: Functional Flow Diagram